Squirmer microswimmers under gravity

vorgelegt von
M.Sc.

Felix Raoul Lukas Rühle

ORCID: 0000-0001-6493-7204

von der Fakultät II - Mathematik und Naturwissenschaften
der Technischen Universität Berlin
zur Erlangung des akademischen Grades
Doktor der Naturwissenschaften
- Dr. rer. nat. -

genehmigte Dissertation

Promotionsausschuss

Vorsitzender:	Prof. Dr. Michael Lehmann
Gutachter:	Prof. Dr. Holger Stark
Gutachter:	Prof. Dr. Andreas Menzel

Tag der wissenschaftlichen Aussprache: 24.11.2022

Berlin 2022

Zusammenfassung

Mikroschwimmer sind biologische Organismen sowie künstlich hergestellte Teilchen mikroskopischer Größe, die sich selbständig in einer Flüssigkeit fortbewegen. In dieser Arbeit wird ein Modell-Schwimmer untersucht, der *Squirmer* genannt wird. Dieser approximiert verschiedene reale Schwimmer, indem er deren Flussfelder imitiert. Der Squirmer-Parameter β dient zur Unterscheidung von Pushern ($\beta < 0$), Pullern ($\beta > 0$) und neutralen Squirmern ($\beta = 0$) und ein endlicher Chiralitäts-Parameter χ erzeugt Squirmer mit Rotlet-Dipol.

Wir verwenden die numerische Methode der *Vielteilchen-Stoß-Dynamik*, um ein Fluid bei kleinen Reynolds-Zahlen und die darin gelösten Schwimmer mitsamt ihrer hydrodynamischen Wechselwirkungen und thermischen Fluktuationen zu simulieren. Zugleich wird eine externe Gravitationskraft auf die Schwimmer angewendet. Diese wird durch das Verhältnis der aktiven Geschwindigkeit zur Sedimentationsgeschwindigkeit beschrieben, welches α genannt wird. Weiterhin wenden wir ein Gravitationsdrehmoment an, welches durch Bodenlastigkeit der Squirmer entsteht.

Unsere Studie des einzelnen Squirmers zeigt die Vielzahl möglicher Trajektorien auf, die durch die hydrodynamischen Wechselwirkungen in der Nähe einer Wand erzeugt werden. Wir beobachten schwebende Zustände, die entweder stabil oder metastabil sein können. Ersteres ist für neutrale Squirmer und Puller der Fall. Puller schweben jedoch nur dann, wenn ein Schwellwert des Geschwindigkeitsverhältnisses α_{th} überschritten wird. Ansonsten stecken sie aufgrund hydrodynamischer Anziehungswirkung an der Wand fest. Pusher gleiten horizontal in der Nähe der Wand und erreichen ihre Schwebehöhe, sobald sie an dieser aufgerichtet werden. Da die vertikale Orientierung nicht stabil gegenüber dem vorherrschenden hydrodynamischen Flussfeld ist, kommt es zu periodisch wiederauftretenden Schwebe- und Gleitzuständen.

Die Kombination aus der Vortizität der Stokeslet-Felder und einem Gravitationsdrehmoment wird *Gyrotaxis* genannt, die zu Musterbildung führen kann. An einem Squirmer-Paar beobachten wir gekoppelte Oszillationen, die tanzenden Volvox-Algen ähneln. Bei großen Teilchenzahlen stellen wir im Zustandsdiagramm neben konventionellen und invertierten Sedimentationsprofilen auch kollektive Konvektionsbewegungen fest. Diese bestehen für neutrale Squirmer aus langgestreckten sinkenden Clustern, die wir Schwaden nennen. Weiterhin treten am Boden des Systems Konvektionsrollen auf, wenn die externen und die hydrodynamisch erzeugten Winkelgeschwindigkeiten vergleichbar sind. Bei starker externer Kraft und starkem Drehmoment treten poröse Cluster auf, aus denen einzelne Squirmer herausschnellen. Im Gegensatz zu neutralen Squirmern zeigen Pusher und Puller nur schwache Schwadenbildung und keine Konvek-

tionsrollen.

Wir untersuchen die gyrotaktische Strukturbildung quantitativ an sedimentierten bodenlastigen Squirmern, die über der unteren Wand schweben. Wir stellen fest, dass für neutrale Squirmer eine ausgeprägte Clusterbildung bei endlichem Drehmoment auftritt. Für schwache Drehmomente sind diese Cluster zunächst fragil, aufgrund starker Squirmer-Bewegung. Bei höheren Drehmomenten verdichten sich die Cluster und der typische Clusterabstand nimmt ab. Eine Verdichtung der Cluster tritt auch bei höheren Gravitationskräften durch die Wechselwirkung mit der Wand auf. Pusher bilden keine stabilen Cluster, während Pullersysteme pyramidale Strukturen zeigen. Allerdings ist das zur Clusterbildung notwendige Drehmoment höher als für neutrale Squirmer. Squirmer mit Rotletdipol bilden Cluster aus, solange der Parameter χ nicht zu hoch ist. Diese Cluster zirkulieren an der unteren Wand durch die hydrodynamische Wechselwirkung der einzelnen Squirmer mit der Oberfläche.

Abstract

Microswimmers are biological organisms or artificially produced particles with microscopic size, which move autonomously inside a fluid. In this work a model swimmer called *squirmer* is investigated. It approximates different real swimmers by mimicking their flow fields. The squirmer parameter β distinguishes pushers ($\beta < 0$) from pullers ($\beta > 0$) and neutral squirmers ($\beta = 0$) and a finite chirality parameter χ creates squirmers with a rotlet dipole.

We use the numerical method of *multi-particle collision dynamics* in order to simulate a fluid at low Reynolds numbers and the suspended swimmers, including their hydrodynamic interactions and thermal fluctuations. At the same time, we apply an external gravitational force to the swimmers. It is characterized by the ratio of the active velocity to the sedimentation velocity, which is called α. Furthermore, we apply a gravitational torque which arises from bottom-heaviness of the squirmers.

Our study of the single squirmer shows the variety of possible trajectories which are generated by the hydrodynamic interactions in proximity to a wall. We observe floating states, which can be stable or metastable. The former case applies to neutral squirmers and pullers. However, pullers only float, if a threshold value of the velocity ratio α_{th} is exceeded. Otherwise, they are pinned to the wall due to hydrodynamic attraction. Pushers slide horizontally close to the wall and approach their floating height, as soon as they reach an upright orientation. Since the vertical orientation is unstable in the surrounding hydrodynamic flow field, sliding and floating states occur recurrently.

The combination of Stokeslet vorticity fields and a gravitational torque is called *gyrotaxis* and can lead to pattern formation. We observe coupled oscillations of a squirmer pair, which resemble dancing Volvox algae. At large particle numbers, in addition to conventional and inverted sedimentation profiles, we observe convective motion. For neutral squirmers, it consists of elongated sinking clusters, which we call plumes. Furthermore, convective rolls occur at the bottom of the system, when the external and the hydrodynamically induced angular velocities are comparable. At large external force and torque, porous spawning clusters occur, which eject single squirmers. In contrast to neutral squirmers, pushers and pullers show only weak plume formation and no convective rolls.

We investigate gyrotactic cluster formation quantitatively with sedimented bottom-heavy squirmers which float above the bottom wall. We find a pronounced cluster formation of neutral squirmers at finite torques. These clusters are fragile at weak torques, due to strong squirmer motion. At larger torques the clusters compactify and the typical cluster distance decreases. Higher gravitational forces also cause a

compactification of clusters due to hydrodynamic wall interactions. Pushers do not form stable clusters, whereas puller systems show pyramidal structures. However, the necessary torque for cluster formation is higher than for neutral squirmers. Rotlet dipole squirmers form clusters, as long as the parameter χ is not too high. These clusters circulate at the bottom wall due to the hydrodynamic surface interactions of the individual squirmers.

Contents

1. Introduction

The interdisciplinary field of *active motion* is an intriguing research topic at the intersection of biology and physics, which has elicited a lot of interest in recent years [1–3]. From an evolutionary perspective, motion satisfies an organism's needs of finding food, mating, or escaping predators. Seen from a physicist's perspective, active motion is a process far from thermodynamic equilibrium. Non-equilibrium dynamics pervades active motile systems since energy is consumed locally by the individual agents, which transform it into self-propulsion [2, 3]. This leads to states and patterns unreachable in equilibrium, implicating both single-particle behaviour and collective dynamics. Analysing single self-propelled particles, one can identify and distinguish different fascinating forms of *taxis*. For example, sperm cells are able to swim upstream against flow (rheotaxis) and *E. coli* bacteria control their rotational diffusion in response to the distribution of nutrients (chemotaxis). Furthermore, large-scale collective structures and dynamics emerge from the local interactions of individual agents [4, 5]. Important examples are phase separation [6, 7], cluster formation [8, 9] and swarming [10, 11].

Fascinatingly, active motion in nature transcends length scales and thus a wide range of self-propelled agents are the subject of research. Examples include flocks of birds [12], schools of fish [13], and herds of sheep [14], as well as accumulation of algae [15] and bacterial turbulence [16]. Already on the micron scale biological examples include a plethora of organisms, both eukaryotes and prokaryots [2, 3, 17]: amoeba, ciliates, algae, sperm cells, as well as bacteria and pathogens, such as trypanosomes [18, 19]. The desired fruits of microswimmer research are very diverse. For instance, one aim is to drive microscopic motors with bacteria [20]. Furthermore, treatment options for cervical cancer [21] and infectious biofilms [22] are considered. A better understanding of the spatial distribution of marine phytoplankton [23] has high ecological importance.

In addition to biological swimmers, numerous artificial active particles have been manufactured, in order to study novel states of matter and ultimately harness non-equilibrium self-organization for technology [17, 24]. Active colloids use chemical or physical reactions in a solute for phoresis, *i.e.*, self-propulsion along induced gradients of a macroscopic physical quantity, such as concentration or temperature [25, 26]. Active emulsion droplets use the *Marangoni* effect, which leads to fluid motion on the droplet's surface due to inhomogeneous surface tension, and thus to self-propulsion [27, 28]. Application of such synthetic particles include cargo-carrying microrobots, for example for drug delivery [29, 30] and removing microplastics as a form of water treatment [31].

In parallel, numerous theoretical model particles have been studied, in order to look for the generic properties of active systems. These include the famous Vicsek model

[32], as well as active Brownian particles [33], and self-propelled rods [34].

Another important active particle is the squirmer model [35, 36]. It uses a flow field on its surface for self-propulsion and was intended to describe ciliates like *Paramecium*. The squirmer is therefore a model for so-called *microswimmers*. These are active particles that move inside a fluid and create flow fields which lead to long-range interactions with surfaces and with other swimmers [37, 38]. These hydrodynamic interactions are an important aspect of emergent collective behaviour [39–44]. Importantly, microswimmers mostly move under conditions of low *Reynolds number*. Hence, viscous forces dominate over inertial forces. This challenges locomotion profoundly, since no motion can be achieved by any reciprocal body deformation [45, 46]. Furthermore, thermal noise often interferes with the directed motion of a microswimmer. To deal with these conditions, a large number of swimming techniques have evolved, using deformations, such as helical rotations of flagella [47] or metachronal ciliary waves [48]. The synthetic particles we mentioned use hydrodynamic surface flows to achieve locomotion. An interesting example for the importance of flow for biological pattern formation, is the so-called paradox of the plankton [49], which states that there is an oversupply of plankton species in violation of standard biological theories of competition. Current research suggests that interactions with external flow fields can segregate species from each other [50].

In this work, we are interested in the influence and effect of gravity on single-swimmer dynamics and collective patterns. Gravity is a ubiquitous influence on any laboratory experiment, as well as in nature. It is therefore highly relevant for both biological and artificial swimmer systems, where it results in novel phenomena [51]. For example, non-equilibrium sedimentation of active swimmers has evoked much attention in recent years [52–55]. Here, a strongly enhanced sedimentation length [53], as well as polar order [54] were observed. Furthermore, patterns formed under gravity are particularly appealing and are summarized under the term *bioconvection* [56]. An important aspect of this collective motion is a phenomenon called *gyrotaxis*, which consists of a combination of gravitational and viscous torques [57–60]. This effect is important for biological matter and has been shown to lead to motion of a pair of Volvox algae which resembles a minuet dance [61], or sinking plumes of micro-organisms [62].

Since the fluid dynamics equations are hard to tackle analytically, especially with many moving suspended particles, numerical simulations are a much-used tool for studying fluid systems, including hydrodynamically interacting swimmers [34, 42, 63]. Here, we use the method of multi-particle collision dynamics (MPCD) to solve the fluid dynamics equations [64, 65], called the Navier-Stokes equations. The motion of the fluid is computed by performing a streaming and a collision step on point-like fluid particles, which conserve momentum. It is thus a mesoscopic simulation technique. Importantly, it incorporates thermal fluctuations which are relevant for most active swimmer systems.

In our numerical simulations, using multi-particle collision dynamics, we show the relevance of hydrodynamics on a single squirmer system under gravity. In particular, the importance of both near field and far field interactions with a no-slip wall at the bottom of the system is demonstrated by comparing simulation results to analytical calculations. We then test the effects of gyrotaxis on a two-squirmer system by ad-

ditionally applying a gravitational torque. Furthermore, we study collective motion at higher density and scan the state diagram of more than 900 bottom-heavy squirmers. We find conventional and inverted sedimentation states, as well as sinking plumes. Plumes in puller and pusher systems are more fragile. Neutral squirmers additionally form convective rolls and spawning clusters. Lastly, we investigate how gyrotactic clusters form in the sedimentation state by varying the external torque, the global density, the amount of gravity, and the hydrodynamic flow fields of the squirmers. We characterize the emerging structures by measuring the cluster sizes and radial distribution functions.

This thesis is structured as follows: In Chapter 2 we introduce the necessary theoretical framework to study microswimmers. This includes both the laws of hydrodynamics and the physics of self-propulsion in a low Reynolds number fluid, as well as stochastic motion. We also introduce our model swimmer, the spherical squirmer. In Chapter 3 we introduce our numerical method, called multi-particle collision dynamics (MPCD). In Chapter 4 analytical and numerical results for a single squirmer under gravity and close to the bottom wall of the system are presented. Chapters 5-7 study collective dynamics. We give a brief overview over the pair dynamics of bottom-heavy squirmers in Chapter 5. In Chapter 6 we discuss the diverse collective states arising at higher densities of squirmers under gravity. Finally, we study cluster formation at the bottom wall due to gyrotaxis in Chapter 7. We present our final conclusions and offer an outlook in Chapter 8.

2. Physics of microswimmers

The physics of active swimmers consists of two aspects. On the one hand, their propulsion mechanisms drive them out of equilibrium and create novel dynamics and patterns. On the other hand, the laws governing their fluid surroundings need to be specified. The surrounding fluid is responsible for friction and hydrodynamic interactions. In the following, we first discuss the laws of hydrodynamics. Here, we especially consider low Reynolds number flows, because microswimmer motion usually occurs in this regime. The governing equation is the Stokes equation and we discuss solutions, in particular the multipole expansion.

Furthermore, we discuss different swimming mechanisms, *i.e.*, self-propulsion in a fluid. Among the many forms of swimming, we present biological swimmers using a non-reciprocal motion of cilia or flagella. We also discuss synthetically manufactured microswimmers, which induce a surface flow field, for example due to catalytic reactions or the influence of surface-active molecules. Furthermore, we discuss stochastic motion, which is of utmost importance on the micrometer scale. Then, we introduce the squirmer model, which is used throughout this work.

Hydrodynamic interactions, between swimmers and between a swimmer and a boundary, play an important role in our study. We introduce the method of hydrodynamic images to describe interactions with a no-slip boundary in Stokes flow. This gives a description of the flow structure in the far field. Since near field interactions can be relevant for collective dynamics of swimmers, we also discuss the laws of lubrication.

Finally, this work is concerned with the motion of microswimmers under gravity. We describe the sedimentation of passive colloids and then discuss the state of the art of active systems under gravity.

2.1 Dynamics of the Newtonian fluid

Microswimmers self-propel inside a fluid. For the type of swimmers we are interested in, the detailed dynamics of the fluid and an understanding of the occurring flow fields is very important. Therefore, we describe systems of *wet active matter* [3]. In contrast, in *dry* systems the interactions with the fluid only consist of the friction and fluctuations experienced by each individual particle.

There is a large variety of active swimmers, which occur in many different environments. These range from biological fluids, like blood [18, 66], gut fluid [67], or cervical mucus [68, 69] to turbulent oceanic flows [70, 71]. Furthermore, swimmers have been

placed in a wide variety of complex fluids in experiments [72–76]. Thus, the surroundings of active swimmers can be very diverse in terms of Reynolds number, fluid rheology, pH, ion distributions, or chemical fields. In this work, we focus on single-component Newtonian fluids and will ultimately restrict ourselves to low Reynolds numbers. Furthermore, no chemical reactions or charged particles occur in our systems. For Newtonian fluids, the most important equations are the Navier-Stokes equations. For our purposes, the regime of creeping flow is the most important, which is described by the Stokes equations.

2.1.1 Balance equations of continuum mechanics

Even though fluids consist of molecules, they are often treated as a continuum. Here, the fluid is divided into small volume elements, which are much smaller than the macroscopic length scale and much larger than the molecules that make up the fluid [77]. Using this picture, we present the balance equations of fluid dynamics and the constitutive relation that define the Newtonian fluid.

Mass conservation

The first balance equation is that of mass. The mass density of a fluid is denoted by $\rho(\mathbf{r})$, where $\mathbf{r}$ is the position of a fluid volume element. A change of mass within a control volume V is accomplished only by a net flux through the boundary ∂V. This reflects the principle of *mass conservation*. Let $\mathbf{n}$ be the outward-pointing surface normal of the control volume, then

$$\partial_t \int_V \rho dV = -\int_{\partial V} \mathbf{j} \cdot \mathbf{n} dA. \tag{2.1}$$

The quantity $\mathbf{j}(\mathbf{r}) := \rho(\mathbf{r})\mathbf{u}(\mathbf{r})$ is the mass current density. From dimensional analysis, one can see that it can also be considered a momentum density. Switching integration and time differentiation and applying Gauss' theorem leads to the *continuity equation* of mass

$$\partial_t \rho + \nabla \cdot \mathbf{j} = 0. \tag{2.2}$$

An important special case is $\rho = \text{const}$, which expresses that the fluid is *incompressible*. Then we have

$$\nabla \cdot \mathbf{u} = 0. \tag{2.3}$$

Momentum conservation

Next, we consider the momentum of the fluid and discuss the relevant terms and concepts in more detail. Inside the control volume the total momentum of the fluid $\mathbf{P}$ is given by the volume integral over the current density $\mathbf{P} = \int_V \mathbf{j} dV$. As we will see below, the time derivative of this term yields a convective momentum current density, and also a force density. Furthermore, we have to take both volume and surface forces into account.

Convective momentum current density Equivalent to matter, fluid flow can transport momentum $\rho\mathbf{u}$ into or out of a fluid volume. The convective momentum current density can be written as $\rho\mathbf{u} \otimes \mathbf{u}$ and is a tensorial quantity .

Surface stresses *Volume* or *body* forces have an external source, such as gravity or electromagnetism. We usually use the respective force densities, which we write as $\rho\mathbf{b}$. In contrast, *surface* forces originate from the local interaction between fluid elements [78]. A surface force $\mathbf{f}_S$ can be expressed through the surfaces force density $\mathbf{t}$ as

$$\mathbf{f}_S = \int_{\partial V} \mathbf{t} dA. \tag{2.4}$$

It leads to a deformation of the fluid volume, which is captured by the velocity gradient $\nabla \otimes \mathbf{v} \equiv \nabla\mathbf{v}$ [79] . The velocity gradient can be divided into the rate-of-strain tensor

$$\mathbf{L} := \frac{1}{2}\left(\nabla\mathbf{v} + \nabla\mathbf{v}^T\right), \tag{2.5}$$

and the spin tensor

$$\mathbf{W} := \frac{1}{2}\left(\nabla\mathbf{v} - \nabla\mathbf{v}^T\right). \tag{2.6}$$

Note that a fluid volume may experience both isotropic and anisotropic stress, *i.e.*, the surface forces depend on the respective surface normal, $\mathbf{t} = \mathbf{t}(\mathbf{x}, t, \mathbf{n})$. Furthermore, there is an important distinction between normal stress and shear stress. Shear stress consists of non-zero tangential forces on the surface element with normal $\mathbf{n}$ and thus represents the concept of fluid layers pulling on each other. For example, in simple shear flow, shear stress induces a scalar *shear rate* $\dot{\gamma} = \dfrac{\Delta v}{h}$ over the distance h [78]. Normal stresses on the other hand lead to an expansion or contraction of the fluid volume as a whole.

The surface stress $\mathbf{t}$ in three dimensions has three components per surface normal. We express these components via the *Cauchy stress tensor* $\boldsymbol{\sigma}$, which reads[1]

$$\mathbf{t}(\mathbf{x}, t, \mathbf{n}) = \boldsymbol{\sigma}(\mathbf{x}, t)\mathbf{n}. \tag{2.7}$$

Balance equation Eq. (2.7) is used in our force balance relation. We can now write the total force as

$$\mathbf{f} = \mathbf{f}_V + \mathbf{f}_S = \int_V \rho\mathbf{b} dV + \int_{\partial V} \boldsymbol{\sigma}\mathbf{n} dA. \tag{2.8}$$

Thus, analogous to Eq. (2.2), we arrive at the momentum balance equation

$$\partial_t(\rho\mathbf{u}) + \mathrm{div}(\rho\mathbf{u} \otimes \mathbf{u}) - \mathrm{div}\boldsymbol{\sigma} = \rho\mathbf{b}, \tag{2.9}$$

where we define the divergence of a tensor as $(\mathrm{div}\boldsymbol{\sigma})_i = \partial_j \sigma_{ij}$. The term $\rho\mathbf{b}$ describes an external force density.

[1] We present this equation rather succinctly here and without much preparation. It should be mentioned that more mathematical rigor is required to really prove this relation, which is also called the *Cauchy stress theorem* [78].

The terms with spatial derivatives can be summarized by defining the total momentum current density $\mathbf{\Pi}$:

$$\Pi_{ij} = \rho u_i u_j - \sigma_{ij}. \tag{2.10}$$

By using the continuity equation, Eq. (2.2), we arrive at the following equations of motion

$$\rho \partial_t \mathbf{u} + \rho(\mathbf{u} \cdot \nabla)\mathbf{u} - \nabla \cdot \boldsymbol{\sigma} = \rho \mathbf{b}. \tag{2.11}$$

Constitutive equation

In an incompressible fluid at rest, all shear stresses are zero and the normal stress is isotropic [78]. Hence, it can be described by a scalar quantity, which by convention is the *pressure* p. The isotropic component $-p\mathbf{1}$ is the only contribution to the frictionless or *ideal fluid*, where $\mathbf{1}$ is the unit tensor. If dissipation exists, another term is added, called the viscous stress tensor $\boldsymbol{\sigma}'$

$$\boldsymbol{\sigma} = -p\mathbf{1} + \boldsymbol{\sigma}'. \tag{2.12}$$

The dependence of $\boldsymbol{\sigma}'$ on other variables is called the constitutive equation. It captures the viscous properties of the fluid and needs to be satisfied in addition to the balance equations. In Sec. 2.1.2, we introduce the constitutive equation for the Newtonian fluid.

Energy conservation

The conservation of the sum of kinetic energy density $\rho u^2/2$ and internal energy density $\rho\varepsilon$ is achieved by another balance equation [77]. The convective energy transport out of a volume element is $\rho\mathbf{u}\,(u^2/2 + \varepsilon)$. The work done on a fluid element by surface and bulk forces is captured by the term $\nabla \cdot (\boldsymbol{\sigma}^t \mathbf{u}) + \rho \mathbf{b} \cdot \mathbf{u}$. Furthermore, due to the possibility of thermal conduction one has to include the divergence of the heat flux density $\nabla \cdot \mathbf{q}$. The precise form of the heat flux density is again a characteristic of the material. We here ignore the effect of heat sources or sinks in the fluid. After some calculations, these expressions can be reformulated as [77]

$$\rho\,(\partial_t \varepsilon + \mathbf{u} \cdot \nabla\varepsilon) + \nabla \cdot \mathbf{q} = \boldsymbol{\sigma}^t \bullet \nabla \otimes \mathbf{u}. \tag{2.13}$$

Here, the *contraction operation* on two tensors $\mathbf{M}$, $\mathbf{N}$ is defined as

$$\mathbf{M} \bullet \mathbf{N} := M_{ij} N_{ji} = \mathrm{Tr}(\mathbf{MN}).$$

2.1.2 The Navier-Stokes equations

In the following we present the Newtonian fluid, which is a ubiquitous and useful model for a viscous fluid. The momentum balance equations of this fluid are known as the Navier-Stokes equations.

Viscous stress tensor

In a Newtonian fluid, it is assumed that the viscous stress tensor $\boldsymbol{\sigma}$ is linear in the rate-of-strain tensor $\mathbf{L} = \frac{1}{2}(\nabla\mathbf{v} + \nabla\mathbf{v}^t)$. Hence, it is also called a *linear fluid* [78] and the most general form of the viscous stress tensor is [79]

$$\sigma'_{ij} = \eta_{ijkl} L_{kl}. \tag{2.14}$$

The tensor with components η_{ijkl} is called the *viscosity*. We assume an isotropic fluid in the following. Here, it is assumed that the asymmetric part of the velocity gradient $\mathbf{W}$ does not contribute. The reason for this is that no friction should be associated with uniform rotation of a fluid volume [77]. We note, that the asymmetric term $\mathbf{W}$ becomes relevant for the model fluid we introduce in Chapter 3.We arrive at the constitutive equation for the Newtonian fluid

$$\boldsymbol{\sigma}' = 2\eta\mathbf{L} + \left(\lambda - \frac{2}{3}\eta\right)\nabla\cdot\mathbf{u}, \tag{2.15}$$

where η is the dynamic viscosity and λ is the bulk viscosity. For incompressible fluids Eq. (2.15) becomes

$$\boldsymbol{\sigma}' = 2\eta\mathbf{L}. \tag{2.16}$$

Momentum balance

Finally, we arrive at the momentum balance equation of the Newtonian fluid. We insert the constitutive equation (2.15) into the momentum balance Eq. (2.11) and arrive at the compressible momentum equations [77], assuming that η and λ are just constants:

$$\rho\left(\partial_t\mathbf{u} + \mathbf{u}\cdot\nabla\mathbf{u}\right) = -\nabla p + \eta\nabla^2\mathbf{u} + \left(\lambda + \frac{1}{3}\eta\right)\nabla\left(\nabla\cdot\mathbf{u}\right) + \rho\mathbf{b}. \tag{2.17}$$

These equations are called the *Navier-Stokes equations*. For an incompressible fluid, we obtain

$$\rho\left(\partial_t\mathbf{u} + \mathbf{u}\cdot\nabla\mathbf{u}\right) = -\nabla p + \eta\nabla^2\mathbf{u} + \rho\mathbf{b}, \tag{2.18}$$

where, due to incompressibility, the bulk viscosity λ no longer appears.

Thus, we have derived a non-linear partial differential equation for the fluid dynamics. In general, solving this equation is a hard task. As we will do in following chapters, one often has no choice but to resort to numerical schemes. However, it is useful to tackle this equation by means of similarity laws. In particular, this lets us transition to the regime of creeping flow, where we encounter a linear equation.

2.1.3 Creeping flow

Characteristic numbers and concept of similarity

We transform the Navier-Stokes equations into a dimensionless form by introducing characteristic parameters. The benefit of this procedure is that a solution found for the normalized equation can yield a whole family of solutions for different combinations of

these parameters. This is known as *similarity* [80]. For example, the flow around a small particle in water can be determined by measuring a larger particle in a fluid with a larger viscosity [80]. Specifically, we use a typical velocity U and a typical length scale a as our characteristic parameters. The sizes of these quantities depend on the specific hydrodynamic problem. For example, the typical length scale could correspond to the size of the channel or of a suspended particle, or a typical wavelength. Other characteristic quantities are introduced when the physical problem requires it. For example, an oscillatory boundary necessitates defining a typical time scale, related to frequency of the oscillation.

We express the observable quantities, as well as the differential operators, in Eq. (2.18) in terms of our length and velocity units, following Ref. [80]. A unit of time is given by a/U. Furthermore, we introduce a typical pressure difference Δp. Then, we arrive at an equation for the dimensionless quantities, which we marked with a prime:

$$\nabla' \cdot \mathbf{u}' = 0 \tag{2.19}$$

$$\frac{\rho U^2}{a} \left(\partial_t' \mathbf{u}' + \mathbf{u}' \cdot \nabla' \mathbf{u}'\right) = -\frac{\Delta p}{a} \nabla' p' + \frac{\eta U}{a^2} \nabla'^2 \mathbf{u}' + \rho b \mathbf{b}'. \tag{2.20}$$

Reynolds number Transforming the Navier-Stokes equations into dimensionless form, the non-linear inertial term $(\mathbf{u} \cdot \nabla)\mathbf{u}$ scales with $\rho U^2/a$, whereas the viscous term $\eta \nabla^2 \mathbf{u}$ scales with $\eta U/a^2$. The ratio between both terms is called the *Reynolds number* [81]

$$\mathrm{Re} = \frac{\rho U a}{\eta} = \frac{U a}{\nu}. \tag{2.21}$$

The Reynolds number determines the importance of inertial forces relative to viscous forces [81]. It is the most important dimensionless number for our purposes. The Navier-Stokes equations can now be expressed as

$$\mathrm{Re} \left(\partial_t' \mathbf{u}' + \mathbf{u}' \cdot \nabla' \mathbf{u}'\right) = -\frac{\Delta p a^2}{\eta U} \nabla' p' + \nabla'^2 \mathbf{u}' + \frac{b a^2}{\nu U} \mathbf{b}'. \tag{2.22}$$

We can likewise define a rotational Reynolds number [81]

$$\mathrm{Re}_{\mathrm{rot}} = \frac{\Omega a^2}{\nu} \tag{2.23}$$

with the typical angular velocity Ω.

Euler number Another characteristic dimensionless number is the ratio between pressure and inertial forces. It is called the *Euler number*

$$\mathrm{Eu} = \frac{\Delta p}{\rho U^2}. \tag{2.24}$$

Using the Euler number, we recognize that the pre-factor in front of the pressure term in Eq. (2.22) is $-\mathrm{EuRe}$.

Froude number The Froude number is defined as $\mathrm{Fr} = U/\sqrt{ba}$ [80], where $b = |\mathbf{b}|$. Thus, the pre-factor to the body-force term in Eq. (2.22) is Re/Fr. The Froude number is large, when the external force is large compared to the inertial force. Thus, we obtain

$$\mathrm{Re}\left(\partial_t' \mathbf{u}' + \mathbf{u}' \cdot \nabla' \mathbf{u}'\right) = -\mathrm{ReEu}\nabla' p' + \nabla'^2 \mathbf{u}' + \frac{\mathrm{Re}}{\mathrm{Fr}^2}\mathbf{b}'. \tag{2.25}$$

Stokes equations

If we drop the non-linear convective term of the Navier-Stokes equations, we end up with a linear equation. We also assume that all time scales in the fluid are fast compared to the time scales of our problems of interest. This allows us to assume stationarity and the time-dependent term disappears. Thus, we arrive at the *Stokes equations*, which represent fluid motion at negligible Reynolds numbers [81, 82]:

$$\nabla \cdot \mathbf{u} = 0, \tag{2.26}$$

$$-\nabla p + \eta \nabla^2 \mathbf{u} = \rho \mathbf{b}. \tag{2.27}$$

Stokes flow or *creeping flow* is laminar and no turbulence occurs. As we will see later, the inertia-less fluid makes it impossible to swim with a drift, like a human swimmer does in water.

The Stokes equations satisfy an interesting condition, known as *kinematic reversibility*. In short, reversing the solution of the velocity field to $-\mathbf{u}$ yields a valid solution to the Stokes equation with inverted pressure and force terms $-p$ and $-\rho\mathbf{b}$. Note that the Stokes equations do not have an intrinsic time scale. This implies that the reaction of the flow field to a boundary condition is instantaneous.

Stokes paradox It was shown by Oseen that the Stokes approximations can lead to inconsistencies [83]. Concretely, at large distances from an object the inertial term cannot be neglected compared to the viscous term, which explains the unphysical behaviour known as *Stokes' paradox*: The magnitude of the creeping flow velocity past an infinite cylinder, *i.e.*, the flow past a sphere in two dimensions, cannot stay finite at large distances from the obstacle surface, where the flow velocity is assumed to be zero [81].

Solutions of the Stokes equations

Due to the paramount importance of the Stokes equations for meso- and microhydrodynamics [81, 82, 84, 85], a number of techniques have been developed to solve it under various boundary conditions. In the following we introduce two methods of particular importance to the Stokes equations, the Green function approach, yielding the Oseen tensor, and Lamb's solution in spherical coordinates.

Oseen tensor Since the Stokes equations are linear, it is possible to define Green's function for both the velocity and pressure fields. Those Green's functions solve equations (2.26) for a delta-distributed inhomogeneity, which is also called a point force. The

solution for a general inhomogeneity or body force $\rho\mathbf{b}$ can be found by using Green's functions as integration kernels:

$$\mathbf{u}(\mathbf{r}) = \int \mathbf{O}(\mathbf{r}-\mathbf{r}')\rho\mathbf{b}(\mathbf{r}')d^3r, \tag{2.28}$$

$$p(\mathbf{r}) = \int \mathbf{g}(\mathbf{r}-\mathbf{r}')\rho\mathbf{b}(\mathbf{r}')d^3r. \tag{2.29}$$

Green's functions for the Stokes equations are called the Oseen tensor $\mathbf{O}$ and the pressure vector $\mathbf{g}$ and they are given by

$$\mathbf{O}(\mathbf{r}) = \frac{1}{8\pi\eta r}\left(\mathbf{1} - \frac{\mathbf{r}\otimes\mathbf{r}}{r^2}\right), \tag{2.30}$$

$$\mathbf{g}(\mathbf{r}) = \frac{1}{4\pi r^3}\mathbf{r}. \tag{2.31}$$

The flow induced by the Oseen tensor is also called a stokeslet or force monopole. We write a stokeslet $\mathbf{G}_S$ with direction $\hat{\mathbf{f}}$, belonging to a unit point force, as

$$\mathbf{G}_S(\hat{\mathbf{f}},\mathbf{r}) = \mathbf{O}(\mathbf{r})\hat{\mathbf{f}}. \tag{2.32}$$

Here, we assume the stokeslet to be at the origin. This could for example model a dragged particle, viewed from a large distance.

Lamb's solution in spherical coordinates Solving the Stokes equations can be easier when symmetries are present. One such case is Lamb's solution in spherical coordinates. As we study spherical microswimmers at low Reynolds numbers, this solution becomes relevant for us when we discuss the flow field of a squirmer in Sec. 2.2.4. We sketch a derivation for Lamb's solution in Appendix A. The end result in spherical coordinates is [81, 82]

$$\mathbf{u} = \sum_{n=-\infty}^{\infty}\left[\frac{(n+3)r^2\nabla p_n - 2n\mathbf{r}p_n}{2\eta(n+1)(2n+3)}\right] + \nabla\phi_n + \nabla\times(\mathbf{r}\chi_n), \tag{2.33}$$

with harmonic functions p_n, ϕ_n, χ_n. The equation for the pressure is

$$p = \sum_{n=-\infty}^{\infty} p_n. \tag{2.34}$$

We are concerned with solutions of the Stokes equation outside of a spherical body, the so-called *external problem*. Hence, the relevant parts of the series expansion in Eq. (2.33) are $n \leq 0$, because $\mathbf{u}$ should decay to zero for $r \to \infty$ [see Eq. (A.3) and also Refs. [81, 82]]. Lamb showed that $n = 0$ is associated with source or sink solutions [84]. While relevant for expanding droplets, these solutions are unphysical for objects with finite, constant radii and can therefore be discarded.

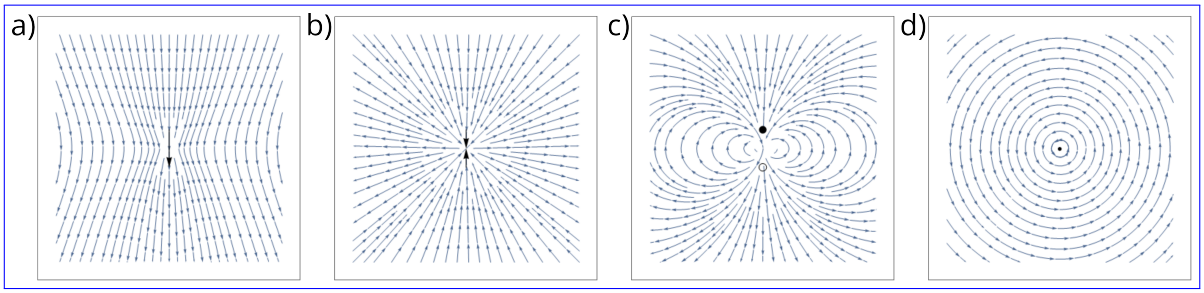

Figure 2.1: Flow fields of selected Stokes flow singularities. a) stokeslet, b) symmetric force dipole, c) source dipole, d) rotlet. The singularities are located at the origin, in the center of the figure.

2.1.4 Hydrodynamic multipoles

Above, we have introduced the Oseen tensor as the Green's function of the velocity field. For arbitrary force distributions in Eq. (2.28), one can use higher order multipoles. We follow Kim and Karrila [82] who expand the Oseen tensor $\mathbf{O}(\mathbf{x}-\mathbf{y})$ around $\mathbf{y}=0$ [82]. The Taylor expansion yields

$$\begin{aligned} O_{ij}(\mathbf{x}-\mathbf{y}) &= \sum_{n=0}^{\infty} \frac{1}{n!} (\mathbf{y}\cdot\nabla_y)^n O_{ij}(\mathbf{x}-\mathbf{y})|_{\mathbf{y}=0} \\ &= \sum_{n=0}^{\infty} \frac{(-1)^n}{n!} (\mathbf{y}\cdot\nabla)^n O_{ij}(\mathbf{x}). \end{aligned} \tag{2.35}$$

This yields higher-order tensorial multipoles of the form $\partial_{k_1}\cdots\partial_{k_n} O_{ij}(\mathbf{x})$ [82, 86]. Alternatively, we can express the flow fields created by these multipoles. The intuition of these flow singularities works similarly to electrostatics: Seen from a large distance, the flow field resembles the force monopole term with a strength corresponding to the total hydrodynamic force. Importantly, for a force-free swimmer, this contribution is zero. With decreasing distance, more details of the flow signature become apparent and higher-order singularities are relevant.

In Stokes flow, we can distinguish between force and source singularities. The force multipoles are also called Stokes multipoles. They are created by iteratively applying the gradient operator to the stokeslet [85]. Thus, the force dipole $\mathbf{G}_D$ and quadrupole $\mathbf{G}_Q$ are defined as

$$\mathbf{G}_D(\hat{\mathbf{f}},\hat{\mathbf{e}},\mathbf{x}-\mathbf{y}) = \hat{\mathbf{e}}\cdot\nabla_y \mathbf{G}_S(\hat{\mathbf{f}},\mathbf{x}-\mathbf{y}), \tag{2.36}$$

$$\mathbf{G}_Q(\hat{\mathbf{f}},\hat{\mathbf{e}},\hat{\mathbf{d}},\mathbf{x}-\mathbf{y}) = \hat{\mathbf{d}}\cdot\nabla_y \mathbf{G}_D(\hat{\mathbf{f}},\hat{\mathbf{e}},\mathbf{x}-\mathbf{y}). \tag{2.37}$$

Each higher order multipole includes a further unit vector, representing a direction of the singularity. For example, the stokeslet has the direction $\hat{\mathbf{f}}$, which is the direction of the point force. The most general force dipole $\mathbf{G}_D$ has two directions and the force quadrupole $\mathbf{G}_Q$ has three directions. The force dipole term $\mathbf{G}_D$ can be decomposed

into a symmetric and an antisymmetric part [82][2]. For the symmetric part, we assume that $\hat{\mathbf{e}}$ and $\hat{\mathbf{f}}$ are parallel. The symmetric dipole field then becomes

$$\mathbf{G}_{D,\mathrm{symm}}(\hat{\mathbf{f}},\mathbf{x}) = \frac{1}{8\pi\eta x^2}\left(-\frac{1}{x} + 3\frac{\left(\hat{\mathbf{f}}\cdot\mathbf{x}\right)^2}{x^3}\right)\mathbf{x}. \tag{2.38}$$

Importantly, the asymmetric part is called a rotlet, if $\hat{\mathbf{e}} \perp \hat{\mathbf{f}}$. The rotlet, which we denote by $\mathbf{R}$, is the leading order flow field of a rotating sphere [82] and is thus an important singularity:

$$\mathbf{R}(\hat{\mathbf{s}},\mathbf{x}) = \frac{\hat{\mathbf{s}}\times\mathbf{x}}{8\pi\eta x^3}. \tag{2.39}$$

Here, the vector $\hat{\mathbf{s}}$ forms an orthonormal basis with the vectors $\hat{\mathbf{e}}$ and $\hat{\mathbf{f}}$ introduced above [87]. Then, we can also define a rotlet dipole with the same rule as above:

$$\mathbf{R}_D(\hat{\mathbf{t}},\hat{\mathbf{s}},\mathbf{x}-\mathbf{y}) = \hat{\mathbf{t}}\cdot\nabla_y\mathbf{R}(\hat{\mathbf{s}},\mathbf{x}-\mathbf{y}), \tag{2.40}$$

which yields

$$\mathbf{R}_D(\hat{\mathbf{t}},\hat{\mathbf{s}},\mathbf{x}) = \frac{1}{8\pi\eta x^3}\left(\hat{\mathbf{t}}\times\hat{\mathbf{s}} - \frac{3\left(\hat{\mathbf{t}}\cdot\mathbf{x}\right)\hat{\mathbf{s}}\times\mathbf{x}}{x^2}\right). \tag{2.41}$$

We are mainly interested in the case where $\hat{\mathbf{s}}$ and $\hat{\mathbf{t}}$ are anti-parallel to each other. This results in the rotlet dipole field

$$\mathbf{R}_D(-\hat{\mathbf{s}},\hat{\mathbf{s}},\mathbf{x}) = \frac{3\left(\hat{\mathbf{s}}\cdot\mathbf{x}\right)\hat{\mathbf{s}}\times\mathbf{x}}{8\pi\eta x^5}. \tag{2.42}$$

Source singularities represent additional solutions, where the pressure field is zero. A source field (or source monopole) of unit strength is defined as

$$\mathbf{G}_{\mathrm{SM}}(\mathbf{x}) = \frac{\mathbf{x}}{8\pi\eta x^3}. \tag{2.43}$$

Applying the same operation as before, we can calculate the source dipole $\mathbf{G}_{SD}$, which describes the field of a source and a sink brought together to a small distance.

$$\mathbf{G}_{SD}(\hat{\mathbf{f}},\mathbf{x}) = \frac{1}{8\pi\eta x^3}\left(-\hat{\mathbf{f}} + 3\frac{\left(\hat{\mathbf{f}}\cdot\mathbf{x}\right)\mathbf{x}}{x^2}\right) \tag{2.44}$$

The source dipole can also be calculated from the stokeslet via

$$\mathbf{G}_{SD}(\hat{\mathbf{f}},\mathbf{x}-\mathbf{y}) = -\frac{1}{2}\nabla_y^2\mathbf{G}_S(\hat{\mathbf{f}},\mathbf{x}-\mathbf{y}). \tag{2.45}$$

Finally, the source quadrupole is defined as

$$\mathbf{G}_{SQ}(\hat{\mathbf{f}},\hat{\mathbf{e}},\mathbf{x}-\mathbf{y}) \;=\; \hat{\mathbf{e}}\cdot\nabla_y\mathbf{G}_{SD}(\hat{\mathbf{f}},\mathbf{x}-\mathbf{y}) \tag{2.46}$$

We show the flow fields of the stokeslet, symmetric force dipole, source dipole and rotlet singularities in Fig. 2.1.

[2]Ref. [82] first subtracts the isotropic part of the dipole before splitting the terms.

2.1.5 Suspended particles

Hydrodynamic forces and torques

Rigid bodies suspended in a fluid are subject to hydrodynamic forces $\mathbf{F}$ and torques $\mathbf{T}$ that the fluid exerts on them. They are given by the total surface force or torque integral over the body surface S:

$$\mathbf{F} = \int_S \boldsymbol{\sigma}\mathbf{n} d^2r, \tag{2.47}$$

$$\mathbf{T} = \int_S \mathbf{r}_P \times (\boldsymbol{\sigma}\mathbf{n}) d^2r. \tag{2.48}$$

Here, the torque depends on the choice of the center of rotation inside the body, from which we measure the vector $\mathbf{r}_P$ to the particle surface [81].

According to Eqs. (2.47) and (2.48), a solution of the Stokes equations enables us to calculate the hydrodynamic forces and torques of a suspended body. The boundary conditions of the rigid body are determined by its translational and rotational motion and the induced slip velocities on its surface:

$$\mathbf{u}|_S = \mathbf{U} + \boldsymbol{\Omega} \times \mathbf{r}_S + \mathbf{u}_{\text{slip}}(\mathbf{r}_S), \tag{2.49}$$

where $\mathbf{U}$ is the body's translational, $\boldsymbol{\Omega}$ is its rotational velocity and $\mathbf{r}_S$ is a vector to the surface.

Force and torque in Lamb's solution An external force on a particle results in a stokeslet component of the flow, whereas a torque results in a rotlet component. They characteristically decay with $1/r$ and $1/r^2$, respectively. Ref. [81] uses Lamb's solution from Eq. (2.33) to calculate the infinite series of the stress tensor. Using Eqs. (2.47) and (2.48), one can then demonstrate that the force $\mathbf{F}$ and torque $\mathbf{T}$ on a sphere are expressed by

$$\mathbf{F} = -4\pi\nabla \left(r^3 p_{-2}\right)|_{r=R}, \tag{2.50}$$

$$\mathbf{T} = -8\pi\eta\nabla \left(r^3 \chi_{-2}\right)|_{r=R}. \tag{2.51}$$

Friction and Mobility

Both the hydrodynamic forces $\mathbf{F}$ and the translational velocity of the body $\mathbf{U}$, as well as the hydrodynamic torques $\mathbf{T}$ and the angular velocity of the body $\boldsymbol{\Omega}$ are connected by a linear relation [82, 88]. Assuming a fluid velocity that is zero at infinity, this relation can be written as

$$\begin{pmatrix} \mathbf{F} \\ \mathbf{T} \end{pmatrix} = \begin{pmatrix} \boldsymbol{\gamma}^{\text{tt}} & \boldsymbol{\gamma}^{\text{tr}} \\ \boldsymbol{\gamma}^{\text{rt}} & \boldsymbol{\gamma}^{\text{rr}} \end{pmatrix} \begin{pmatrix} \mathbf{U} \\ \boldsymbol{\Omega} \end{pmatrix} \tag{2.52}$$

with the 3×3 friction matrices $\boldsymbol{\gamma}^{\text{tt}}$, $\boldsymbol{\gamma}^{\text{rr}}$, and $\boldsymbol{\gamma}^{\text{tr}}$ refering to translation, rotation and translation-rotation coupling. The translation and rotation matrices are symmetric,

while the coupling matrices are, in general, not [81][3]. However, for the latter the relation

$$\gamma_{ij}^{\mathrm{tr}} = \gamma_{ji}^{\mathrm{rt}} \tag{2.53}$$

holds. The exact shape of the matrices depends on the geometry of the particle, and sometimes also on its orientation and velocity [81]. Furthermore, hydrodynamic interactions with other suspended bodies or boundaries influence the friction. We address this in Sec. 2.3. First, we consider a spherical body translating or rotating in an otherwise quiescent, infinite fluid. In the following, we apply Lamb's solution Eq. (2.33) to a sphere translating with a speed U. We set the direction of the velocity along the z-direction, without loss of generality, and use spherical coordinates. Then, one arrives at the following expressions for the harmonics [82]

$$p_{-2} = \frac{3}{2}\eta U \frac{R}{r^2}\cos\vartheta, \tag{2.54}$$

$$\chi_{-2} = 0. \tag{2.55}$$

From this, using Eq. (2.50), we arrive at *Stoke's law*

$$\mathbf{F} = -6\pi\eta R\mathbf{U}, \tag{2.56}$$

for a general velocity vector $\mathbf{U}$ of the rigid sphere. For a sphere rotating around the z-axis with angular velocity $\mathbf{\Omega}$, one similarly gets [82]

$$p_{-2} = 0, \tag{2.57}$$

$$\chi_{-2} = \Omega\frac{R^3}{r^{-2}}\cos\vartheta, \tag{2.58}$$

using Eq. (2.51), and thus

$$\mathbf{T} = -8\pi\eta R^3\mathbf{\Omega}. \tag{2.59}$$

Thus, the friction tensors for a passive sphere in bulk flow become

$$\boldsymbol{\gamma}^{\mathrm{tt}} = 6\pi\eta R\mathbf{1}, \tag{2.60}$$

$$\boldsymbol{\gamma}^{\mathrm{rr}} = 8\pi\eta R^3\mathbf{1}, \tag{2.61}$$

$$\boldsymbol{\gamma}^{\mathrm{tr}} = 0. \tag{2.62}$$

The inverse problem is known as the mobility problem and leads to the inverse tensors, called the mobility tensors:

$$\begin{pmatrix} \mathbf{U} \\ \mathbf{\Omega} \end{pmatrix} = \begin{pmatrix} \boldsymbol{\mu}^{\mathrm{tt}} & \boldsymbol{\mu}^{\mathrm{tr}} \\ \boldsymbol{\mu}^{\mathrm{rt}} & \boldsymbol{\mu}^{\mathrm{rr}} \end{pmatrix} \begin{pmatrix} \mathbf{F} \\ \mathbf{T} \end{pmatrix}. \tag{2.63}$$

[3]There exists a unique point in a body, where this tensor is symmetric, called the center of hydrodynamic reaction [81]. However, for spherical particles, the translation-rotation coupling will stay symmetric anyway.

Flow around a dragged sphere

The flow around a dragged sphere in a quiescent background fluid is given by the combination of a stokeslet and a source dipole

$$\mathbf{u}(\mathbf{x}) = 6\pi\eta RU\left(1 + \frac{R^2}{6}\nabla^2\right)\mathbf{G}_S, \tag{2.64}$$

where U is the particle velocity, which we assume is directed in the z-direction. Expressed in spherical coordinates (r, ϑ, φ), this flow field has the following components [82]

$$u_r = U\cos\vartheta\left(\frac{3}{2}\frac{R}{r} - \frac{1}{2}\left(\frac{R}{r}\right)^3\right), \tag{2.65}$$

$$u_\vartheta = -U\sin\vartheta\left(\frac{3}{4}\frac{R}{r} + \frac{1}{4}\left(\frac{R}{r}\right)^3\right), \tag{2.66}$$

$$u_\varphi = 0. \tag{2.67}$$

2.2 Self-propulsion on the micron scale

The name microswimmers implies two main characteristics of these agents. First, they are microscopically small, on the order of a couple of microns. Unless they are in a turbulent external flow, this means that fluid inertia plays no role for them and that their motion in a fluid is governed by the Stokes equations. Furthermore, thermal fluctuations can have a big effect on their dynamics. Second, they are swimmers, *i.e.*, they self-propel in the fluid by some sort of body deformation [46]. Since the continuous motion depends on the consumption of food or another energy source, the system is far from thermodynamic equilibrium.

In the following, we consider the conditions of low Reynolds number swimming and describe swimming mechanisms. Steric effects, or the dynamics of a chemical can be very important [89–93]. We note that in our model system those are not considered. Instead, we focus on hydrodynamic aspects. Furthermore, we treat active matter using an agent-based approach, *i.e.*, the active material consists of distinct particles. However, there exists a large body of work where active matter is treated with continuum theories [3, 94–96]. We will not be considering these theories in our work.

The small size of microswimmers makes them susceptible to Brownian motion. We briefly discuss the relevant laws and relations that result from stochastic molecular collisions, mainly based on a passive particle. In addition, we introduce the active Brownian particle. Finally, we present the swimmer that we study during the course of this work, the spherical *squirmer*. In our simulations, it is both subject to low Reynolds number hydrodynamics and thermal noise.

2.2.1 Life at low Reynolds numbers

Microorganisms move at very low Reynolds numbers on the order of 10^{-4} and consequently fluid inertia is irrelevant to their motion [46]. Hence, any motion requires a non-stop propulsive force and the organism will stop performing directed motion as soon as the force stops. This is fundamentally different from a human swimmer in water or a ship in the ocean, both of which rely on inertia to a large extent.

Scallop theorem

There is an important restriction to the kinds of body deformation that a swimmer at low Reynolds number can perform. The reason for this is that motion at low Reynolds numbers requires a non-reciprocal actuation. Let us assume that the body deformation consists of a power stroke and a recovery stroke. Then, a motion is reciprocal if the second stroke is the exact reversal of the first one. A famous example is that of a scallop, which opens to self-propel and then closes again in order to revert to its original shape. Obviously, the second step results in a motion in the opposite direction. The scallop theorem states that this cycle of deformation results in no net motion at low Reynolds numbers [46]. No matter how fast or slow the opening and closing motions are performed, the forward and backward travel distances of the body are always exactly the same. The irrelevance of the rate of change is a direct consequence of the Stokes equations, which do not depend on time [97]. In the words of Purcell [46], who acts as the namesake of the theorem: '*Time, in fact, makes no difference - only configuration*'. Thus, in order to achieve any net propulsion, the body's cycle of movement has to be non-reciprocal. This implies, that more than one degree of freedom is necessary for the deformation. We present examples of such swimming mechanisms below.

Note, the scallop theorem only applies in a Newtonian fluid. It has been shown, that it does not apply to a shear-thickening or shear-thinning fluid. Therefore self-propulsion is possible in these fluids with a symmetrical motion, as long as forward and backward motion are performed at different rates [98, 99].

Force-free swimming

In Stokes flow, the sum of all forces is always zero, because the friction force compensates all other forces. Nonetheless, the 'force-free' condition of active swimmers is frequently invoked. The meaning of this condition is that no external forces aid the swimmer's locomotion, which implies that the stokeslet component in the flow field is zero [100]. Thus, it is immediately clear that the hydrodynamic signature of microswimmers can only decay faster or equal to r^{-2}. On the other hand, a swim force is sometimes defined as $\mathbf{F}_{\text{swim}} = 6\pi\eta R\mathbf{u}$ (for the spherical swimmer) [101]. To clarify and avoid confusion with respect to the force-free condition, we note that here the internal forces responsible for swimming are meant. Brady and co-workers have shown that this swim force is essential for the understanding of swim pressure against a boundary [101]. Alternatively, the swim force can be understood as the force that is needed to keep a swimmer from moving [101]. Note, when this is in fact done and the swimmer stops moving, the force-free condition no longer applies and a stokeslet term will appear in

the equations. The total flow field in this situation is sometimes referred to as the pumping field [100]. In contrast, if the swimmer is able to move freely, the internal forces (such as body surface deformations [35]) only induce higher-order fields, such as force or source dipoles.

2.2.2 Swimming mechanisms

Locomotion fulfills a variety of functions for biological microswimmers, such as searching for food and escaping predators [37], and is exploited for artificial microswimmers performing targeted drug delivery and minimally invasive medical interventions [21, 102, 103] or to study autonomous aggregation [104–107]. While the principles governing locomotion at low Reynolds numbers are the same, they can be implemented in a variety of ways by different swimmers. Among the most prominent mechanisms, we find body deformations, movement of appendices like flagella and cilia, as well as electro-, thermo- or diffusiophoretic effects, which induce a fluid flow at or close to the swimmer's surface [1, 17].

Importantly, active swimmers react to environmental cues. Such a response of a swimmer's motion to its surroundings is called *tactic behaviour*. Depending on the type of environmental stimulus, one can distinguish many kinds of taxis. The motion towards or away from a certain substance is called positive or negative chemotaxis [108]. For example, one speaks of aerotaxis in the case of oxygen [109]. Human sperm cells perform rheotaxis, which enables them to swim upstream in the cervical canal [68, 69, 110]. The motion towards light is known as phototaxis and along a temperature gradient as thermotaxis [111–114]. Bacteria can be magnetotactic [115]. The alignment along or against the direction of gravity is called gravitaxis or geotaxis [56, 59, 116].

The swimmer's interaction with the environment can happen with a rudimentary sensorial apparatus which scans for food or oxygen [117], but also by purely passive physical effects. Sometimes, the nature of the response can be a contested issue. In the case of gravitaxis it was believed that some cells could actively measure gravity and respond to it [118, 119]. In contrast, other researchers believe that the passive reorientation, due to the mismatch between the center of mass and the geometrical center, is responsible for the swimmer's reorientation [120, 121].

Biological microswimmers

In the following, we discuss some examples of active motion and of taxis. First, we want to focus on two ways of propulsion for biological swimmers. These are sketched in Fig. 2.2 a)-c). The bacterium *Escherichia coli* has one or more helical flagella with a length on the order of 10 μm at the back of its body [37]. Due to rotary molecular motors [67, 123], they can rotate clockwise or counter-clockwise. The propulsion happens due to, first, anisotropic translational drag and, second, translation-rotation coupling (matrices $\boldsymbol{\gamma}^{\mathrm{tt}}$ and $\boldsymbol{\gamma}^{\mathrm{tr}}$ in Eq. (2.52)) [37]. Thus, the rotating helix is able to move the cell body forward. Furthermore, the flagella can bundle together, or unbundle and lose synchronization, which is responsible for run-and-tumble motion [124]. The bacterium induces the tumble phase via intra-cellular pathways, depending on the surrounding food, thus

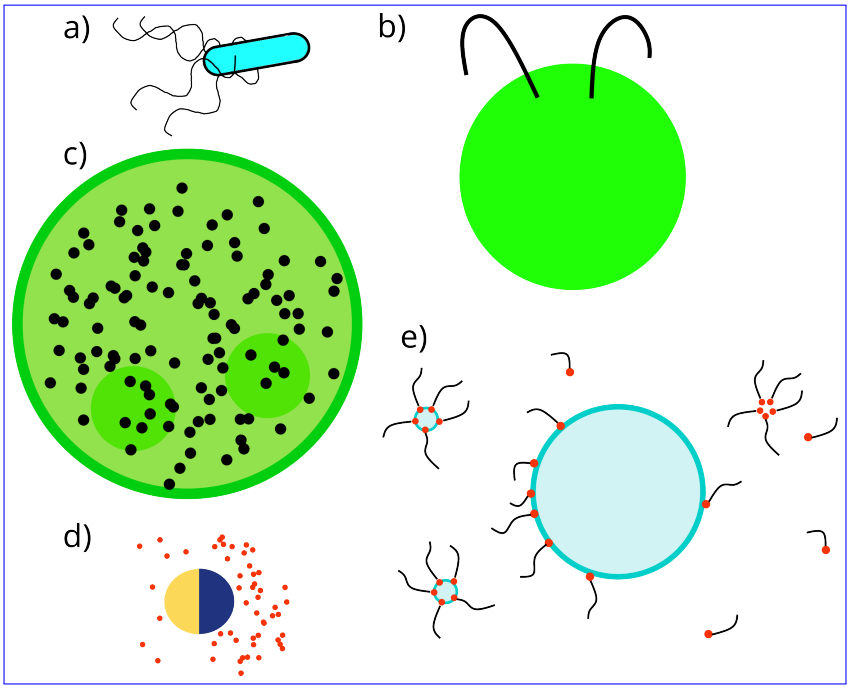

Figure 2.2: Sketches of different microswimmers. a) *E. coli* bacterium with several flagella (length around 2 μm). b) Biflagellate alga *Chlamydomonas* (radius around $10 - 20$ μm). c) *Volvox* with two daughter cells and distributed appendages over the whole body (radius around $100 - 200$ μm). d) Janus colloid surrounded by a chemical field (radius around 10 μm). e) Active emulsion droplet inhomogeneously covered with surfactants (radius around 50 μm) and within a solution of surfactants, some of which form filled and unfilled micelles (adapted from Ref. [122]).

using chemotaxis [117, 125]. The body counter-rotates relative to the flagellum, which adds a rotlet dipole to the hydrodynamic signature [87]. The speed of E.coli is on the order of $20 - 30$ μm/s [37, 126].

Common other examples are various algal species. This is significant, because algae are eukaryotic cells, and thus belong to a completely different biological domain than bacteria [127], so it is surprising that aspects of their swimming are comparable. These organisms are larger than bacteria and the molecular motors are distributed over the whole flagellum [37]. The alga *Chlamydomonas reinhardtii* possesses two flagella in the front of its body performing a bending motion, which resembles a breast-stroke swimmer [128]. Since there is a difference of drag between the power and recovery strokes, a net forward motion is achieved [37, 129]. The motion of *C. reinhardtii* is directed towards light, thus it is a phototactic organism [128, 130].

Some organisms have appendices distributed over their whole body and use synchronization among these cilia for their self-propulsion [48, 131, 132]. Their collective beating patterns create flow fields along their surface [17, 37]. We briefly describe the *Volvox* alga which has a radius of approximately 200 μm [48, 132]. Volvox is a multicellular organism with spherical shape, whose somatic cells on the surface each have a pair of beating flagella [132]. In their totality, they cause a coordinated metachronal

wave from the cell's north pole to its south pole. The transport of fluid across the surface results in a force-free motion of the organism [35, 131]. Importantly, Volvox algae carry small daughter colonies in their inside, which modifies the mass distribution of the whole cell [61, 132]. The cell is *bottom-heavy* and orients anti-parallel to a gravitational field.

Artificial microswimmers

Creating artificial microswimmers and controlling their motion from the outside is a fascinating research avenue [24, 102, 103]. It is often inspired by the swimming mechanisms visible in nature or to study swimming without the complicated molecular signalling that biological matter often involves [7, 28]. In particular, mimicking flagellar motion is a frequent procedure for artificial microswimmers, which has been proven to work by high-impact experiments, such as the manufactured flagellum by Dreyfus et al. [133].

A different and equally successful technique to create artificial microswimmers is the manufacture of catalytic swimmers [24, 29, 134]. Here, the necessary break of symmetry is not achieved by a deformation, but by self-generated fields or gradients [134]. An important class of synthetic active swimmers is given by *Janus particles* [25, 26, 53, 106, 111, 135–137]. We sketch a Janus particle in Fig. 2.2 d), together with its surrounding chemical field. Janus is a two-faced god in ancient Roman mythology and, accordingly, the symmetry breaking in Janus colloids is achieved by coating two sides of a spherical colloid (made for example from polystyrene [26] or gold [8]) by different materials. For example, half-coatings of the catalyst platinum result in an asymmetric chemical reaction around the particle when it is put in a H_2O_2 solution [8, 25, 26, 55]. An excess of product molecules develops on the catalytic side of the colloid, which creates a particle flux and a fluid flow around the colloid. This again results in a force-free propulsion of the colloid. A similar mechanism involving charged molecules is called electrophoresis [113, 138–140]. Another promising idea is using radiation energy as the particles' fuel, *i.e.*, using synthetic phototactic particles [106, 112, 135, 141]. In these experiments, one cap is light-absorbing, leading to an asymmetric heating of the colloid. Since they reside in a near-critical mixture, the local temperature increase results in demixing [135], which achieves a concentration gradient around the particle.

Finally, *active emulsion droplets* also propel due to self-induced chemical gradients [28, 122, 142]. However, since they are made from liquid materials their response to gravity can be tailored more narrowly, *e.g.*, by changing the density of the solvent [143, 144]. In the case of liquid crystal droplets [27, 28, 142, 145], the chemical acting as a fuel is a surfactant molecule that changes the surface tension of the droplet locally. Thus, a surface slip appears due to the Marangoni effect [28, 146, 147]: fluid flows to the side of the droplet with a higher surface tension, and thus a lower surfactant molecule coverage. This results in self-propulsion. The droplet gets smaller over time, since it ejects emulsion-filled surfactant micelles. This also results in a lack of fuel behind the droplet, so that other droplets effectively stay clear from the visited path. This self-avoiding behaviour is called *autochemotaxis* [148]. We show a sketch of the active emulsion droplet in Fig. 2.2 e). An important difference to Janus particles is that the swimming direction does not result from the manufacturing of the droplet but happens

from a spontaneous symmetry breaking [28].

2.2.3 Stochastic motion of microswimmers

Due to the small size of microswimmers they can be strongly influenced by molecular collisions. Thus, microswimmers have to adapt their locomotion to a fluctuating environment, which is illustrated nicely by the run-and-tumble motion of *E.coli*. For passive particles, the most famous stochastic process is that of *Brownian motion*. We introduce the relevant concepts of Brownian motion in the following and then combine these thermal fluctuations[4] with the concept of persistent locomotion, which leads us to the model of the *active Brownian particle*. The laws of diffusion that govern this model particle are also relevant for the swimmer model we use in our studies. Furthermore, the laws of stochastic motion are important for our simulation method.

Stochastic processes and the insights of statistical physics constitute large and exhaustive fields, thus, we constrain ourselves here to the concepts that are most relevant to our setting. These include the Langevin equation and the Stokes-Einstein relation for diffusion and friction.

Langevin equation

A Brownian particle moves in a very irregular way and the molecular collisions responsible for it are analytically intractable. However, by making assumptions about the distribution of the random forces, it is possible to write down a stochastic differential equation, also known as the *Langevin equation*. It can be written as [150]

$$m\frac{d^2\mathbf{x}}{dt^2} = -\mathbf{\Gamma}_{\text{trans}}\frac{d\mathbf{x}}{dt} + \mathbf{F}_{\text{ext}} + \boldsymbol{\xi}(t). \tag{2.68}$$

We have retained the external force $\mathbf{F}_{\text{ext}}$ on the particle, which leads to a drift in addition to diffusion.

When we assume that the system is *overdamped*, we can neglect the acceleration term. The term proportional to the particle velocity is the hydrodynamic drag force acting on the particle with the friction tensor for particle translation $\mathbf{\Gamma}_{\text{trans}}$. The term $\boldsymbol{\xi}$ represents the stochastic force, which is a random variable. We make the following assumptions about its distribution

$$\langle \xi_i(t) \rangle = 0, \tag{2.69}$$

$$\langle \xi_i(t)\xi_j(t') \rangle = 2g_{ij}\delta(t-t'), \tag{2.70}$$

where $\langle \ldots \rangle$ denotes the ensemble average. The noise is distributed according to a Gaussian distribution. Additionally, the second property states that different stochastic forces are uncorrelated, which is why the stochastic forces represent *white Gaussian noise*.

[4] We note that active swimmers can have additional noise sources that do not originate from thermal fluctuations. This is sometimes called *active* or *intrinsic* noise and poses a further challenge to the stochastic modelling of microswimmers [149].

Diffusion tensor

Next, we define the diffusion tensor via the second moment of the displacement

$$\langle \mathbf{x}(t) \otimes \mathbf{x}(t) \rangle = 2\mathbf{D}_{\text{trans}} t. \tag{2.71}$$

The linear scaling of the square displacement with time is typical for a diffusive process. The diffusion tensor captures the fluctuation properties of the system. It is related to the friction $\mathbf{\Gamma}_{\text{trans}}$ via the *fluctuation-dissipation relation*, which in this case is also called the Stokes-Einstein law:

$$\mathbf{D}_{\text{trans}} = k_B T \mathbf{\Gamma}_{\text{trans}}^{-1}. \tag{2.72}$$

Another aspect of the fluctuation-dissipation theorem involves the velocity autocorrelation $\langle v_i(t) v_j(0) \rangle$ for which we have the *Green-Kubo relation* [151, 152]

$$\mathbf{D}_{\text{trans}} = \int_0^\infty \langle \mathbf{v}(t) \otimes \mathbf{v}(0) \rangle dt. \tag{2.73}$$

or alternatively [153]

$$\mathbf{\Gamma}_{\text{trans}} = \frac{1}{k_B T} \int_0^\infty \langle \mathbf{F}(t) \otimes \mathbf{F}(0) \rangle dt. \tag{2.74}$$

The magnitude of the correlations in Eq. (2.70) can be calculated to be [154]

$$g_{ij} = 2 k_B T \Gamma_{ij}. \tag{2.75}$$

Note that the friction tensor for a spherical particle is $\Gamma_{ij} = \gamma \delta_{ij}$. In the following, we switch to that assumption.

Ballistic and diffusive motion

If we take the inertial term in Eq. (2.68) into account, we can estimate the time scale at which diffusive behaviour sets in. First, we calculate the solution for the velocity

$$\mathbf{v}(t) = \mathbf{v}(0) e^{-t/\tau_B} + \frac{1}{m} \int_0^t e^{-(t-t')/\tau_B} \xi(t') dt'. \tag{2.76}$$

Thus, the mean velocity $\langle \mathbf{v} \rangle$ decays exponentially in time, unless there is an external drift. The time scale of this decay is the *momentum relaxation time* τ_B, defined as $\tau_B = m/\gamma$. One can arrive at the following expression for the displacement $\mathbf{x}(t)$ [155]

$$\mathbf{x}(t) = \mathbf{v}(0) \tau_B \left(1 - e^{-t/\tau_B}\right) + \frac{1}{\gamma} \int_0^t \left(1 - e^{-(t-t')/\tau_B}\right) \xi(t') dt', \tag{2.77}$$

where we set the initial displacement to zero. Then, the second moment of the displacement is

$$\begin{aligned} \langle x_i(t) x_j(t) \rangle &= \tau_B^2 v_i(0) v_j(0) \left(1 - e^{-t/\tau_B}\right)^2 \\ &\quad + 2 \frac{k_B T}{\gamma} \delta_{ij} \int_0^t \left(1 - 2e^{-(t-t')/\tau_B} + e^{-2(t-t')/\tau_B}\right) dt' \delta_{ij} \\ &= \tau_B^2 v_i(0) v_j(0) \left(1 - e^{-t/\tau_B}\right)^2 + \\ &\quad \frac{2 k_B T}{\gamma} \left(t - \frac{3}{2}\tau_B + 2\tau_B e^{-t/\tau_B} - \frac{1}{2}\tau_B e^{-2t/\tau_B}\right) \delta_{ij}, \end{aligned} \tag{2.78}$$

where we have already used $\langle \xi_i(t)\xi_j(t')\rangle = 2k_BT\gamma\delta(t-t')$. We recognize that the diffusive scaling $x^2 \sim t$ is reached exactly when $t \gg \tau_B$, *i.e.*, for times much larger than the momentum relaxation time. In particular, it follows that the *mean squared displacement* $\langle|\mathbf{x}|^2\rangle$ behaves as [33, 155]

$$\langle|\mathbf{x}|^2\rangle = 6D_{\text{trans}}t. \tag{2.79}$$

Note that the second moment of the velocity can be calculated to be [155]

$$\langle v_i(t)v_j(t)\rangle = \frac{k_BT}{m}\left(1-e^{-2t/\tau_B}\right). \tag{2.80}$$

Thus, consistent with the equipartition theorem, we have for long times [155]

$$\frac{m}{2}\langle|\mathbf{v}|^2\rangle = \frac{3}{2}k_BT. \tag{2.81}$$

It is possible to estimate the time scale of the diffusive processes. For a sphere of radius R, we use the translational diffusion constant D_{trans} in order to express the typical time it takes the particle to be displaced a distance R. This time is

$$\tau_{\text{diff}} = R^2/D_{\text{trans}}. \tag{2.82}$$

Rotational diffusion

Since a suspended colloid usually experiences random torques along with random forces, we also have to consider rotational diffusion. This is typically important for rod-shaped particles [155]. However, as we will see below, a spherical active particle has a fluctuating orientation vector, therefore we have to consider rotational diffusion. The laws of rotational diffusion are similar to those of translational diffusion. First, the overdamped Langevin equation for the angular velocity $\mathbf{\Omega}$ is [155]

$$\mathbf{\Omega} = \mathbf{\Gamma}_{\text{rot}}^{-1}\mathbf{T}_{\text{ext}} + \mathbf{\Gamma}_{\text{rot}}^{-1}\boldsymbol{\zeta}(t), \tag{2.83}$$

using the external torque $\mathbf{T}_{\text{ext}}$ and the rotational friction $\mathbf{\Gamma}_{\text{rot}}$. The stochastic torque $\boldsymbol{\zeta}$ is again characterized by white Gaussian noise.

The Stokes-Einstein relation also exists for rotational diffusion and has the form [154]

$$\mathbf{D}_{\text{rot}} = k_BT\mathbf{\Gamma}_{\text{rot}}^{-1}, \tag{2.84}$$

For a scalar friction coefficient γ_{rot}, we have $D_{\text{rot}} = k_BT/\gamma_{\text{rot}}$. Then, the time scale for rotational diffusion is given by $\tau_r = 1/D_{\text{rot}}$.

Smoluchowski equation

Considering the motion of a particle under thermal fluctuations, it is possible to derive an equation for the probability density of the particle position, $\rho(\mathbf{r},t)$, from the stochastic differential equations [155]. This *Smoluchowski equation* takes the form

$$\partial_t\rho = -\nabla\cdot\mathbf{D}\left(\frac{\mathbf{F}}{k_BT} - \nabla\right)\rho, \tag{2.85}$$

where $\mathbf{F}$ is an external force. One often writes the right-hand side as the negative divergence of a probability current,

$$\mathbf{j} = \boldsymbol{\mu}\mathbf{F}\rho - \mathbf{D}\nabla\rho, \tag{2.86}$$

where $\boldsymbol{\mu} = \mathbf{D}/k_BT$ is the mobility matrix. This offers a good intuition: A stationary probability density is reached, when the diffusive and deterministic currents balance each other.

Persistence

In contrast to passive colloids, active particles move with a drift velocity. This introduces an additional time scale $\tau_0 = R/v_0$, where R is the radius of the active particle and v_0 is the active velocity. The *active Péclet number* Pe is the ratio between the diffusive time scale and the ballistic time scale of active motion:

$$\mathrm{Pe} = \frac{\tau_{\mathrm{diff}}}{\tau_0} = \frac{v_0 R}{D_{\mathrm{trans}}}. \tag{2.87}$$

A high Péclet number means that the swimmer's self-propulsion dominates translational diffusion. However, we still need to consider orientational noise, since the persistence of the swimming direction is also affected by rotational diffusion [154]. Hence, we compare the ballistic time scale τ_0 to the rotational diffusion time, which yields the *persistence number*

$$\mathrm{Pe}_r = \frac{v_0}{R D_{\mathrm{rot}}}. \tag{2.88}$$

Typical Péclet numbers are on the order of several 100 for biological swimmers like E. coli and B. subtilis [67, 156, 157], and $10 - 100$ for catalytic Janus particles [8, 141]. The persistence number is around 150 for E. coli and around 20 for the catalytic particle.

The active Brownian particle

The active Brownian particle is one of the simplest model descriptions of active matter and one of the most used [33]. Despite its simplicity, it shows complex collective behaviour, such as motility-induced phase separation [7] and polar order under gravity [158]. This complexity emerges from the microscopic dynamics: since each particle has its own self-propulsion, energy is introduced into the system on a local scale and each particle goes through an irreversible process [7]. This characterizes the system as far from thermal equilibrium, and sets it apart from a global driving of the whole system with an external force [7].

The active Brownian particle is a spherical object with a self-propulsion velocity $v_0\mathbf{e}$, where v_0 is the constant speed and $\mathbf{e}$ the swimming direction, *i.e.*, the particle's orientation. The dynamics of the particle is described as follows

$$\dot{\mathbf{r}}(t) = v_0\mathbf{e}(t) + \frac{D_{\mathrm{trans}}}{k_BT}\boldsymbol{\xi}(t), \tag{2.89}$$

$$\dot{\mathbf{e}}(t) = \frac{D_{\mathrm{rot}}}{k_BT}\boldsymbol{\zeta} \times \mathbf{e}. \tag{2.90}$$

The translational and rotational noise terms $\boldsymbol{\xi}$ and $\boldsymbol{\zeta}$ satisfy the conditions of the Brownian process outlined above.

Enhanced diffusion The diffusion process for active Brownian particles is different than for passive particles, since the rotational noise couples to the translational motion [33]. The mean squared displacement of the active Brownian particle is [26, 33]

$$\langle |\mathbf{x}|^2 \rangle = \left(6D_{\text{trans}} + v_0^2 \tau_r\right) t - \frac{1}{2} v_0^2 \tau_r^2 \left(1 - e^{-t/\tau_B}\right). \tag{2.91}$$

Here, we used the rotational decorrelation time $\tau_r = 1/D_{\text{rot}} = 4R^2/(3D_{\text{trans}})$. Thus, for long times, we have the effective diffusion constant

$$D_{\text{eff}} = D_{\text{trans}} + \frac{1}{6} v_0^2 \tau_r = D_{\text{trans}} \left(1 + \frac{2}{9}\text{Pe}^2\right), \tag{2.92}$$

which grows quadratically with the Péclet number.

Motility-induced phase separation The non-equilibrium nature of active colloids becomes especially apparent in their phase behaviour. In particular, a liquid-gas phase transition takes place in systems where particle-particle interactions are not attractive but only repulsive, in contrast to passive systems [6, 7, 159, 160]. The speed of the particles depends strongly on the density. This effect is a result of particle-particle collisions, which slow the particles down locally [7]. Importantly, above a critical Péclet number and a critical density, the purely diffusive reorientation away from an accumulation of particles takes longer than the addition of external active particles that swim into the cluster [6, 161]. Thus, density inhomogeneities start to grow. The topic of motility-induced phase separation has attracted a lot of fascination and goes far beyond the model of the active Brownian particle. Thus, implications for hydrodynamic swimmer systems have been discussed [42, 43, 162], as well as extensions and alternative models, such as particles with social interactions [32, 161, 163], or run-and-tumble particles [164, 165]

2.2.4 Squirmer model

For an incompressible Newtonian fluid at low Reynolds number the Stokes equations (2.26) hold. As we have seen, a large variety of swimming mechanisms exist, from using cilia and flagella to different forms of phoretic effects. In order to model different kinds of self-propulsion, we use a versatile approximation, which is called the squirmer model. Here, we restrict ourselves to spherical squirmers, even though elongated squirmer models have been developed, as well [166, 167]. Lighthill [35] and Blake [36] were first to describe the squirmer model. It is a swimmer that implements a surface actuation via a prescribed surface velocity. In the following, we assume the velocity to be a purely tangential slip velocity. The squirmer model is mainly inspired by ciliated organisms, such as *Paramecium*. In the following, we write down a general squirmer model, using Lamb's solution. We calculate the flow field of a squirmer and discuss it in terms of hydrodynamic multipoles.

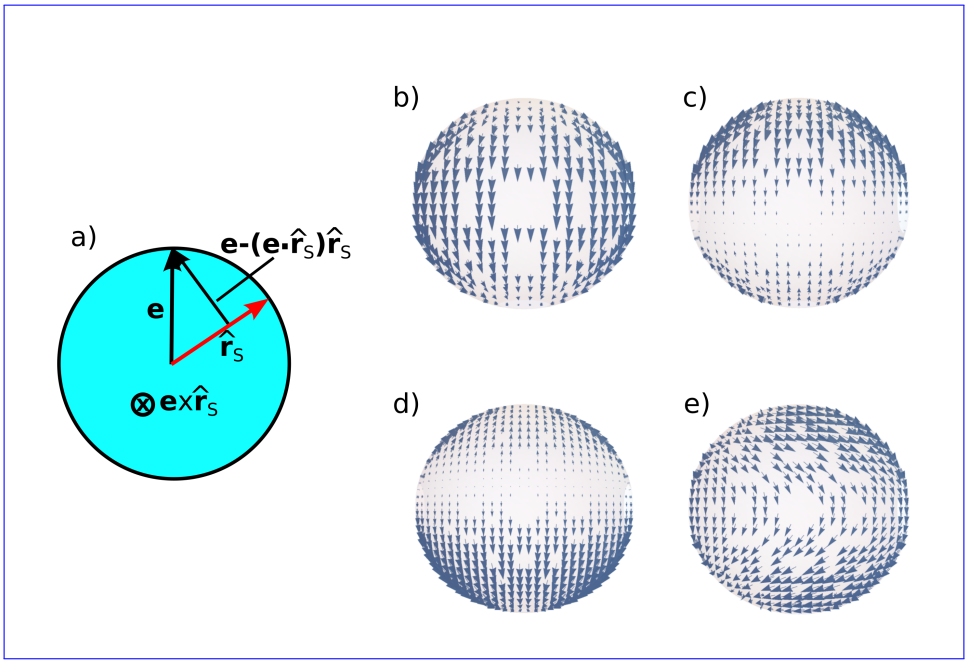

Figure 2.3: a) Sketch of a squirmer with orientation vector $\mathbf{e}$ and the attached orthonormal system consisting of surface vector $\hat{\mathbf{r}}_\mathbf{S}$, $\mathbf{e}\times\hat{\mathbf{r}}_\mathbf{S}$ and $\mathbf{e}-(\mathbf{e}\cdot\hat{\mathbf{r}}_\mathbf{S})\,\hat{\mathbf{r}}_\mathbf{S}$. b)-e) Surface flow fields of spherical squirmers. All squirmers have a finite B_1 mode of $B_1 = 0.1$, so that they can self-propel. b) Neutral squirmer $B_2 = C_2 = 0$, c) puller squirmer $B_2 = 0.5$, $C_2 = 0$, d) pusher squirmer $B_2 = -0.5$, $C_2 = 0$, e) rotlet dipole squirmer $B_2 = 0$, $C_2 = 0.3$.

Application of Lamb's solution to squirmer

We use Lamb's solution to the external problem from section 2.1.3, and use it to model our swimmer with radius R. For the surface flow field we follow Pak and Lauga [100] and assume an axisymmetric flow field[5]. We note that swimmers with more general surface velocities can be modelled, as well [100]. With these requirements Lamb's solution from Eq. (2.33) yields [100]

$$\begin{aligned}\mathbf{u}(\mathbf{r}) &= \sum_{n=1}^{\infty}\tilde{B}_n\frac{(n+1)P_n}{r^{n+2}}\left(\frac{r^2}{R^2}-1\right)\mathbf{e}_r \\ &+ \sum_{n=1}^{\infty}\tilde{B}_n\sin\vartheta P_n'\left(\frac{n-2}{nR^2r^n}-\frac{1}{r^{n+2}}\right)\mathbf{e}_\vartheta \\ &+ \sum_{n=1}^{\infty}\tilde{C}_n\frac{\sin\vartheta P_n'}{r^{n+1}}\mathbf{e}_\varphi \end{aligned} \tag{2.93}$$

Here, P_n' is the derivative of the Legendre polynomial P_n. For the flow field in Eq. (2.93), the swimming direction $\mathbf{e}$ is identical with the z-axis, *i.e.*, where the angle $\vartheta = 0$.

[5]This amounts to setting $m = 0$ for the associated Legendre polynomials in Eq. (A.4)

The flow field at the surface $r = R$ is consistent with the squirmer model by Lighthill [35] and Blake [36], when setting $\tilde{B}_n = -\frac{R^{n+2}}{n+1} B_n$ and $\tilde{C}_n = C_n R^{n+1}$. We change the notation slightly and express the base vectors using the squirmer orientation $\mathbf{e}$, see also Fig. 2.3 a). Then the surface flow field of the spherical squirmer is

$$\begin{aligned} \mathbf{u}(\mathbf{r})|_{r=R} =& \sum_{n=1}^{\infty} B_n \frac{2P_n'(\mathbf{e}\cdot\hat{\mathbf{r}})}{n(n+1)} \left[-\mathbf{e} + (\mathbf{e}\cdot\hat{\mathbf{r}})\hat{\mathbf{r}}\right] \\ &+ \sum_{n=1}^{\infty} C_n P_n'(\mathbf{e}\cdot\hat{\mathbf{r}}) \left[\mathbf{e}\times\hat{\mathbf{r}}\right] . \end{aligned} \tag{2.94}$$

We truncate the series after the B_2 and C_2 terms. Fig. 2.3 b)-e) show different kinds of surface flow fields that can be realized with the remaining modes. We discuss them further below. The resulting flow field becomes

$$\begin{aligned} \mathbf{u}(\mathbf{r}) =& \frac{B_1}{2}\Bigg[\left(-\frac{R}{r}\left[\mathbf{e} + (\mathbf{e}\cdot\hat{\mathbf{r}})\hat{\mathbf{r}}\right] + \frac{R^3}{r^3}\left[-\mathbf{e} + 3(\mathbf{e}\cdot\hat{\mathbf{r}})\hat{\mathbf{r}}\right]\right) \\ &- \beta\frac{R^2}{r^2}\left(-\hat{\mathbf{r}} + 3\left(\mathbf{e}\cdot\hat{\mathbf{r}}\right)^2\hat{\mathbf{r}}\right) + 6\chi\frac{R^3}{r^3}(\mathbf{e}\cdot\hat{\mathbf{r}})\left[\mathbf{e}\times\hat{\mathbf{r}}\right] + \mathcal{O}\left(\frac{R^4}{r^4}\right)\Bigg]. \end{aligned} \tag{2.95}$$

We have defined the squirmer parameter $\beta = B_2/B_1$ and the chirality parameter $\chi = C_2/B_1$.

Note that the stokeslet field - decaying with $1/r$ - has not yet been eliminated. Therefore, the flow structure described in Eq. (2.95) allows for external fields acting on the swimmer and is not yet the field of a free squirmer. The reason for this is, that we have not yet included the squirmer's self-propulsion velocity v_0 into the flow field, with which it swims in the force-free case. We can therefore interpret the flow field Eq. (2.95) as the pumping field of a squirmer held at constant position [100], which means that the force acting on the squirmer is precisely the stall force $\mathbf{F}_a = 6\pi\eta R v_0 \mathbf{e}$. Taking the definition of the force in Lamb's solution in Eq. (2.50), we can set

$$\mathbf{F}_a = 4\pi\eta R \nabla(\mathbf{e}\cdot\mathbf{r}) B_1 = 4\pi\eta R B_1 \mathbf{e} \stackrel{!}{=} 6\pi\eta R v_0 \mathbf{e}. \tag{2.96}$$

We arrive at the known relation for the active squirmer velocity

$$v_0 = \frac{2}{3} B_1. \tag{2.97}$$

Thus, the B_1 mode is responsible for self-propulsion, corresponding to a source dipole flow field.

Free squirmer

So far, we have described a squirmer that is not moving but is held by an external force, which we calculated above. We note that these calculations and the introduced flow

fields are used later when we discuss our simulation results for squirmers under gravity. In order to determine the flow field $\mathbf{u}_{\text{free}}$ of the freely moving squirmer, consider that the moving body creates the same flow field as a dragged sphere, which was introduced in Eq. (2.64), *i.e.*, a stokeslet and a source dipole term [100]. The stokeslet contribution of the dragged particle field exactly cancels the stokeslet term of Eq. (2.95). Consequently, we have

$$\begin{aligned}\mathbf{u}_{\text{free}}(\mathbf{r}) =& B_1 \Bigg[\frac{1}{3}\frac{R^3}{r^3}\left[-\mathbf{e} + 3(\mathbf{e}\cdot\hat{\mathbf{r}})\hat{\mathbf{r}}\right] \\ &- \frac{\beta}{2}\frac{R^2}{r^2}\left(-\hat{\mathbf{r}} + 3\left(\mathbf{e}\cdot\hat{\mathbf{r}}\right)^2\hat{\mathbf{r}}\right) + 3\chi\frac{R^3}{r^3}(\mathbf{e}\cdot\hat{\mathbf{r}})\left[\mathbf{e}\times\hat{\mathbf{r}}\right] + \mathcal{O}\left(\frac{R^4}{r^4}\right)\Bigg].\end{aligned} \tag{2.98}$$

We can read off the coefficients p, s, q of the force dipole, source dipole, and rotlet dipole, that were introduced in section 2.1.4, where

$$\mathbf{u}_{\text{free}}(\mathbf{r}) = p\mathbf{G}_D(\mathbf{e},\mathbf{e},\mathbf{r}) + s\mathbf{G}_{SD}(\mathbf{e},\mathbf{r}) + q\mathbf{R}_D(\mathbf{e},\mathbf{r}). \tag{2.99}$$

The parameter s is linked to the active velocity, as explained above. The parameter p comes from the squirmer parameter β [87, 168], whereas the rotlet dipole strength q is connected to the chirality parameter χ:

$$p = -\frac{3}{4}\beta v_0 R^2 \quad , \quad s = \frac{1}{2}v_0 R^3 \quad , \quad q = \frac{9}{2}\chi v_0 R^3. \tag{2.100}$$

Flow fields of squirmers

While the source dipole is necessary for the propulsion of the swimmer, we can tailor the surface slip velocity and thereby the hydrodynamic signature, as we show in Fig. 2.3 b)-e). As Eq. (2.98) shows, the highest order contribution is the force dipole, as required by the force-free condition. The force dipole is controlled via the squirmer parameter β. A squirmer with $\beta < 0$ is called a pusher, a squirmer with $\beta > 0$ a puller, and a squirmer with $\beta = 0$ a neutral squirmer. The terms pusher and puller are inspired by biological organisms. A breast-stroke motion, as performed by the biflagellate Chlamydomonas, pulls the fluid from the front of the swimmer. Puller squirmers mimic the fluid flow that is induced in this way, as we show in Figure 2.4 b) and e). Pushers, on the other hand, push fluid with their appendices in the back, such as sperm cells or E.coli bacteria. The flow field of a pusher squirmer is shown in Fig. 2.4 c) and f). The flow fields of pullers and pushers result from the strong fluid flow from the north pole to the equator, and from the equator to the south pole, respectively, which can be seen in Fig. 2.3 b) and c). Active emulsion droplets have been called 'model squirmers', because they propel due to an induced surface flow field. Furthermore, the squirmer model was originally inspired by ciliated protists [35]. Both of these cases can be approximated by a neutral squirmer, whose flow field we also depict in Fig. 2.4 a) and d).

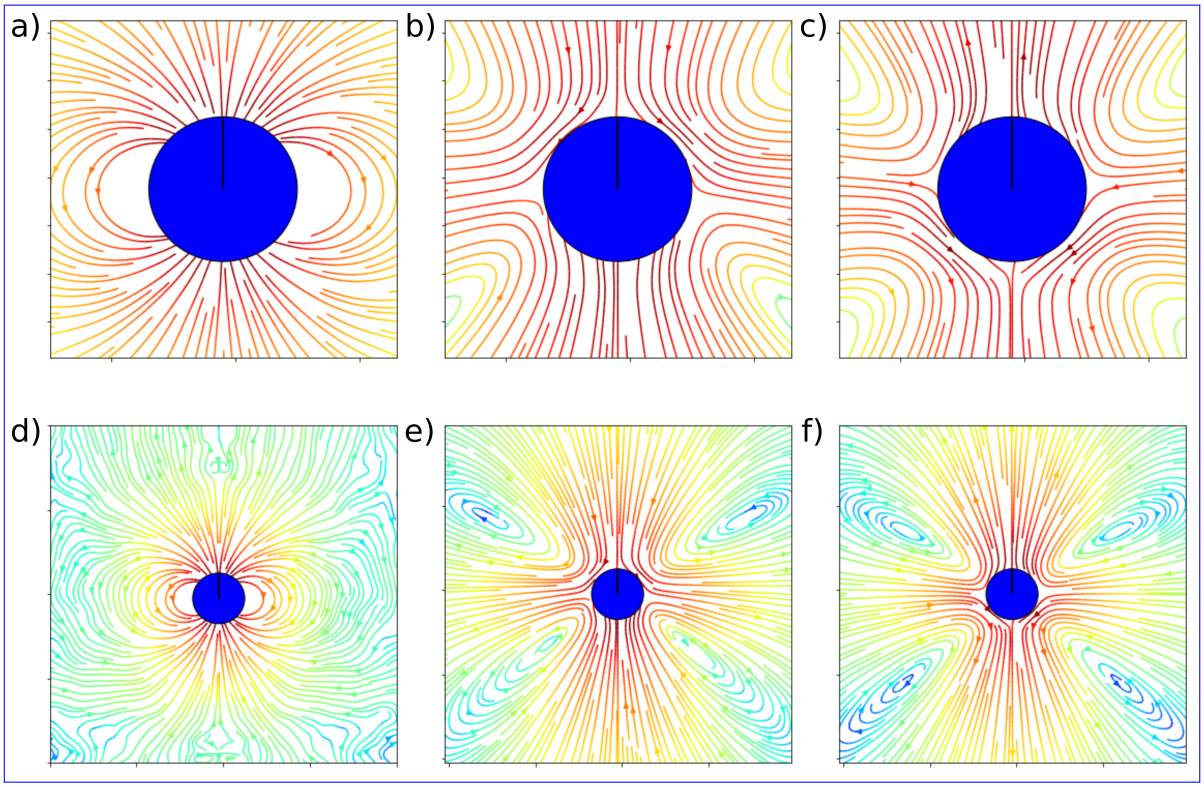

Figure 2.4: Bulk flow fields of a) a neutral squirmer $\beta = 0$, b) a puller $\beta = 5$ and c) a pusher $\beta = -5$, shown as streamlines in the laboratory frame. Squirmers are oriented towards the top of the figure. Subfigures d)-f) show the far fields.

The example of *E.coli* shows that this picture is not yet complete. Due to the rotating motion of the flagella, a counter rotation is induced in the cell body. This creates a rotlet dipole field for this swimmer [169, 170]. By setting the squirmer chirality parameter $\chi \neq 0$, we can also model rotlet dipole fields [100]. The intrinsic chirality of the rotlet dipole can be seen in the surface flow field of Fig. 2.3 e).

The representation of real swimmers by the squirmer model has some limitations. For example, the experimentally occurring flow fields may vary in time due to a beating cycle [171, 172], or may further depend on a chemical processes [122, 173].

2.3 Hydrodynamic interactions

Microswimmers induce a signature flow field in the fluid they inhabit. In some models, such as the active Brownian particle, the details of these fields are ignored and swimmers interact only via a particle-particle or particle-wall potential. However, the importance of flow on swimmer dynamics is well established [39–44]. This includes both external flow and interactions with surfaces or between swimmers [37, 174].

For many of the phoretic swimmers we discussed above, the dynamics of the chemicals that supply the catalytic or surfactant reactions is very important. The dynamics of the chemicals induces additional interactions between swimmers and with surfaces

[91, 175, 176]. For our studies, we will neglect the dynamics of these solvent particles and the emerging additional interactions, which strongly depend on the particular swimmer. Instead, we study the generic effects of hydrodynamic interactions that are relevant for any swimmer. This helps to understand and estimate the role of hydrodynamic interactions even in the presence of other interactions.

In the following, we present the important Faxén theorems for translation and rotation and discuss both far- and near-field hydrodynamic interactions.

2.3.1 Faxén Theorems

The rigid body motion of a particle is influenced by its surrounding flow field. The force and torque experienced by a spherical particle in an ambient flow has been calculated by Faxén [82, 177]. The formulae are called the *Faxén theorems* of translation and rotation and state that

$$\mathbf{F} = 6\pi\eta R \left(1 + \frac{R^2}{6}\nabla^2\right)\Big|_{\mathbf{x}=\mathbf{x}_c} \mathbf{u}_0(\mathbf{x}) - 6\pi\eta R\mathbf{U}, \tag{2.101}$$

$$\mathbf{T} = 8\pi\eta R^3 \left(\frac{1}{2}\nabla \times \mathbf{u}_0(\mathbf{x})\right)\Big|_{\mathbf{x}=\mathbf{x}_c} - 8\pi\eta R^3\mathbf{\Omega}. \tag{2.102}$$

Here, $\mathbf{x}_c$ is the center of mass of the particle and $\mathbf{u}_0$ is the surrounding flow field without the particle.

These laws are relevant for interactions with a boundary and for swimmer-swimmer interactions. In the case of the no-slip boundary, the swimmer interacts with its own flow field and experiences effective attraction, repulsion, and reorientation due to the modifications of the flow by the no-slip wall [87]. On the other hand, the background flow field can also be induced by a another particle, or indeed by a whole suspension of particles. For example, we know the flow field of a particle dragged by a force $\mathbf{F}_1$ from Eq. (2.64), which is a combination of a stokeslet and a source dipole. If we consider this induced flow as the ambient flow of a second sphere, Faxén's law of translation dictates for the velocity of this second sphere $\mathbf{V}_2$ [82]

$$\mathbf{V}_2 = \frac{1}{6\pi\eta R}\mathbf{F}_2 - \left(1 + \frac{R^2}{6}\nabla^2\right)\Big|_{\mathbf{x}=\mathbf{x}_2} \left(1 + \frac{R^2}{6}\nabla^2\right) \mathbf{O}\left(\mathbf{x} - \mathbf{x}_1\right)\mathbf{F}_1, \tag{2.103}$$

with the Oseen tensor $\mathbf{O}$. For simplicity, we have assumed that both spheres have the same radius R.

Obviously, the same formula can be applied to the first particle from which follows another correction. The iterative calculation of the forces and torques in a suspension by a repeated application of the Faxén theorem is known as the *method of reflections* [155]. However, we will usually only consider the leading orders of the flow fields we encounter.

2.3.2 Interactions with a no-slip boundary

Colloids or microswimmers in a fluid encounter boundaries. Clearly, the presence of boundaries changes the solution of the Stokes equations, since they impose additional

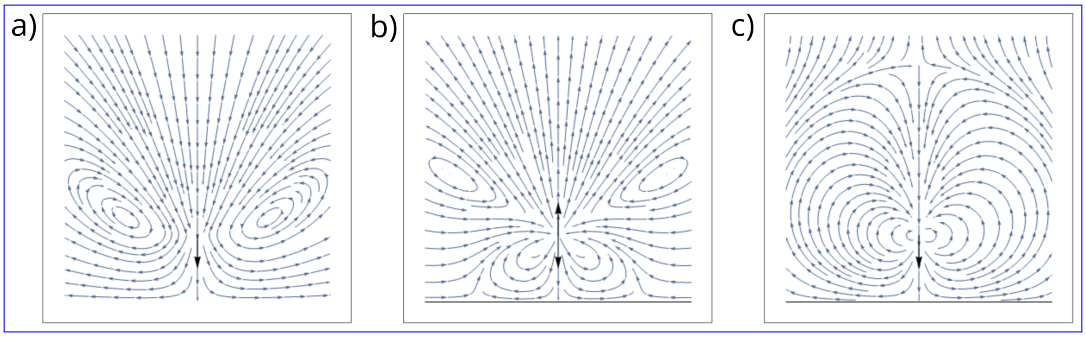

Figure 2.5: Singularity flow fields for a multipole located above a no-slip wall including its image singularities. The wall coincides with the $z = 0$ plane at the bottom of the plot. We confirmed that the flow field there is zero. a) Stokeslet pointing in negative z direction, b) force dipole with $\hat{\mathbf{e}} = -\hat{\mathbf{f}} = -\mathbf{e}_z$ and c) source dipole with $\hat{\mathbf{f}} = -\mathbf{e}_z$.

Table 2.1: Composition of the wall image singularities for different multipoles of Stokes flow

Multipole	Image singularities
stokeslet	stokeslet, force dipole, source dipole
force dipole	force dipole, force quadrupole, source dipole, source quadrupole
source dipole	source dipole, force quadrupole, source quadrupole
rotlet	rotlet, force dipole, source dipole
rotlet dipole	rotlet dipole, force quadrupole, source dipole, source quadrupole

conditions on the fluid flow. Green's function in half-space — a fluid with an infinite no-slip wall in the $z = 0$ plane — can be calculated and is called the *Blake tensor* [178]. Similar to electrostatics, it consists of a system of image singularities in the region $z < 0$, opposite to the fluid. This image system counteracts the stokeslet in a way that fulfills the no-slip condition. The Blake tensor for a wall at $z = 0$ and a point force at position $\mathbf{r}_0 = (x, y, \Delta z)$ is [87, 178]

$$\begin{aligned}\mathbf{B}(\mathbf{r}, \mathbf{r}_0, \mathbf{e}) =& \mathbf{G}_S(\mathbf{r} - \mathbf{r}_0, \mathbf{e}) + \mathbf{G}^*_S(\mathbf{r} - \mathbf{r}_0, \mathbf{e}) \\ =& \mathbf{G}_S(\mathbf{r} - \mathbf{r}_0, \mathbf{e}) - \mathbf{G}_S(\mathbf{r} - \mathbf{r}^*_0, \mathbf{e}) + \\ & \sin\vartheta \left(2\Delta z \mathbf{G}_D(\mathbf{r} - \mathbf{r}^*_0, \mathbf{e}_\rho, \mathbf{e}_z) - 2\Delta z^2 \mathbf{G}_{SD}(\mathbf{r} - \mathbf{r}^*_0, \mathbf{e}_\rho)\right) + \\ & \cos\vartheta \left(-2\Delta z \mathbf{G}_D(\mathbf{r} - \mathbf{r}^*_0, \mathbf{e}_z, \mathbf{e}_z) + 2\Delta z^2 \mathbf{G}_{SD}(\mathbf{r} - \mathbf{r}^*_0, \mathbf{e}_z)\right),\end{aligned} \tag{2.104}$$

where $\mathbf{r}^*_0 = \mathbf{r} - 2\Delta z \mathbf{e}_z$ is the position of the image, $\mathbf{e}$ is the orientation of the point force, and we measure the angle ϑ from the vertical. Finally, we have $\mathbf{e}_\rho = (\cos\varphi, \sin\varphi)$ in the plane. The mirrored stokeslet term $\mathbf{G}_S(\mathbf{r} - \mathbf{r}^*_0, \mathbf{e})$ directly counteracts the stokeslet above the wall. However, it is not enough to fulfill the no-slip boundary condition at $z = 0$. Therefore force dipole and source dipole terms are needed, as well.

In the same way, we can introduce image singularities for higher order singularities. Various terms have been calculated by Blake and Chwang [179], and Spagnolie and Lauga [87]. We provide an overview in Table 2.1. Note that all the image singularities are positioned at the mirrored position $\mathbf{r}^*_0$. The terms are not simply added together, but

have specific pre-factors. Furthermore, the composition of singularities differ depending on whether one looks at the direction parallel or perpendicular to the wall. The concrete image systems can be found in Appendix B and in Ref. [87]. We show the flow fields of a stokeslet, a symmetric force dipole and a source dipole singularitiy close to a wall in Figure 2.5. These are the most relevant contributions for a squirmer under gravity.

2.3.3 Mobility matrix

A passive sphere dragged in wall proximity experiences a non-homogeneous hydrodynamic resistance. For example, it is obvious that the friction has to increase the closer a particle gets to the no-slip wall in order to not crash into it. The resulting mobility matrix has wall-parallel and wall-perpendicular contributions and consists of a translational part, a rotational part and a translation-rotation coupling. We provide the first terms of the series expansion for no-slip walls, computed by Perkins and Jones [180].

$$6\pi\eta R\mu_{\perp}^{\mathrm{tt}}(z) = 1-\frac{9}{8}\frac{R}{z}+\frac{1}{2}\left(\frac{R}{z}\right)^3-\frac{135}{256}\left(\frac{R}{z}\right)^4+\mathcal{O}\left(\left(\frac{R}{z}\right)^5\right), \tag{2.105}$$

$$6\pi\eta R\mu_{\parallel}^{\mathrm{tt}}(z) = 1-\frac{9}{16}\frac{R}{z}+\frac{1}{8}\left(\frac{R}{z}\right)^3-\frac{45}{256}\left(\frac{R}{z}\right)^4+\mathcal{O}\left(\left(\frac{R}{z}\right)^5\right), \tag{2.106}$$

$$8\pi\eta R^2\mu_{\parallel}^{\mathrm{tr}}(z) = \frac{1}{8}\left(\frac{R}{z}\right)^4+\mathcal{O}\left(\left(\frac{R}{z}\right)^5\right), \tag{2.107}$$

$$8\pi\eta R^3\mu_{\perp}^{\mathrm{rr}}(z) = 1-\frac{1}{8}\left(\frac{R}{z}\right)^3+\mathcal{O}\left(\left(\frac{R}{z}\right)^8\right), \tag{2.108}$$

$$8\pi\eta R^3\mu_{\parallel}^{\mathrm{rr}}(z) = 1-\frac{5}{16}\left(\frac{R}{z}\right)^3+\mathcal{O}\left(\left(\frac{R}{z}\right)^6\right). \tag{2.109}$$

The indices $\perp$ and $\parallel$ refer to motion perpendicular or parallel to the plane of the wall. For the translation-rotation coupling term μ^{tr}, there exists no component perpendicular to the wall.

Additionally, Brenner obtained an exact result for the friction associated with motion perpendicular to the wall [181]

$$\begin{aligned}\gamma_{\perp}^{\mathrm{tt}}(z) =& \frac{4}{3}\sinh q(z)\sum_{n=1}^{\infty}\frac{n(n+1)}{(2n-1)(2n+3)}\times \\ & \left[\frac{2\sinh\left([2n+1]q(z)\right)+(2n+1)\sinh\left(2q(z)\right)}{4\sinh^2\left([n+1/2]q(z)\right)-(2n+1)^2\sinh^2\left(q(z)\right)}-1\right],\end{aligned} \tag{2.110}$$

with

$$q(z)=\mathrm{Arcosh}(z/R). \tag{2.111}$$

Two-wall friction For the two-wall system, Green's function has been determined by Liron and Mochon [182], which is particularly useful for Hele-Shaw geometries (*i.e.*, fluid

compartments with very close vertical walls) [167]. It has been extended to solutions for force multipoles by Bhattacharya and Bławzdziewicz [183]. For walls that are far apart, a superposition approximation for the friction can be used [184, 185]:

$$\gamma_{2w}(\mathbf{r}) = \gamma_{\text{wall}}(z - w_1) + \gamma_{\text{wall}}(w_2 - z) - 1, \tag{2.112}$$

where without loss of generality, the direction perpendicular to the walls is the z-direction, w_1 is the position of the bottom wall and w_2 the position of the top wall. This approximation has been tested against solutions using hydrodynamic images, with the result that for large enough separations the error stays small [183–185].

2.3.4 Lubrication

For particles in close proximity to walls or to each other, lubrication theory provides approximations for the flow fields, which are often not known exactly. For the discussion of flow fields at small distances one introduces the smallness parameter ε, which determines the minimum clearance between two particles [82, 186], denoted here by $\Delta = \varepsilon R$. The case of interactions between a colloidal particle and a wall is then treated by setting the radius of the second particle to infinity. The motion at close distance creates frictional forces and torques that differ from the far field terms. In particular, they show a particular type of divergence for $\varepsilon \to 0$, when expanded in terms of ε. The characteristic scaling depends on the direction of motion that the particle performs. Thus, one differentiates between shearing and squeezing motion.

We present the results for squeezing and shearing motion of a colloid at a wall in the following. A more detailed treatment can be found in Refs. [82, 186]. Importantly, the treatment provided here does not include a slip velocity on the colloid's surface. However, this becomes relevant when we consider the near field interactions of squirmer microswimmers [187].

Squeezing motion

We consider here the motion of a colloidal particle towards a no-slip wall, at close contact. We use cylindrical coordinates (ρ, ϑ, z) and, without loss of generality, assume that the colloid moves in the z-direction with velocity U. The no-slip boundary condition on the surfaces dictates that the flow velocity at the boundaries is zero. Following Ref. [82], one can approximate the spherical surface of the particle in the vicinity of the closest point to the wall by

$$z(\rho) = \varepsilon R + \frac{\rho^2}{2R} + \mathcal{O}\left(\frac{\rho^4}{R^3}\right). \tag{2.113}$$

After introducing the stretched coordinates $\tilde{\rho} = \rho/(\sqrt{\varepsilon}R)$ and $\tilde{z} = z/(\varepsilon R)$ [82], the equation for the surface in stretched coordinates becomes

$$\tilde{z}(\tilde{\rho}) = 1 + \frac{\tilde{\rho}^2}{2} + \frac{\varepsilon\tilde{\rho}^4}{8} + \mathcal{O}(\varepsilon^2). \tag{2.114}$$

This approximation simplifies the boundary condition to the Stokes equations.

Here, the typical way of solving the Stokes equation consists of using a stream function ψ with $u'_\rho = 1/\rho\ \partial\psi/\partial z$ and $u'_z = -1/\rho\partial\psi/\partial\rho$, where $\mathbf{u}' = \mathbf{u}/U$ is the flow field normalized by the particle velocity U. The resulting equation [82]

$$\left(\frac{\partial^2}{\partial\tilde{z}^2} + \varepsilon\left(\frac{\partial^2}{\partial\tilde{\rho}^2} - \frac{1}{\tilde{\rho}}\frac{\partial}{\partial\tilde{\rho}}\right)\right)^2 \psi = 0 \tag{2.115}$$

is solved by performing a regular expansion in ε [82, 186]. The resistance force follows from the solution of the flow field, by integrating the stress tensor over the sphere surface, as shown in Eq. (2.47) [82, 186].

For the squeezing motion, the leading orders of the resistance force F_R on the passive sphere are [82]

$$F_R/(6\pi\eta RU) = -A_1\varepsilon^{-1} - B_1\ln\left(\varepsilon^{-1}\right) + C_1 - D_1\varepsilon\ln\left(\varepsilon^{-1}\right) + \mathcal{O}(\varepsilon), \tag{2.116}$$

where Refs. [82, 188] have $A_1 = 1$, while the constants B_1, C_1, D_1 can be determined by a matching procedure to the far field and depend on the exact geometry of the problem, such as the radii of two spheres at close contact.

Shearing motion

We also briefly present the result for the shearing motion at close contact. Here, the resistance force is [82, 189]

$$F_R/(6\pi\eta RU) = -B_2\ln\left(\varepsilon^{-1}\right) + C_2 - D_2\varepsilon\ln\left(\varepsilon^{-1}\right) + \mathcal{O}(\varepsilon). \tag{2.117}$$

Ref. [82] has $B_2 = 8/15$. The induced torque has terms of the same order in ε [82, 189]:

$$T_R/(8\pi\eta R^2U) = \beta_2\ln\left(\varepsilon^{-1}\right) + \gamma_2 + \delta_2\varepsilon\ln\left(\varepsilon^{-1}\right) + \mathcal{O}(\varepsilon), \tag{2.118}$$

with $\beta_2 = 1/10$ and matching constants γ_2 and δ_2 [82].

2.4 Motion under gravity

The motion of active colloids under external fields is an exciting aspect of their non-equilibrium dynamics [5, 51–56, 59, 190, 191]. Real microswimmers often sediment due to their weight [53, 55, 91, 192, 193], therefore it is important to understand how gravity affects their dynamics. Fascinating phenomena in nature, such as patch and layer formation of plankton [23, 70], hovering rafts of active emulsion droplets [144] and dancing states of algae [61] can be attributed to the motion of swimmers under gravity.

We start by discussing the sedimentation of passive particles and active Brownian particles. Then we describe how gravity is used as a cue for specific forms of taxis, which are called gravitaxis and gyrotaxis. We also provide examples from biology, where hydrodynamic interactions lead to pattern formation in systems under gravity. These effects are subsumed under the name bioconvection.

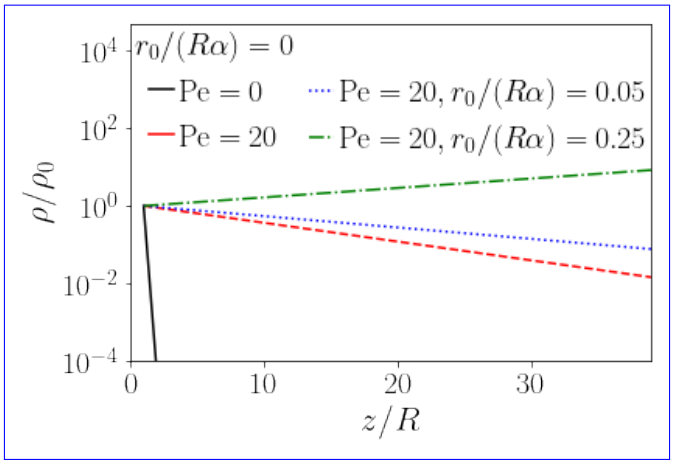

Figure 2.6: Vertical density profiles for systems of active Brownian particles. Using the gravitational Péclet number $\mathrm{Pe}_g = 10$, we show the height profiles of passive sedimentation (black solid line) and the sedimentation of active Brownian particles with $\mathrm{Pe} = 20$ without (red dashed line) and with bottom-heaviness. We measure bottom-heaviness via the rescaled torque $r_0/(R\alpha)$, where r_0 is the backward shift of the center of mass. The blue dotted line corresponds to a weaker strength of bottom-heaviness and shows conventional sedimentation, whereas the green dash-dotted line shows inverted sedimentation. Adapted from Ref. [158], where we have set up the systems such that the concentration at the wall ρ_0 is equal for all cases.

2.4.1 Passive sedimentation

Under gravity, a passive colloid sinks to the bottom of the system, which is a deterministic motion. Additionally, the particle diffuses, as outlined in Section 2.2.3. This results in an exponential density profile with a characteristic length called the *sedimentation length* δ_0, which describes how high the thermal fluctuations typically raise the particle above the bottom wall. In mathematical terms, the density profile is

$$\rho(z) = \rho_0 e^{-(z-z_{\mathrm{wall}})/\delta_0}. \tag{2.119}$$

It is clear that δ_0 must depend on the buoyant weight of the particle, as well as on the temperature. In fact, balancing the fluxes in the Smoluchowski equation [Eq. (2.85)] immediately gives the above equation with the sedimentation length [51]

$$\delta_0 = \frac{k_B T}{\Delta m g}, \tag{2.120}$$

where Δm is the buoyancy mass.

2.4.2 Active Brownian particles under gravity

Palacci *et al.* studied the non-equilibrium sedimentation of active Janus colloids [53] and discovered that the sedimentation length is much larger than for the passive case. Using active Brownian particles, one can understand this behaviour, by balancing the

drift and diffusion current [51, 54]. This is the same calculation one can do for passive colloids, however, the enhanced diffusion creates a new effective sedimentation length [51]

$$\delta_{\text{eff}} = \delta_0 \left(1 + \frac{2}{9}\text{Pe}^2\right). \tag{2.121}$$

One can define the gravitational Péclet number

$$\text{Pe}_g = \frac{\Delta m g R}{k_B T} = \frac{R}{\delta_0}, \tag{2.122}$$

which compares the radius of the particle to the sedimentation length. Combining the active and gravitational Péclet numbers, we arrive at the parameter

$$\alpha := \frac{\text{Pe}}{\text{Pe}_g} = \frac{v_0 k_B T}{\Delta m g D} = \frac{v_0}{v_{\text{sed}}}. \tag{2.123}$$

which is the velocity ratio between the active velocity and the passive sedimentation velocity in bulk $v_{\text{sed}} = \Delta m g/\gamma$. The parameter α is an important control parameter in our studies.

In Fig. 2.6 one can see the stark contrast between passive and active sedimentation by comparing the black solid line of a passive particle with the red dashed line of a sedimenting active Brownian particle. Both particles experience the same gravity corresponding to $\text{Pe}_g = 10$. However, the active sedimentation length is much larger, thus the decay is much slower.

Importantly, the orientational dynamics play a big role for active particles, because they couple directly to their translational motion. It was shown that the kinematics under gravity lead to an increase of polar order of active Brownian particles. This increase is balanced by a diffusive current, thus resulting in a stationary orientational distribution [51, 54]. One can further manipulate the orientational dynamics by introducing an external gravitational torque. For example, for a bottom-heavy particle the center of mass is offset by a length r_0 from the geometrical center. This induces the torque

$$\mathbf{T}_{\text{bh}} = m g r_0 \mathbf{e}_z \times \mathbf{e}, \tag{2.124}$$

which tends to align the particle anti-parallel to the gravity vector $-g\mathbf{e}_z$. Here, we can define the rescaled bottom-heavy torque $r_0/(R\alpha)$ as a dimensionless measure. Studying bottom-heavy active Brownian particles, Wolff *et al.* discovered that the sedimentation profile can be inverted [158]. Thus, at sufficiently high external torques, particles are more likely to have a high potential energy than a low one in the external field, in strong contrast to the expectations in thermodynamic equilibrium. We can see the effects of bottom-heaviness in Fig. 2.6, firstly by the increased sedimentation length of the dotted blue line for $r_0/(R\alpha) = 0.05$. Secondly, we indeed observe an inversion at a higher external torque of $r_0/(R\alpha) = 0.25$ (green dash-dotted line).

2.4.3 Gravitaxis and gyrotaxis

A gravitational torque strongly influences microswimmer dynamics, as explained in the previous section for active Brownian particles. The tendency to move anti-parallel to

the direction of gravity is also called *negative gravitaxis* [158, 190, 191]. Note that we have used different symbols for the mass occurring in the sedimentation velocity (Δm) and the bottom-heavy torque (m). The reason is as follows. While sedimentation depends on the buoyancy and thus on the density difference between the sinking body and the fluid, the reorientation from bottom-heaviness depends on the gravitational mass itself. However, in the following, we use the assumption $\Delta m \approx m$. Alternatively, one may simply redefine r_0 as $r_0 m/\Delta m$ [158].

Furthermore, there exist other mechanisms of gravitational reorientation. In particular, fore-aft asymmetries induce a different, viscosity-based gravitational torque, which is an effect of the sedimentation and thus of Δm [59, 71, 190]. We note that the results of our studies in the following chapters do not depend on the source of the gravitational torque. However, since we use spherical swimmers without fore-aft asymmetry, bottom-heaviness remains the natural choice for creating the external torque.

Gravitaxis of biological organisms could be a purely passive effect, or it could be the result of physiological and perceptive mechanisms in a cell. Already in the 19th century, Verworn considered this question and expressed doubt that the response to gravity would be an active reaction of the organism [194]. This topic remains controversial, since for some organisms there is evidence of a perceptive apparatus [118, 119, 195]. Similarly, it is unclear if gravitaxis brings an evolutionary advantage [196]. It could for example influence the access to oxygen or sunlight or offer a predatory advantage [56, 197]. Interestingly, phytoplankton can strategically diversify its gravitactic response in order to avoid turbulent regimes [71], supporting the idea of gravitaxis as an evolved, learned response.

Importantly, gravity acting on a swimmer also induces a flow, represented by a stokeslet in the far field, which strongly influences the effective sedimentation of passive clusters [198]. The importance of flow is further emphasized by the phenomenon of *gyrotaxis*. Here, gravity and flow both influence the dynamics of a swimmer or the collective behaviour of many swimmers [15, 56]. Here, the effects of fluid vorticities is especially important [57, 58, 60]. Studies on the formation of a fluid pump in a harmonic trap potential can serve as an illustration for this behaviour [51, 192, 199]: Active particles in the trap are first oriented radially outward. Due to their stokeslet vorticity fields the swimmers are reoriented and swim towards each other, which changes the configuration. If rotational diffusion and viscous reorientation from the stokeslets are balanced, a stable cluster with high polar order forms - since this transports fluid from one side to the other, it is referred to as a pump [192, 199].

Bioconvection

As we described in Sec. 2.2.2, both prokaryotic and eukaryotic cells evolved to swim under low Reynolds number conditions. Likewise, bioconvection occurs for the bacterium *Bacillus subtilis* [157, 200], the protists *Paramecium* and *Tetrahymena* [201, 202] and various forms of the *Chlamydomonas* alga [56, 109, 197, 203, 204].

In general, one can understand bioconvection as the self-organized collective motion of biological cells [204, 205]. For example, it is known that bacteria orient upstream in a channel flow and thus form an focussed state [15]. Another example is the collective

patch formation of phytoplankton resulting from gyrotaxis in turbulent flows [23, 58, 70]. Plumes are among the most studied patterns of bioconvection. They are finger-like sinking structures that emerge from the homogenous phase [56, 157, 203, 206]. They can either appear at the top layer of the system and sink down due to density fluctuations in the stratified layers [56, 206–208], or they can emerge as bottom-standing plumes [56], which do not require the top wall to form. The formation of the latter is likely caused by a gyrotactic mechanism [56, 109, 203, 209–211]. For systems of Chlamydomonas and Bacillus subtilis, other mechanisms have been suggested which include either phototactic effects [204, 212], or chemotaxis and chemodiffusion in the oxygen field [200]. Thus, there is no clear and concise picture of what exactly causes plumes to appear. In particular, the roles of hydrodynamic interactions and of gyrotaxis need to be specified further.

3. Numerical methods

In Chapter 2 in the sections on hydrodynamics, we introduced the momentum balance equation for the continuum fluid, which brought us to the Navier-Stokes and Stokes equations. These equations can be solved numerically by discretization techniques, such as the finite element or finite volume methods [213, 214] or the smoothed-profile method [215]. The special properties of the Stokes equations can be exploited in order to find a solution with the boundary element method [216]. Here the problem is reduced to finding a solution on the boundaries.

The above methods solve a differential or integral equation in an approximate way. We use a different approach to determine the fluid dynamics, by using a mesoscopic method. After introducing this family of techniques, we present the algorithm of multi-particle collision dynamics (MPCD), which we will use throughout this work. It consists of a streaming and a collision step. We discuss the hydrodynamic properties of our model fluid. Later, we describe how boundaries, such as solute particles and walls, can be introduced to the system and discuss the effective friction experienced by a colloid.

3.1 Mesoscale simulation techniques

The term *mesoscopic* denotes a regime within the hierarchy of length scales between the atomic or molecular scale and the continuum scale. Historically, the continuous description of fluids predates the knowledge of the corpuscular structure of matter. With the wisdom of hindsight, in the 20th century, fluid dynamic equations were derived from the dynamics on a smaller scale. This justifies methods working on a scale smaller than the continuum scale which nonetheless recover the correct fluid dynamics. To be specific, if l_a is the atomic length scale that resolves the details of the chemical constituents, we are concerned with the scale $l_{\mathrm{mfp}} \gg l_a$ of the mean free path of these atoms or molecules, *i.e.*, the typical distance they travel between collisions. On this length scale the details of the constituents are irrelevant, therefore the highly fluctuating dynamical variables, such as positions and velocities, can be replaced by their average values [65].

Examples for mesoscopic methods are Dissipative Particle Dynamics (DPD) and Lattice-Boltzmann simulations. DPD models the fluid as a motion of point-like fluid particles. On the one hand they move ballistically, which is called the streaming step. On the other hand, they transfer momentum between each other due to effective collisions within a pre-defined interaction radius [217]. In Lattice-Boltzmann simulations, the fluid is modelled on a discrete lattice by distribution functions of microscopic den-

sity and velocity [218]. Momentum transport is achieved by streaming fluid to a finite set of neighbor lattice sites according to the velocity distributions. In a subsequent step the Boltzmann collision equation is solved on each lattice site. We revisit the organization into a streaming and a collision steps when we describe the method of our choice, multi-particle collision dynamics.

Mesoscale simulation methods are able to recover the Navier-Stokes equations at the coarse-grained scale [219, 220], meaning that their hydrodynamic fields are governed by the same differential equations, which conserve mass and momentum. However, the constitutive relation of the simulated fluid, as well as the transport coefficients can be different than in continuum theory [65], and one usually cannot match all of them to the experimental setting at the same time. Importantly, the algorithm has to satisfy symmetries, such as Galilean invariance [65].

An advantage of mesoscale methods is that conservation equations can be enforced directly. For example, in Lattice-Boltzmann methods the right velocity distribution is prescribed and in MPCD we include momentum or angular momentum conserving steps. Of course, it has to be shown rigorously that the continuum equations are indeed recovered. For MPCD, this has been done by Malevanets and Kapral using the Boltzmann equation and the Chapman-Enskog expansion [64].

Thermal fluctuations are an important factor in choosing a simulation technique. These are typically not included in the continuum equations, but are important for a wide range of phenomena, in particular in biological and soft matter physics. DPD and MPCD already include thermal fluctuations and they can be incorporated into Lattice-Boltzmann schemes, as well. Thus, we can summarize the advantage of mesoscale simulation techniques in two main points: since microscopic degrees of freedom are averaged out, behaviour at larger time scales can be studied efficiently; at the same time, thermal fluctuations can still be included.

3.2 Multi-particle collision dynamics

Multi-particle collision dynamics (MPCD) models the fluid by point-like fluid particles with unit mass whose averaged dynamics represents the flow field of the fluid [64]. In contrast to the Lattice-Boltzmann method, position and velocity of the fluid are continuous variables [65]. It is thereby related to the Dissipative Particle Dynamics (DPD) approach [65, 221].

MPCD has been used for a large variety of systems [65, 222], including polymers [223], studies of inertial effects [224, 225], chemically driven systems [226], vesicles [227], and the African trypanosome parasite [18]. It has also been succesfully used for squirmer microswimmer simulations [42, 43, 162, 228–230].

In this chapter, we first present the algorithm of the MPCD method, which consists of a streaming and a collision step. We then present some options for the choice of the collision operator. Afterwards, we discuss the hydrodynamic consequences that follow from the way the fluid is modelled, such as the expression for the fluid stress and kinematic viscosity. Furthermore, we discuss how boundaries, colloidal particles or microswimmers are included in the algorithm.

3.2.1 Main algorithm

In the following we describe the dynamics of the fluid particles that lead to a flow field consistent with the Navier-Stokes equations. As mentioned above, the method consists of two steps, the streaming step and the collision step.

Streaming step

The streaming step consists of updating the fluid particles, *i.e.*, solving Newton's equations of motion. Thus, momentum is transported through the fluid along with the particles. Additionally, the dynamics of any materials in solution, such as colloids, are calculated in the streaming step. This coupling is described in further detail in Sec. 3.3. The choice of the duration of the streaming step Δt is important, because it influences the physical properties of the fluid.

The positions of the fluid particles are updated during this step via

$$\mathbf{r}_i(t + \Delta t) = \mathbf{r}_i(t) + \mathbf{v}_i(t)\Delta t. \tag{3.1}$$

We can add pressure gradients by accelerating fluid particles with a constant force. In this case one has to use further integration for the accelerated fluid particles, such as Velocity-Verlet integration [231].

Collision step

For the collision step, we define a length scale a_0 which serves as the lattice constant of a cubic lattice. The cells of the lattice - which we call the MPCD collision cells - serve as the interaction volume of the fluid particles in the collision step. The average number n_{fl} of fluid particles per collision cell is an important property of the MPCD fluid. The collision step consists of reorienting all fluid particle velocities in a cell using a collision operator, in a way that leaves the average velocity in a cell constant. All particles in a cell are rotated simultaneously and different cells can have different collision operators [64].

We express the collision step as

$$\mathbf{v}_i(t + \Delta t) = \overline{\mathbf{V}}_\mu + \mathcal{C}\left(\{\mathbf{r}_j\}_\mu, \{\mathbf{v}_j\}_\mu\right) \tag{3.2}$$

with the collision operator $\mathcal{C}$ and the average velocity $\overline{\mathbf{V}}_\mu$ of the collision cell with index μ. The sets $\{...\}_\mu$ refer to all particles within this cell. In the original paper by Malevalets and Kapral [64] the collision operator consisted of rotating the difference vectors $\mathbf{v}_i(t) - \overline{\mathbf{V}}_\mu$ by a fixed angle α around a random axis. Therefore, this original method is also called stochastic rotation dynamics (SRD) [64]. In Sec. 3.2.2 we describe various collision rules in more detail.

Galilean invariance The MPCD method works under the assumption of molecular chaos for the fluid particles [65]. This also ensures translational symmetry. Therefore, correlations between them have to be avoided, in order to ensure Galilean invariance

[232]. However, the collision step introduces correlations between the fluid particles. In order to amend this, a grid shift procedure is performed, where for every new collision step, the whole grid of collision volumes is translated by a random amount $\mathbf{d}_{\text{shift}}$ between $-a_0/2$ and $a_0/2$ [232].

Technical aspects

Units The MPCD method entails natural units for our simulations. We use the edge length of the collision cells a_0 as a unit for length and the mass m_0 of the fluid particles as a unit for mass. The thermal energy k_BT_0 serves as a unit of energy. Thus, forces are given in units of k_BT_0/a_0 and velocities in units of $\sqrt{k_BT_0/m_0}$. While the unit of time follows as $a_0\sqrt{m_0/k_BT_0}$, we sometimes also use the duration of the streaming step Δt as a reference time.

Implementation Performing computer simulations of fluid systems can incur high computational cost. For example, a typical cubic system with size $108a_0 \times 108a_0 \times 108a_0$ with $n_{\text{fl}} = 10$ fluid particles per cell means that trajectories of more than 10^7 fluid particles need to be calculated. Thus, the software we use is compiled such that it can be run on multiple processing units simultaneously. For parallelization, we use a high-performance computing cluster using approximately 150 CPU cores with a software written in C. Alternatively, we also run simulations on graphics processing units implemented in a software written in C++ and CUDA*.

3.2.2 Collision rules

The collision step presented above allows for several different implementations of a collision operator. Here we present a selection of collision rules, which are established in research.

The original method is called the MPC-SRD algorithm and is presented first. In a SRD collision, the kinetic energy of the fluid particles is conserved locally, since they are only rotated [64]. In contrast, other methods use a thermostat, connecting the system to a heat bath [233]. Thus, different simulation methods can operate in different thermodynamical ensembles. Momentum conservation is ensured by all the presented collision rules, as it is a necessary pre-condition for recovering the Navier-Stokes equation on a coarse-grained level. However, angular momentum conservation is not satisfied automatically and has to be added to the algorithm by hand.

SRD

The stochastic rotation dynamics algorithm was the original algorithm proposed by Malevanets and Kapral [64]. Its collision rule is

$$\mathcal{C}_\mu(\mathbf{r}_i, \{\mathbf{r}_j\}_\mu, \{\mathbf{v}_j\}_\mu) = \mathbf{R}_\mu \Delta\mathbf{v}_i, \tag{3.3}$$

*The core algorithms of the C and C++ programs have been written by M. Maurer and A. W. Zantop, respectively. The CPU high computing power resources were provided by the North-German Supercomputing Alliance (HLRN).

where $\Delta\mathbf{v}_i = \mathbf{v}_i - \overline{\mathbf{V}}$. In three dimensions, the matrix $\mathbf{R}_\mu$ is a rotation around a random axis $\mathbf{n}_\mu$ by a fixed angle α, which is the same for all collision cells. Note that the axis $\mathbf{n}_\mu$ differs from cell to cell. Consequently [65],

$$\mathcal{C}_\mu(\mathbf{r}_i, \{\mathbf{r}_j\}_\mu, \{\mathbf{v}_j\}_\mu) = \Delta\mathbf{v}_{i,\perp}\cos\alpha + (\Delta\mathbf{v}_{i,\perp} \times \mathbf{n}_\mu)\sin\alpha + \Delta\mathbf{v}_{i,\parallel}. \tag{3.4}$$

The parallel and perpendicular parts are determined with respect to $\mathbf{n}_\mu$. It has been shown that an H-theorem can be derived for this collision rule and that the velocity distribution is Maxwellian [64]. Since the energy is conserved locally, the states of the fluid particles in a collision cell are part of the microcanonical ensemble.

Thermostats

In order to control the temperature of the system, it is necessary to connect it to a heat bath. Consequently, we want to set up the system in the canonical ensemble, where a collision cell can exchange heat with its surroundings. The new collision rule substitutes the random rotations of SRD by random relative velocities with respect to the average [65, 221]. We present two different rules to achieve this. One is called the Andersen thermostat, after H. C. Andersen [234], which we call MPC-AT. The other one is the Langevin thermostat [221], which we call MPC-LT. Note that angular momentum is not conserved by these collision rules.

Andersen thermostat The MPCD collision operator of the Andersen thermostat is:

$$\mathcal{C}_\mu(\mathbf{r}_i, \{\mathbf{r}_j\}_\mu, \{\mathbf{v}_j\}_\mu) = \mathbf{v}_i^{\text{rand}} - \frac{1}{N_\mu^c}\sum_{j\in\mu}\mathbf{v}_j^{\text{rand}}, \tag{3.5}$$

where N_μ^c is the number of fluid particles in the respective collision cell. The random velocities are drawn from a Maxwell-Boltzmann distribution at the desired temperature T_0.

Langevin thermostat Noguchi, Kikuchi, and Gompper [221] describe an alternative thermostat, called the Langevin thermostat. It applies the friction and noise parts of the Langevin equation on a particle, *i.e.*, a force of the form [221]

$$\mathbf{f}_{LT} = -\gamma\mathbf{v}_i + \sqrt{2k_BT_0\gamma}\boldsymbol{\xi}_i. \tag{3.6}$$

As usual, $\boldsymbol{\xi}_i$ is described by Gaussian white noise. We need to adjust the deterministic and random terms, in order to ensure the fluid properties that we have discussed before. Then, the force applied to a fluid particle reads:

$$\mathbf{f}_{MPC-LT} = -\gamma\left(\mathbf{v}_i - \overline{\mathbf{V}}_\mu\right) + \sqrt{2k_BT_0\gamma}\left(\boldsymbol{\xi}_i - \frac{1}{N_\mu^c}\sum_{j\in\mu}\boldsymbol{\xi}_j\right). \tag{3.7}$$

Therefore, in this method, no random velocities are drawn, but instead stochastic forces are used. In the MPC-LT rule, a friction coefficient γ of the fluid particles is provided explicitly, and thus does not have to be calculated from the fluid properties [221]. The

numerical integration of the velocities is more involved, due to the stochastic nature of the force. Here, the leap-frog algorithm can be used during the streaming step [221].

Angular momentum conservation

Both SRD and the collision rules with thermostats recover the correct hydrodynamic equations. However, as we will see in the next chapter, the stress tensor is not symmetric, which leads to the unphysical lack of angular momentum conservation. This drawback creates incorrect results [235]. To restore angular momentum conservation the collision rules have to be changed further [221, 235, 236].

For the SRD algorithm the collision angle α cannot stay constant, but needs to be different for each cell. Actually, it depends explicitly on the particular fluid particle positions according to the equations [65, 236]

$$\sin\alpha = -\frac{2AB}{A^2+B^2}, \tag{3.8}$$

$$\cos\alpha = \frac{A^2-B^2}{A^2+B^2}, \tag{3.9}$$

$$A = \sum_{i=1}^{N_\mu^c} \left(\mathbf{r}_i \times (\mathbf{v_i} - \overline{\mathbf{V}})\right) \cdot \mathbf{e}_z, \tag{3.10}$$

$$B = \sum_{i=1}^{N_\mu^c} \mathbf{r}_i \cdot \left(\mathbf{r}_i \times (\mathbf{v_i} - \overline{\mathbf{V}})\right). \tag{3.11}$$

This algorithm is called SRD+a. The authors of Ref. [65] describe it as rather time-consuming, since the collision angle α needs to be calculated for every cell in every time step.

The angular momentum conserving version of MPC-AT is called MPC-AT+a. It consists of calculating the induced angular momentum by the collision step and compensating it explicitly. Thus

$$\begin{aligned}\mathcal{C}_\mu^{\mathrm{MPC-AT+a}}(\mathbf{r}_i, \{\mathbf{r}_j\}_\mu, \{\mathbf{v}_j\}_\mu) =& \mathcal{C}_\mu^{\mathrm{MPC-AT}} + \\ & m_0 \mathbf{N}_\mu^{-1} \left[\sum_{j\in\mu} (\mathbf{r}_j - \mathbf{R}_\mu) \times \left(\mathbf{v}_j - \mathbf{v}_j^{\mathrm{rand}}\right)\right] \times (\mathbf{r}_i - \mathbf{R}_\mu),\end{aligned} \tag{3.12}$$

where m_0 is the mass of a fluid particle, $\mathbf{R}_\mu$ is the center of mass of the fluid particles in a collision cell, and $\mathbf{N}_\mu$ is the moment of inertia tensor. When applying the algorithm, one first computes collisions without the correction and then calculates the angular momentum difference $\Delta\mathbf{L}$. The restoring angular velocity $\boldsymbol{\omega}$ is then provided by solving the equation $\mathbf{N}\boldsymbol{\omega} = -\Delta\mathbf{L}$ [65, 235]. For the Langevin thermostat, the angular momentum conserving version MPC-LD+a works analogously to MPC-AT+a [221].

The compensation of the angular momentum has both technical and physical implications for the fluid simulation. Transport coefficients, such as the viscosity, are

influenced by the new rule. Furthermore, one often uses virtual fluid particles inside the solid object during the collision step (see Sec. 3.3.2). With angular momentum conservation, one has to be more careful with the placement of the virtual particles, because their positions influence the cell center of mass in Eq. (3.12). However, the corrections are straightforward. The virtual particles merely need to be added to the fluid particle sum when calculating the center of mass and moment of inertia tensor, or for calculating the induced angular momentum [168].

In our simulations, we use the Andersen thermostat with angular momentum conservation, hence the collision rule MPC-AT+a.

3.2.3 Properties of the MPCD fluid

In this chapter we explore the emergent physical properties of the fluid model and of the different collision rules. A Chapman-Enskog expansion was performed by Malevanets and Kapral for the original algorithm, showing that the viscous stress tensor has the correct form of a Newtonian fluid [64, 237]. Thus, the streaming and collision steps recover the Navier-Stokes equations. Importantly, the hydrodynamics of the fluid is generally influenced by both steps independently. On the one hand, the streaming step provides the so-called kinetic contribution to the viscosity. Since the fluid particles are not interacting, it is also called an ideal gas contribution [65, 238]. On the other hand, the redistribution of velocities in the collision step also changes the physical properties of the fluid. Through any arbitrary plane chosen within a MPCD cell, the distribution of linear momentum during the collision time Δt creates an effective momentum flux [233], and thus a collisional contribution to the viscosity. As we see below, the kinetic and collisional parts of the viscosity enter the constitutive equations, which connect the stress to the velocity gradient.

Pressure

For the SRD and MPCD methods discussed here, the fluid pressure consists only of the ideal gas contribution [65]. This term is known from thermodynamics and expressed by the equation of state [239]

$$p = \frac{N k_B T}{V}, \tag{3.13}$$

with the total particle number N. More elaborate MPCD algorithms implement a non-ideal equation of state and thus have an additional contribution from the collision step, which consists of an effective *virial* term [65, 240, 241].

Viscous stress tensor

We now consider the constitutive equations that are represented by different MPCD collision rules. As mentioned, the viscous stress tensor has both kinetic and collisional contributions. Note that it is possible that the stress tensor is not symmetric. Thus, in general, angular momentum is also transported [238], which is addressed by the MPC-AT+a method that we have introduced above.

Kinetic and collisional parts of the viscosity A good qualitative understanding of the kinetic and collisional viscosities is offered by Ref. [65]. The kinematic viscosity ν is the diffusion coefficient for momentum diffusion, thus $\nu \sim \lambda^2/\Delta t$, where λ is the mean free path. If we consider the kinetic contribution, the appropriate mean free path is the distance that a fluid particle travels unobstructed during the streaming step. With the average particle velocity $\sqrt{k_B T_0/m_0}$, we have $\lambda_{\mathrm{mfp}} \sim \sqrt{k_B T_0/m_0}\Delta t$. The kinetic contribution therefore is

$$\nu_{\mathrm{kin}} = \frac{k_B T_0 \Delta t}{m_0} f_{\mathrm{kin}}(n_{\mathrm{fl}}, \alpha). \tag{3.14}$$

The function f_{kin} depends on the simulation parameters, such as the number of fluid particles per cell n_{fl} and - if the SRD algorithm is used - the collision angle α.

For the collision step, momentum is distributed on the length scale of the entire collision cell of edge length a_0, therefore this is the appropriate length scale, instead of the mean free path above. This yields

$$\nu_{\mathrm{coll}} = \frac{a_0^2}{\Delta t} f_{\mathrm{coll}}(n_{\mathrm{fl}}, \alpha). \tag{3.15}$$

The size of either viscosity is influenced by Δt, controlling which one of the two contributions dominates. In our simulations, the collisional part is more important.

Asymmetric part of the stress tensor Collisional stress in the MPCD fluid consists of a symmetric and an asymmetric part [238]. The viscous stress tensor of the Newtonian fluid was presented in Sec. 2.1.2. We already mentioned that the contribution of the asymmetric part of the velocity gradient $\nabla \otimes \mathbf{v}$ is unphysical for isotropic fluids, since it does not conserve angular momentum. However, angular momentum conservation is not available for all MPCD collision rules. Therefore, we must use a more general form for the viscous stress tensor [235]

$$\boldsymbol{\sigma}' = \left(\lambda - \frac{2}{3}\eta_1\right)(\nabla \cdot \mathbf{u})\mathbf{1} + \eta_1\left[\nabla \otimes \mathbf{v} + (\nabla \otimes \mathbf{v})^T\right] - \eta_2\left[\nabla \otimes \mathbf{v} - (\nabla \otimes \mathbf{v})^T\right], \tag{3.16}$$

where η_2 is an additional scalar viscosity, associated with the asymmetric part. Note that the effective total dynamic shear viscosity is $\eta = \eta_1 + \eta_2$ [242], while λ is the bulk viscosity. The generalized stress tensor leads to the momentum equation

$$\rho\left(\partial_t \mathbf{u} + (\mathbf{u} \cdot \nabla)\mathbf{u}\right) = -\nabla p + (\lambda + \eta_1 - \eta_2)\nabla(\nabla \cdot \mathbf{u}) + (\eta_1 + \eta_2)\nabla^2 \mathbf{u}. \tag{3.17}$$

It can be shown that the symmetric and antisymmetric parts of the collisional viscosity η_1 and η_2 have equal size [233]. Equation (3.17) obeys the Navier-Stokes equation for $\nabla \cdot \mathbf{u} = 0$, if we define viscosity as the sum of the symmetrical and asymmetrical viscosities. The velocity fields of such a fluid are therefore the same as with angular momentum conservation in bulk [235]. However, it leads to the appearance of spurious torques [235]. Furthermore, if compressibility is non-negligible, the bulk viscosity becomes important, which does not have the same value as for fluids without angular momentum conservation [235].

Viscosities for different algorithms We have introduced the different contributions to the viscosity in general form. We now collect the exact results that have been derived for the viscosities, using different MPCD algorithms. We note that corrections of higher-order in Δt than those in Eqs. (3.14) and (3.15) can be necessary, which are only tractable with numerical simulations. Zöttl showed with measurements in Poiseuille flow that deviations become especially large for small $\Delta t \leq 0.1$ [168].

SRD For the SRD algorithm f_{kin} and f_{coll} have been calculated by Kikuchi et al. [243] using kinetic theory and by Gompper et al. [65] using an alternative method which yielded the same results. They arrive at the following result for the kinetic part of the viscosity [65, 243]

$$\nu_{\text{kin}} = \frac{k_B T_0 \Delta t}{2m_0} \left(\frac{5n_{\text{fl}}}{(n_{\text{fl}} - 1 + e^{-n_{\text{fl}}})(2 - \cos(\alpha) - \cos(2\alpha))} - 1 \right). \tag{3.18}$$

The exponential functions occur because averaging was performed over the Poisson-distributed occupation of the collision cells. For high enough mean fluid particle occupancy n_{fl}, this is less important, because we can approximate the actual occupancy in a cell with the mean value n_{fl}. This is also done for the MPC-AT formula below.

The results for the collisional viscosity of the SRD algorithm is [65, 238]

$$\nu_{\text{col}} = \frac{a^2}{18\Delta t} \left(\frac{n_{\text{fl}} - 1 + e^{-n_{\text{fl}}}}{n_{\text{fl}}} (1 - \cos\alpha) \right). \tag{3.19}$$

MPC-AT The MPC-AT algorithm, without angular momentum conservation, has the following kinetic and collisional viscosity contributions [221]

$$\nu_{\text{kin}}^{\text{MPC-AT}} = \frac{k_B T \Delta t}{m_0} \left(\frac{n_{\text{fl}}}{n_{\text{fl}} - 1 + e^{-n_{\text{fl}}}} - \frac{1}{2} \right), \tag{3.20}$$

$$\nu_{\text{col}}^{\text{MPC-AT}} = \frac{a^2}{12\Delta t} \left(\frac{n_{\text{fl}} - 1 + e^{-n_{\text{fl}}}}{n_{\text{fl}}} \right). \tag{3.21}$$

The collisional contribution includes the asymmetric viscosity term ν_2, thus we have $\nu_{\text{coll}} = \nu_1 + \nu_2$ with $\nu_2 = \nu_1$.

MPC-AT+a The asymmetric part of the stress tensor disappears in MPC-AT+a, due to angular momentum conservation. The viscosities then become [233, 235]

$$\nu_{\text{kin}}^{\text{MPC-AT+a}} = \frac{k_B T \Delta t}{m_0} \left(\frac{n_{\text{fl}}}{n_{\text{fl}} - \frac{5}{4}} - \frac{1}{2} \right), \tag{3.22}$$

$$\nu_{\text{col}}^{\text{MPC-AT+a}} = \frac{a_0^2}{24\Delta t} \left(\frac{n_{\text{fl}} - \frac{7}{5}}{n_{\text{fl}}} \right). \tag{3.23}$$

The above collisional contribution is the total collisional viscosity without any asymmetric term ν_2. It is roughly half of the total collisional viscosity without angular momentum conservation. Since the collisional part dominates in our simulations, the

total viscosity of the fluid (for both streaming and collision steps) with angular momentum conservation is also around half of the viscosity in the algorithm without angular momentum conservation. Note that Eq. (3.23) only applies, if $n_{\mathrm{fl}} > 3$ [65, 233]; for small n_{fl} the results differ [233].

MPC-LT For the Langevin thermostat, we have [221]

$$\nu_{\mathrm{kin}}^{\mathrm{MPC-LT}} = k_B T \left(\frac{n_{\mathrm{fl}}(1+\gamma\Delta t/2m_0)^2}{2\gamma/m_0(n_{\mathrm{fl}} - 1 + e^{-n_{\mathrm{fl}}}) - \dfrac{\Delta t}{2}} \right) \tag{3.24}$$

and

$$\nu_{\mathrm{col}}^{\mathrm{MPC-LT}} = \frac{a_0^2}{12 n_{\mathrm{fl}}} \left(\frac{\gamma(n_{\mathrm{fl}} - 1 + e^{-n_{\mathrm{fl}}})}{1+\gamma\Delta t/2m_0} \right). \tag{3.25}$$

Note that these expressions can be transferred into the MPC-AT forms in Eqs. (3.20) and (3.21) by identifying the friction of the fluid particles as $\gamma = \dfrac{2m_0}{\Delta t}$ [221].

Compressibility

The Stokes equation describes an incompressible fluid. In contrast, MPCD models a compressible fluid. One therefore has to ensure that the *Mach number* is low, by using small enough velocity fields, in order to avoid high density fluctuations. Here, the Mach number Ma is defined as the ratio of the maximum flow velocity to the speed of sound:

$$\mathrm{Ma} = v_{\max}\sqrt{\frac{m_0}{k_B T_0}}. \tag{3.26}$$

For squirmer simulation, this essentially requires that the mode B_1, which controls the swimming velocity, is small enough. Note that the compressibility in MPCD limits how fast flow fields can propagate, whereas from a theoretical point of view, hydrodynamic fields following the Stokes equation react instantaneously to a disturbance in an arbitrary distance [65].

3.3 Colloids and walls in MPCD

We use a swimmer model called squirmer in our MPCD simulations, which has been introduced in Sec. 2.2.4. Simulations of squirmers under MPCD have confirmed quantitatively correct single particle behaviour [228–230]. We use the squirmer model to study the behaviour of microswimmers in their fluid habitat. Arguably, the most important aspect of the simulation technique then becomes the coupling of the fluid to the objects in solution. In the following, we consider how passive and active particles behave in the MPCD fluid, in particular how we implement the forces on moving objects and the squirmer boundary conditions. Of course, the boundaries of the system also enforce

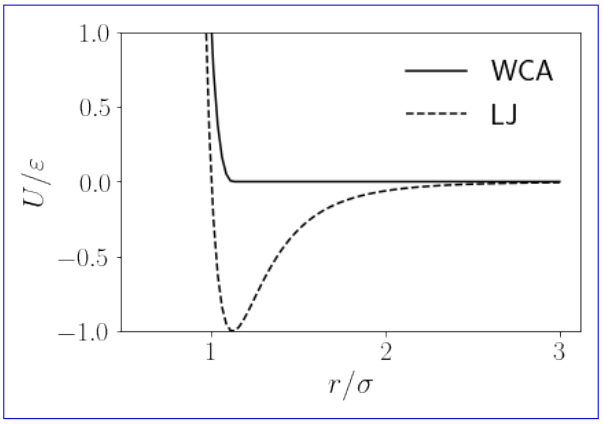

Figure 3.1: Lennard-Jones (LJ) and Weeks-Chandler-Andersen (WCA) potentials.

conditions on the fluid, specifically a no-slip or a periodic boundary condition. We also consider the friction experienced by a dragged particle and discuss how it changes in MPCD compared to a continuum fluid.

3.3.1 Forces and torques on suspended colloidal particles

Weeks-Chandler-Andersen potential

The interaction of the solute particles with walls and with each other should be such that no overlap can occur. One possibility is to use event-driven collisions [231], which can model hard-core interactions. Instead, we use a steep Weeks-Chandler-Andersen (WCA) potential [244], which avoids the discontinuous jumps in energies of the hard-core potential.

The WCA potential is a truncated version of the Lennard-Jones potential, which has the known form

$$V_{\mathrm{LJ}}(r) = 4\varepsilon \left(\left(\frac{\sigma}{r}\right)^{12} - \left(\frac{\sigma}{r}\right)^{6} \right). \tag{3.27}$$

The parameter ε defines the depth of the energy minimum and the parameter σ provides the interaction radius of the potential. In order to arrive at the WCA potential, one truncates the potential at its minimum at $r = 2^{1/6}\sigma$. Afterwards the potential is shifted up by the amount ε, so that truncation happens at zero energy:

$$V_{\mathrm{WCA}}(r) = \begin{cases} 4\varepsilon \left(\left(\frac{\sigma}{r}\right)^{12} - \left(\frac{\sigma}{r}\right)^{6} \right) + \varepsilon & r/\sigma < 2^{1/6}, \\ 0 & \text{otherwise.} \end{cases} \tag{3.28}$$

We plot both the Lennard-Jones and the WCA potentials in Fig. 3.1.

Molecular dynamics step

Colloids and swimmers under gravity experience external forces, as well as a torque for bottom-heavy swimmers. In order to apply these external deterministic terms, as well as

the above mentioned steric interactions, the velocity-Verlet algorithm is used during the streaming step. In contrast, hydrodynamic interactions are mediated via the momentum transfer from fluid particles on solute particles in both the streaming and collision steps. We describe this process further below. In order to achieve good resolution of the rigid body motion, the duration Δt of the streaming step is divided further into N_{md} molecular dynamics steps. Typically, we use $N_{\mathrm{md}} = 10$ in our simulations. This introduces the molecular dynamics time step $t_{\mathrm{md}} = \Delta t / N_{\mathrm{md}}$.

During these steps, we perform the Verlet algorithm in order to implement the ballistic motion of solute particles. This algorithm updates position and velocity as follows [245]

$$\mathbf{r}(t+\delta t) = \mathbf{r}(t) + \left(\mathbf{v}(t) + \frac{1}{2M}\mathbf{F}(t)|\delta t|\right)\delta t, \tag{3.29}$$

$$\mathbf{e}(t+\delta t) = \mathbf{e}(t) + \left(\left(\mathbf{\Omega}(t) + \frac{1}{2I}\mathbf{T}(t)|\delta t|\right) \times \mathbf{e}(t)\right)\delta t, \tag{3.30}$$

$$\mathbf{v}(t+\delta t) = \mathbf{v}(t) + \frac{1}{2M}\left(\mathbf{F}(t) + \mathbf{F}(t+\delta t)\right)\delta t, \tag{3.31}$$

$$\mathbf{\Omega}(t+\delta t) = \mathbf{\Omega}(t) + \frac{1}{2I}\left(\mathbf{T}(t) + \mathbf{T}(t+\delta t)\right)\delta t. \tag{3.32}$$

Here, M is the colloidal mass and I the moment of inertia, here a scalar, as is valid for a spherical body. The motion of the fluid particles in the streaming step is also divided into the N_{md} shorter molecular dynamics episodes. In Fig. 3.2 a) we sketch the processes involved in the streaming step. On the one hand, fluid particles are advected, on the other hand, gravitational and inter-particle forces act on the squirmers.

3.3.2 Bounce-back rule

Our systems of interest include no-slip walls, as well as slip conditions on the surfaces of the squirmers. In order to implement these, we apply the bounce back rule during the streaming step [228, 246]. We describe first its application on a no-slip boundary. While fluid particles stream during the molecular dynamics time step with duration t_{MD}, they sometimes end up inside a boundary at the end of the step. The bounce back rule then provides a systematic way to reset the fluid particle into the fluid, and also to reset its velocity. First, the particle within the boundary is moved backwards according to its velocity $\mathbf{v}_{\mathrm{f}}$ for a time $t_{MD}/2$ and it is then reset to the closest position directly on the boundary. We call this position $\mathbf{r}_{\mathrm{bound}}$. Second, the velocity is inverted to the new velocity

$$\tilde{\mathbf{v}}_{\mathrm{f}} = -\mathbf{v}_{\mathrm{f}}, \tag{3.33}$$

i.e., it now moves away from the boundary. Third, the particle is moved with this new velocity $\tilde{\mathbf{v}}_{\mathrm{f}}$ forward in time during a time period $t_{MD}/2$. The resulting position is then again checked for overlaps with a boundary. If it overlaps again, the corrections backward and forward in time will now occur during the time periods $t_{MD}/4$, and so on [168]. Interactions with multiple boundaries during the same step also help to avoid depletion interactions between colloidal particles or swimmers [65, 247].

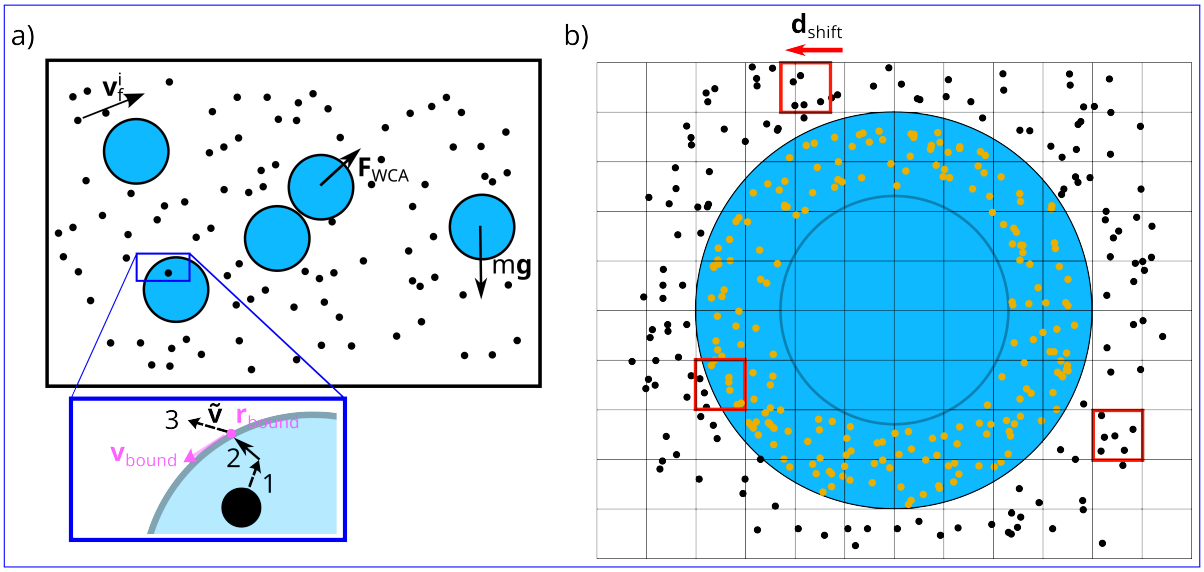

Figure 3.2: a) Sketch of MPCD streaming step including external and interparticle forces on squirmers. Blown-up image shows bounce back rule on a squirmer with slip velocity. b) Sketch of collision step showing collision cells inside and outside a squirmer with radius $4a_0$. Red collision cell at the top shows grid shift operation with random vector $\mathbf{d}_{\text{shift}}$. Black dots: fluid particles. Orange dots: virtual particles. Partially adapted from Refs. [168, 231].

Applying the bounce-back rule to a squirmer's boundary is straightforward. We show the relevant steps in the blown-up part of Fig. 3.2 a). Note that all colloids are moved first during a molecular dynamics step, before the fluid particles are moved [231]. The fluid particle is again transported backwards along its original velocity vector (step 1 in Fig. 3.2 a)). Then, its position is set to the closest position on the squirmer boundary $\mathbf{r}_{\text{bound}}$ (step 2). In comparison with walls, two new contributions appear. First the squirmer's finite velocity and angular velocity in the lab frame has to be added to the velocity $\tilde{\mathbf{v}}_f$ of the bounced-back particle. This also applies to colloidal particles. The updated velocity is [228, 231]

$$\tilde{\mathbf{v}}_{\text{f}} = -\mathbf{v}_{\text{f}} + \mathbf{v}_{\text{bound}}(\mathbf{r}_{\text{bound}}). \tag{3.34}$$

We show this velocity as step 3 in Fig. 3.2 a). Since squirmers and other microswimmers do not obey no-slip boundary conditions on their surface, we also have to add the slip velocity $\mathbf{v}_{\text{slip}}$. In concrete, the velocity at the boundary at the fluid particle's end position $\mathbf{r}_{\text{bound}}$ is

$$\mathbf{v}_{\text{bound}}(\mathbf{r}_{\text{bound}}) = \mathbf{v}_{\text{slip}}(\mathbf{e}, \mathbf{r}_{\text{bound}}) + \boldsymbol{\Omega} \times (\mathbf{r}_{\text{bound}} - \mathbf{r}) + \mathbf{V}. \tag{3.35}$$

Here, $\mathbf{V}$ and $\boldsymbol{\Omega}$ are the colloid's or swimmer's linear and angular velocities. These include effects of steric interactions or external forces. We use here that $\mathbf{r}$ and $\mathbf{e}$ are the position and orientation of the squirmer. As we have shown before, the slip velocity $\mathbf{v}_{\text{slip}}$ of a squirmer depends on $\mathbf{e}$.

3.3.3 Virtual particles

If a collision cell partly overlaps with an immersed particle or a wall, the number of fluid particles interacting within this cell is less than the prescribed value n_{fl}. This locally changes the fluid properties in this cell, *i.e.*, the viscosity is not homogenous. In order to recover the original fluid particle density, we fill up the solid particle or wall with virtual particles for the duration of the collision step [246, 248]. In this way, collision cells that are partially overlapping with the boundary are completely filled. For cells completely submerged within a wall or colloid, no virtual particles are needed. In concrete, we fill up a layer of thickness a_0 within a wall with virtual particles, and a layer of thickness $\sqrt{3}a_0$ within a colloid or squirmer [231][1]. This is shown in Fig. 3.2 b), where the inner circle represents the part of the squirmer, that does not have to be filled. Since the number of fluid particles that take part in the momentum transfer is increased, slip and no-slip boundary conditions are satisfied with a higher precision during the collision step. In Fig. 3.2 b) we show collision cells both with and without participation of virtual particles.

The virtual particles are initialized with a velocity corresponding to the fluid velocity on the surface [231, 248]. This also applies to the tangential surface velocity of a squirmer during the collision step. Additionally, the virtual particles are assigned a random velocity $\mathbf{v}_{\mathrm{rand}}$, where each component is drawn from a normal distribution with standard deviation $\sigma = \sqrt{k_B T_0/m_0}$. In total the velocity of a virtual particle $\mathbf{v}_{\mathrm{vp}}$ is [231]

$$\mathbf{v}_{\mathrm{vp}} = \mathbf{v}_{\mathrm{rand}} + \mathbf{v}_{\mathrm{bound}}(\mathbf{r}^*_{\mathrm{vp}}). \tag{3.36}$$

Here, the boundary effects on the fluid velocity are contained in the term $\mathbf{v}_{\mathrm{bound}}$, which is evaluated at the point closest to the virtual particle. We call this point on the surface $\mathbf{r}^*_{\mathrm{vp}}$. The boundary term includes slip velocities and velocities or angular velocities of the moving colloid from external sources.

The addition of virtual particles requires a change to the Andersen thermostat in the MPC-AT methods, which has to act on the virtual particles: During the collision step, all virtual particles in a collision cell are added to the sum over the fluid particles and take part in the collisions.

3.3.4 Momentum transfer to a colloid or squirmer

While walls are fixed in the system, colloids or squirmers do not just absorb momentum from the fluid, but change their own velocity. In the streaming step this is caused by the scattering of fluid particles during the bounce-back algorithm. In the collision step, it is caused by virtual particles within the squirmer. At the end of the collision step, their velocities have changed with respect to their initial values, which translates into a momentum change of the squirmer.

For the streaming step, the bounce-back momentum transfer can be readily obtained

[1]For the algorithm using graphics processing units, this is not necessary, since it does not lead to a considerable speeding up of the computation. Here, the entire colloid is filled with virtual particles.

[231]:

$$\Delta \mathbf{p}_{\mathrm{bb}} = m_0 \sum_{i=1}^{N_{\mathrm{bb}}} \left(\mathbf{v}_{\mathrm{f}}^i - \tilde{\mathbf{v}}_{\mathrm{f}}^i \right), \tag{3.37}$$

where the sum is over all N_{bb} fluid particles that landed inside the squirmer during the molecular dynamics step t_{MD}. Therefore, the momentum transferred to the squirmer is the sum of the negative momentum differences affecting the fluid particles. Likewise, the angular momentum changes according to

$$\Delta \mathbf{L}_{\mathrm{bb}} = m_0 \sum_{i=1}^{N_{\mathrm{bb}}} \left(\mathbf{r}_{\mathrm{bound}}^i - \mathbf{r} \right) \times \left(\mathbf{v}_{\mathrm{f}}^i - \tilde{\mathbf{v}}_{\mathrm{f}}^i \right), \tag{3.38}$$

with the squirmer position $\mathbf{r}$.

For the collision step, the momentum gain of the squirmer depends on the exchange between physical and virtual fluid particles [231]. The momentum gain of the squirmer is the sum over the momentum gains of all virtual particles. Hence,

$$\Delta \mathbf{p}_{\mathrm{vp}} = m_0 \sum_{i=1}^{N_{\mathrm{vp}}} \left(\tilde{\mathbf{v}}_{\mathrm{VP}}^i - \mathbf{v}_{\mathrm{vp}}^i \right) \tag{3.39}$$

for the momentum and

$$\Delta \mathbf{L}_{\mathrm{vp}} = m_0 \sum_{i=1}^{N_{\mathrm{vp}}} \left(\mathbf{r}_{\mathrm{vp}}^i - \mathbf{r} \right) \times \left(\tilde{\mathbf{v}}_{\mathrm{vp}}^i - \mathbf{v}_{\mathrm{vp}}^i \right) \tag{3.40}$$

for the angular momentum. N_{vp} is the number of virtual particles, which can vary for each squirmer and for each instance the collision step is performed.

The velocities and angular velocities of a squirmer are both updated after each molecular dynamics step and after the collision step, according to its mass and moment of inertia [231].

3.3.5 Corrections to hydrodynamic friction

The particle description of the fluid influences the friction experienced by a suspended particle. Furthermore, periodic boundary conditions change the hydrodynamic friction compared to its bulk value. We discuss both the solvent, as well as the geometry effects below.

Local friction

As we have seen, the fluid properties, such as viscosity, are influenced by the discrete fluid model of MPCD. Likewise, a colloidal particle experiences friction that is not completely consistent with the Stokes-Einstein friction law at low Reynolds numbers. This was confirmed in measurements by Imperio, Padding, and Briels [153]. Rather, the continuum hydrodynamic friction is only one part of the total friction the particle experiences. There is an additional *local Brownian friction* [246, 249], which originates

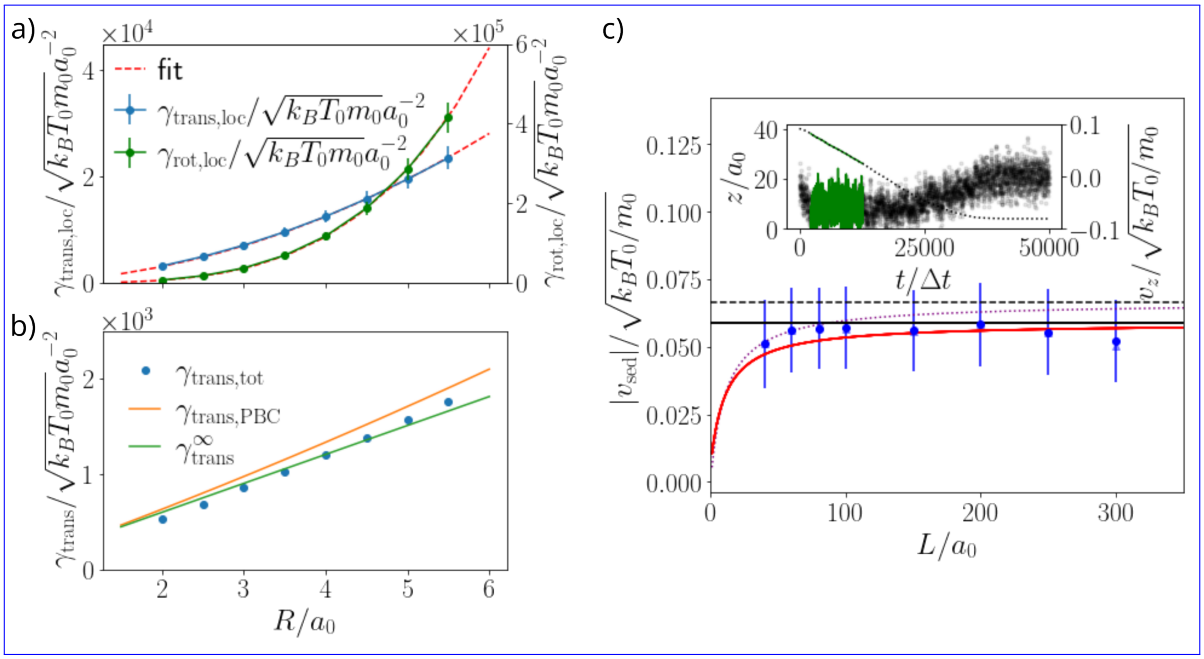

Figure 3.3: a) Translational (blue) and rotational (green) local friction coefficients as a function of particle radius, together with the fits proportional to R^2 and R^4. b) Comparison of the predictions for the hydrodynamic friction: bulk friction γ^{∞} (green line), including periodic boundary conditions (orange line), and in combination with local friction (blue dots). c) Sedimentation velocities of a colloid with $R = 4$ at different lateral system sizes measured from MPCD simulations (blue dots) compared to various theoretical predictions: using bulk friction (dashed black line), hydrodynamic friction including wall effects and local friction (solid black line), hydrodynamic friction with periodic boundaries (dotted purple line), and a combination of wall friction, local friction and periodic boundaries (solid red line). The blue triangles correspond to an alternative measurement of the sedimentation velocities using the slope of the trajectories, but they mostly overlap with the blue circles. Inset: Vertical trajectory $z(t)$ and vertical velocity $v_z(t)$ for a sinking colloid. The portions used to measure the sedimentation velocities are in green color.

from collisions with the solvent particles and is thus due to the gas character of the MPCD fluid. In theory, this friction term can be calculated, if uncorrelated, two-body collisions are assumed. For a spherical colloid the local translational and rotational friction according to this theory is [246]

$$\gamma^{\mathrm{E}}_{\mathrm{trans,loc}} = \frac{8}{3}\sqrt{\frac{2\pi k_BT_0m_0M}{m_0+M}}n_{\mathrm{fl}}/a_0^3R^2\frac{1+2\chi_{\mathrm{gyr}}}{1+\chi_{\mathrm{gyr}}}, \tag{3.41}$$

$$\gamma^{\mathrm{E}}_{\mathrm{rot,loc}} = \frac{8}{3}\sqrt{\frac{2\pi k_BT_0m_0M}{m_0+M}}n_{\mathrm{fl}}/a_0^3R^4\frac{\chi_{\mathrm{gyr}}}{1+\chi_{\mathrm{gyr}}}, \tag{3.42}$$

where M is the mass of the colloid and R is its radius, and the gyration ratio is $\chi_{\mathrm{gyr}} = \frac{2}{5}$ for spherical particles. The coefficients are also called *Enskog* friction coefficients, hence

we indexed them with an 'E'. However, this value still considerably underestimates the friction in MPCD simulations [153], because the collision step introduces additional effective collisions, via the interaction with virtual particles. That also implies that the strength of the local friction depends on the collision operator and the length of the collision step [168]. The total local friction coefficients are

$$\gamma_{\mathrm{trans,loc}} = \gamma^{E}_{\mathrm{trans,loc}} + \gamma^{\mathrm{VP}}_{\mathrm{trans,loc}}, \tag{3.43}$$

$$\gamma_{\mathrm{rot,loc}} = \gamma^{E}_{\mathrm{rot,loc}} + \gamma^{\mathrm{VP}}_{\mathrm{rot,loc}}. \tag{3.44}$$

These coefficients can only be determined by numerical simulations. We can use the Green-Kubo relation (2.74) to measure the local friction, by measuring the force and torque autocorrelation [153, 168]. Here, the force and torque are determined by the difference quotients

$$\mathbf{F}(t) = \frac{M\Delta\mathbf{V}}{\Delta t} \tag{3.45}$$

and

$$\mathbf{T}(t) = \frac{I\Delta\mathbf{\Omega}}{\Delta t}, \tag{3.46}$$

where $\Delta\mathbf{V}$ and $\Delta\mathbf{\Omega}$ are the change of velocity and angular velocity of the colloid after both streaming and collision step. The local friction coefficients for translation and rotation are shown in Fig. 3.3 a) as a function of particle size R, using the MPC-AT+a algorithm. We have added curve fits proportional to R^2 and R^4, respectively, which describe the data excellently. The fit parameters confirm that the local friction is higher than described by the theoretical Enskog law: For our system with $R = 4a_0$, $\Delta t = 0.02a_0\sqrt{m_0/k_BT_0}$, $n_{\mathrm{fl}} = 10$ we measure a translational friction growing as $782.2 \pm 1.7R^2$ and a rotational friction growing as $455.8 \pm 1.0R^4$. These values are consistent with measurements in Ref. [168]. In contrast, the theoretical values using the Enskog friction calculated from Eqs. (3.43)-(3.44) are $85.9R^2$ and $43.0R^4$, respectively.

For sufficiently large colloid radii, we can use the following formulae for the total friction [153, 246, 249, 250]

$$\gamma^{-1}_{\mathrm{trans}} = \gamma^{-1}_{\mathrm{trans,hd}} + \gamma^{-1}_{\mathrm{trans,loc}}, \tag{3.47}$$

$$\gamma^{-1}_{\mathrm{rot}} = \gamma^{-1}_{\mathrm{rot,hd}} + \gamma^{-1}_{\mathrm{rot,loc}}. \tag{3.48}$$

Here, the hydrodynamic contributions $\gamma_{\mathrm{trans,hd}}$ and $\gamma_{\mathrm{rot,hd}}$ can in some situations be provided by the bulk values $6\pi\eta R$ and $8\pi\eta R^3$, but they could also include the hydrodynamic effect of walls.

Corrections from periodic boundary conditions

In the lateral directions of our simulation box, we use periodic boundary conditions. Since this introduces copies of all colloidal particles, which then interact with each other, the friction is different from an infinite system. For a sphere in a full 3D periodic system, Dünweg and Kremer have calculated the approximation [251]

$$\gamma_{\mathrm{PBC}} = \frac{\gamma_{hd}}{1 - 2.837R/L}, \tag{3.49}$$

with boxlength L. Therefore, while hydrodynamic interactions between spheres often decrease the effective friction, for example when they are falling next to each other under gravity, periodic boundary effects increase it. Imperio *et al.* show that this law remains valid for a two-wall system with lateral periodicity, if the system size is large [153]. Furthermore, the increase of friction disappears completely for large enough systems [153]. We compare the effects of periodic boundary conditions to the effects of local friction in Fig. 3.3 b). Interestingly, periodic boundary conditions and local friction on a colloid cancel each other partially, as already noticed by Zöttl [168]. Consequently, the total friction obtained from combining both effects according to Eqs. (3.47) (blue dots in Fig. 3.3 b)) is again close to the hydrodynamic bulk friction (solid green line). Under these circumstances, the wall effects on the friction introduced in Sec. 2.3.3 dominate.

Sedimentation velocity

Finally, we measure the sedimentation velocity of a single passive colloid in the MPCD fluid. We choose a radius $R = 4a_0$ and vary the lateral cross-section via the width L in order to check the finite size and periodic boundary effects. We show the results in Fig. 3.3 c). The blue dots indicate the measured sedimentation velocities. The blue triangles were obtained from an alternative measurement using the slope of the curve $z(t)$ and agree very well with the first measurement. The trajectory $z(t)$ is shown in the inset. Here, the time period used for measuring the sedimentation velocity is marked in green color. The fluctuating curve depicts the sedimentation velocity and shows how its absolute value decreases, as the colloid approaches the wall. This illustrates the effect of the wall on friction. In the main plot of Fig. 3.3 c), we show the expected sedimentation velocity, when we assume the bulk value for the friction $6\pi\eta R$ as the dashed black line, while the dotted purple line includes the finite-size correction from Eq. (3.49). The solid black horizontal line assumes the two-wall approximation from Eq. (2.112) and gives a good estimate for the measured sedimentation velocities. For system sizes greater than $L = 100a_0$, the measurements also agree well with the values found for combining walls, periodic boundaries and local friction, which is shown as the solid red line. Therefore, we can confirm that the hydrodynamic friction value, including wall interactions, offers a good approximation for the total friction.

3.3.6 Depletion and fluid compressibility

In some settings the particle description of the fluid can lead to unphysical depletion of fluid between solute particles in close contact. The depletion of fluid between colloids is problematic, because it prevents the application of the correct lubrication forces. Solvent-induced forces can draw colloids closer together [247, 252]. However, this is mainly a problem for attractive colloid-solvent interactions [252]. Furthermore, in the case of swimmers with a prescribed surface velocity (*e.g.* squirmers), the use of virtual particles has been shown to prevent depletion attraction [252].

Several strategies of addressing compressibility of MPCD have been suggested: Theers et al. [162] argued that the particle number per cell has to be increased in very dense systems and the speed of the active particles lowered. This way, viscosity is

increased but the active Péclet number stays the same. Furthermore, the Mach number and Reynolds number are decreased. Their work focused on Hele-Shaw geometries. Another possibility for reducing compressibility effects is to model the fluid as a non-ideal gas [167]. This has been shown to decrease the compressibility.

3.4 Parameters

Our system consists of two walls that are separated vertically by a height H. These walls have a no-slip boundary condition. The system has a quadratic cross section with edge length L. However, we use periodic boundary conditions in lateral direction. We set the duration of the streaming step to $\Delta t = 0.02 a_0 \sqrt{m_0/k_B T_0}$ and the fluid-particle number density to $n_{\mathrm{fl}} = 10$, which means a dynamic viscosity of $\eta = 16.05\sqrt{m_0 k_B T_0}/a_0^2$ [168]. Our Reynolds number is determined by $\mathrm{Re} = v_0 R n_{\mathrm{fl}}/\eta = 0.17$. Reaching this value is computationally feasible and means that viscous effects dominate over inertial effects. Lowering it further would add considerable numerical costs.

Our squirmers have a radius of $R = 4a_0$. The squirming mode $B_1 = 0.1\sqrt{k_B T_0/m_0}$ is fixed, while the B_2 and C_2 modes can vary. This implies an active Péclet number $\mathrm{Pe} = \frac{R v_0}{D_{\mathrm{trans}}} = 330$, comparable, for example, to bacteria [156, 157]. The persistence number of a squirmer is $\mathrm{Pe}_r = v_0/(R D_{\mathrm{rot}}) = 420$. We can determine these values from the bulk diffusivities of a sphere in Stokes flow, *viz.* $D_{\mathrm{trans}} = k_B T_0/(6\pi\eta R) = 8 \cdot 10^{-4} a_0 \sqrt{k_B T_0/m_0}$ and $D_{\mathrm{rot}} = 4 \cdot 10^{-5} \sqrt{k_B T_0/m_0}/a_0$.

4. Single squirmer under gravity

In this chapter, the dynamics of a single squirmer under gravity is investigated, both analytically and with numerical simulations. Most results of this chapter are based on publication [A].

4.1 Introduction

Active particles are inherently out of equilibrium, which leads to intriguing and counter-intuitive dynamics. A lot of focus is - deservedly - put on collective effects, such as giant number fluctuations [2, 253], motility-induced phase separation [165] or pattern formation [254], for example of biofilms [255]. However, since the activity is introduced on small scales, *i.e.*, from the self-propulsion of the individual agent, non-equilibrium dynamics are present already for the single particle. The striking differences to passive particles become visible, for example, by subjecting a swimmer to an external field or putting it under flow. One example are swimmers that react to magnetic fields [133, 256–258], opening the possibility to steer synthetic particles or magnetotactic bacteria [259–261]. One can observe swinging trajectories for simple model swimmers in Poiseuille flow [262, 263], as well as in studies of the parasite *Trypanosome brucei* [18]. Furthermore, live sperm cells can sense chemoattractants and also use external flow to navigate [110, 264]. Under gravity, an asymmetrically shaped phototactic colloid switches from straight to complex trochoidal motion, depending on the illumination strength [59]. We have presented further examples of the motion under gravity in Sec. 2.4.

Since swimmers create hydrodynamic flow fields, interactions with surfaces become important. This has been shown in both experiments and computer simulations [38, 175, 265, 266]. Under gravity, this is particularly relevant, since swimmers sink down to the bottom surface [61, 91]. Importantly, these hydrodynamic interactions depend on the distance to the wall.

A single squirmer in wall proximity is a conceptually simple system and can be tackled analytically to a certain extent. Thus, we start by discussing its deterministic dynamics. We take into account that hydrodynamic near field and far fields differ considerably for a squirmer [38, 266]. Thus, both have to be calculated in order to arrive at a good representation. Furthermore, we perform MPCD simulations of a single squirmer. These include the full hydrodynamic flow field, as well as thermal noise. We simulate a squirmer in a rectangular box of height H. At $z = 0$ and $z = H$ a no-slip wall is placed, whereas periodic boundary conditions are used in lateral direction. We

apply a gravitational acceleration $-g\mathbf{e}_z$ to the single squirmer and briefly discuss the effect of a gravitational torque. In our studies, we neglect the influence of gravity on the fluid particles. Thus, we assume that the fluid particles' sedimentation length is larger than H.

In Appendix C we summarize the most important symbols for both physical and simulation parameters that we use in our studies in Tables C.1 and C.2.

4.2 Deterministic dynamics of a single squirmer in wall proximity

In the following, we describe the dynamics of a single squirmer and use the insights collected in previous chapters. At this point, we do not take the effects of thermal fluctuations into account. However, these will be present in our numerical simulations. The squirmer's deterministic motion consists of three different effects: its active motion, the influence of gravity and the hydrodynamic interactions with the no-slip boundary. Since the motion in vertical direction is especially important for the single-squirmer dynamics, we begin by introducing these three contributions while considering only the height z and polar angle ϑ from the vertical. Then, we calculate the height-dependent sedimentation velocity, and the height-dependent angular velocity from the gravitational torque. Furthermore, we discuss both far-field and near-field effects of the wall interactions caused by the squirmer's own flow field.

4.2.1 Vertical motion

The first velocity contribution we identified is self-propulsion. The active velocity is present in bulk and without any external forces, which is why we call it v_0. Furthermore, since the systems we study are subject to gravity, the squirmer experiences a sedimentation velocity v_1 and an angular velocity Ω_1 from bottom-heaviness. These effects are passive in nature, *i.e.*, they also occur for a simple colloidal particle. The external force and torque on the squirmer induce a hydrodynamic flow field in the system. This leads to height-dependent mobility close to walls, which we discuss below. Third, the self-generated flow fields in combination with the no-slip wall lead to a self-interaction of the squirmers. This creates the contributions v_2 and Ω_2. We present all contributions in Fig. 4.1. In total, one arrives at the vertical velocity and angular velocity,

$$v = v_0 \cos\vartheta - v_1 + v_2 \quad \text{and} \quad \Omega = \Omega_1 + \Omega_2 \,. \tag{4.1}$$

4.2.2 Gravitational force and torque

We apply the gravitational force

$$\mathbf{F}_g = -mg\mathbf{e}_z \tag{4.2}$$

on a squirmer. This tunable force could for example arise from a density mismatch between fluid and swimmer density, as has been applied to active emulsion droplets in Ref. [144], from an inclined plane [55, 267], or from a centrifuge [51].

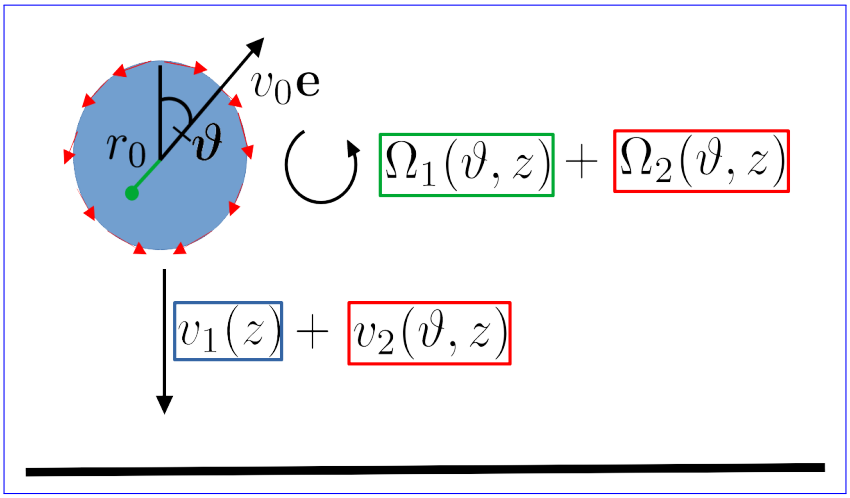

Figure 4.1: The different velocity and angular velocity contributions to a squirmer in wall proximity: Sedimentation with the velocity v_1 and the angular velocity Ω_1 created by bottom-heaviness are passive effects. The latter appears due to an offset of the center of mass (shown in green). The self-propulsion velocity is v_0 and its vertical component is $v_0 \cos\vartheta$. We do not consider an active angular velocity. In addition, the self-generated flow field of the squirmer induces the linear velocity v_2 and the angular velocity Ω_2. We sketched the responsible surface flow field in red.

Furthermore, making the squirmer bottom-heavy induces a gravitational torque. It results from an offset r_0 of its center of mass from the geometrical center [158]. The resulting torque is

$$\mathbf{T}_{\mathrm{bh}} = mgr_0(-\mathbf{e}_z \times \mathbf{e}). \tag{4.3}$$

The resulting angular velocity in bulk is

$$\mathbf{\Omega}_{\mathrm{bh}} = \mathbf{T}_{\mathrm{bh}}/(8\pi\eta R^3) = \frac{3}{4}\frac{v_0}{R}\frac{r_0}{R\alpha}(-\mathbf{e}_z \times \mathbf{e}). \tag{4.4}$$

Here, we use the rescaled torque $r_0/(R\alpha)$.

Flow field

A squirmer with orientation $\mathbf{e}$ under gravity and close to a wall moves with the velocity

$$\mathbf{v} = v_0\mathbf{e} + \mathbf{M}^{\mathrm{tt}}\mathbf{F}_g + \mathbf{M}^{\mathrm{tr}}\mathbf{T}_{\mathrm{bh}}, \tag{4.5}$$

where $\mathbf{M}^{\mathrm{tt}}$ is the translational mobility and $\mathbf{M}^{\mathrm{tr}}$ the translation-rotation coupling. Far enough from the wall, we can apply the pumping field derived in Sec. 2.2.4, where the part of the flow field induced by gravity is expressed as a stokeslet and a source dipole, the same as for a passive sphere. Hence,

$$\mathbf{u}_g = \mathbf{u}_g^S + \mathbf{u}_g^{SD}, \tag{4.6}$$

where the two components are

$$\mathbf{u}_{\mathrm{g}}^{\mathrm{S}} = -\frac{3}{4} v_{\mathrm{sed}} \frac{R}{r} \left(\mathbf{e}_z + \frac{z}{r} \hat{\mathbf{r}} \right) \tag{4.7}$$

$$\mathbf{u}_{\mathrm{g}}^{\mathrm{SD}} = \frac{1}{4} v_{\mathrm{sed}} \frac{R^3}{r^3} \left(-\mathbf{e}_z + 3 \frac{z}{r} \hat{\mathbf{r}} \right) , \tag{4.8}$$

and where $z = \mathbf{r} \cdot \mathbf{e}_z$. The gravity-induced flow fields play a central role, when we consider collective motion of squirmers.

The flow field of a rotating sphere under the influence of an external torque is the rotlet [82],

$$\mathbf{u}_{\mathrm{bh}} = \mathbf{u}_{\mathrm{bh}}^{\mathrm{R}} = \frac{R^3}{r^2} \mathbf{\Omega}_{\mathrm{bh}} \times \hat{\mathbf{r}} = \frac{3}{4} v_0 \frac{r_0}{R\alpha} \frac{R^2}{r^2} \left((\mathbf{e} \cdot \hat{\mathbf{r}}) \mathbf{e}_z - \frac{z}{r} \mathbf{e} \right) . \tag{4.9}$$

Here, $\mathbf{\Omega}_{\mathrm{bh}} = \mathbf{T}_{\mathrm{bh}} / (8\pi\eta R^3)$ is the angular velocity resulting from the bottom-heavy torque. Note that the flow field in Eq. (4.9) vanishes for $\mathbf{e} \to \mathbf{e}_z$.

4.2.3 Effective sedimentation and reorientation

We have discussed the effective mobility induced by walls in Sec. 2.3.3. We truncate the expressions at the z^{-3} order and consequently neglect the translation-rotation coupling. However, the mobility is still anisotropic, *i.e.*, a horizontal motion and a vertical motion create different forces. For a single wall the translational mobility to leading order is [268]

$$\mu_{\perp}^{\mathrm{tt}}(z) = \mu_{\infty} \left[1 - \frac{9}{8} \frac{R}{z} + \frac{1}{2} \left(\frac{R}{z} \right)^3 + \mathcal{O} \left(\left(\frac{R}{z} \right)^4 \right) \right] \tag{4.10}$$

for the direction perpendicular to the wall and

$$\mu_{\parallel}^{\mathrm{tt}}(z) = \mu_{\infty} \left[1 - \frac{9}{16} \frac{R}{z} + \frac{1}{8} \left(\frac{R}{z} \right)^3 + \mathcal{O} \left(\left(\frac{R}{z} \right)^4 \right) \right] \tag{4.11}$$

for the direction parallel to the wall. The bulk mobility is $\mu_{\infty} = 1/(6\pi\eta R)$. Furthermore, the approximate rotational mobility for a rotation about a wall-parallel axis is

$$\mu_{\parallel}^{\mathrm{rr}}(z) = \mu_{\infty}^{r} \left[1 - \frac{5}{16} \left(\frac{R}{z} \right)^3 + \mathcal{O} \left(\left(\frac{R}{z} \right)^6 \right) \right] \tag{4.12}$$

with $\mu_{\infty}^{r} = 1/(8\pi\eta R^3)$.

We also re-state the series expansion for the friction of Eq. (2.110), which we use below for more exact results.

$$\begin{aligned} \gamma_{\perp}^{\mathrm{tt}}(z) = & \frac{4}{3} \sinh q(z) \sum_{n=1}^{\infty} \frac{n(n+1)}{(2n-1)(2n+3)} \times \\ & \left[\frac{2 \sinh\left([2n+1]q(z)\right) + (2n+1) \sinh\left(2q(z)\right)}{4 \sinh^2\left([n+1/2]q(z)\right) - (2n+1)^2 \sinh^2\left(q(z)\right)} - 1 \right] , \end{aligned}$$

with $q(z) = \mathrm{Arcosh}(z/R)$.

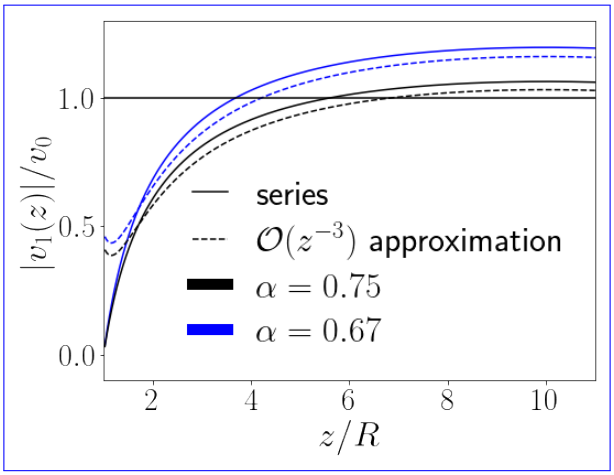

Figure 4.2: Height-dependent sedimentation velocity $v_1(z)$ for $\alpha = 0.67$ and $\alpha = 0.75$ using the series expansion for the friction (solid lines) or the approximation up to order z^{-3} (dashed line). Due to the decrease in magnitude at lower z the sedimentation velocity falls below the active velocity v_0 (horizontal line), leading to a stable floating height.

Height-dependent sedimentation velocity

Using the above mobilities, we can express the height-dependent sedimentation velocity as

$$v_1(z) = \mu_\perp^{\mathrm{tt}}(z) mg = v_{\mathrm{sed}} \left(\kappa(z) + \kappa(h - z) - 1\right). \tag{4.13}$$

The bulk sedimentation velocity v_{sed} can be expressed as

$$v_{\mathrm{sed}} = v_0/\alpha, \tag{4.14}$$

with the velocity ratio α introduced in Eq. (2.123). The correction factor in parentheses reflects the two-wall approximation with

$$\kappa(z) = \mu_\perp^{\mathrm{tt}}(z)/\mu_\infty = \left(1 - \frac{9}{8}\frac{R}{z} + \frac{1}{2}\left(\frac{R}{z}\right)^3\right). \tag{4.15}$$

Alternatively, using the series expansion for $\gamma_\perp^{\mathrm{tt}}(z)$, we have $\kappa(z) = \gamma_\infty/\gamma_\perp^{\mathrm{tt}}(z)$ with the bulk friction $\gamma_\infty = 1/\mu_\infty$.

Stable floating heights due to height-dependent friction Height-dependent friction has an important consequence on the vertical velocity balance of a squirmer. Consider a value of $\alpha \lessapprox 1$, *i.e.*, the active velocity v_0 is smaller than the bulk sedimentation velocity v_{sed}, but stays comparable to it. Since the magnitude of the effective sedimentation velocity decreases closer to the wall, the active velocity v_0 can overcome the downward buoyancy at a certain height. This *floating height* is stable for the squirmer, since the total vertical velocity is positive below this height (active velocity

overcomes effective sedimentation velocity) and negative above it (active velocity is smaller than sedimentation velocity). We show this behaviour in Fig. 4.2, where we plot $v_1(z)$. A stable height can be expected, where the curves intersect the horizontal line $v_1(z) = v_0$. At the larger plotted value $\alpha = 0.75$ the floating height is larger than at the smaller value $\alpha = 0.67$. Furthermore, there are quantitative differences between the series expansion for the friction (solid lines) and the approximation in Eq. (4.10) (dashed lines), in particular close to the wall at $z = R$.

Note that for these brief considerations we neglected the hydrodynamic contribution v_2, which is presented below in Sec. 4.2.4. Furthermore, we assumed a upright orientation of the squirmer, which strongly depends on Ω_2.

Height-dependent angular velocity

We now consider the angular velocity, which acts on the polar angle ϑ, measured from the vertical. Thus, we use the z-component of the torque in Eq. (4.3), which is given by $-mgr_0 \sin\vartheta$. Using the two-wall approximation and the rotational mobility from Eq. (4.12) the height-dependent angular velocity Ω_1 yields

$$\Omega_1(z) = -\mu_{\parallel}^{\mathrm{rr}}(z) mgr_0 \sin\vartheta = -\Omega_{\mathrm{bh}} \sin\vartheta \left(\kappa^R(z) + \kappa^R(h-z) - 1\right) \tag{4.16}$$

with

$$\kappa^R(z) = \left(1 - \frac{5}{16}\left(\frac{R}{z}\right)^3\right) \tag{4.17}$$

and

$$\Omega_{\mathrm{bh}} = \frac{3}{4}\frac{v_0}{R}\frac{r_0}{R\alpha}, \tag{4.18}$$

which is the absolute value of Eq. (4.4). From Eq. (4.18) we see that the rescaled torque $r_0/(R\alpha)$ is directly proportional to the ratio of the ballistic active time R/v_0 to the reorientation time $\Omega_{\mathrm{bh}}^{-1}$. The leading order correction induced by the wall is proportional to z^{-3} and therefore more short-ranged than the translational one.

4.2.4 Hydrodynamic wall interactions from squirmer flow fields

We now consider the hydrodynamic contributions from the active actuation. In concrete, the squirmer self-propels due to a surface flow field, which varies with parameters v_0, β and χ. This flow field is reflected by the no-slip wall and therefore induces linear and angular velocities. We take two different approximations into account. First, we discuss the far field. This corresponds to approximating the squirmer by multipole moments, consequently the boundary condition on the squirmer surface is not satisfied by the approximate flow field close to the wall. Secondly, we consider the lubrication approximation, which is valid at small distances. Both considerations need to be taken into account, since we expect squirmer trajectories to include positions both close to and far from the wall.

Far-field hydrodynamic interactions

The velocity far field of a squirmer at position $\mathbf{r}_0$ and with orientation vector $\mathbf{e}$ consists of a force dipole with strength p, a source dipole with strength $s > 0$ and a rotlet dipole with strength q:

$$\mathbf{u}(\mathbf{r}) = -\frac{p}{r^2}[1 - 3\,(\mathbf{e}\cdot\hat{\mathbf{r}})^2]\hat{\mathbf{r}} + \frac{s}{r^3}[\mathbf{e} - 3\,(\mathbf{e}\cdot\hat{\mathbf{r}})\,\hat{\mathbf{r}}] + \frac{q}{r^3}[(\mathbf{e}\cdot\hat{\mathbf{r}})\,\mathbf{e}\times\hat{\mathbf{r}}]\,. \tag{4.19}$$

We repeat here the dipolar strengths derived in Eqs. (2.100)

$$p = -\frac{3}{4}\beta v_0 R^2 \quad , \quad s = \frac{1}{2}v_0 R^3 \quad , \quad q = \frac{9}{2}\chi v_0 R^3\,. \tag{4.20}$$

Wall-induced squirmer velocity We calculate the wall-induced velocity of the squirmer in the far field $\mathbf{v}^{\mathrm{ff}}$, using the multipole representation of the flow field in Eqs. (4.19) and (4.20). According to Sec. 2.3.2, the multipoles induce wall images, which influence the squirmer according to Faxén's theorem of translation [see Eq. (2.101)] [87, 269]. We neglect the higher-order terms appearing from the Laplace operator and arrive at

$$v_\rho^{\mathrm{ff}} = \frac{v_0}{8}\left(\frac{R}{z}\right)^2\left[-\frac{9}{4}\beta\sin\vartheta\cos\vartheta - \frac{R}{z}\sin\vartheta\right] \tag{4.21}$$

$$v_z^{\mathrm{ff}} = \frac{v_0}{2}\left(\frac{R}{z}\right)^2\left[\frac{9}{16}\beta\left(1 - 3\cos^2\vartheta\right) - \frac{R}{z}\cos\vartheta\right]. \tag{4.22}$$

Here v_ρ^{ff} represents the velocity in the wall-parallel plane and v_z^{ff} represents the vertical velocity. There is no contribution in the azimuthal $\mathbf{e}_\varphi$ direction. Furthermore, the rotlet dipole does not contribute to the wall-induced velocity [87]. The reason for this is that the combined wall singularities induced by the rotlet dipole lead to a net zero velocity at the squirmer position.

Wall-induced angular velocity The wall-induced angular velocity in the far field $\mathbf{\Omega}^{\mathrm{ff}}$ can be calculated in the same way. Here, we use the formula $\mathbf{\Omega} = \frac{1}{2}\nabla\times\mathbf{u}$ according to Faxén's theorem of rotation in Eq. (2.102). Again, $\mathbf{u}$ is the flow field of the image singularities. The induced angular velocity has components along the radial, azimuthal, and vertical directions, which read

$$\Omega_\rho^{\mathrm{ff}} = \frac{81}{32}\frac{v_0}{R}\chi\sin\vartheta\cos\vartheta\frac{R^4}{z^4} \tag{4.23}$$

$$\Omega_\varphi^{\mathrm{ff}} = -\frac{3}{16}\frac{v_0}{R}\frac{R^3}{z^3}\sin\vartheta\left(\frac{3}{2}\beta\cos\vartheta + \frac{R}{z}\right) \tag{4.24}$$

$$\Omega_z^{\mathrm{ff}} = -\frac{27}{64}\frac{v_0}{R}\chi(1 - 3\cos^2\vartheta)\frac{R^4}{z^4}\,. \tag{4.25}$$

The force and source dipoles of the squirmer both contribute only to the φ-component, which affects the polar angle ϑ of the squirmer's orientation vector, while leaving the wall-parallel contribution unchanged. The latter is altered by the rotlet-dipole component.

Lubrication approximation

The lubrication approximation for a squirmer with finite β was calculated by Ishikawa and Pedley [187] and, with corrections, by Lintuvuori et al. [266]. In contrast to the passive colloid sketched in the lubrication calculation in Section 2.3.4, the squirmer microswimmer has a slip velocity on its surface. Therefore, the functional forms of the translational and angular velocities differ. We limit our considerations here to the angular velocity in $\mathbf{e}_\varphi$ direction, which we need to discuss the vertical motion of squirmers. This angular velocity is [266]

$$\Omega_\varphi^{\mathrm{nf}} = \frac{3}{2}\frac{v_0}{R}\sin\vartheta\,(\beta\cos\vartheta - 1) + \mathcal{O}(1/\log(\varepsilon)), \tag{4.26}$$

where $\varepsilon = (z-R)/R$ is the smallness parameter giving the reduced distance of the squirmer surface from a wall. For the translational velocity in lubrication approximation, we note that the constant term with respect to ε vanishes [266]. Hence, the induced velocity is zero at the leading order of Eq. (4.26).

4.2.5 Stable orientations and heights

We now focus on the vertical dynamics of the squirmer. We identify stable squirmer heights and orientations for the near and far field. We here consider both approximations in isolation. In our numerical simulations, which we present in the next section, squirmers move both close to the wall and far from the wall, therefore both aspects are combined.

Total vertical velocity and angular velocity

We use the vertical components of the sedimentation and wall-induced velocities found above to specify the total vertical velocity $v_0\cos\vartheta + v_1 + v_2$ introduced in Eq. (4.1). The same applies to the angular velocity $\Omega_1 + \Omega_2$ around an axis parallel to the wall. At the moment, we leave open whether we use the near field or the far field approximation for v_2 and Ω_2.

Deterministic system in vertical direction The deterministic system of the vertical squirmer motion can be written as

$$\begin{pmatrix} \dot{z} \\ \dot{\vartheta} \end{pmatrix} = \begin{pmatrix} v \\ \Omega \end{pmatrix} =: f(z,\vartheta). \tag{4.27}$$

We now look for fixed points (z^*, ϑ^*) of the system, *i.e.*, states with $f(z^*,\vartheta^*) = 0$. Following linear stability analysis, we check the eigenvalues of the Jacobian $Df(z^*,\vartheta^*)$. States with negative eigenvalues correspond to stable fixed points of the dynamical system. One finds different conventions for the sense of rotation induced by an angular velocity in literature [87, 266] — in our case we define Ω such that $\dot{\vartheta} = +\Omega$.

In the following, we consider the rotational and translational equations separately. We first look for stable angles in the system. Here, we differentiate between squirmers with and without bottom-heaviness, *i.e.*, $\Omega_1 = 0$ and $\Omega_1 \neq 0$. Furthermore, we distinguish between the near and the far field interaction $\Omega_2 = \Omega_\varphi^{\mathrm{nf}}$ or $\Omega_2 = \Omega_\varphi^{\mathrm{ff}}$.

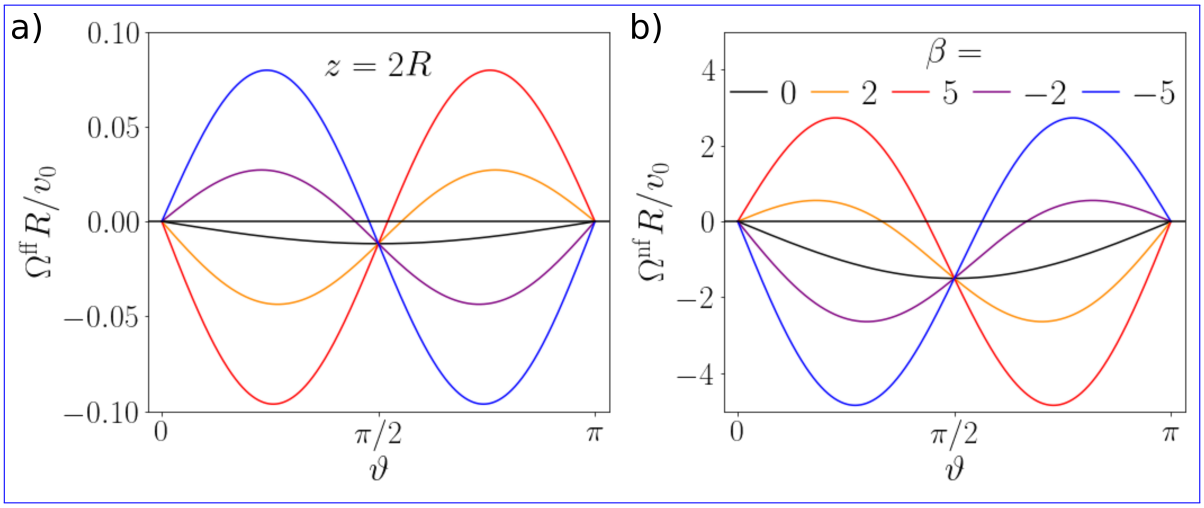

Figure 4.3: Wall-induced angular velocity of a squirmer *versus* angle ϑ against the vertical a) in far-field approximation at $z = 2R$ b) in lubrication approximation for different values of β.

Stable orientations at zero external torque

Without the external torque, setting the angular component of Eq. (4.27) to zero amounts to:

$$\Omega_{\varphi}^{\mathrm{nf}} = 0 \qquad \text{or} \qquad \Omega_{\varphi}^{\mathrm{ff}} = 0, \tag{4.28}$$

depending on whether we use the near- or the far-field approximation. Figure 4.3 plots the far field and near field angular velocities *versus* ϑ for different squirmer types β. Zeros with positive and negative slopes correspond to unstable and stable fixed points, respectively. Thus, we calculate the derivatives:

$$\frac{\partial \Omega^{\mathrm{ff}}}{\partial \vartheta} \propto -\frac{3}{2}\beta\left(\cos^2\vartheta - \sin^2\vartheta\right) - \frac{R}{z}\cos\vartheta < 0 \tag{4.29}$$

$$\frac{\partial \Omega^{\mathrm{nf}}}{\partial \vartheta} \propto -\cos\vartheta + \beta(\cos^2\vartheta - \sin^2\vartheta) < 0\,. \tag{4.30}$$

We have summarized the solutions to the equation $\Omega_2 = 0$, which satisfy the stability conditions in Eq. (4.29) or Eq. (4.30), in Tab. 4.1. As the table shows, in both cases, the angles $\vartheta_1^* = 0$ and $\vartheta_2^* = \pi$ are stable under some conditions, which we discuss below. Additionally, a stable angle ϑ_3^* can occur, with a value between ϑ_1^* and ϑ_2^*.

Both in Tab. 4.1, as well as in Fig. 4.3, the positions of the fixed points vary with the squirmer parameter β. For the neutral squirmer, the upright position $\vartheta_1^* = 0$ is stable. In the far-field approximation, this is due to the image force-quadrupole field, induced by a source dipole at a no-slip wall. However, the same configuration is still stable for a neutral squirmer in the lubrication approximation. In contrast, pushers and pullers, switch their stable configurations going from the near field to the far field. The magnitude of β also has an effect: Weak pushers and pullers have an upright stable orientation, just like neutral squirmers. For pullers, the unstable fixed point at $\vartheta_2^* = \pi$ becomes stable beyond a threshold $\beta > \frac{2R}{3z}$ which depends on the distance. However,

Table 4.1: Stable orientation angle ϑ^* for different squirmer types from lubrication theory and in far-field approximation.

ϑ^*	lubrication	far field
pusher	0 π if $\beta < -1$	$\operatorname{acos}\left[\frac{2}{3\lvert\beta\rvert}\frac{R}{z}\right]$ if $\lvert\beta\rvert > \frac{2R}{3z}$ 0 otherwise
neutral	0	0
puller	0 if $\beta < 1$ $\operatorname{acos}\beta^{-1}$ if $\beta > 1$	0 π if $\beta > \frac{2R}{3z}$

this threshold is rather low. The pullers in our study exceed this value and therefore have two stable orientations. In contrast, for all but very weak pushers, the upright orientation becomes unstable and the only stable orientation ϑ_3^* has a tilt against the vertical, which gets stronger for higher values of $|\beta|$.

Stable orientations with torque due to bottom-heaviness

Bottom-heaviness extends the range of the stable upright orientation in both the near and the far field. For simplicity, we neglect the height dependence of the bottom-heavy angular velocity. This results in a quantitative error, particularly in the near field, but still illustrates the consequences of the external torque well. We have calculated the wall-induced angular velocity in Eq. (4.16) to $-\frac{3}{4}r_0/(R\alpha)v_0/R\sin\vartheta$. Adding this term to the angular-velocity balance yields new angular fixed points

$$\vartheta_1^* = 0, \quad \vartheta_2^* = \pi, \quad \vartheta_3^* = \arccos\left[\frac{2R}{3\beta z} + \frac{8}{3\beta}\frac{r_0}{R\alpha}\left(\frac{z}{R}\right)^3\right] \tag{4.31}$$

in the far field, as well as

$$\vartheta_1^* = 0, \quad \vartheta_2^* = \pi, \quad \vartheta_3^* = \arccos\left[\frac{1}{\beta} + \frac{1}{2\beta}\frac{r_0}{R\alpha}\right] \tag{4.32}$$

in the lubrication regime. We again arrive at the vertically up- and down-pointing configurations ϑ_1^* and ϑ_2^*, as well as a solution with a tilted angle ϑ_3^*. In comparison to the solutions at zero torque [see Tab. 4.1], the third angle is smaller, *i.e.*, the squirmer orientation is more vertical. The stability conditions ϑ_3^*, as well as for $\vartheta_2^* = \pi$ change to

$$|\beta| > \frac{2R}{3z} + \frac{8}{3}\frac{r_0}{R\alpha}\left(\frac{z}{R}\right)^3 \tag{4.33}$$

in the far field, and

$$|\beta| > 1 + \frac{1}{2}\frac{r_0}{R\alpha} \tag{4.34}$$

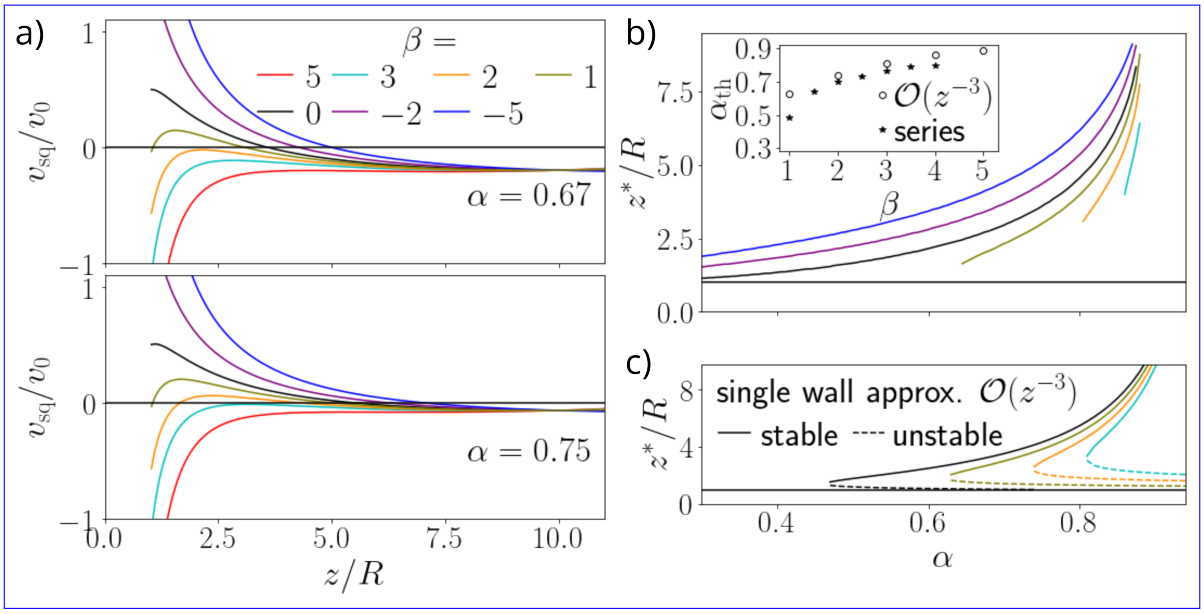

Figure 4.4: a) Total vertical velocity at $\cos\vartheta = 1$ for $\alpha = 0.67$ (top) and $\alpha = 0.75$ (bottom) *versus* height z. We use the series expansion Eq. (2.110) for the hydrodynamic friction and the far field approximation for the the squirmer flow field. b) Stable heights calculated from the total vertical velocity at $\cos\vartheta = 1$. c) Stable and unstable solutions for $v_{\mathrm{sq}} = 0$ using the simpler approximation of Eq. (4.15). Solid lines represent the stable heights. Inset in b) Threshold values α_{th} for both approximations.

in the near field, respectively.

Clearly, for high values of the rescaled torque $r_0/(R\alpha)$, the upright orientation becomes the only stable one for all squirmer types in the far field. Closer to the wall, the condition in the lubrication regime suggests that viscous torques can compete with the external torque at smaller values of β since typical values for the rescaled torques are $0 < r_0/(R\alpha) < 1$.

Stable heights

Depending on the stable orientation, different stable heights z^* can be reached by the squirmer, such that we obtain the fixed point (z^*, ϑ^*) of the whole dynamical system. The first and most important case is that of vertically oriented squirmers $\vartheta^* = 0$. Here, the active velocity and the sedimentation velocity are directly opposed to each other, while the hydrodynamic interaction velocity v_2 depends on the squirmer type. Since $v_1(z)$ increases with height z, a fixed point can appear for $\alpha < 1$, as we have described above. This floating height is further influenced by the sign and strength of v_2. We quantify these insights in Fig. 4.4 a), where we plot the squirmer velocity, using the far field approximation for v_2. Here, we have used the series expansion of Eq. (2.110) for the friction coefficient in order to be more precise, and truncated the sum at the $n = 10$ term. We change the velocity ratio α from the value 0.67 in the top to 0.75 in the bottom plot by decreasing the gravitational acceleration. For $\beta = 1$ and lower, the

stable fixed point, *i.e.*, the zero of the curve where the slope is negative, is shifted to larger values of z. Furthermore, for $\beta = 2$ (orange curve) no stable height exists for $\alpha = 0.67$ but appears at $\alpha = 0.75$, since only then the self-propulsion velocity starts to exceed the effective sedimentation velocity close to the wall. We determined the floating heights over a wide range of α and show them in Fig. 4.4 b). We see that for pullers, a threshold value for α has to be overcome until a stable floating height can exist. This threshold value α_{th} depends on β.

This property can be nicely illustrated for the simpler approximation of the one-wall mobility used in Eq. (4.15), up to the order $\mathcal{O}(z^{-3})$. Setting the vertical velocity to zero leads to the equation

$$1 - 1/\alpha\kappa(z) + \frac{1}{2}\left(\frac{R}{z}\right)^2\left[-\frac{9}{8}\beta - \frac{R}{z}\right] = 0 \tag{4.35}$$

which yields a cubic equation for z. The number of positive, real-valued solutions displays a bifurcation behaviour. In particular, in the lower half of the system, the number of fixed points change from 0 to 2, controlled by the parameter α. One of the appearing fixed points is stable and the other one is unstable. Figure 4.4 c) shows the stable and unstable manifolds, and the stable ones agree qualitatively with Fig. 4.4 b). However, neutral squirmers (solid black line) in the approximation from Eq. (4.35) lose their stable fixed point around $\alpha \approx 0.5$, while this is not the case for the series expansion in Eq. (2.110) which was used in the main plot of Fig. 4.4 b). In simulations, we later show that the latter prediction is correct. In the inset of Fig. 4.4 b) we show the resulting values for the threshold α_{th}, which also shows quantitative differences between the two approximations. In both cases, α_{th} increases monotonically with β, but does no longer exist for strong pullers. The maximum values are $\beta = 4$ for the truncated series expansion and $\beta = 5$ for the simpler approximation up to order z^{-3}. The reason for this is that upright pullers are hydrodynamically attracted to the bottom wall and thus cannot escape it. This prevents floating.

We also show the stable heights of pushers in Fig. 4.4 b) (blue and purple curves), using the orientation $\cos\vartheta = 0$. Note however that this does not reflect a stable far field solution for the pusher, unless an external torque is applied.

For $\vartheta^* = \pi$, both self-propulsion and gravity act downwards. Therefore, unless there is a strong hydrodynamic repulsion, the analytical model predicts the squirmer to crash into the wall.

The tilted orientations that arise as stable configurations in both the near and the far field under certain conditions (see Tab. 4.1), have a small positive z component, resulting only in weak up-swimming. Thus, the sedimentation velocity is dominating and the squirmer collides with the wall, as well. We can conclude that a stable upright orientation, induced by the bottom wall, is a necessary condition for the appearance of a floating height in the squirmer system.

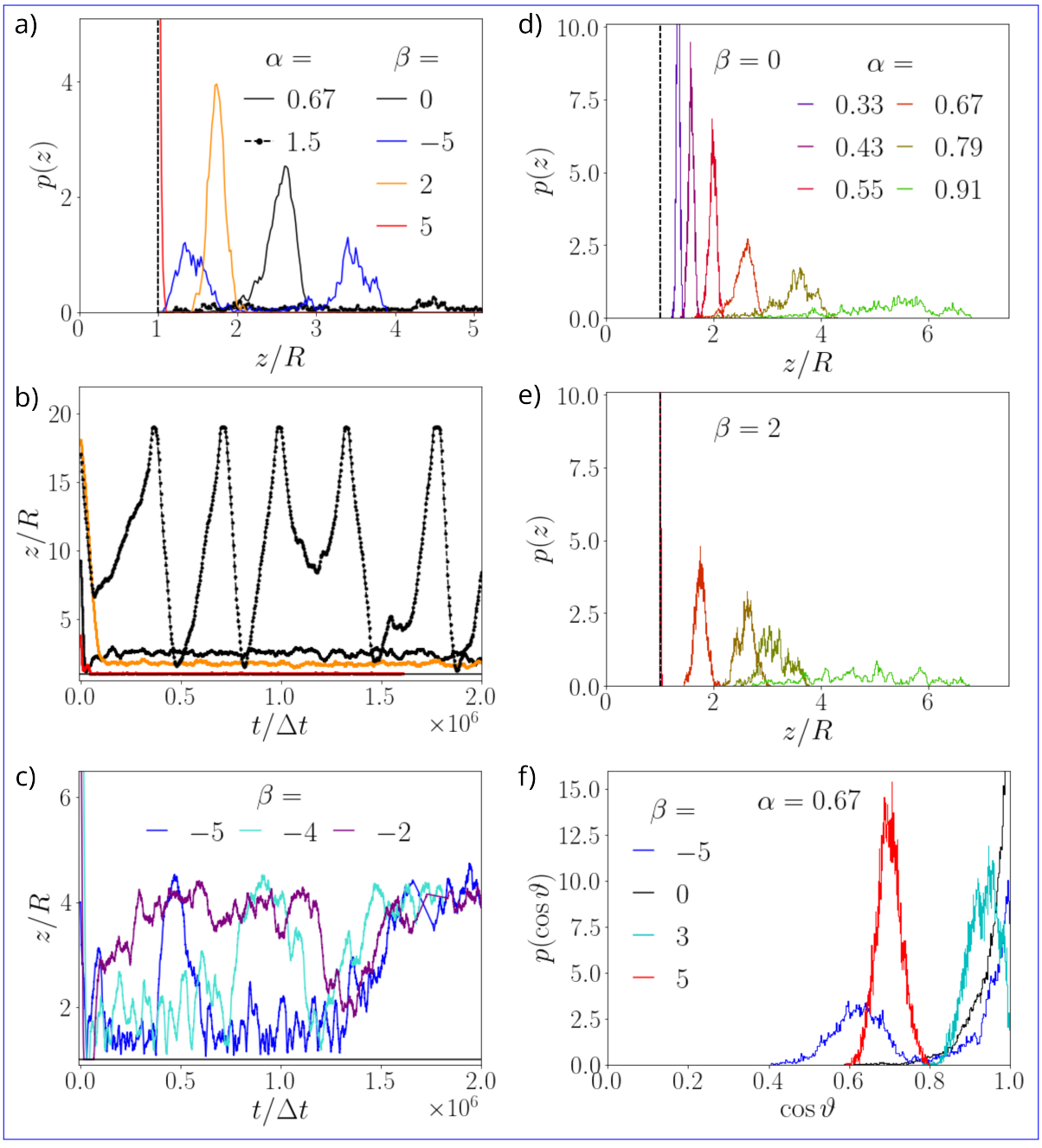

Figure 4.5: a) Height distributions $p(z)$ of typical squirmer states. b) Vertical part of the corresponding trajectories $z(t)$. c) Trajectories $z(t)$ for pushers with $\beta = -5$, -4, and -2 at $\alpha = 0.75$, showing the alternation between floating and wall sliding. d) Height distributions $p(z)$ of neutral squirmers for different values of α. (e) Height distributions $p(z)$ of pullers with $\beta = 2$ for different values of α . f) Distributions $p(\cos\vartheta)$ of vertical orientation $\cos\vartheta$ for $\alpha = 0.67$ for recurrent floating ($\beta = -5$) and wall-pinned states ($\beta = 3$ and $\beta = 5$).

4.3 Numerical results

The analysis performed in the last section used the multipole approximation of the squirmer in order to capture its behaviour far from the wall, and the angular velocity in the lubrication regime for the behaviour close to the wall. In order to probe how the squirmer actually behaves in a low-Reynolds-number fluid, we use the method of multi-particle collision dynamics (MPCD). As introduced, this method includes thermal fluctuations, which were ignored until this point. In our simulations, we vary the squirmer parameter β and the velocity ratio α. We present the different types of trajectories that appear from the different combinations of these parameters. We do not take the rotlet dipole component into account at this point, since it neither contributes to the wall-induced velocity nor to the vertical orientation [87].

4.3.1 Cruising trajectories

We start with a neutral squirmer, whose active velocity is larger than the bulk sedimentation velocity, *i.e.*, $\alpha > 1$. Then, the trajectory alternates between the top and the bottom wall and is not constrained to the bottom wall by gravity. In Fig. 4.5 a) we see the resulting height distribution for $\alpha = 1.5$, which is flat and approximately constant (dashed black line with dots). The alternation is clearly visible in the cruising trajectory in Fig. 4.5 b). It occurs because the neutral squirmer orients upwards at the bottom wall and downwards at the top wall. The downward motion from the top wall is faster than the upward motion, since here self-propulsion and gravity cooperate, whereas they compete for upward motion. This is also visible in Fig. 4.5 b). Furthermore, around $t \approx 1.25 \cdot 10^6 \Delta t$ the squirmer turns around in the center of the simulation box, beyond the influence of the bottom wall. This results from a reorientation due to rotational noise, which also influences the trajectories.

4.3.2 Stable floating

For values of $0 < \alpha < 1$, the active velocity is weaker than the bulk sedimentation velocity. Following our analytical results, a vertical velocity balance can be reached for neutral squirmers and pullers, characterized by the orientation $\vartheta^* = 0$ and the floating height z^*. This is confirmed by the squirmers' height distributions for $\beta = 0$ and $\beta = 2$, which peak at a finite distance above the wall. The same is shown by the corresponding trajectories in Fig. 4.5 b). Figs. 4.5 d) and e) show the height profiles for $\beta = 0$ and $\beta = 2$, respectively and at different α. As expected, the floating height increases with increasing α. Furthermore, the height fluctuations increase as well, as can be seen from the broader histograms. Note that these height fluctuations do not result from translational noise, but rather rotational noise driving the orientation away from the vertical. This impacts the velocity balance and can cause the squirmer to sink. The wall induces a counteracting angular velocity, which directs the squirmer back to the vertical. It takes the squirmer longer to regain its upright orientation at larger heights, because this angular velocity gets weaker.

In Fig. 4.6 a) we show the average vertical orientations for the floating steady state.

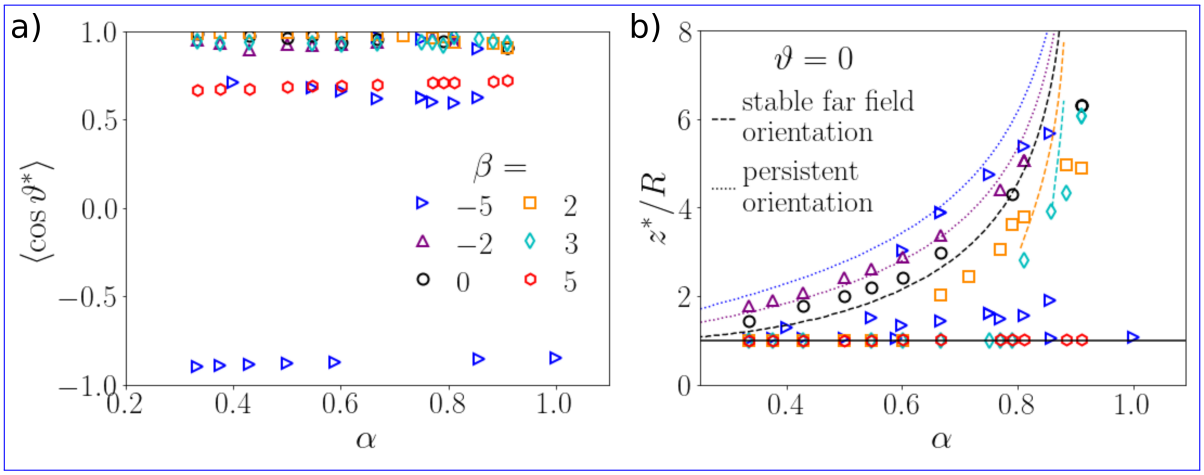

Figure 4.6: a) Mean stable orientation $\langle \cos \vartheta^* \rangle$ and b) stable and metastable heights z^* determined from numerical simulations plotted at different values of β and *versus* α. The height z^* can refer to floating, sliding, and wall-pinned heights. Dashed and dotted lines: floating heights from theory, using $\vartheta = 0$, which is a stable far field orientation for neutral squirmers and pullers, and a persisting near field orientation for recurrent floating of pushers.

Indeed, squirmers are almost perfectly vertical at $\beta = 0$ and $\beta = 2$. For the measurement of the floating height z^*, we choose the maximum height observed. This is a good estimation for the height where all deterministic vertical velocities cancel, since the translational thermal fluctuations are not very strong. We show the values of z^* in Fig. 4.6 b).

The floating heights of pullers are lower than for neutral squirmers at the same value of α. The reason for that is that their flow field attracts them to the bottom wall, as shown by the far field approximation. Furthermore, for pullers we observe that α needs to exceed a threshold value α_{th} in order for floating to happen, and thus for the stable fixed point to exist. This confirms the prediction made by the analytical calculations in the previous section, and can be seen in the density profiles in Fig. 4.5 e), where the density at low α is concentrated at the bottom wall. We call this the *wall-pinned* state. The thresholds α_{th} can be seen in Fig. 4.6 b) for $\beta = 2$ and $\beta = 3$. Clearly, α_{th} increases with the squirmer parameter β. Finally, for $\beta = 5$, we do not observe floating any more, but only wall-pinned squirmers.

4.3.3 Wall pinning

As we have seen, pullers assume a wall-pinned state below the threshold value $\alpha = \alpha_{\text{th}}$, and strong pullers do not escape from this state. For wall-pinned states, we plot the average heights and not their respective maxima in Fig. 4.6 b). Due to the short distance to the wall, we expect the average orientations to deviate from the far field approximation. While for $\beta = 2$, they stay very vertical and only slightly tilt for $\beta = 3$, we find $\langle \cos \vartheta^* \rangle \approx 0.7$ for $\beta = 5$. We show distributions of the vertical orientation $\cos \vartheta$ for the case $\alpha = 0.67$ in Fig. 4.5 f), where these average values for the cases $\beta = 3$

and $\beta = 5$ correspond to the peaks of their respective distributions. Compared to the neutral squirmer, the orientations of the puller squirmers tilt away from the vertical, which is an effect of the near field regime. However, the measured angle does not reproduce the prediction from lubrication theory in Tab. 4.1, which yields $\cos\vartheta^* = 0.2$ for $\beta = 5$ and $\cos\vartheta^* = 0.33$ for $\beta = 3$.

In addition, we observe a wall-pinned state for strong pushers with $\beta = -5$, as can be seen from the blue triangles around $z = R$ in Fig. 4.6 b). Fig. 4.6 a) shows that the pushers point down towards the wall, almost vertically. This again reveals the influence of near-field hydrodynamics. In this case, the prediction from lubrication theory $\vartheta^* = \pi$ (see Tab. 4.1) is recovered relatively well, since $\langle\cos\vartheta^*\rangle \approx -1$ in Fig. 4.6 a).

4.3.4 Recurrent floating and sliding

Interestingly, pushers have bistable states, as we show for the case $\beta = -5$ in the density profile in Fig. 4.5 a). In this state, they can both reside close to the wall or float above the wall, which is visible for long simulation times. In Fig. 4.5 c) the height variations for three pushers with $\beta \in \{-5, -4, -2\}$ are shown, depicting alternations between the floating height and a position close to the wall. The distribution of the vertical orientation for a pusher with $\beta = -5$ in Fig. 4.5 f) also shows bistability, with a vertical and an upwards tilted orientation. These two orientations are also depicted in Fig. 4.6 a) over a wide range of α. The tilted angle of the pusher when it is closer to the wall leads to horizontal motion. Hence, we call this behaviour *wall-sliding*.

Fig. 4.6 b) shows that a pusher's height during the floating phases is larger than that of floating neutral squirmers and pullers, consistent with the far field approximation. This approximation also predicts that the upright orientation $\cos\vartheta = 1$ is not stable for pushers. Thus, in contrast to neutral and puller squirmers, pushers can be driven out of the floating state by thermal fluctuations or the wall-induced angular velocity. Consequently, they eventually sink down to the wall. Here, they adopt a tilted angle, shown in Fig. 4.5 f), and slide horizontally along the wall. Therefore, we call this state *recurrent floating and sliding*. For $\beta = -2$, the floating is recovered after a short excursion to the bottom wall, as can be seen in Fig. 4.5 c). Thus, the difference between floating and sliding states is not clearly established here, and we only plot the floating heights in Fig. 4.6 b) and not the sliding heights.

The value of the tilt angle matches the prediction of far field hydrodynamics, but not quantitatively. For the sliding heights at $\beta = -5$, which are around $z = 1.5R$, the expected far-field stable angle is almost horizontal, whereas we measure $\cos\vartheta = 0.6$. But note that the lubrication approximation dictates a vertical orientation, therefore it is likely that the sliding angle results from a cross-over between both regimes.

Finally, we note that no transition between recurrent floating and downward wall-pinned states could be observed for pushers, even though both can occur in the same parameter range in Fig. 4.6. We think the reason for this is that the thermal energy required for this transition occurring randomly is too large.

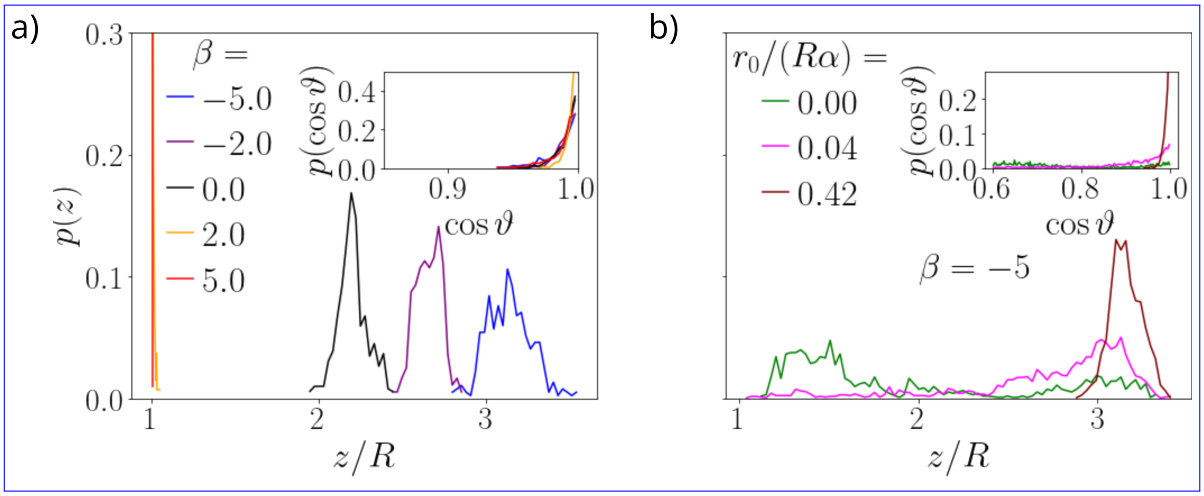

Figure 4.7: a) Height distributions of single squirmers at $\alpha = 0.6$ with a dimensionless gravitational torque of $r_0/(R\alpha) = 0.21$. b) Height distributions for pushers with $\beta = -5$ at different rescaled torques. Insets: Distributions of vertical orientations $\cos\vartheta$.

4.3.5 Influence of bottom-heaviness

Fig. 4.7 a) illustrates the influence of a gravitational torque due to bottom-heaviness on the single squirmer states using $\alpha = 0.6$, by showing the distributions of height z at different squirmer parameters β. The inset shows the distributions of $\cos\vartheta$ from which we see that squirmers are strongly vertical. Neutral squirmers keep their floating state and pushers acquire a stable floating state, as expected. There is no recurrent wall sliding, since the external torque stabilizes the vertical orientation. In Fig. 4.7 b) we show the transition of the pusher system from the bistable to the floating state. Without the external torque (green curve), the squirmer spends more time in the sliding state, since α is relatively low. This reverses already at a weak rescaled torque $r_0/(R\alpha) = 0.04$ (magenta curve). While the squirmer has a low probability of sinking to the wall, it is more likely to float. At high torque $r_0/(R\alpha) = 0.42$, the floating height is completely stable (brown curve). The maximum heights of all three systems agree well with each other. The inset shows the development of the strong directional bias in the angular distribution.

Since the systems in Fig. 4.7 a) are below the threshold α_{th} for the pullers with $\beta = 2$ and $\beta = 5$, they do not show floating, even under an external torque. This is because the wall-pinned state is a consequence of the hydrodynamic attraction to the wall and not of the squirmer orientation. In fact, a more vertical orientation even increases the attraction to the bottom wall. As a consequence, the pinning is very strong, as suggested by the density profiles.

4.4 Discussion

4.4.1 Comparison of simulation and theory

As mentioned above, stable upright orientations occur in simulations of neutral squirmers and pullers, as predicted by the far field analysis. Furthermore, close to the bottom wall we find states with orientation vectors tilted against the vertical. While the angles do not fit exactly, wall-pinned states are expected from the stable orientations we have calculated. In particular, in the lubrication regime, wall-pinned pusher squirmers should point towards and puller squirmers point away from the wall, with a tilt increasing with β. For strong pullers the simulation results quantitatively differ from the calculations, in that the tilt is weaker than expected. We note that neutral squirmers point away from the wall also in the near field, thus they also turn around at the top wall. This explains their cruising behaviour at $\alpha > 1$, where they never get stuck at a wall.

The threshold of α for pullers is recovered nicely in our simulations and separates wall-pinned states from floating states. Furthermore, we can see in Fig. 4.6 b) that α_{th} increases with β as expected. We have superimposed the analytical predictions for the floating heights (see Fig. 4.4 b)) into Fig. 4.6 b) as dashed and dotted lines. The predictions fit the simulation results fairly well. However, the calculated thresholds for $\beta = 2$ and $\beta = 3$ do not coincide, since the simulated squirmers are able to float at lower value than the analytical curves suggest.

We have distinguished between floating with a stable far-field orientation $\vartheta = 0$ (dashed lines) and a persistent orientation of $\vartheta = 0$ (dotted lines). The reason for this distinction is that only for neutral squirmers and pullers floating actually appears as a stable fixed point of the system, particularly in the far field. Consequently, the fixed point analysis explains stable floating for $\beta \geq 0$, whereas floating for pushers does not come out of the analytical calculations. Therefore, we further consider the pusher dynamics in the following.

4.4.2 Interpretation of pusher dynamics

Wall sliding Our simulations confirmed that the vertical orientation is not stable for the pusher in the far field. However, a stable orientation $\vartheta = 0$ pointing away from the wall is predicted in lubrication approximation, while in our simulations a finite average sliding angle is observed in the cross-over regime between near and far field. Note that the left peak of the bimodal angular distribution of the strong pusher in Fig. 4.5 f) is relatively broad, implying strong fluctuations around the mean sliding angle. Indeed, Fig. 4.5 e) shows strongly varying up-and-down motion in the sliding regime $1 < z/R \lessapprox 3$. We also see that stronger pushers have smaller sliding heights.

Persistent pusher orientation Due to random fluctuations and near field interactions, pushers can eventually assume a vertical configuration close to the bottom wall, which allows them to escape it. Pushers swim up until they reach their floating height, however the vertical orientation is not stabilized in the far field. Therefore, reaching the

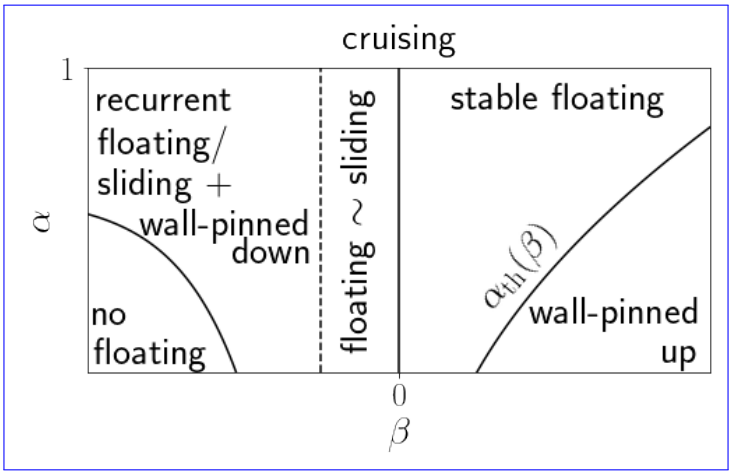

Figure 4.8: Qualitative sketch of the single squirmer state diagram.

floating height is only possible due to the directional persistence of the pusher squirmer. Eventually, the orientation rotates away from the vertical and the pusher sinks down again. We call the vertical direction a *persistent orientation* in this case, in contrast to pullers and neutral squirmers, where it is a fixed point of the angular velocity in the far field.

Recurrent floating is limited to higher values of α for strong pushers: We do not observe the recurrent floating at $\beta = -5$ for $\alpha \lesssim 0.5$, as can be seen in Fig. 4.6 b). This is understandable since stronger gravity requires a more vertical configuration for up-swimming, which makes the transition to floating less probable. While the wall-sliding state is extractable from our analytical considerations, the floating state and the recurrent alternations between both states are not. This underlines the importance of combining both the near and far field picture, as well as the potential of thermal fluctuations in active systems.

4.5 Conclusions

We studied the dynamics of a single squirmer microswimmer under gravity in wall proximity, using both analytical calculations and numerical simulations. In spite of the simplicity of the system, we observed a considerable variety of states. For the deterministic vertical dynamics of the squirmer, we identify the three contributions of active motion, height-dependent sedimentation and the squirmer's own flow field, reflected by the no-slip wall. These are complemented by translational and more importantly rotational noise in MPCD simulations.

We summarize the states found in our simulations in Fig. 4.8 in a qualitative sketch with the axes α and β. For the velocity ratio $\alpha > 1$, we observe trajectories cruising back and forth between the top and bottom walls. When $\alpha = v_0/v_{\mathrm{sed}} < 1$ we find that the balancing of active velocity and the height-dependent sedimentation velocity creates a stable floating height. These floating heights are indeed realized for neutral squirmers and pullers, because the vertical orientation is stabilized by far field vorticities arising

from the interaction of the squirmer with the wall. Furthermore, the reflected flow field changes the velocity of the squirmer. For upright pullers it creates an effective attraction, which prevents floating when it becomes too strong. We find in calculations and confirm in simulations that a threshold α_{th} exists, below which pullers do not float. This threshold increases with β, and for values above $\beta = 4$ no floating is observed. Instead, pullers are pinned to the wall with a slightly tilted orientation. The tilt we observe is smaller than expected from lubrication theory. Wall-pinned states also exist for pushers that point towards the wall, in agreement with the theoretical lubrication torque.

We observe floating pushers, as well, but this state is not stable for long times. The upright orientation is not a fixed point of the pusher's angular velocity, unless a bottom-heavy torque is applied. Thus, pushers orient away from the vertical orientation and sink to the bottom wall. There, they enter a wall-sliding state, until they are oriented again along the vertical by fluctuations and near field hydrodynamics. A high orientational persistence due to high active Péclet numbers allows this vertical state to survive for a considerable time and the pusher can reach its floating height again. Thus, pushers have a bistable configuration alternating between recurrent floating and sliding phases. Floating for strong pushers only exists for high enough values of α, such that they are able to escape the bottom wall.

Our simulations underline the importance of hydrodynamic interactions, in particular, how both near-field and far-field regimes are important. Furthermore, the ingredients of thermal noise, no-slip walls, and gravity are ubiquitous components of microswimmer systems. Therefore, our results are relevant for future experimental and computational studies. In particular, our system can serve as a basis for modifications and additions, such as phoretic effects [91, 175, 270] or complex fluids [76].

5. Gyrotaxis of a squirmer pair

One of the most important effects of the hydrodynamic flow fields of squirmers that we have introduced are their interactions with other swimmers. We use this chapter to briefly discuss the dynamics of a pair of bottom-heavy neutral squirmers under gravity, in order to prepare the later investigations of the collective dynamics at large squirmer numbers. Particularly, the phenomenon of gyrotaxis is important, leading for example to focussing in Poiseuille flow [15] or vertical trapping of cells [271].

5.1 Hydrodynamic interactions

Squirmers in our study are subject to a gravitational force, a gravitational torque, as well as flow originating from other squirmers. In the following, we calculate the flow fields and their vorticities in bulk.

5.1.1 Flow fields

From a far-field perspective, the hydrodynamic signature of a squirmer can be expressed by multipoles. The multipoles in our system are, first, a stokeslet and source dipole due to the gravitational force acting on the squirmer, expressed by Eqs. (4.6)-(4.8), second, a rotlet from bottom-heaviness, described by Eq. (4.9), and, third, the flow multipoles induced by the free squirmer at position $\mathbf{r}_1$. The field of the free squirmer $\mathbf{u}_{\text{free}}(\mathbf{r}-\mathbf{r}_1)$ is noted in Eq. (2.98) and consists of force dipole, rotlet dipole, and source dipole contributions. In order to calculate the induced velocity $\mathbf{v}_{\text{hd}}^{(2)}$ of a second squirmer at position $\mathbf{r}_2$, we use Faxén's law, and keep terms up to the order r^{-3}. Then we arrive at

$$\mathbf{v}_{\text{hd}}^{(2)} = \mathbf{u}_{\text{free}}(\mathbf{r}_2-\mathbf{r}_1)+\mathbf{u}_{\text{g}}(\mathbf{r}_2-\mathbf{r}_1)+\frac{R^2}{6}\nabla^2\mathbf{u}_{\text{g}}(\mathbf{r}_2-\mathbf{r}_1)+\mathbf{u}_{\text{bh}}(\mathbf{r}_2-\mathbf{r}_1)+\mathcal{O}\left(|\mathbf{r}_2-\mathbf{r}_1|^{-4}\right). \quad (5.1)$$

We note that the term $\nabla^2\mathbf{u}_{\text{g}}(\mathbf{r}_2-\mathbf{r}_1)$ creates another source dipole contribution. We ignore the terms $\nabla^2\mathbf{u}_{\text{free}}$ and $\nabla^2\mathbf{u}_{\text{bh}}$ because they decrease faster with distance than r^{-3}. Hydrodynamic interactions between squirmers strongly depend on the squirmer type, in particular, on the force dipole components included in $\mathbf{u}_{\text{free}}$. Two pullers attract each other, when they are in a head-to-head, head-to-tail or tail-to-tail configuration, whereas two pushers repel each other in these cases [37]. The pushers attract each other when they swim next to each other with parallel orientation vectors.

5.1.2 Flow vorticity

The flow vorticities induced by squirmers play an important role for gyrotaxis. The vorticity is defined as

$$\boldsymbol{\omega}(\mathbf{r}) := \nabla \times \mathbf{u}(\mathbf{r}). \tag{5.2}$$

We now calculate the flow vorticities of the involved multipoles. The stokeslet component $\boldsymbol{\omega}^{\mathrm{S}}$ results from the gravitational force $\mathbf{u}_{\mathrm{g}}^{\mathrm{S}}$ in Eq. (4.7) and the rotlet component $\boldsymbol{\omega}^{\mathrm{R}}$ from the flow field induced by the external torque Eq. (4.9). The flow field induced by the squirmer, shown in Eq. (2.98), results in force dipole and rotlet dipole vorticities $\boldsymbol{\omega}_{\mathrm{D}}$ and $\boldsymbol{\omega}_{\mathrm{RD}}$. Source dipole fields are vorticity-free and do not contribute. All in all, we have the vorticities

$$\begin{aligned}
\boldsymbol{\omega}_{\mathrm{S}} &= \frac{3}{2} v_{\mathrm{sed}} \frac{R}{r^2} \hat{\mathbf{r}} \times \mathbf{e}_z && (5.3)\\
\boldsymbol{\omega}_{\mathrm{R}} &= \frac{3}{4} v_0 \frac{r_0}{R\alpha} \frac{R^2}{r^3} \left(2\mathbf{e} \times \mathbf{e}_z - 3 \left((\mathbf{e} \cdot \hat{\mathbf{r}}) \hat{\mathbf{r}} \times \mathbf{e}_z - \frac{z}{r} \hat{\mathbf{r}} \times \mathbf{e} \right) \right) && (5.4)\\
\boldsymbol{\omega}_{\mathrm{D}} &= -\frac{9}{2} v_0 \beta \frac{R^2}{r^3} (\mathbf{e} \cdot \hat{\mathbf{r}}) (\mathbf{e} \times \hat{\mathbf{r}}) && (5.5)\\
\boldsymbol{\omega}_{\mathrm{RD}} &= -\frac{27}{2} v_0 \chi \frac{R^3}{r^4} \left(2(\mathbf{e} \cdot \hat{\mathbf{r}}) \mathbf{e} + \left(1 - 5 (\mathbf{e} \cdot \hat{\mathbf{r}})^2 \right) \hat{\mathbf{r}} \right) && (5.6)\\
\boldsymbol{\omega}_{\mathrm{SD}} &= 0. && (5.7)
\end{aligned}$$

The above vorticities induce an angular velocity on a neighboring squirmer, which we call $\boldsymbol{\Omega}_{\mathrm{hd}}^{(2)}$. If we assume the position $\mathbf{r}_2$ for the second squirmer, the induced angular velocities is

$$\boldsymbol{\Omega}_{\mathrm{hd}}^{(2)} = \frac{1}{2} \boldsymbol{\omega}(\mathbf{r}_2 - \mathbf{r}_1), \tag{5.8}$$

where $\boldsymbol{\omega} = \boldsymbol{\omega}_{\mathrm{S}} + \boldsymbol{\omega}_{\mathrm{R}} + \boldsymbol{\omega}_{\mathrm{D}} + \boldsymbol{\omega}_{\mathrm{RD}}$ is the sum of the above vorticities. The contribution with the longest range is the stokeslet vorticity. It reorients a neighboring squirmer towards the sinking squirmer. Due to the squirmers' self-propulsion this leads to an effective attraction between them. The rotlet component $\boldsymbol{\omega}_{\mathrm{R}}$ is typically small, as we discussed before, since it disappears for the vertical configuration $\mathbf{e} \to \mathbf{e}_z$. The force dipoles again cause strong differences in dynamics: A puller dipole induces a reorientation that aligns a neighbor's orientation parallel or antiparallel to the distance vector. In contrast, two pushers tend towards orientation vectors that are perpendicular to the distance vector [37]. We can understand this behaviour from the term $-(\mathbf{e} \cdot \hat{\mathbf{r}}) (\mathbf{e} \times \hat{\mathbf{r}})$ in Eq. (5.5). Its magnitude is $-\sin\psi \cos\psi$ if ψ is the angle between the orientation vector and the distance vector. The resulting minima of the angular velocity at $\psi = 0$, $\pi/2$, and π cause the pair configurations of puller and pusher dipoles, where $\psi = 0$ and $\psi = \pi$ are stable for pullers and $\psi = \pi/2$ is stable for pushers.

The vorticity induced by the rotlet-dipole term decays with r^{-4} and we therefore neglect it. Importantly, the source dipole field is vorticity-free, which means that neutral squirmers do not reorient each others via their propulsion fields.

5.2 Balance of angular velocities

The competition of hydrodynamic torques with the external torques determines the resulting angular velocity for every orientation and position of a squirmer. Using the flow vorticities introduced above, we offer some estimates for the two-squirmer system in the following.

Here, we assume that both squirmers are at the same height and have a lateral distance Δx. Their tilting angle against the vertical is, to leading order, determined by the stokeslet vorticity of Eq. (5.3) and the angular velocity Ω_{bh} caused by the external torque [see Eq. (4.18)]. Balancing both terms in this particular configuration leads to

$$\frac{3}{4}\frac{v_0}{R}\frac{r_0}{R\alpha}\sin\vartheta = \frac{3}{4}\frac{v_0}{\alpha}\frac{R}{\Delta x^2}\,. \tag{5.9}$$

The closest possible distance is $\Delta x = 2R$. For this distance, we can identify the angle at which both terms are momentarily in balance. This angle ϑ_0 is given by

$$\sin\vartheta_0 = \frac{1/(4\alpha)}{r_0/(R\alpha)}\,. \tag{5.10}$$

Thus, a lower bound for the nondimensional gravitational torque in order to compete considerably against viscous effects is given by

$$r_0/(R\alpha) \geq 1/(4\alpha). \tag{5.11}$$

Gyrotactic effects arise in a regime where external and hydrodynamic torques are comparable. The above calculations provide us with an estimate of when this is the case, *i.e.*, how large the external torque has to be.

5.3 Coupled oscillations

Considering all hydrodynamic contributions is not necessary in order to induce complex behaviour. A two-swimmer system interacting only via stokeslet vorticity and under the influence of external force and torque has been considered by Drescher *et al.* [61]. Their dynamical system shows coupled oscillations which nicely describe the experimental observations of 'dancing' Volvox algae [61, 272]. We here reproduce the oscillatory trajectories with a two-squirmer system.

Figure 5.1 a) shows snapshots of our system of two neutral squirmers at $\alpha = 0.8$. As we have seen in Chapter 4, neutral squirmers float several radii above the bottom wall at this value. Due to bottom-heaviness, the initial orientations of both squirmers is vertical in the beginning (first snapshot), *i.e.*, the polar tilt angle ϑ shown in the last snapshot is close to zero. The subsequent dynamics offer an illustration of the gyrotactic mechanism: Stokeslet vorticities incline the orientation vectors of both squirmers towards each other (second snapshot). Then, active self-propulsion results

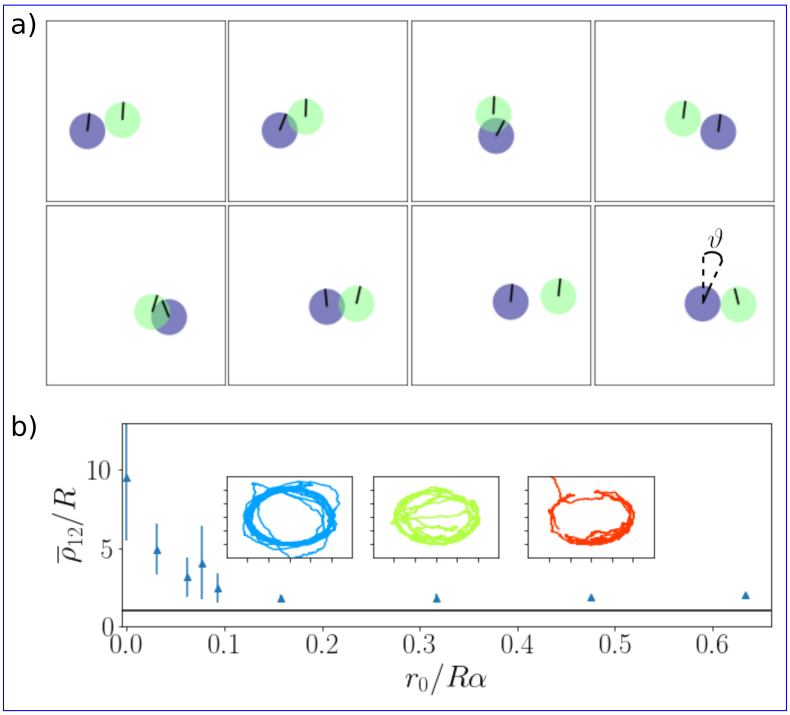

Figure 5.1: a) Snapshots of a squirmer pair performing coupled oscillations above the bottom wall. The simulations used the parameters $\alpha = 0.8$ and $r_0/R\alpha = 0.16$. Replicated from [C]. b) Average distance $\overline{\rho}_{12}$ between pairs *versus* rescaled torque. Insets show the distance vector $(\Delta x, \Delta y)$ between both squirmers in the plane.

in a rapprochement. Eventually, both squirmers pass each other (snapshots 3 and 4)[1]. The squirmer with the stronger tilting sinks to a lower height and swims slightly underneath the other squirmer. After the squirmers have switched places, the direction of the vorticity interaction is reversed and thus the reciprocal motion starts (snapshots 5-8).

The external torque is decisive for the periodicity of the motion. Without or with a weak torque, the distance of the squirmers continues to increase after they have passed each other and no oscillation occurs, in agreement with Ref. [61]. Thus, the tendency of both squirmers to orient upwards stabilizes the pair, and keeps the distance between both squirmers limited. Consequently, for larger torques, the oscillation amplitude becomes smaller. We show this in Fig. 5.1 b), where the time average over the squirmer-squirmer distance is plotted. Furthermore, the insets over selected data points show the trajectory of the planar distance vector $(\Delta x, \Delta y)$. Interestingly, we continue to observe pair formation also at large torques, thus the orientations are never completely frozen. This is because the gravitational torque approaches zero for $\mathbf{e} \to \mathbf{e}_z$, as already mentioned. Thus, a small tilt away from the vertical can always be induced by a neighboring squirmer, which leads to horizontal swimming and initiates (small) oscillations.

[1]The overlap seen in the trajectories is due to the projection. The squirmers do not touch or penetrate each other.

6. Emergent collective dynamics of bottom-heavy squirmers

We present MPCD simulations and analysis of the collective motion of bottom-heavy squirmers under gravity. We base the results of this chapter mainly on materials from our original work [B].

6.1 Introduction

Many fascinating phenomena of active systems arise from collective motion [40, 273]. Intriguing novel transitions occur, such as motility-induced phase separation [7], pearling instabilities [115], focussing in channels [15] and plume formation [109, 206]. Collective systems of synthetic swimmers show new states of matter due to tunable orientational or social interactions [161, 163, 274], while biological swimmers self-organize into manifold living patterns, such as biofilms [22, 275] and algal patches [70, 276], or lead to non-equilibrium collective motion, as seen in convective currents under the influence of magnetic forces [277], swarming states [11, 278], and bacterial turbulence [16, 94].

For collective motion under high density, hydrodynamic interactions become particularly relevant [37, 279]. They influence, among other things, the phase separation of squirmers in Hele-Shaw geometry [42, 43, 162], flock formation of rollers [105], synchronization of micro-rotors [280], and circulation of bacterial suspensions [281]. For systems under gravity, the external force induces flows originating at each sinking particle and thus creates additional interactions [198]. Many-body systems of active swimmers under gravity revealed convection of sedimenting squirmers [282] (see also Ref. [D] in list of publications), 'Wigner fluid' states, swarms and chains in monolayers under strong gravity [283] (see also Ref. [E] in list of publications), as well as chiral spinning clusters [284]. For bioconvection, the swimmers' response to gravity and their hydrodynamic interactions are essential, as is demonstrated by gyrotactic plumes of biological organisms [56, 109].

In Chapter 5 we have discussed the pair dynamics of two neutral bottom-heavy squirmers. Here, we expand our system to higher squirmer numbers in order to investigate their collective dynamics, and also consider pushers and pullers. Thus, we increase the squirmer number to 914, while keeping the radius at $R = 4a_0$. Unless otherwise stated, we use a boxsize of $108a_0 \times 108a_0 \times 210a_0$, where the last length refers to the height of the system. This corresponds to a volume fraction of 0.1. Since some

squirmer states are strongly concentrated at the bottom of the system, we also convert this to the mean area fraction in a vertical slab of width $2R$, where the volume fraction of squirmers is equal to the average. This squirmer area fraction is 0.15. However, we stress that the density in some of the observed states is highly inhomogeneous due to collective effects. We initialize the system with an approximately uniform distribution, *i.e.* choose the squirmer initial positions randomly, such that no overlaps between squirmers or with walls occur. The initial orientations are random, too.

In the following, we vary the velocity ratio α and the rescaled torque $r_0/R\alpha$ and find a variety of states that we describe in detail. The phenomenology we found occurred at values $1 < \alpha \lessapprox 7$. Since α decreases quadratically with the radius at constant v_0, a large range of values should be experimentally accessible. Furthermore, α decays linearly with the buoyant mass. The latter can be changed by different materials or by changing the surrounding fluid, where relative density differences have been adjusted in experiments (by mixing H_2O and D_2O) up to $\Delta\rho/\rho = \pm 0.02$ [144]. Likewise, the bottom-heaviness of swimmers varies naturally or can be manipulated by experimentalists. Alternatively, one can introduce a shape-induced gravitational torque, for example, with L-shaped active colloids [59], where the effective lever arm can be controlled.

6.2 State diagram and phenomenology

Figure 6.1 a) shows the state diagram of neutral squirmers. As stated above, the varied parameters are α and $r_0/R\alpha$. We first describe the general properties of the different states before analysing them in a more detailed way. We focus on states with $\alpha > 1$ in this study, *i.e.*, states above the thin dotted horizontal line in Fig. 6.1 a). As shown in Chapter 4, a single neutral squirmer would explore the simulation box on cruising trajectories. The background colors in subfigure a) express the general tendency of the density profile. For the blue regions in the state diagram, the steady state is mainly concentrated in the top region or at the top wall. In the yellow regions, squirmers mainly reside at the bottom wall. In the dark grey region we observe a continuous vertical motion of squirmers. We then classify the simulation data into more specific states: Sedimentation states (yellow stars), inverted sedimentation (blue dots), transient plumes that transition into inverted sedimentation (blue stars), stable plumes and convective rolls (black dots) and spawning clusters (black stars). We have marked four exemplary parameter pairs $(\alpha, r_0/(R\alpha))$ in the state diagram, for which we show the vertical density profile in Fig. 6.1 b) using the same colors. For two of them, we show snapshots in Fig. 6.1 c).

For the classification of the respective states, we have used several criteria. First, we consider the shape of the height profile, as is shown in Fig. 6.1 b). The sedimentation state (red curve) has a characteristic exponential decay over the majority of the system height. The state diagram shows that the sedimentation state occurs for weak torques and $\alpha \lessapprox 3.0$. It was shown in Ref. [282] (see also original work [D] in list of publications) that already at zero torque, the non-equilibrium sedimentation of squirmers has a much larger sedimentation length than passive systems. Furthermore, squirmers can move around considerably, in contrast to sedimentation under thermal noise. We call this

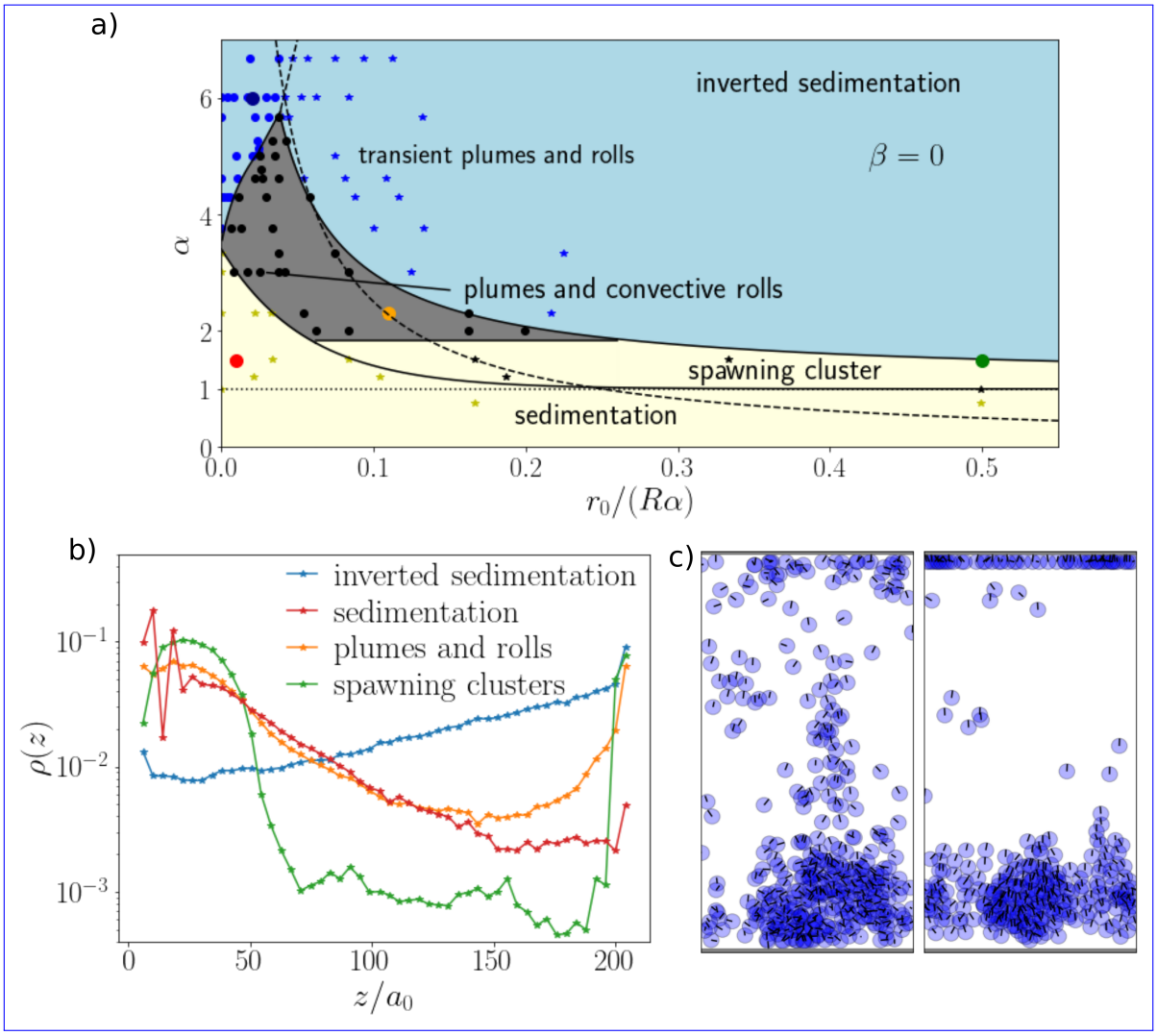

Figure 6.1: a) State diagram of neutral squirmers in the parameter space α *versus* $r_0/R\alpha$. Dashed line: Balance condition from Eq. (5.11), where stokeslet vorticity and rotation due to bottom heaviness are balanced at a distance of $2R$. b) Vertical density profiles for non-equilibrium sedimentation, inverted sedimentation, stable plumes and convection rolls, and the spawning cluster state. Colors of the curves refer to the colors of the large dots in the state diagram c) Left: Snapshot of a system at $\alpha = 2.3$ and $r_0/R\alpha = 0.11$ showing a plume and convection roll. Right: Snapshot at $\alpha = 1.50$ and $r_0/(R\alpha) = 0.50$ showing a spawning cluster.

state *conventional sedimentation*, because it still shows exponential decay. In contrast, the exponential function is mirrored for the inverted sedimentation state (blue curve), as we have introduced for active Brownian particles in Section 2.4.2. *Inverted sedimentation* occurs at large α and finite torques. Due to the orientational bias, squirmers accumulate at the top. For high enough α, we can observe this enrichment already at small torques.

The state of plumes and convective rolls (orange curve) has a local density maximum

at the bottom of the system, but also includes layers of squirmers at the top wall. Its main characteristic is the appearance of large sinking clusters, that can be seen in the left snapshot of Fig. 6.1 c). Such curtain-like microswimmer structures are called *plumes* in bioconvection experiments [56, 157, 197, 285]. Furthermore, we observe squirmer currents in *convective rolls* close to the bottom of the system in these states, which we describe below in more detail. Note that plumes and convective rolls have not been observed in dilute suspensions of active Brownian particles, since they appear from hydrodynamic interactions.

The *spawning cluster* state is characterized by a strong density maximum at the bottom of the system and an almost entirely depleted region in the center of the simulation box. The large cluster of squirmers floating above the bottom wall and the depletion above can also be seen in the right snapshot of Fig. 6.1 c). In this state, no convection occurs and sinking clusters are very rare. However, single squirmers are sometimes ejected out of the bottom cluster with high velocity, which is why we call it a spawning cluster. The orientations of the spawning clusters are strongly vertical, since this state occurs at a high torque. Nonetheless, the cluster stays close to the bottom wall due to hydrodynamic interaction which decreases the effective friction per squirmer.

The dashed line describes a hyperbolic function satisfying the torque balance in Eq. (5.11). It predicts the region where plumes and rolls occur fairly well. The other lines separating the states from each other were obtained numerically from fitting the state boundaries.

In the following, we investigate conventional and inverted sedimentation of neutral squirmers, including transient plumes in Section 6.3 and the state with stable plumes and convective rolls in Section 6.4. In Section 6.5 we address the spawning-cluster state. Finally, we show how the state diagram changes for pusher and puller squirmers in Section 6.6.

6.3 Conventional and inverted sedimentation

6.3.1 Sedimentation states

In Sec. 2.4 we have described the sedimentation of active particles. Furthermore, the collective sedimentation of squirmers has been previously studied without any external torque [282]. In agreement with these results, we observe a sedimentation of squirmers when bottom-heaviness is weak. In Fig. 6.2 b) we show the measured sedimentation lengths for $\alpha = 1.50$ and $\alpha = 2.31$ that we found by fitting an exponential function to the vertical density profiles. The sedimentation lengths are orders of magnitude larger than that for passive systems, which is defined as $\delta_0 = k_B T_0/(mg)$. Furthermore, the values are consistent with those found in Ref. [282]. Note that sedimenting squirmers are mainly restricted to the bottom of the system, even at $\alpha > 1$, and do not perform cruising trajectories, as we expect from the single squirmer simulations. This points to the hydrodynamic influence of squirmers on each other: Gravity-induced stokeslets create a flow field which pulls nearby squirmers down and a vorticity which reorients

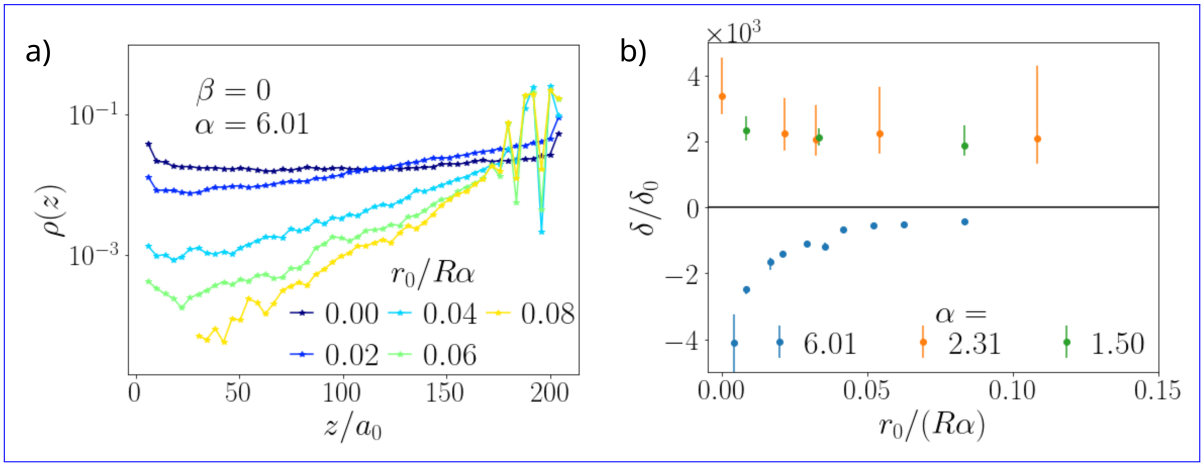

Figure 6.2: a) Density profiles for the inverted sedimentation state for $\alpha = 6.01$ and different torque values. b) Sedimentation lengths for conventional ($\alpha = 1.50$) and inverted sedimentation ($\alpha = 6.01$) *versus* dimensionless torque. We normalize the sedimentation length by the passive value $\delta_0 = k_B T_0/(mg)$.

nearby squirmers away from the vertical; see Eq. (5.3). These interactions extend the sedimentation state to $\alpha > 1$. We consider the dynamics of sedimented squirmers at $\alpha < 1$ in more detail when we study the emergent cluster formation of bottom-heavy squirmers under strong gravity in Chapter 7.

6.3.2 Inverted sedimentation states

Bottom-heaviness leads to an external gravitational torque which can overcome the hydrodynamic tilting of squirmers. Naturally, the required torque is lower for lower gravitational forces, which is reflected by the narrowing of the sedimentation state and the broadening of the inverted sedimentation state at high α in the state diagram in Fig. 6.1 a). We show the density profiles for constant $\alpha = 6.01$ and an increasing torque in Fig. 6.2 a). Without the external torque, the profile is almost uniform. With increasing torque, an inverted exponential profile develops with a (negative) sedimentation length that decreases with the torque. We plot the sedimentation lengths at $\alpha = 6.01$ in Fig. 6.2 b). The behaviour of the system agrees qualitatively with results on bottom-heavy active Brownian particles [158]. However, we also observe the formation of layers at the top wall when the inversion becomes strong enough. These layers are clearly visible in the density profile as sharp peaks that break the underlying exponential profile. Note that the density profile has been determined for only the last $5 \cdot 10^5$ timesteps of the simulation and that we base the classification as an inverted sedimentation state in Fig. 6.1 a) on this long-time limit. We mention this, because a significant transient state is observed at high torques, which we discuss in the following. In concrete, we observe transient plumes that are marked in Fig. 6.1 a) as the blue stars right of the dashed line.

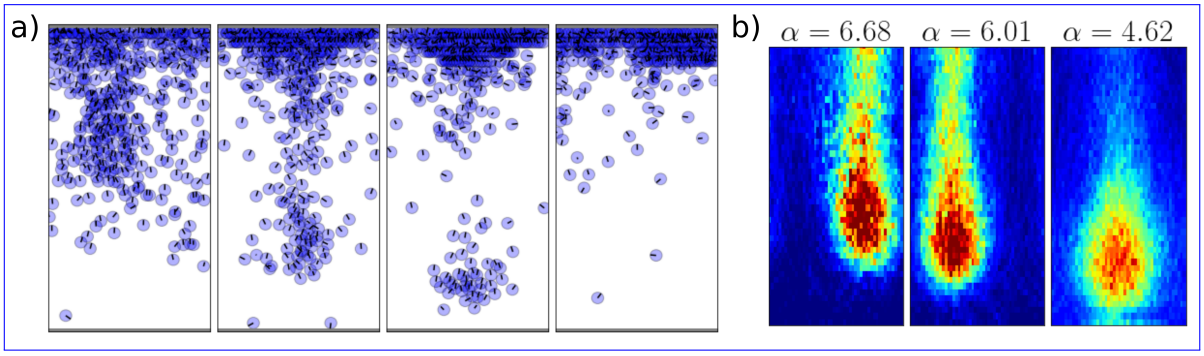

Figure 6.3: a) Snapshots of the evaporating plume for $\alpha = 6.01$ and $r_0/(R\alpha) = 0.08$. b) Time-integrated squirmer density during the transient is shown with decreasing α from left to right.

6.3.3 Evaporating plumes

Transient plumes appear during the formation of layers at the top wall at high torque and α. First, we observe a protrusion of squirmers which eventually separates from the layers and forms a sinking cluster. Note that squirmers swimming against the top layers without advancing still induce a stokeslet and hence a vorticity field is present. This orients squirmers towards each other and leads to the formation of the sinking cluster. The structure attracts more squirmers in its wake, leading to the typical elongated shape of a plume. We show a time series of the sinking plume in Fig. 6.3 a) and the average density profiles during the transient for different dimensionless torques in Fig. 6.3 b).

After the protrusion has formed, the cluster sinks as a whole, as the first two snapshots in subfigure a) show. It then starts to lose single squirmers into the bulk. These join the top wall layers which now remain stable, as can be seen in the third snapshot. The cluster thus becomes smaller and eventually disappears; see fourth snapshot. Therefore, we call this sinking cluster an evaporating plume. The cluster's initial size increases with the gravitational force. It survives for longer times and therefore sinks deeper. This can be seen in Fig. 6.2 b), where we plot the two-dimensional squirmer density during the sinking of three different plumes at different values of α. Note that at the lowest α, the sinking plume almost reaches the bottom wall before it evaporates. If gravity is increased even more, long-term stable plume and roll states can appear, which we discuss in Sec. 6.4.

6.4 Formation of stable convective structures

So far, we discussed evaporating plumes that do not form continuously and therefore end up in an inverted sedimentation state. However, we additionally observe states with constantly forming plumes. In these states, a convective roll appears at the bottom wall that absorbs squirmers from the plumes. We have already shown a snapshot of this state in Fig. 6.1 c). As can be seen in the state diagram Fig. 6.1 a), this happens at

torques exceeding the conventional and inverted sedimentation, whereas stable plumes disappear when the torque becomes very strong. In the following, we first characterize the features of the sinking plumes and then investigate the convective rolls at the bottom of the system.

6.4.1 Characterization of plumes

In the stable plume and convective roll state, plumes form continuously at the top wall and sink down. We discuss the mechanism of this sinking, and the clusters' statistics and sizes.

Collective sinking

The left snapshot in Fig. 6.1 c) suggests that squirmers in plumes have overwhelmingly an upright orientation. Since α is larger than 1, it is not immediately clear why the plumes are sinking. Therefore, we consider the statistics of down-moving squirmers, *i.e.*, those whose vertical velocity is negative. In Fig. 6.4 a), we plot the mean vertical squirmer orientation $\langle \cos\vartheta \rangle_{xy}$ as a function of height z for squirmers with $v_z < 0$ at different values of rescaled velocity α and torque $r_0/(R\alpha)$. This allows us to contrast the plume state with the sedimentation and inverted sedimentation states. To support our argument, we have included a dashed line for every curve at the respective threshold orientation $\cos\vartheta_{\mathrm{th}} = 1/\alpha$. This orientation, for a given α, indicates the maximum value that allows a *single* squirmer to sink down.

As we explained before, squirmers in the sedimentation state are tilted by the flow vorticities of their neighbors. As a consequence, their mean vertical orientation is always below the threshold value, as Fig. 6.4 a) shows: Squirmers in the sedimentation state (red curve) sink down due to the sedimentation velocity dominating the active part $v_0 \cos\vartheta$. For the inverted sedimentation states (blue curve), the orientation is also below its threshold value. However, this orientation is negative, which means that both sedimentation and self-propulsion contribute to the downward motion. We conclude that the squirmers are swimming down in this case, rather than sinking down.

The mean orientation of squirmers in the plume state (orange curve) is markedly different: The threshold value $\cos\vartheta_{\mathrm{th}}$ is overcome in the center of the simulation box (away from the walls), which is where sinking plumes can be found. For a single squirmer in bulk this implies upward swimming. Thus, single squirmer dynamics cannot explain the sinking of the squirmers in the plume. In fact, the sedimentation velocity is increased compared to a single squirmer in bulk due to hydrodynamic interactions with other squirmers in the plume. Stated another way, the friction per squirmer is reduced in the plume. The leading order hydrodynamic contribution from a squirmer's neighbor is again the stokeslet contribution, which indeed reinforces the downward drift from the external force, as the flow in Eq. (4.7) has a negative z component. Studies on the Rotne-Prager mobilities of passive colloids have also found this increase in downward mobility [198, 286–288].

We have thus identified three different forms of squirmer motion in negative z-direction in our system: Individual sinking for the sedimentation state, down-swimming

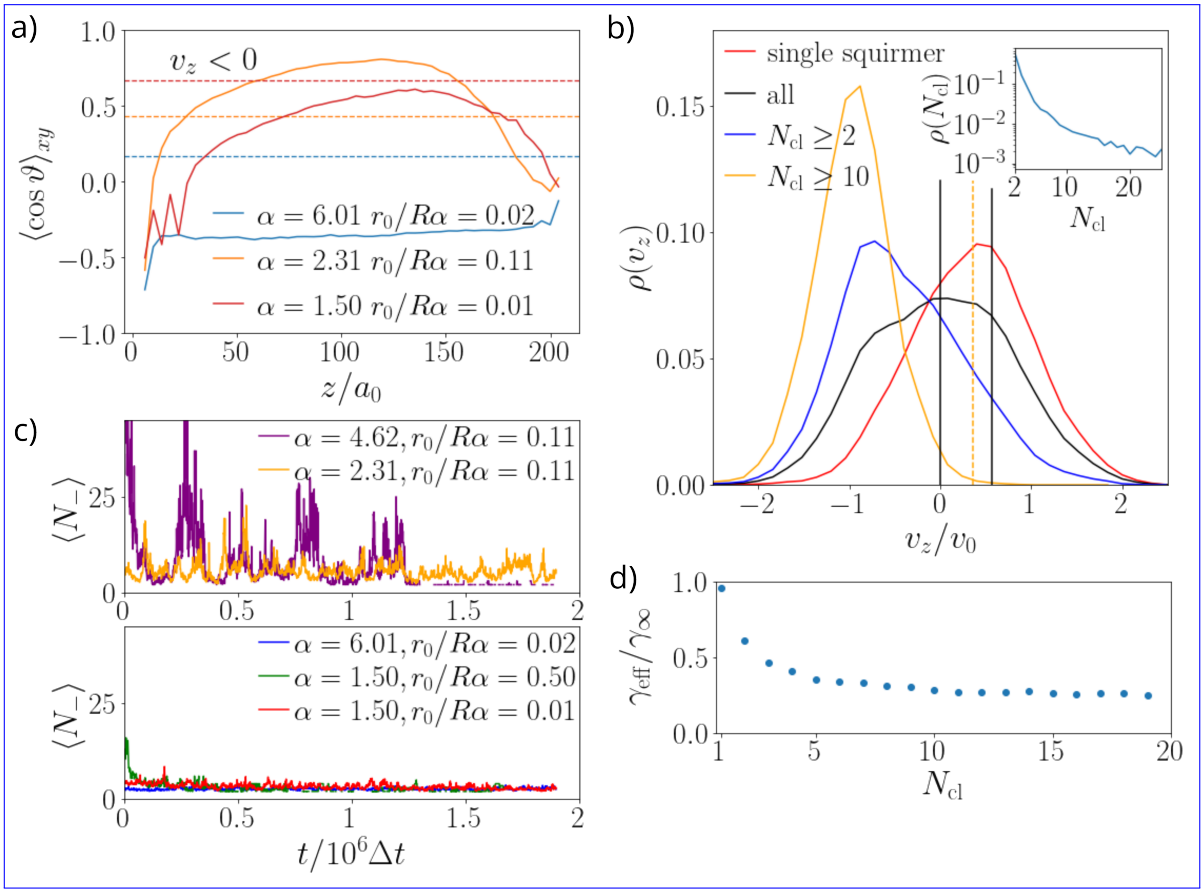

Figure 6.4: a) Mean vertical squirmer orientation $\langle \cos\vartheta \rangle_{xy}$ as a function of height z for all squirmers with drift velocity $v_z < 0$. Red: sedimentation, blue: inverted sedimentation, orange: plumes and convective rolls. Horizontal lines: condition $\cos\vartheta_{\rm th} = 1/\alpha$. b) Distribution of vertical velocities of neutral squirmers at $\alpha = 2.31$ and $r_0/R\alpha = 0.11$ for different cumulative cluster sizes $N_{\rm cl}$. Left black vertical line: mean velocity of all squirmers, which is almost zero. Right black vertical line: maximum bulk velocity $v = v_0 - mg/\gamma_\infty$. Orange vertical line: velocity for the mean vertical orientation of all squirmers from $\rho(v_z)$ for $N_{\rm cl} \geq 10$. Inset: probability density of cluster sizes. c) Mean number of squirmers in sinking clusters ($N_- \geq 2$) *versus* simulation time. Plumes and transient plumes (orange and purple curves) show characteristic spikes. d) Effective friction coefficient experienced by squirmers in a cluster as a function of cluster size.

in the inverted sedimentation state and collective sinking in the plume state. The latter is now investigated further.

Cluster velocity distribution

Cluster definition In order to verify the mechanism of collective sinking, we measure the velocity distributions of the plumes. In order to do this, we first need a way to identify squirmers inside a cluster. This is done by identifying groups of squirmers with a sufficiently small distance d from at least one neighbor within the same cluster. Here,

we choose $d < R/4$. We call the number of squirmers in a cluster the *cluster size* N_{cl}. Every 1000th timestep we determine the clusters in the system and then measure the vertical velocity distribution of all squirmers within each cluster. This way, we are able to distinguish the distributions at different cluster sizes from each other, and also from solitary squirmers with $N_{\mathrm{cl}} = 1$.

Velocity distributions We restrict the measurement to squirmers with medium heights $60 < z/a_0 < 160$. The reason is that we want to avoid including clusters or layers at either wall into our statistics, since these clusters are not the sinking plumes we are interested in. The parameters for which we performed this specific measurement are $\alpha = 2.31$ and $r_0/(R\alpha) = 0.11$, thus placing it within the grey area of plume states in the state diagram of Fig. 6.1 a).

We show the velocity distributions of the plumes in the main plot of Fig. 6.4 b). The solid black curve corresponds to the distribution of all squirmers in the chosen range. It is roughly symmetric around $v_z = 0$, which is also its approximate mean (left solid black vertical line). Thus, in total, the recorded squirmers fulfill a zero-flux condition and sinking plumes are balanced with up-swimming squirmers. This is an indication that steady state is reached. Furthermore, we include the vertical velocity distributions of solitary squirmers (red line) and for the clusters with 2 squirmers or more (blue line), as well as those with at least 10 squirmers (orange line). In addition to the mean of the entire distribution at approximately $v_z = 0$, we include two other characteristic velocities: The right black vertical line indicates the maximum upward velocity achievable in bulk $v = v_0 - mg/\gamma_\infty$ at the chosen value of α. Last, the dashed vertical orange line indicates the expected single squirmer vertical velocity

$$v_{\mathrm{sing},z} = v_0 \langle \cos\vartheta \rangle - mg/\gamma_\infty, \tag{6.1}$$

when assuming its polar angle to be the mean vertical orientation $\langle \cos\vartheta \rangle$ of all squirmers contributing to the orange curve.

Single squirmers move both up- and downwards, visible in the broad shape of their velocity distribution (red curve). However, the up-swimming squirmers are in the majority and the peak of their distribution is close to the bulk maximum velocity, indicated by the right vertical black line. Interestingly, a single squirmer's velocity can exceed this value, and more remarkably, even the free-swimming limit $v_z = v_0$. The reason for this are the flow fields originating from the convective rolls at the bottom of the system, which give the up-swimming squirmers a boost. We have verified that this velocity boost is not present for inverted sedimentation states where the bottom cluster is missing.

Next, we analyse clusters with a size of 2 and larger. We observe that increasing the lower limit of the cluster sizes considered — the integer k such that $N_{\mathrm{cl}} \geq k$ — shifts the vertical velocities in negative direction. This can be seen by comparing the blue ($N_{\mathrm{cl}} \geq 2$) with the orange curve ($N_{\mathrm{cl}} \geq 10$), and also comparing both of them against the black curve ($N_{\mathrm{cl}} \geq 1$). Furthermore, the distributions become narrower than both the total distribution and the single squirmer distribution. While the blue curve with $k = 2$ still retains a long positive velocity tail, this gets significantly reduced for the

orange curve, indicating that squirmers in large clusters move down most of the time. We here stress again that the orientations of these squirmers are still biased towards the top. Thus, the expected velocity of a non-interacting single squirmer, written in Eq. 6.1 and shown as the orange dashed vertical line, is positive, but only a negligible amount of squirmers with a comparable velocity are measured. Incidentally, the orange line agrees reasonably well with the peak of the single squirmer distribution (red curve), which underlines that the orientations of single squirmers and squirmers in clusters are similar on average.

Effective friction The actual peak of the orange distribution is near the negative self-propulsion velocity $-v_0$. It follows that the effective sedimentation velocity acting on the clusters' squirmers has increased, as predicted above, due to hydrodynamic interactions. The correction can be neatly expressed in terms of the friction experienced by a squirmer. For the dashed orange line, we used the friction of a single squirmer in bulk. We now quantify the influence of the close presence of the other squirmers on the friction in Fig. 6.4 d).

The effective friction coefficient, depending on the cluster size N_{cl}, is given by

$$\gamma_{\mathrm{eff}}(t, N'_{\mathrm{cl}}) = \left(-mg/\langle v_{\mathrm{eff}}\rangle_{N_{\mathrm{cl}}=N'_{\mathrm{cl}}}\right), \tag{6.2}$$

using the effective sedimentation velocity

$$v_{\mathrm{eff}} = v_z - v_0 \cos\vartheta \tag{6.3}$$

and averaging it over all squirmers within clusters of size N_{cl}. We subsequently took a time average over a range of $10^6\Delta t$, in order to obtain the curve in Fig. 6.4 d). Additionally, we normalized the data points by the bulk friction. We observe a strong size dependence of the effective friction coefficient, which saturates at large cluster sizes.

Cluster sizes

We show the distribution of cluster sizes in the inset of Fig. 6.4 b), this time excluding the case of individual squirmers. It shows a monotonic decrease with cluster size. In order to find a further characteristic signature of plumes, we look at the time series of the average number of squirmers in each sinking cluster. We call this number N_-, which exists for each cluster. We stress that for finding the cluster size N_{cl} all squirmer velocities were allowed, whereas now we restrict ourselves to those squirmers with $v_z < 0$.

We calculate the average number N_- in sinking clusters with two squirmers or more for each timestep, and plot this quantity for squirmers within the range $60 < z/a_0 < 160$ in Fig. 6.4 c). The upper plot shows the time series for both a transient plume (purple) and a continuous plume (orange) simulation. The lower plot shows sedimentation, inverted sedimentation and spawning cluster states.

We can clearly see sharp peaks in the plume states, setting them apart from the other states. These sudden events signal the sinking clusters falling through the observation window. The measurement for the transient plume state was done for the same number

of timesteps, but we clearly see that the spikes disappear around $1.3 \cdot 10^6 \Delta t$, due to evaporation. In contrast to the high spikes in these two states, the curve for the inverted sedimentation (blue line) stays relatively constant at a low value. The conventional sedimentation state (red line) shows some small variation, visible as occasional flat spikes. The reason for this is that small clusters can transiently form that then sink down again, as was also observed in Ref. [282]. The same applies for the spawning cluster state (green curve), but with very few and rare spikes.

Effect of flow vorticity

While the hydrodynamic flow fields are responsible for the reduction of friction per squirmer, the flow vorticity is decisive for the formation of the clusters. It is determined by the stokeslet fields everywhere, since we simulate neutral squirmers. As we have described for squirmer pairs, flow vorticity and external torque combined create the conditions of a stable configuration: Due to the flow field originating from a cluster, nearby squirmers are oriented towards it and approach it. They arrive slightly above it, since the cluster sinks, while the joining squirmers swim upwards. A vertically extended wake of squirmers develops, resulting in the curtain- or finger-like shape of a plume. The mechanism of plume formation that we describe here is similar to that of gyrotactic algae forming so-called 'bottom-standing' plumes [56]. It is not achieved in a stable way for the transient plumes, where squirmers ultimately escape from the sinking cluster towards the top wall. The transient states lie beyond the dashed hyperbolic curve which indicates the balance between external and hydrodynamic torques, thus we conclude that the external torque is too high.

Furthermore, the state diagram in Fig. 6.1 a) suggests that plumes are more robust at lower α, where the plume state is broader. This is because high values of α improve the chance of escape, as we can see from the angle threshold $\cos\vartheta > 1/\alpha$ of a solitary squirmer, which decreases with α.

6.4.2 Large-scale convective roll

As we indicated before, sinking plumes occur in the middle section of the simulation box, while at the bottom wall squirmers form a recirculating pattern, which we call a *convective roll*. Similar patterns are known from swimmers in experiments [109, 144, 157]. The convective roll is shown from a side-view projection in the left snapshot of Fig. 6.1 b). We offer additional perspectives in Fig. 6.5. In Fig. 6.5 a) we show a three-dimensional view of the roll. We have color-coded the squirmers with their respective vertical velocities. This helps us to clearly distinguish two regions: In yellow or red, we see the upwards swimming squirmers that escape from a gap between two high-density regions. There is not much vertical motion in the dense regions themselves, however, we can see a plume joining the right cluster. Squirmers in the plume are colored blue, *i.e.*, with negative vertical velocity.

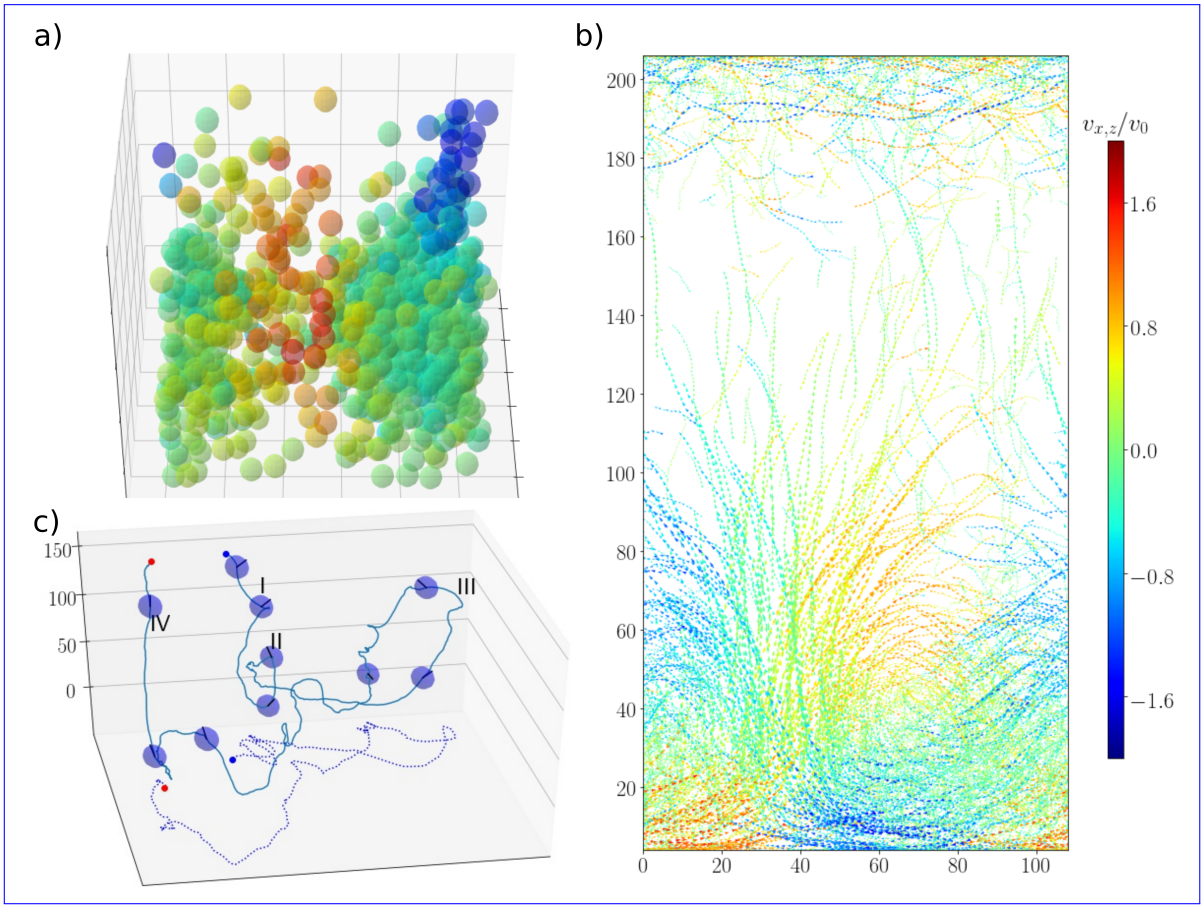

Figure 6.5: a) 3D snapshot of a convective roll in the region $0 \leq z/a_0 \leq 100$ with color-coded vertical velocity components v_z. b) Cumulated squirmer velocity vectors during a time period $9 \cdot 10^5 \Delta t$ within a layer of width $2R$ in y-direction. The color of the arrows marks the horizontal velocity component v_x. The color bar applies to both a) and b). Parameters are $\alpha = 2.31$ and $r_0/R\alpha = 0.11$. c) Exemplary squirmer trajectory inside a convective roll: The squirmer enters the roll (blue dot) and reaches the bottom cluster (I). It meanders through the cluster and sometimes reaches the edges of the cluster without escaping (II, III). Finally, it is ejected out of the roll (IV) and continues to swims upwards (red dot). Blue circles are squirmer positions, including their orientation vectors (radii are increased for better visibility). Dashed line: Projection on the x-y plane.

Recirculation pattern

Figure 6.5 b) illustrates the recirculation pattern of the convective roll. We accumulate the velocity vectors of squirmers on their trajectories over a time period of $9 \cdot 10^5 \Delta t$ within a thin slab of the system with width $\Delta y = R$. Thus, the entire system consists of many such slabs, and we show one representative example. The color of the velocity arrows corresponds to its horizontal components. In the upper and middle section of the simulation box, one sees the traces of squirmers moving up or down, whereas the majority of squirmers is at height $z = 100a_0$ or lower. In particular, squirmers swimming

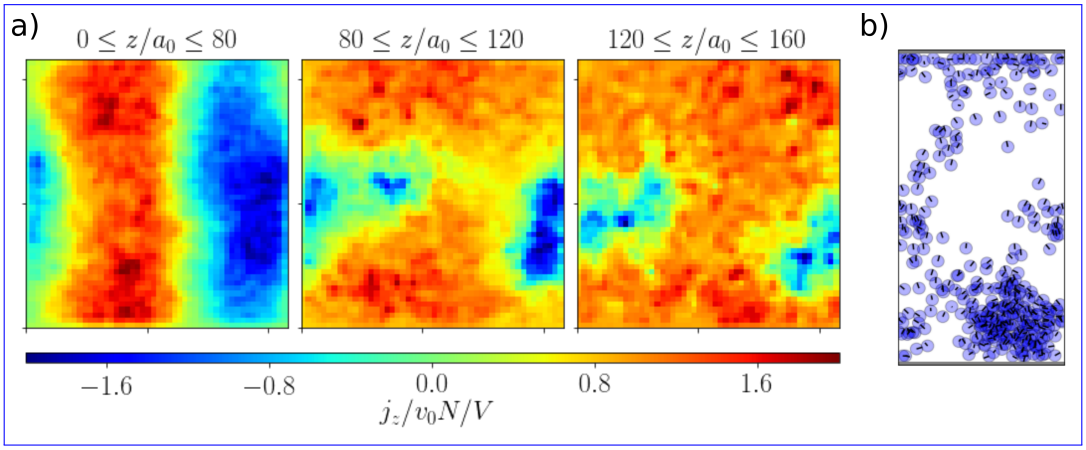

Figure 6.6: a) Mean vertical current density $j_z(x, y)$ at $\alpha = 2.31$ and $r_0/(R\alpha) = 0.11$. We averaged over three different regions, where each has a height $40a_0$. In an intermediate step, we smoothened the data by applying a low-pass filter. b) Snapshot capturing a timestep during the averaging procedure.

to the left (blue arrows) and squirmers swimming to the right (orange and red arrows) combine to visible macroscopic convective patterns. Most notably, a circular structure emerges in the horizontal center. In the bottom left, a second roll pattern is present, but is not complete due to the periodic boundaries. The sense of rotation of the two rolls is opposite. Both rolls exchange squirmers frequently; from the left roll they swim up and to the right towards the right roll, and vice versa. At the same time, squirmers also escape the convective rolls entirely, swimming up from the gap between them, in slightly curved trajectories.

We introduce the mean vertical current density of squirmers [282]

$$j_z(x, y) := \overline{\langle \rho(\mathbf{r}) \rangle_{\parallel} \langle v_z(\mathbf{r}) \rangle_{\parallel}}. \tag{6.4}$$

We use the squirmer density ρ and define $\overline{\cdots}$ as the time average and $\langle \dots \rangle_{\parallel}$ as the average along the vertical. We show $j_z(x, y)$ for the convective roll in Fig. 6.6 a) for three different subsections of the system. The left plot shows the bottom of the system ($0 \leq z/a_0 \leq 80$), and we clearly see the gap region where squirmers escape (red), as well as the roll on the right and, weaker, the counterrotating roll on the left (blue). The convective roll is elongated. However, its size is comparable to the lateral boxsize, and thus its shape is an effect of the finite system size. We discuss larger simulation boxes in the following section.

The middle plot shows the middle section of the simulation box ($80 \leq z/a_0 \leq 120$), *i.e.*, where we observe plumes. Indeed, the regions of sinking squirmers are spatially much more compressed, since squirmers reorient towards each other and sink collectively. Note that the positions and extensions of the sinking regions can change over time, and thus depend on the period of time integration. The blue peak in the center of the plot demonstrates that plumes can have a lateral displacement with respect to the roll underneath. While they sink, they move to the side considerably and are drawn into the convective roll, illustrating the strong hydrodynamic flows. This is also nicely

shown by the snapshot of Fig. 6.6 b).

The right plot in subfigure a), corresponding to the top region of the system ($120 \leq z/a_0 \leq 160$), shows weak sinking activity in the spots of emerging plumes, otherwise, up-swimming dominates.

Meandering trajectories

The convective rolls steadily reside at the bottom of the simulation box and form a regular pattern. However, this structure emerges from an irregular motion of the individual squirmers. In Fig. 6.5 c), we show the trajectory of a squirmer within the convective roll in subfigure a), seen from the side and rotated by 90 degrees. We have compensated for the periodic boundary conditions in the plot of the trajectory, to make its appearance more clear. Hence, the squirmer does not leave and re-enter from the boundaries. We start our description of the trajectory at the blue dot. Here, the squirmer falls towards the bottom cluster and joins the roll at position I. After passing through positions II and III, the squirmer leaves the cluster at position IV and its trajectory ends at the red dot. Additional to the three-dimensional motion, we show the projection on the $x - y$ plane as a dotted line below.

Note that at position II and III, the squirmer is on its way to leave the cluster. However, it is reoriented too strongly towards the horizontal in both cases. In summary, the irregular motion of squirmers inside a convective roll, expressed by the plotted trajectory, appears from self-propulsion with an orientation vector that is constantly disturbed by vorticity fields, and also influenced by the external torque. Thus, we again observe gyrotaxis, and we can consider the meandering motion as a many-swimmer extension of the pair dynamics from Chapter 5. Only stokeslet interactions are necessary for this, and simulations with neutral squirmers represent this situation well, since their flow field has zero vorticity.

6.4.3 System with multiple rolls

We now address the finite-size effects limiting convective rolls that we mentioned in Sec. 6.4.2. In order to avoid that a convective roll extends over the whole edge length L of the simulation, and thus interacts strongly with itself, we double L. Furthermore, we double the number of squirmers, such that we study a more dilute system, with half the squirmer volume fraction from before. Since more space is available for the distribution of squirmers in lateral direction, we observe more convective rolls than before. Fig. 6.7 shows a top and a side view of this system. The islands of convective rolls, seen on the left, are still supplied by sinking plumes, as before, which is depicted in the right snapshot.

For the previous geometry, the sizes and distances of the rolls were limited by the system size. In the larger system, we discover that both the extensions, as well as the distances of clusters from each other, seem to have a characteristic scale. In order to check this, we doubled the volume fraction to 10%, which increases the cluster sizes. As a result, they sometimes touch, but the distances between their centers remain approximately constant. We revisit the formation of regular clusters from bottom-

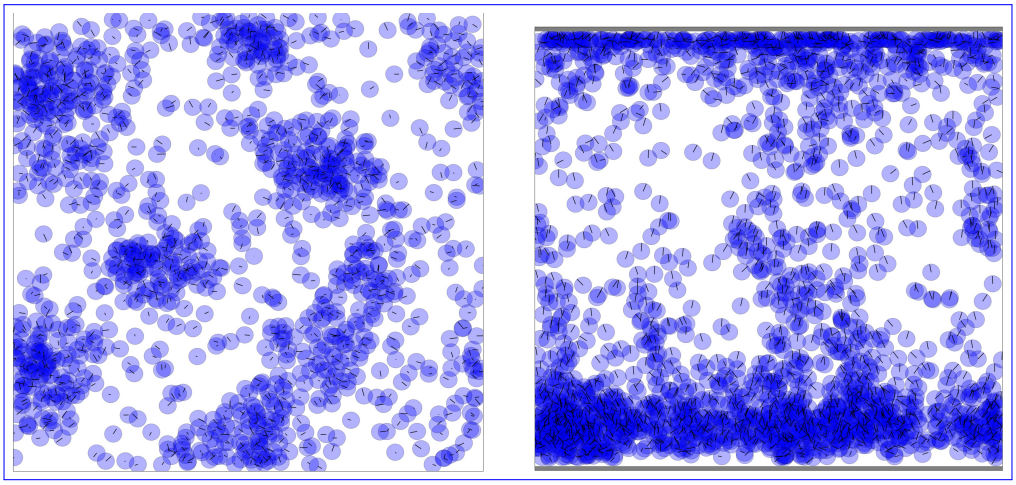

Figure 6.7: Snapshots for an array of convective rolls in a system with a horizontal cross-section that has been increased by a factor of four in comparison to Fig. 6.5, *i.e.*, $L = 216a_0$, while keeping the height constant. Left: Top view showing all squirmers below $z = 100a_0$. Right: Side view.

heaviness in Chapter 7 at $\alpha < 1$.

Toroidal squirmer flow

In Fig. 6.8 a) we take a look at the mean squirmer current density in vertical direction for the larger system. Again, the outlines of the rolls are clearly identifiable: The blue regions indicate sinking squirmers, both inside the rolls, as well as from the plumes supplying them with fresh squirmers. Squirmers swim up in the gap regions, shown in red. The larger system size with more rolls allows us to look at the dynamics within a single cluster more closely. As we have seen, a squirmer performs a meandering trajectory and is reoriented often by its neighbors, yet globally a consistent pattern is seen. In Fig. 6.8 b) we visualize the horizontal velocities of the squirmers within slices of the system that have a height of $4R$. The lower plot shows the bottom of the convective rolls, and the upper plot shows its top. Scanning through the roll in this way gives us insight into the three-dimensional flow of the squirmers. In the bottom right of the right figure, we show the color-code for the directions in which squirmers are moving. Interestingly, squirmers move radially outwards at the bottom, and inwards towards the cluster centers on the top. Since we know the vertical motion of squirmers from Fig. 6.5, we can conclude that the global flow pattern of the squirmer rolls has a toroidal shape.

6.4.4 Transient rolls

Convective rolls can become unstable, too, when the external torque becomes too strong. The tendency of squirmers to form plumes is counteracted by a strong vertical bias, as we have seen before. If plumes disappear, the convective rolls at the bottom wall also slowly disappear, since they continuously lose squirmers without re-

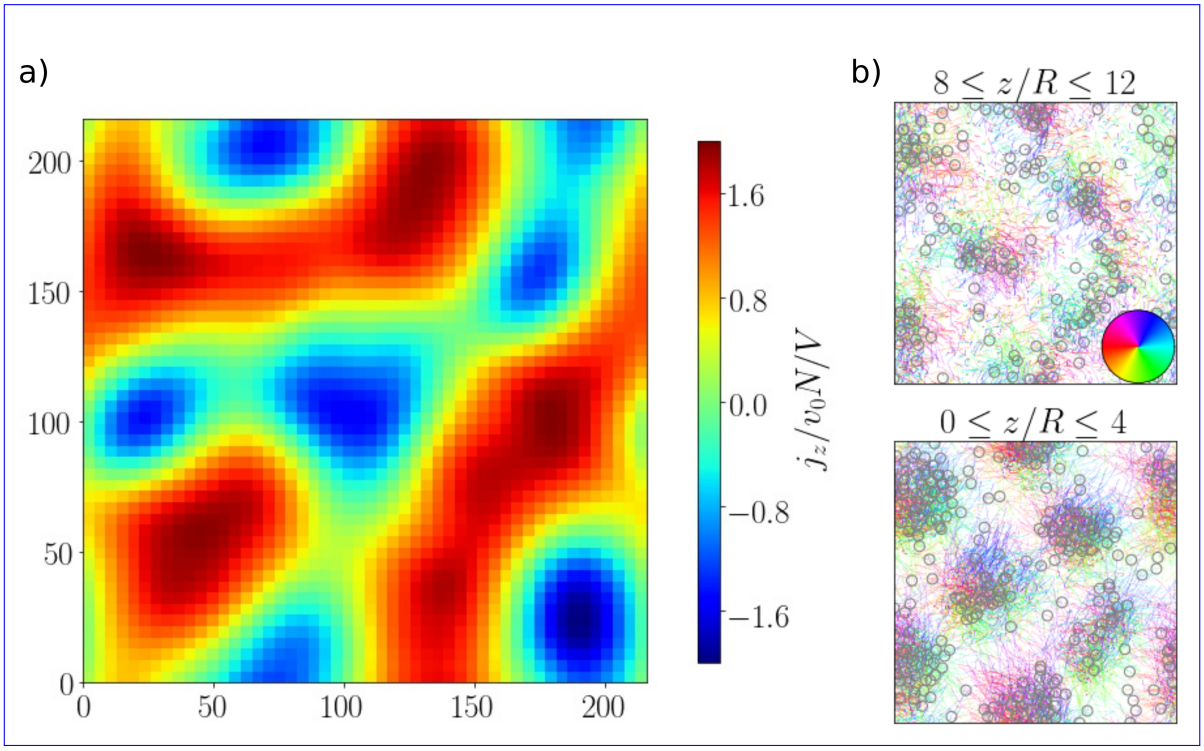

Figure 6.8: a) Mean vertical current density at $L = 216a_0$, averaged over all squirmers within $z/a_0 \in [0, 100]$ and over a time $4.5{\cdot}10^5 \Delta t$. b) Superimposed squirmer trajectories on the horizontal plane during the same time period in the top and bottom of the system. The circular color bar shows the direction of the horizontal velocities. Circles show squirmer positions from the top view snapshot in Fig. 6.7, left.

ceiving sufficient replacement. This can be seen in Fig. 6.9 a), where we plot the volume fraction η *versus* time in the bottom and top half of the box, as well as by the three snapshots in Fig. 6.9 b), which capture the system at three different times. The volume fraction η fluctuates around a constant value for sedimentation and inverted sedimentation steady states, as well as stable plume states. In contrast, in the transient roll state the density is continuously decreasing in the lower half and increasing in the upper half of the system; see subfigure a). As can be seen from subfigure b), the depicted process is rather slow, because the initial fraction of squirmers in the convective roll is high. Consequently, we did not reach equilibration during our simulation time. However, the escaped squirmers form an inverted sedimentation steady state for long times.

6.5 Spawning clusters

At high gravitational force and torque, squirmers are constrained to the bottom of the system, but are oriented vertically. This has the effect that both the translational, as well as the orientational range of motion is strongly restricted. As a consequence, a large cluster appears above the bottom wall, which can be seen in Fig. 6.10 a), at $\alpha = 1.50$ and $r_0/(R\alpha) = 0.50$. The color code is equal to Fig. 6.5, thus we see that

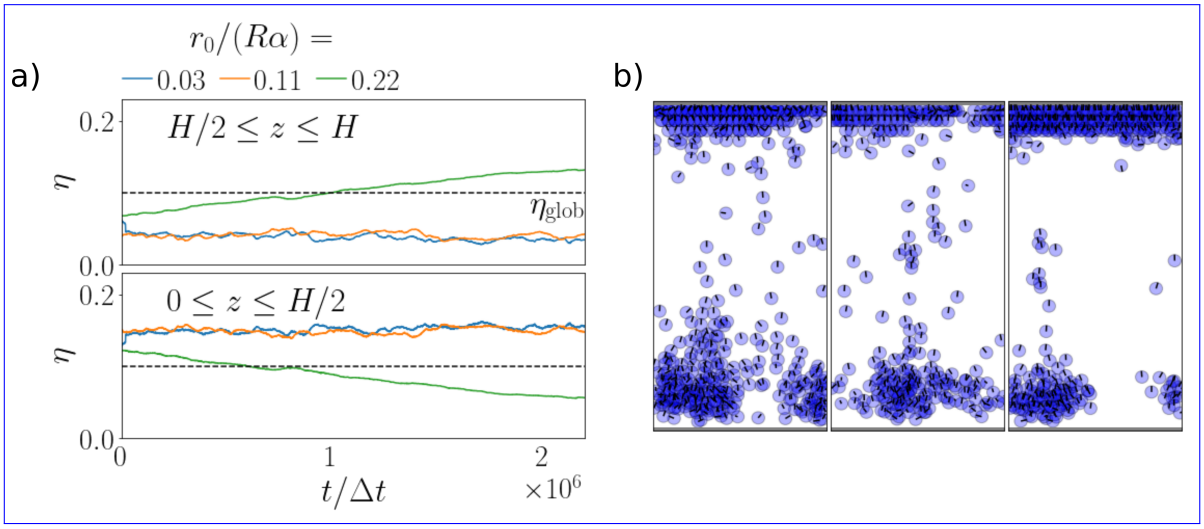

Figure 6.9: a) Time evolution of the volume fraction η at $\alpha = 2.31$. Top: upper half of the system ($H/2 < z < H$). Bottom: lower half of the system ($0 < z < H/2$). Dashed line: global volume fraction $\eta_{\text{glob}} = 0.10$. The curves show conventional sedimentation (blue), stable plumes and convective rolls (orange), and transient rolls (green). b) Snapshots of the corresponding transient roll, as it slowly disappears.

squirmers hardly move in vertical direction. Interestingly, the cluster is not compact, but has a porous structure with large holes completely depleted of squirmers. Thus, despite the small mobility of the squirmers, they still tend to form island and gap regions. Furthermore, on some occasions, squirmers leave the clusters through the gap regions at high velocity. These squirmers are the reason for the term *spawning clusters*. They either rejoin it or escape to the top wall. Thus, a stratum of squirmers develops there, as can be seen from the density profile in Fig. 6.1 b) and the right snapshot in Fig. 6.1 c), whereas the middle region becomes almost completely depleted.

In Fig. 6.10 b) we track the disappearance of convective motion in the central region between both walls with increasing gravitational torque. Therefore, we choose the region $z/a_0 \in [80, 120]$ for the three plots in Fig. 6.10 b), and set $\alpha = 1.50$, while the external torque is varied. In the sedimentation state, $r_0/(R\alpha) = 0.08$, squirmers can occasionally form convective patterns that are unstable. These become visible in the mean vertical current densities as separated regions of up- and down-swimming squirmers, if the period for time averaging is chosen not too long. These areas disappear if the torque is increased, as the middle plot for $r_0/(R\alpha) = 0.17$ shows. We identified this system as the beginning of the spawning cluster state in our state diagram in Fig. 6.1 a). At $r_0/(R\alpha) = 0.50$ (right plot), a nearly uniform value of zero for the current density is reached, except for some small remaining patches. However, as we have explained, these up-swimming squirmers are very characteristic for the spawning cluster state. Note that the same range of height is used in all three plots of Fig. 6.10 b), and all systems experience the same gravitational force.

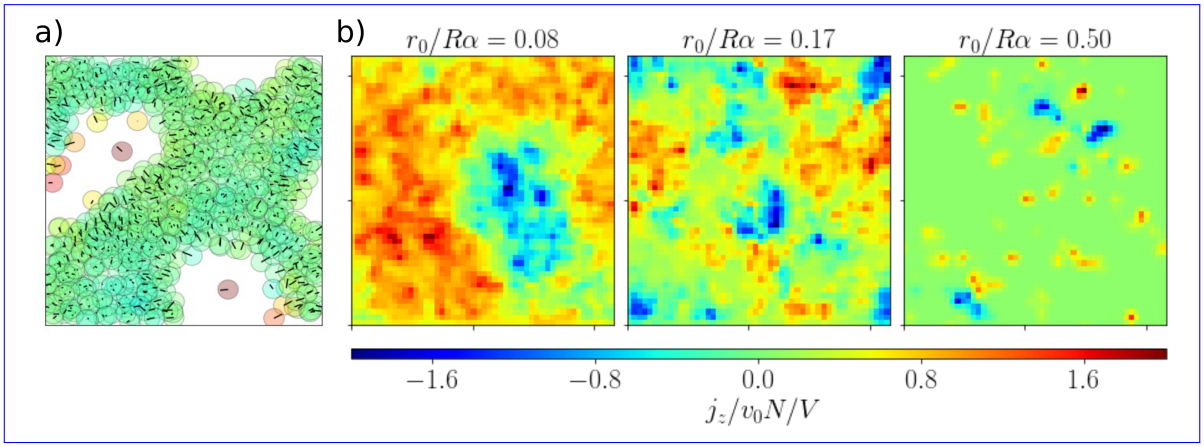

Figure 6.10: a) Top-view snapshot for the spawning cluster state at $\alpha = 1.50$ and $r_0/(R\alpha) = 0.50$. Vertical velocities are color-coded with the same scale as in Fig. 6.5. b) Mean vertical current density $j_z(x, y)$ in the horizontal plane at $\alpha = 1.5$ in the region $80 \leq z/a_0 \leq 120$ and averaged over a time period of $9 \cdot 10^5 \Delta t$. The torque value $r_0/R\alpha$ corresponds to sedimentation (left) and a spawning cluster (middle and right).

6.6 Pusher and puller dynamics

An analysis of the dynamics of puller and pusher squirmers with $\beta = \pm 5$ yields the state diagrams in Fig. 6.11 a) and c). We observe less distinct states than for neutral squirmers. Conventional and inverted sedimentation still occurs. Here, higher torques and higher values of α are needed in order to reach the inversion, as can be seen by comparing the respective separation lines to the neutral squirmer case. Convective rolls and spawning clusters do not occur for either of the two swimmer types, while we do observe plumes. However, they are more fragile than for neutral squirmers. As we describe below, for pullers they are more pronounced than for pushers, and we consider them a separate state. Therefore, we show a grey shaded area in the state diagram.

6.6.1 Sedimentation of bottom-heavy pushers and pullers

Pushers and pullers show a transition from conventional to inverted sedimentation profiles. This is shown in Fig. 6.12 a) for the example of the puller at $\alpha = 6.01$. However, as shown by the state diagrams, the necessary torque for achieving inversion is higher for $\beta \neq 0$. We can see in the angular distributions in Fig. 6.12 b) why this is the case: The neutral squirmers' vertical alignment is stronger than for pushers and pullers, using the same parameters $\alpha = 6.01$ and $r_0/(R\alpha) = 0.04$.

The force dipole component of their flow fields distinguishes pushers and pullers from neutral squirmers. Decaying with $1/r^2$, it is more long-ranged than the source dipole field. Furthermore, the force dipole has a non-zero vorticity. This interferes strongly with the orientations of nearby squirmers, as has been shown in studies of microswimmer suspensions: Polar order in clusters is weakened due to force dipole fields, for pushers more than for pullers [41, 199, 289, 290]. The perpetual deviation from the

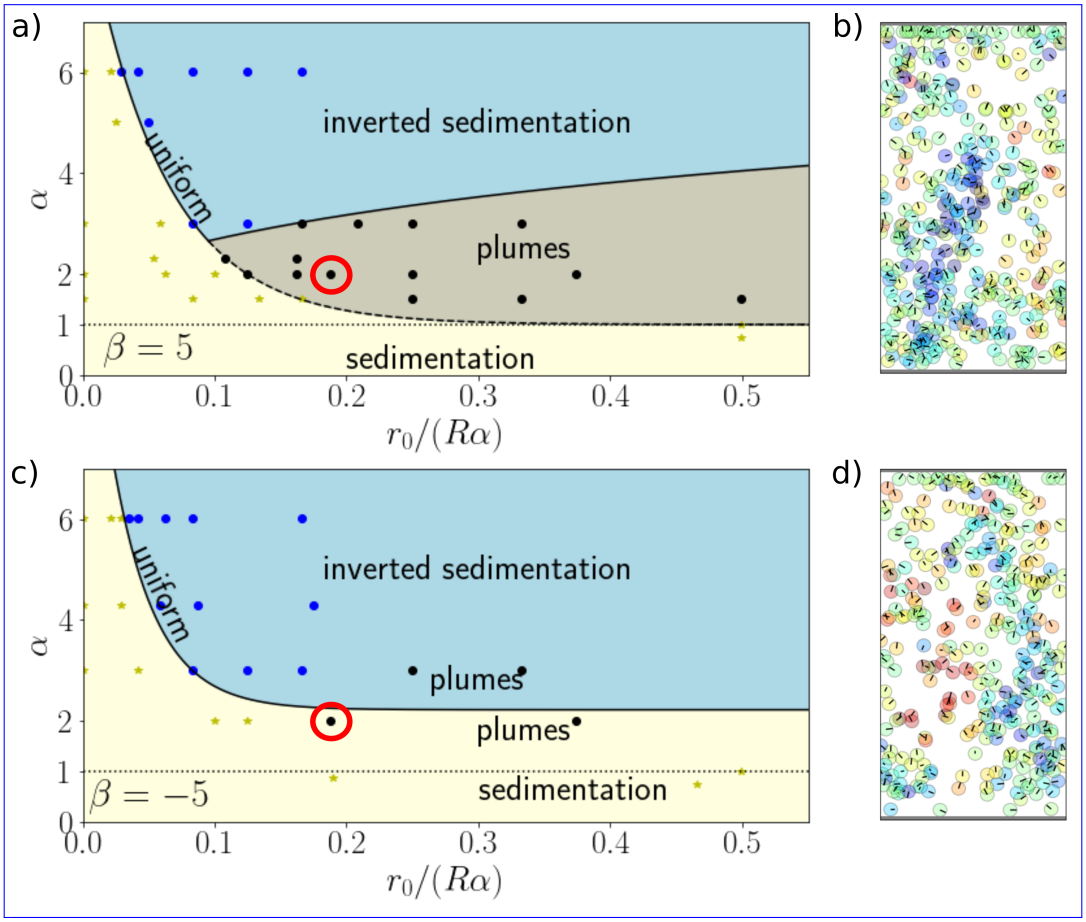

Figure 6.11: a) State diagram for the strong puller with $\beta = 5$. b) Puller plume for system with $\alpha = 2.01$, $r_0/(R\alpha) = 0.19$ (see red circle in a)). c) State diagram for the strong pusher with $\beta = -5$. d) Pusher plume for system with $\alpha = 2.01$, $r_0/(R\alpha) = 0.19$ (see red circle in c)). Color coding of squirmers shows their vertical velocities.

vertical alignment by the pusher and puller vorticity fields necessitates stronger external torques, in order to achieve inverted sedimentation. Furthermore, we hardly observe layering for pullers and pushers at the top wall, as can be seen in the sedimentation profiles. We suggest that the reason is the same.

6.6.2 Pusher and puller plumes

In Fig. 6.12 c), we show the density profiles of pushers, pullers and neutral squirmers at $\alpha = 2.00$. We immediately see that the peak at lower heights is much less pronounced for pushers and pullers, which is due to the missing convective rolls in that region. However, we picked the parameters such that we still observe plumes. This necessitates increasing the rescaled torque to $r_0/(R\alpha) = 0.19$ for pushers and pullers.

The plumes we observed by visual inspection are more fragile than for neutral squirmers. The snapshots in Fig. 6.11 b) and d) confirm this. Puller plumes form at the top wall and disintegrate before the bottom wall is reached. Pusher plumes are

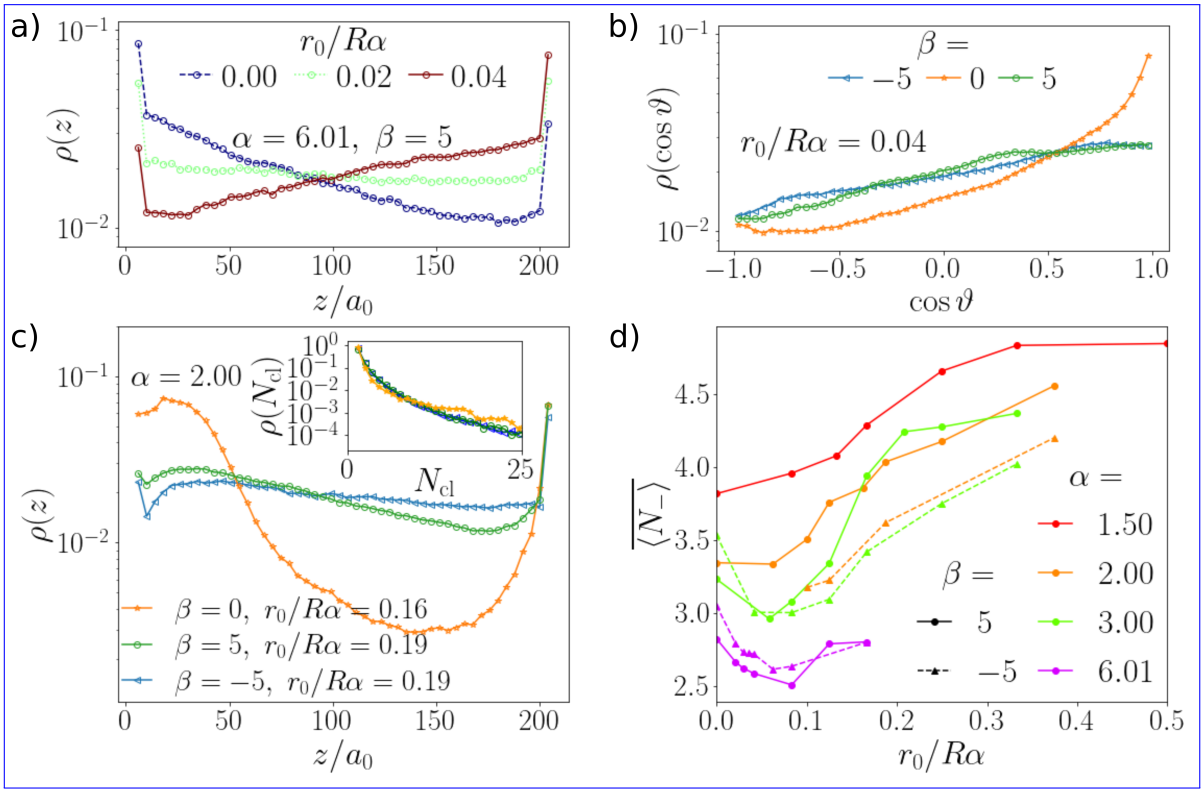

Figure 6.12: a) Exponential, constant and inverted height profiles of strong pullers ($\beta = 5$) at $\alpha = 6.01$. b) Distributions of the vertical orientation for different squirmer parameters β at $\alpha = 6.01$ and $r_0/R\alpha = 0.04$. c) Height distributions of neutral, pusher, and puller squirmers in their respective plume states at $\alpha = 2$. Inset: Cluster size distribution of the sinking plumes. d) Mean size of sinking clusters $\overline{\langle N_- \rangle}$ for strong pullers ($\beta = 5$) as a function of the rescaled torque. Averaging is performed for the region $20 \leq z/a_0 \leq 120$ and over more than $5 \cdot 10^5$ time steps. We considered all sinking clusters with $N_- \geq 2$.

even more volatile. The inset of Fig. 6.12 c) depicts the distribution of cluster sizes and shows that large clusters are less probable for pushers and pullers, thus their plumes have smaller sizes on average. As a consequence, we cannot identify the sinking plumes clearly as spikes in the time series of the mean size of sinking clusters N_-, as we did for neutral squirmers in Fig. 6.4 b). As an alternative, we perform a time average over this series, which we show in Fig. 6.12 d). We plot it versus the rescaled torque and show curves for different velocity ratios α.

As we explained, the plumes are more stable for pullers (solid lines and circles). Since the average cluster sizes have an approximately sigmoidal dependence on the rescaled torque for $\alpha < 6$, we classify the systems with plumes as a distinct state. For $\alpha = 6.01$, there is no crucial change or trend. The state boundaries of the plume state in Fig. 6.11 a) numerically approximate the values of $(\alpha, r_0/(R\alpha))$, where the largest jump in the sinking cluster size occurs. We plot a dashed instead of a solid line in the state diagram for the transition from the sedimentation state, since the jump for $\alpha = 2.01$

and $\alpha = 1.50$ is less clear. Likewise, since the average cluster size merely increases steadily for pushers (dashed lines and triangles), without jumping, we do not identify a transition between two states in pusher systems. We therefore left them classified as sedimentation and inverted sedimentation states, but indicated in the state diagram that sinking plumes occur.

6.7 Conclusions

Fascinating patterns arise for squirmer suspensions which experience a gravitational force and torque. Observing over 900 neutral squirmers, pullers or pushers, we tracked the different states that occur depending on the strength of gravity and bottom-heaviness. Conventional sedimentation profiles occur at low ratios of swimming velocity to sedimentation velocity α, and low rescaled torques $r_0/(R\alpha)$. Increasing α and using finite torques, the exponential height profiles invert. If the external torque becomes comparable to viscous orientation interactions, squirmers start to accumulate, most strongly for neutral squirmers. Since the friction is reduced in a cluster configuration, collective sinking occurs and we observe plumes. At the bottom of the system a convective roll develops for neutral squirmers, which is supplied with squirmers by plumes, while it releases single squirmers into the bulk. These structures appear from gyrotaxis, *i.e.*, a combination of directional alignment with gravity (gravitaxis) and by nearby flow fields (rheotaxis). This is underlined by the fact that plumes and rolls become transient as the external torque becomes too large and starts to dominate. Strong torques at $\alpha \gtrapprox 1$ lead to the formation of porous squirmer structures that float above the bottom wall. We call them spawning clusters because they sometimes eject fast single squirmers.

We find that the force dipole flow fields and vorticities induced by strong pushers and pullers disturb the density inversion, as well as the cluster formation, which we observe for neutral squirmers. Thus, the state diagram loses features for $\beta \neq 0$. The plumes we observe are fragile and no stable convective rolls appear.

Gyrotaxis is definitely relevant for bioconvection, as discussed in the literature [56, 203, 209–211]. However, alternative descriptions of plume formation exist, where a gravitational instability occurs at the top layer. It resembles a Rayleigh-Taylor convection instability and flow vorticity is not needed [56, 157, 197, 206, 207, 291]. For example, these descriptions seem to be relevant for plumes of *Tetrahymena*, where gyrotaxis was ruled out [202]. While this mechanism requires a top wall, collective sinking from gyrotaxis can also emerge in the bulk fluid.

We only observed fragile plumes of pusher and puller squirmers, however stable plumes and convection cells occur in nature for these types of swimmers [109, 157, 203]. Thus, for a concrete microswimmer, one cannot neglect additional effects from their propulsion mechanism. This includes steric interactions due to flagella [89, 292, 293], shape-induced gravitational torques [71, 195], and alternative forms of taxis, such as phototaxis [197, 212] and chemotaxis [157, 200]. Furthermore, the force dipole strength of biological microswimmers is often less than the value corresponding to $\beta = \pm 5$, which we used [269, 294, 295], and can also vary during a flagellar beating cycle [171, 172].

7. Gyrotactic cluster formation

In this chapter, gyrotactic clusters under stronger gravity, their emergence and their properties are studied. Most of the following results are based on our original work [C].

7.1 Introduction

Active constituents, whether they are biological or synthetic, frequently form clusters. The interactions leading to cluster formation can be very different from system to system. They can be merely local, as in motility-induced phase separation of active Brownian particles [7] or the steric interactions among bacteria [296], or long-ranged, such as chemical interactions [8, 9, 106, 297] or hydrodynamics [15, 42]. The impact of such clusters is considerable. Microfabrication of active particle aggregates could become a promising technology [105, 298, 299] and organic patches in the oceans have profound environmental impact [70, 276, 300]. In the last chapter, we found appealing patterns emerging from gyrotaxis, such as plumes and convective rolls. For large systems, the convective rolls separate into several clusters with characteristic distances and sizes. We study the gyrotactic mechanism of cluster formation more quantitatively in the following. In particular, we analyse the structural properties of clusters and test, which parameters influence their size and distance.

While the patterns observed in the last chapter extended over the whole height of the simulation box, we now focus on stronger gravity, comparable to Chapter 4. Thus, vertical motion is still possible, but we expect it to be restricted by the floating heights found previously. At the same time, hydrodynamic interactions continue to strongly influence the collective dynamics.

7.2 Phenomenology of gyrotactic clusters

In order to investigate the formation of neutral squirmer clusters, we vary the external torque, as well as the squirmer density. Furthermore, we consider the effect of hydrodynamic flow fields. As before, we are also interested in pusher and puller squirmers. In addition, we introduce rotlet-dipole squirmers, which we have not used previously, but which have evoked interest in literature [301, 302]. They could be used to model bacteria, such as E.coli.

Again, we use the parameter α as a measure of gravity and the rescaled torque $r_0/(R\alpha)$. We first provide an overview over the phenomenology, before analysing the

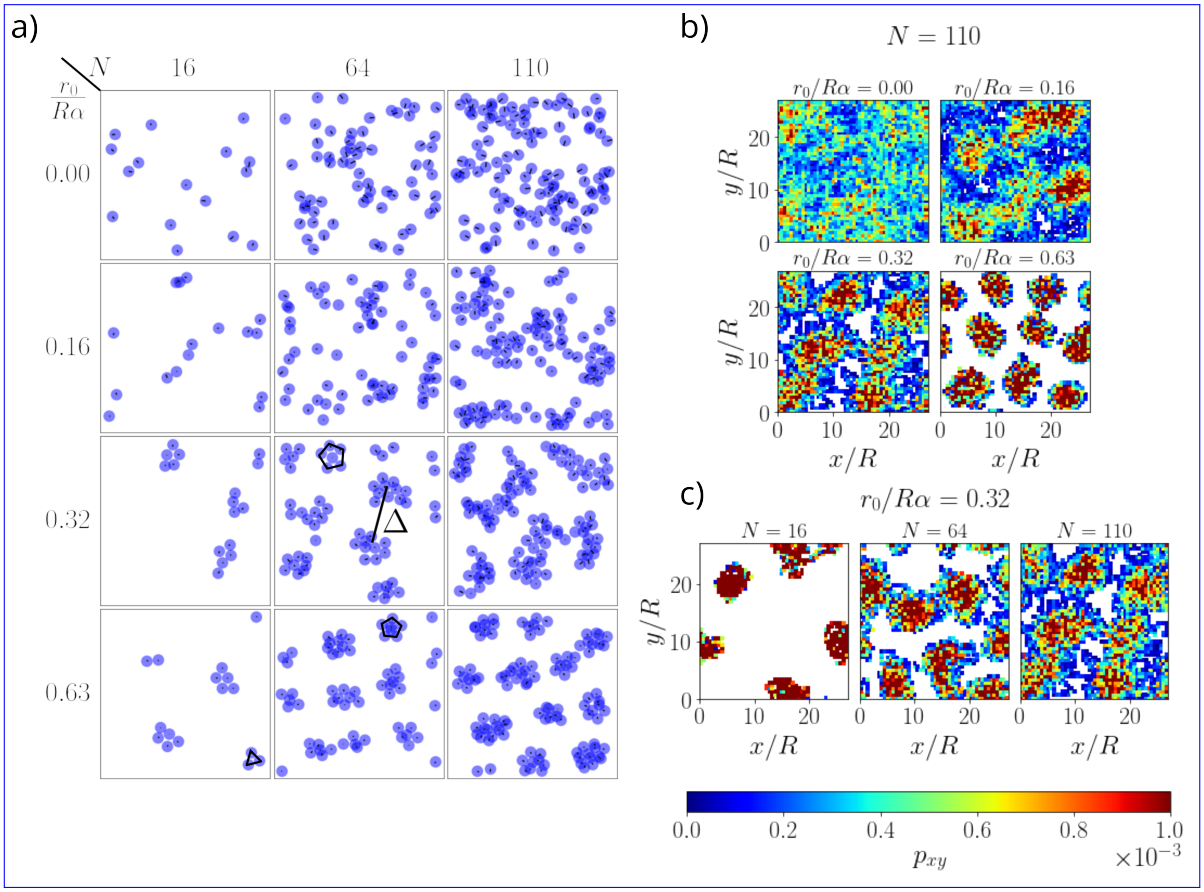

Figure 7.1: a) Top view of simulation snapshots. They show clusters that form at squirmer numbers N and rescaled torques $r_0/(R\alpha)$. Other parameters are $\beta = 0$ and $\alpha = 0.8$. b) Density profiles of systems with $N = 110$ squirmers at different torques. c) Density profiles of systems with $r_0/R\alpha = 0.32$ at different squirmer numbers N. The profiles were obtained after averaging over 10^5 timesteps.

clustering quantitatively.

7.2.1 Initial condition

Squirmers are either initialized with random positions and orientations, such that they do not overlap with walls or with each other, or on a regular horizontal grid in a wall-parallel plane, where we usually choose the central plane at $z = H/2$ with upright orientations. The phenomenology that we describe below is not influenced by the choice of the initial condition. For the random initial conditions, some squirmers can escape to the top wall and stay there pointing upwards, when the external torque is strong. These squirmers have no influence on the rest of the system during the remaining simulation.

7.2.2 Onset of cluster formation

We show a variety of representative snapshots of neutral squirmers in Fig. 7.1 at different values for the rescaled torque and the global squirmer number N. The states are seen from the top, therefore illusory overlaps can be visible. In reality, squirmers do not overlap with each other. The value of $\alpha = 0.8$ is constant in all cases.

From Fig. 7.1 we observe that clusters of squirmers start appearing at a finite torque. These clusters have a typical distance Δ (see central snapshot at $r_0/(R\alpha) = 0.32$). When the torque is absent, as shown in the top row, squirmers can touch during collisions, but do not stay in contact over a longer time. The reason is that rotational noise and hydrodynamic interactions drive the squirmers' orientations towards the horizontal. A typical interaction without torque therefore consists of the squirmers coming into contact randomly, tilting their respective orientations towards the horizontal, and then swimming past each other.

Two-dimensional density profiles

While squirmer pairs perform oscillations, reminiscent of Volvox' 'minuet dance' [61], the interactions of many squirmers in clusters is more complex. They do not show a clear oscillating mode, but reorganize by switching their positions inside the cluster. This can create geometrical structures with high symmetry, such as triangles and pentagons, that we have drawn into some of the snapshots in Fig. 7.1 a), but we stress that they are very fragile. When the torque gets higher, the clusters become more static.

We show two-dimensional density profiles of squirmers in Fig. 7.1 b) and c). For averaging, we choose 10^5 time steps and use the squirmers in the bottom half of the simulation box. In subfigure b), we increase the rescaled torque from zero to 0.63 at a constant squirmer number of $N = 110$. In the course of increasing the torque, the unstructured profile at zero torque changes more and more into clearly defined cluster regions. We attribute the occasional patches at $r_0/(R\alpha) = 0$ to the bottom wall, which induces floating squirmers like in Chapter 4. These floaters move only little in horizontal direction and therefore create the patches, but no clusters appear. In contrast, we observe stable clusters at $r_0/R\alpha = 0.16$, as we can see from the stronger peaks. There is still strong horizontal motion, showing that squirmers frequently leave clusters into the gap regions, or join a different one. The gap regions get less and less explored, if the torque is further increased. At the same time, the clusters get more stable and compactify. Therefore, as an effect of the increased torque, the vertical alignment increases and the horizontal velocities decrease, which prevents the motion away from a cluster. We have already seen this effect of a torque increase when we studied the oscillating squirmer pairs.

In Fig 7.1 c), we keep the external torque constant, but instead vary the number of squirmers. We do this in order to test, how much of an influence the global area fraction $N\pi R^2/L^2$ has on the evolving patterns. However, we find that the patterns look quite similar over the range of $N = 16$ to $N = 110$. The main difference is the disappearance of the white gap regions, which implies that horizontal motion increases with more squirmers. This is expected, because of the additional hydrodynamic stokeslet

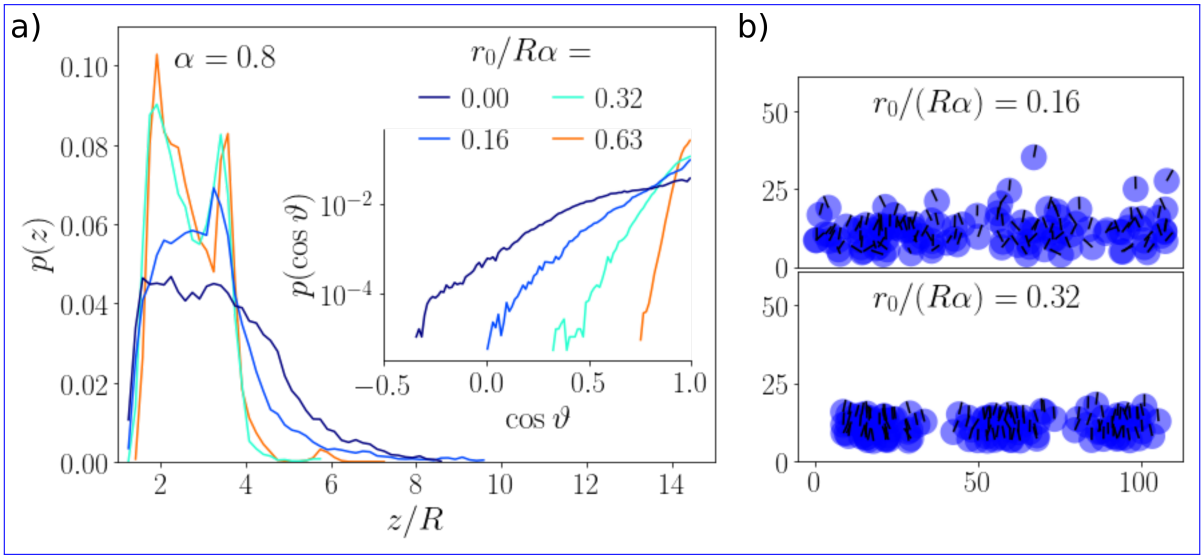

Figure 7.2: a) Vertical density profile *versus* squirmer height z at $\alpha = 0.8$ and $N = 64$, using different rescaled torques. Inset: Distributions of vertical orientations. b) Side views of simulation snapshots at $r_0/(R\alpha) = 0.16$ and 0.32 for a system with $N = 110$ squirmers.

interactions that each new squirmer brings, and which tilts its neighbors towards the horizontal plane.

Vertical density profile

Stacking While overlaps between squirmers in the snapshots are purely a visualization effect, they show that squirmers sometimes organize on top of each other. Figure 7.2 a) shows the vertical density profiles, and confirms this impression for high torques. A double peak appears, which indicates a stacked bilayer configuration. Accordingly, the distance Δz between the peaks is approximately one squirmer diameter. We show snapshots seen from the side for two systems with $N = 110$ squirmers in Fig. 7.2 b), which confirm this.

Collective sinking As introduced in the last chapter, squirmers sink collectively. We can also see this effect in the vertical density profiles in Fig. 7.2 a). The probability to find squirmers at large heights is greater at a rescaled torque of zero than at finite values. This can clearly be seen in the snapshots in Fig. 7.2 b), as well. The reason for this is the reduced friction experienced by squirmers that have self-organized into clusters, in contrast to the individual motion at zero torque, as presented in Sec. 6.4.1. This effect overcompensates the stronger directional alignment at finite torques (see inset of Fig. 7.2 a)), which would lead to upwards swimming in the absence of hydrodynamic interactions.

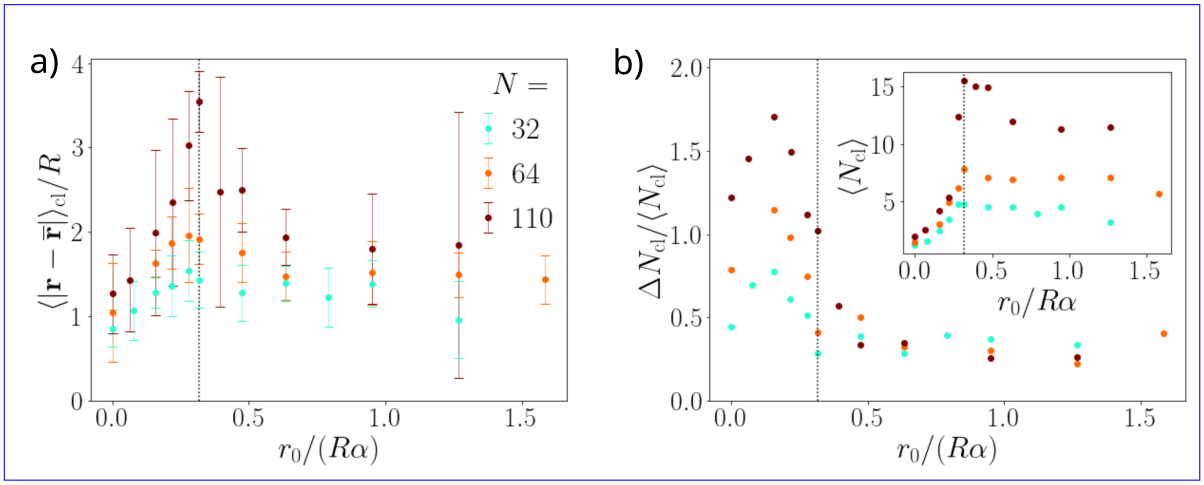

Figure 7.3: a) Mean cluster radius $\langle |\mathbf{r} - \bar{\mathbf{r}}| \rangle_{\mathrm{cl}}$ *versus* rescaled torque $r_0/R\alpha$. b) Standard deviation of the cluster size ΔN_{cl} *versus* rescaled torque, normalized by its mean. Inset: Mean cluster sizes $\langle N_{\mathrm{cl}} \rangle$ *versus* rescaled torque. Dotted vertical lines: equality condition of Eq. (5.11) for $\alpha = 0.8$.

7.3 Parameter study

In the following, we investigate the gyrotactic clusters systematically by measuring the cluster size and cluster extension, and by calculating the radial distribution functions. We vary the global density, the external torque and the external force, and consider the effects of the squirmer flow fields.

7.3.1 Cluster radius and size

In the two-dimensional density profiles in Fig. 7.1 b), we observe a compactification of clusters with increasing torque. We now investigate this in more detail by measuring the mean cluster radius and the cluster size, as a function of the torque. First, we identify clusters using a maximum squirmer-squirmer distance $d < R/4$, as previously described in Sec. 6.4.1, and then determine the cluster size N_{cl}. For each cluster, we can determine the cluster position

$$\mathbf{r}_{\mathrm{cl}} = \frac{1}{N_{\mathrm{cl}}} \sum_{i=1}^{N_{\mathrm{cl}}} \mathrm{r}_i. \tag{7.1}$$

The mean distance of squirmers from $\mathbf{r}_{\mathrm{cl}}$ within a cluster then defines a cluster radius. We now average over all k_{cl} clusters in a timestep and over time, which introduces the mean cluster radius

$$\overline{\left\langle \frac{1}{k_{\mathrm{cl}}} \sum_{\mu=1}^{k_{\mathrm{cl}}} \left(\frac{1}{N_{\mathrm{cl},\mu}} \sum_{i=1}^{N_{\mathrm{cl},\mu}} |\mathbf{r}_i - \mathbf{r}_{\mathrm{cl},\mu}| \right) \right\rangle} =: \left\langle |\mathbf{r} - \mathbf{r}_{\mathrm{cl}}| \right\rangle_{\mathrm{cl}}, \tag{7.2}$$

where we introduced the short-hand notation $\langle \cdots \rangle_{\mathrm{cl}}$ for averaging over all clusters (which are indexed by μ) and over time. We also refer to the mean cluster radius as the mean cluster extension. Note, following this definition, a solitary squirmer has a cluster extension of zero.

Furthermore, we measure the mean cluster size $\langle N_{\mathrm{cl}} \rangle$, *i.e.*, the average number of squirmers in a cluster. We additionally measure the standard deviation of this quantity

$$\Delta N_{\mathrm{cl}} = \sqrt{\langle (N_{\mathrm{cl}} - \langle N_{\mathrm{cl}} \rangle)^2}, \tag{7.3}$$

in order to capture the width of the underlying distribution. Since we want to sample the steady states, we use only the last $2.5 \cdot 10^5$ timesteps for averaging.

The aforementioned quantities are plotted *versus* the rescaled torque in Fig. 7.3, where the standard deviation in part b) is normalized by the mean. We observe a distinct maximum of both the cluster radius and the cluster size N_{cl} (inset of b)) at $r_0/(R\alpha) = 0.32$, with a steep increase at small torque values. The maximum is particularly pronounced for $N = 110$. For torques below the maximum, we can follow the onset of gyrotactic cluster formation. First, squirmers have only transient contact, thus both the cluster sizes and their variance remain small. With increasing torque, squirmers are attracted to each other and clusters can form, as explained before. Since the external torque cannot consistently balance the hydrodynamic interactions, these clusters are short-lived, and their sizes fluctuate strongly. The standard variation of the cluster sizes reaches a maximum around $r_0/(R\alpha) = 0.2$, before the cluster size and radius reach their respective maxima. Thus, with increasing torque, clusters become more stable and reach a maximum extension. An inspection of the snapshots in Fig. 7.1 a), as well as Fig. 7.2 b) reveals that clusters at the maximum value $r_0/(R\alpha) = 0.32$ are still relatively loosely bound.

Beyond the maximum, the clusters compactify and become more static, as the standard deviation decreases. Clusters consist of less squirmers on average, as the cluster sizes in the inset of Fig. 7.3 b) show. On the other hand, the last row of Fig. 7.1 a) demonstrates that the number of clusters k_{cl} increases with increasing torque. The compactification of clusters coincides with the regime where the external torque starts to dominate over the hydrodynamic interactions. This is demonstrated by applying the balance of angular velocities from Eq. (5.9) to $\alpha = 0.8$, which yields $r_0/(R\alpha) = 0.313$ and is therefore approximately at the measured maximum of 0.32. We show this value as dotted vertical lines in all graphs of Fig. 7.3. For torques higher than at the maximum, the cluster radius decreases, and also the standard deviation decreases sharply. The decrease in cluster extension happens because the horizontal mobility of the squirmers is more limited from stronger vertical alignment. Furthermore, as we have shown, squirmers evade in negative z-direction, leading to a stacked arrangement. At high torques beyond $r_0/(R\alpha) = 0.5$, both cluster radius and standard deviation approach a constant value and do not strongly decrease.

7.3.2 Radial distribution function

The radial distribution function $g(r)$ is a good measure for the structure of a liquid or colloidal system and here describes the probability to find a squirmer at a distance r

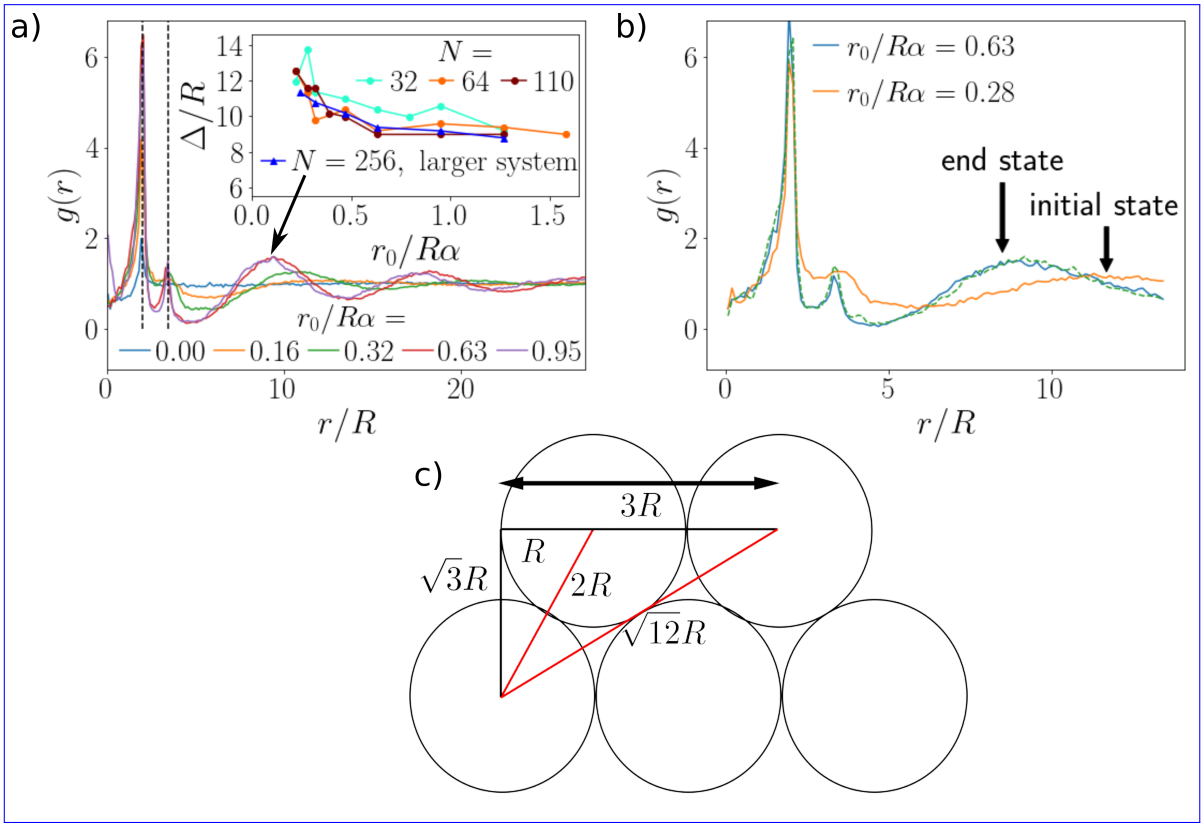

Figure 7.4: a) Radial distribution functions for a larger system with 256 squirmers and box width $L = 216a_0$. Dashed lines: nearest neighbor and next-nearest neighbor distances at $2R$ and $2\sqrt{3}R$. Inset: Mean cluster distance Δ *versus* torque for $N = 32,\ 64,\ 110$ at the smaller system width $L = 108a_0$ and $N = 256$ at the larger width $L = 216a_0$. b) The cluster configuration of a finished simulation with $r_0/(R\alpha) = 0.28$ (orange line) is used as the initial condition at $r_0/(R\alpha) = 0.63$ and we measure the changed radial distribution function after simulating for 3 Million timesteps (blue line). Dashed green line: Radial distribution function of a separate simulation at $N = 64$ and $r_0/(R\alpha) = 0.63$. c) Top view of spheres in hexagonal configuration. Nearest and next-nearest neighbor distances are colored in red.

from another squirmer [303]. The radial distribution function is defined as [303]

$$g(r) = \frac{1}{N/L^2}\langle \sum_{i \neq j} \delta(|\mathbf{r}_i^{2D} - \mathbf{r}_j^{2D}|)\rangle. \tag{7.4}$$

The value $g(r) = 1$ corresponds to a completely unordered system, a non-interacting ideal gas. We here use the two-dimensional version and therefore only take the projection of the squirmer positions on the x-y-plane into account. L^2 is the total area, where L is the lateral boxsize. Furthermore, the $\mathbf{r}_i^{2D}$ are the positions of the squirmers projected onto the plane. We calculate the average over the configurations found in the last $2.5 \cdot 10^5$ timesteps. Furthermore, we restrict the distances $|\mathbf{r}_i^{2D} - \mathbf{r}_j^{2D}|$ to values below $L/2$, because the radial distribution function does not give meaningful values

beyond this value. In order to work around that limitation, we performed additional simulations with an increased system width of $L = 216a_0$. We arrive at the same area fraction as in the smaller system, since we increase the number of squirmers to $N = 256$.

Our measurement of the radial distribution function in the larger system is shown in Fig. 7.4 a), for several different values of the rescaled torque. We observe several maxima, which hints at the existence of characteristic distances in the system. First, a peak at the nearest neighbor distance $r = 2R$ is visible for all curves. Left of the peak, the radial distribution function is broadened due to the partial overlap of squirmers in the planar projection. Most curves possess a further maximum at the next nearest neighbor distance $\sqrt{12}R = 2\sqrt{3}R = 3.46R$ (right dashed line). The only exception is the curve for zero torque, which decays to a constant value of one after the first maximum. This underlines that the squirmers are unstructured and more or less distributed randomly, if the external torque is missing. The next nearest neighbor peak becomes more pronounced at higher torque. It represents a distance within a cluster, namely when a second shell is formed around the center. We plot a hexagonal configuration of spheres in Fig. 7.4 c) in order to explain the values of the nearest and next-nearest neighbor distances.

The third peak for torque values of $r_0/(R\alpha) = 0.16$ and beyond represents distances on a larger scale. In concrete, it is the typical distance Δ between two nearest clusters. In the case of $r_0/(R\alpha) = 0.16$ (orange curve), a minimum around $r = 6R$ is visible, and another very flat peak follows afterwards. After doubling the torque to $r_0/(R\alpha) = 0.32$ (green curves), the maximum amplitude around $r = 10R - 11R$ is much higher. Thus, squirmer clusters with a characteristic distance of separation appear in the system. Interestingly, the peak shifts to lower distances, when the torque is increased, as can be clearly seen in the radial distribution function for $r_0/(R\alpha) = 0.63$ (red curve). On the other hand, increasing it further to 0.95 (purple curve) does not bring about a further shift. This agrees well with the previous result, that the cluster sizes and extensions do not change much after compactification is achieved. For the larger system shown in the main plot of Fig. 7.4 a), a further peak around $r = 17R - 18R$ is visible for torque values beyond $r_0/(R\alpha) = 0.32$. The peak corresponds to the typical distance from a cluster to the next nearest cluster.

We plot the characteristic cluster distance Δ *versus* the rescaled torque in the inset of Fig. 7.4 a), both for the larger system shown in the main plot, as well as for several squirmer numbers N in the smaller system with $L = 108a_0$. The cluster distance Δ consistently decreases with increasing torque, for all squirmer numbers. Furthermore, we confirm that a saturation is reached once clusters become compact at high torques, which happens around $r_0/R\alpha = 0.64$.

We find that the cluster distance depends only weakly on the number of squirmers, and thus on the area fraction. Only a small shift to smaller distances is observed for increasing N. Furthermore, the results for the larger system (blue curve) with $N = 256$ agrees well with the corresponding smaller system with the same area fraction, using $N = 64$ (orange curve).

The decrease of Δ with the torque is an intriguing property of gyrotactic clusters. It can be explained by the fact that clusters get smaller at larger torques, as we found above. Since the number of squirmers stays the same, this implies that the total number

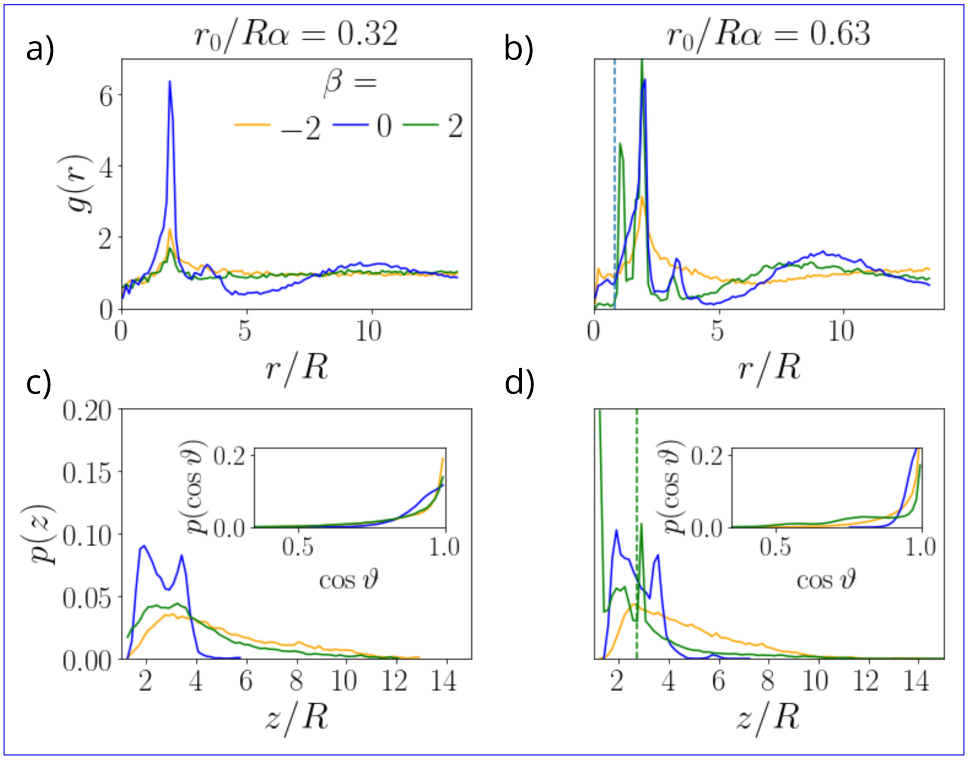

Figure 7.5: a) Radial distribution functions at $r_0/R\alpha = 0.32$, $\alpha = 0.8$ for pusher, puller and neutral squirmer systems. b) Radial distribution functions at $r_0/R\alpha = 0.63$, $\alpha = 0.8$. c) and d) Vertical density profiles. Insets: Distributions of vertical orientations.

of clusters is higher. Consequently, the space between the clusters has to shrink. This connection between the cluster distance and the gyrotactic mechanism suggests that Δ emerges from the system parameters, rather than from the initial conditions. In order to investigate this, we run a simulation at $r_0/(R\alpha) = 0.28$ and let it reach a cluster state, as shown by the radial distribution function in Fig. 7.4 b) (orange curve). The final configuration is then used as the initial condition of a new simulation using $r_0/(R\alpha) = 0.63$, which we run for $3 \cdot 10^6$ timesteps. Indeed, we observe that the typical cluster distance decreases in this simulation, as we can also see in Fig. 7.4 b) (blue curve). Importantly, the radial distribution function shows excellent agreement with a separate simulation at $r_0/(R\alpha) = 0.63$, which uses random initial conditions and is shown as the dashed green curve in Fig. 7.4 b). Thus, we confirm that the typical cluster distance is reached consistently at the chosen parameters and is an intrinsic property of the system, not an effect of initial conditions.

7.3.3 Influence of squirmer flow fields

So far, we have considered the neutral squirmer for gyrotactic cluster formation, inducing source dipole singularities in the far field. As we have established, the hydrodynamic signatures of biological and artificial swimmers often include force and rotlet dipoles, as well. Therefore, we analyse the effects of the squirmer parameter β and the chirality

parameter χ in the following.

Force dipole

In Fig. 7.5 we show radial distribution functions for pushers and pullers in subfigure a) and b) at different torques, as well as the vertical density profiles and vertical orientation profiles in subfigures c) and d).

The force-dipole flow fields, induced by pusher and puller squirmers, add a finite vorticity, see Eq. (5.5). It competes with the external torque and the stokeslet vorticity [87, 269]. Thus, their flow fields interfere directly with the gyrotactic mechanism, in contrast to neutral squirmers. This strongly influences the structural properties of the system, as we can see in the radial distribution functions for $\beta = \pm 2$ in Figs. 7.5 a) and b). In comparison to neutral squirmers, no peak corresponding to the nearest cluster distance Δ exists at low torques, meaning that no clusters exist at these values. This is confirmed by the density profiles in subfigure c), where pushers and pullers are shown to reach larger heights than neutral squirmers. This is possible when there is no collective sinking, hence squirmers swim individually.

When the external torque is doubled, the pusher system still does not show clustering, see subfigure b). In contrast, we observe a peak in the radial distribution function of the puller system at $r \approx 8R$ in subfigure b), which indicates cluster formation. Accordingly, the density profile in Fig. 7.5 d) is more concentrated at the bottom wall. It includes two sharp peaks. The first one corresponds to squirmers directly at the bottom wall, and the second around $r \approx 4R$ belongs to a further layer on top of it. Hence, we find a stacked vertical distribution of squirmers in clusters, similar to neutral squirmers.

Structure of puller clusters Still, the structure of the puller clusters is different from the neutral squirmer clusters. The snapshot in Fig. 7.6 a) shows that the pullers point inwards towards the cluster center. There are two hydrodynamic aspects relevant for this behaviour. First, two interacting force dipoles that start in a parallel configuration, reorient each other until they reach a head-to-head or tail-to-tail arrangement, as has been described in Chapter 5 for the far field regime and also by Ref. [37]. It therefore makes sense that several pullers would point towards a common point. Furthermore, in this configuration, the flow fields lead to a mutual attraction of the pullers, which stabilizes the structure. Second, the near field of a puller close to a no-slip wall also induces a tilt away from the vertical, as has been described in Chapter 4 and Refs. [187, 266]. In Fig. 7.5 d), we show the distribution of vertical orientations. It confirms this tilt, as a small local maximum at $\cos\vartheta \neq 1$ appears in the angular distribution.

Note the additional peak below the nearest neighbor distance $r = 2R$ in the radial distribution function in Fig. 7.5 b) for $\beta = 2$ (green curve). This effect is a combination of stacking and the inwards pointing pullers in the bottom layer. The squirmer layer that settles on top experiences a flow towards the center of the cluster, and thus squirmers settle in a dense packing. This results in a pyramidal three-dimensional structure, which can be seen in the simulation snapshot in Fig. 7.6 a). Indeed, if we assume an equilateral triangle at the base, the horizontal distance between nearest squirmers yields $w = \sqrt{3}/2R$. One of these two squirmers resides in the upper and the other one

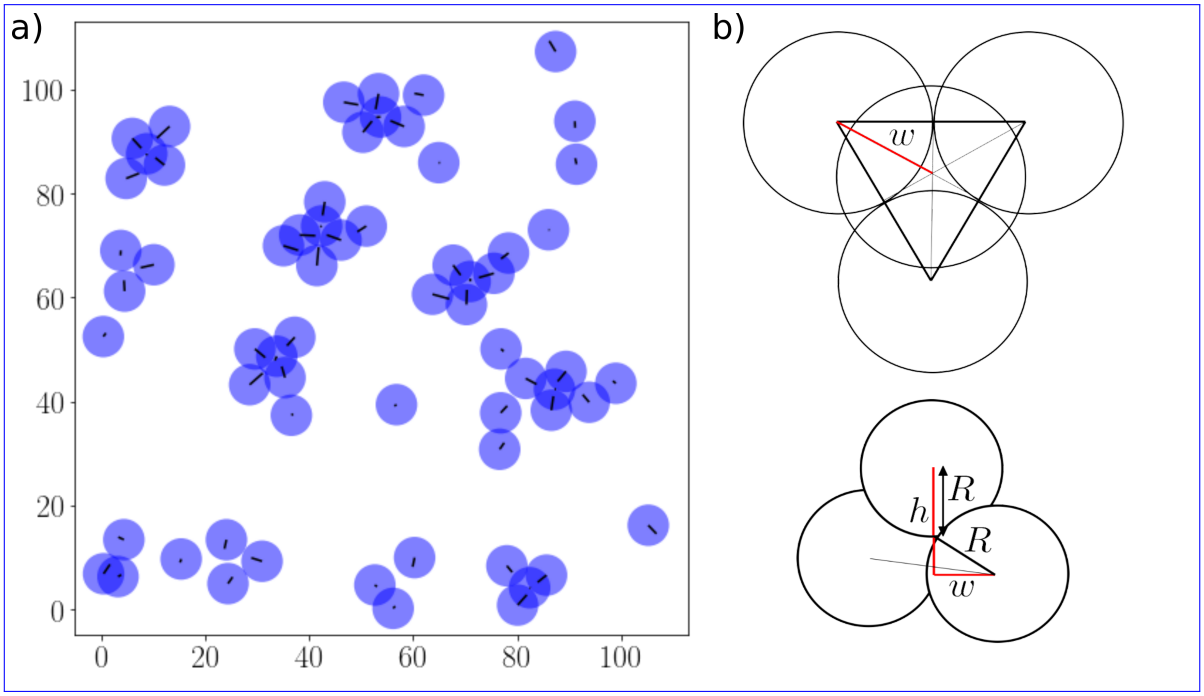

Figure 7.6: a) Snapshot of a puller system with $\beta = 2$ and $\alpha = 0.8$ at $r_0/(R\alpha) = 0.64$. Pullers strongly incline towards the center of the cluster. b) Sketch of a pyramidal structure with equilateral base, including the nearest neighbor vertical distance h and horizontal distance w. Upper figure: Top view. Lower figure: Side view.

in the lower layer of the stacked structure. The closest vertical distance in the pyramid yields $h = 3/2R$. These values can be understood from the sketches in Fig. 7.6 b). Furthermore, we include these lengths as dashed vertical lines in Figs. 7.5 b) and d). The agreement with the additional peaks is very good, thus the simulation results agree with the suggested pyramidal structure.

Rotlet dipole

We now repeat the analysis for the C_2 mode. Again, we show the radial distribution function and the distribution of heights in Fig. 7.7 a)-b), comparing rotlet-dipole squirmers to neutral squirmers. Additionally we show the distribution of horizontal velocities in subfigure c).

At the depicted rescaled torque of 0.63, clusters form for $\chi < 3.3$, as evident from the radial distribution functions and the vertical distributions, which show the familiar shapes in this range. Stronger rotlet dipole strengths inhibit cluster formation. We note, that for a smaller torque of 0.32, the clusters disappear already at $\chi = 1.0$ for neutral squirmers. Puller clusters disappear altogether, if a rotlet dipole component is present.

Subfigure c) shows that the vertical velocity distribution gets broader with the rotlet dipole strength χ, and thus includes higher absolute velocities. We suggest that this enhanced advection prevents further cluster formation. In subfigure d) we can follow

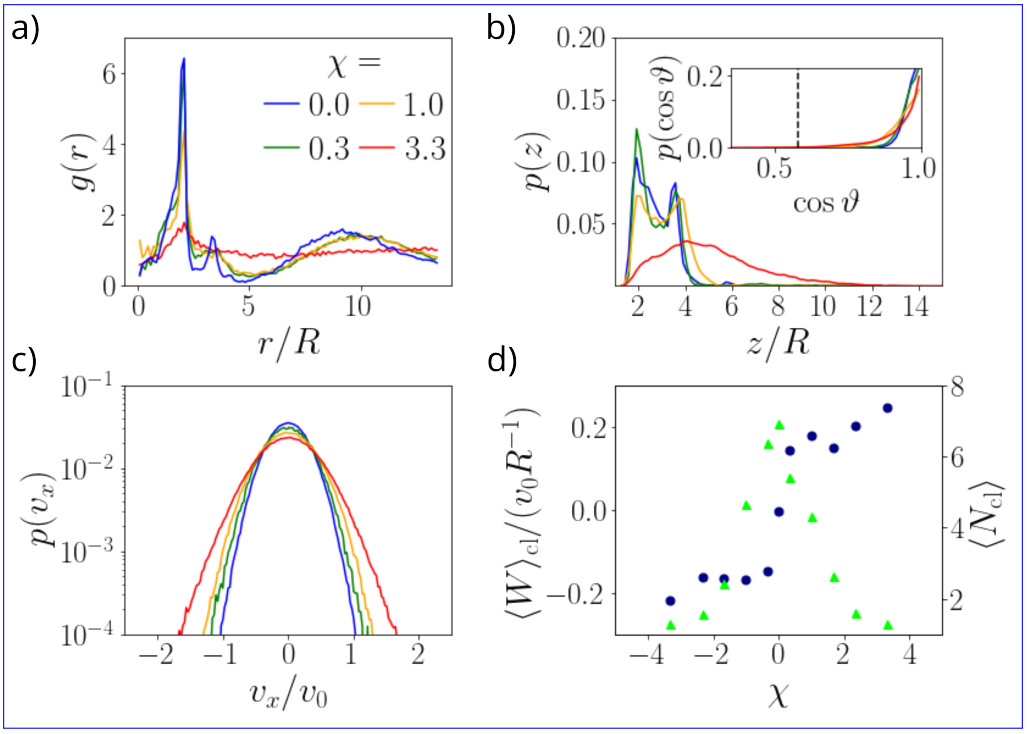

Figure 7.7: a) Radial distribution function at $r_0/R\alpha = 0.63$, $\alpha = 0.8$. b) Vertical density profiles. Inset: Distributions of vertical orientations with dashed line corresponding to $\cos\vartheta = 1/\sqrt{(3)}$. c) Horizontal velocity distributions. d) Mean swirling parameter $\langle W\rangle_{\rm cl}$ *versus* χ (blue dots), and mean cluster size $\langle N_{\rm cl}\rangle$ *versus* χ (green triangles).

the disappearance of clusters in the plot of the mean cluster size $\langle N_{\rm cl}\rangle$ *versus* χ (green triangles). It applies to both positive and negative χ.

Swirling clusters We show snapshots of a rotlet-dipole squirmer system with $\chi = 1.0$ in Fig. 7.8 that follow the squirmer positions over a time period of $10^4\Delta t$. The squirmer clusters visible in the snapshot are more loosely bound than for purely neutral squirmers at $r_0/(R\alpha) = 0.63$. This underlines the role of advection induced by the additional flow fields. More importantly, we observe that rotlet-dipole squirmers swirl around their cluster center. We show this for one exemplary cluster in the snapshots, where we have colored the individual squirmers, and plotted their trajectories. The sense of rotation is counter-clockwise and therefore the inverse of what *E.coli* bacteria show at no-slip walls [169, 170]. The reason for this is that our squirmers swirl with a strongly vertical orientation, whereas the bacteria are oriented parallel to the wall. According to Eq. (4.25) $\Omega_z^{\rm ff} \propto -\chi(1-3\cos^2\vartheta)(R/z)^4$. Accordingly, a sign change of the angular velocity occurs for $\cos\vartheta > \sqrt{1/3} \approx 0.58$. This threshold orientation is exceeded by the squirmers, as shown by the dashed line in the inset of Fig. 7.7 b). In conclusion, squirmers are kept on circular trajectories due to the bottom wall interaction, which leads to swirling behaviour of clusters.

In order to quantify this swirling, we define the swirling parameter W for a cluster

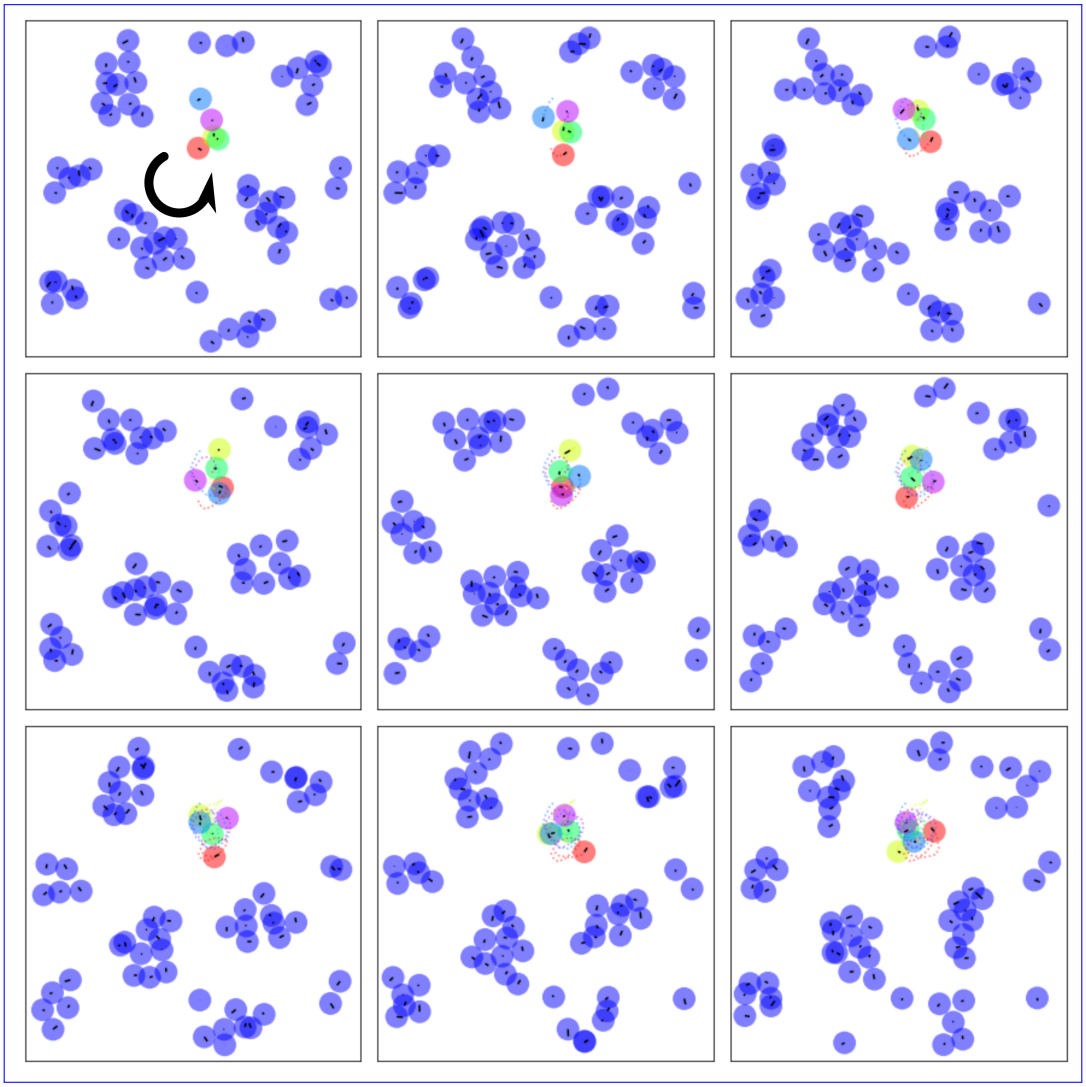

Figure 7.8: Series of snapshots that span over a time of $10^4 \Delta t$ of the system with $\chi = 1.0$, $r_0/(R\alpha) = 0.63$. We show an exemplary rotating cluster, where the individual squirmers are colored and their trajectories are plotted with dotted lines.

with cluster center $\mathbf{r}_{\mathrm{cl}}$:

$$W = \frac{1}{N_{\mathrm{cl}}} \sum_{i=1}^{N_{\mathrm{cl}}} \left\langle \frac{(\mathbf{r}_i - \mathbf{r}_{\mathrm{cl}}) \times \mathbf{v}_i}{|\mathbf{r}_i - \mathbf{r}_{\mathrm{cl}}|^2} \cdot \mathbf{e}_z \right\rangle . \tag{7.5}$$

We calculate the average $\langle W \rangle_{\mathrm{cl}}$ over all clusters and time, but choose only clusters with $N_{\mathrm{cl}} > 2$, ignoring solitary squirmers and pairs. In Fig. 7.7 d) we show the averaged swirling parameter, normalized by the inverse of the ballistic time scale R/v_0. We observe that the swirling parameter jumps from zero to around $0.15 v_0/R$ when the rotlet dipole is switched on. Varying χ, it fluctuates somewhat between $0.15 v_0/R$ and $0.2 v_0/R$. Note that we can still measure the average of W for $|\chi| = 3.3$, due to transient cluster formation. We also measured swirling for negative values of χ. As expected,

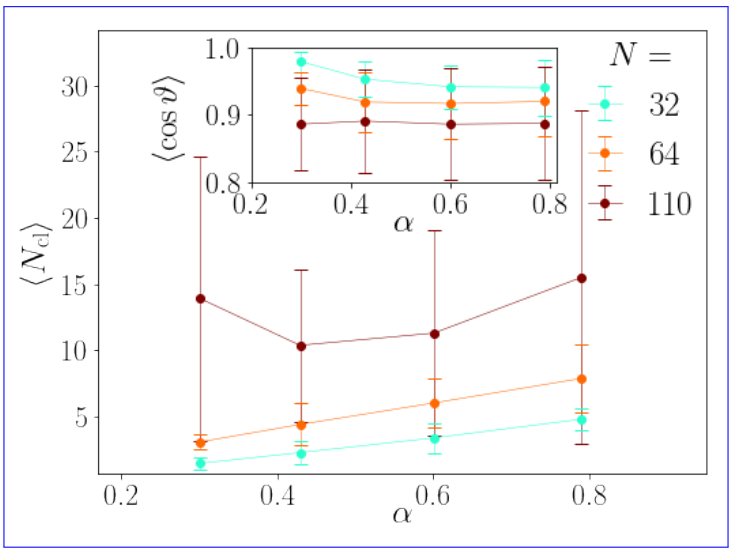

Figure 7.9: Mean cluster size *versus* α for $\beta = 0$ and a rescaled torque of $r_0/(R\alpha) = 0.32$. Inset: Mean vertical squirmer orientation *versus* α.

the chirality of the motion reverses, leading to clock-wise swirling.

7.3.4 Influence of gravity

Last, we consider the effect of changing the gravitational acceleration, and thus the velocity ratio α. We expect several overlapping effects: On the one hand, α controls the stokeslet flow fields of the squirmers. Thus, at lower α, we can expect stronger flow vorticities, and therefore more tilted squirmers. On the other hand, a lower value of α puts the squirmers closer to the bottom wall and thus intensifies the wall-induced effects. In particular, it makes neutral squirmers orient perpendicular to the wall, which is the opposite of the previous effect. On top of that, the gravitational torque also acts towards a vertical orientation, with a strength we left constant at $r_0/R\alpha = 0.32$, .

In Fig. 7.9 we plot the mean cluster size $\langle N_{\mathrm{cl}} \rangle$ versus α to investigate the competition between these effects. For $N = 32$ and $N = 64$ squirmers, we observe a monotonic increase with α. Thus, higher gravity implies smaller clusters, which can even disintegrate completely into single squirmers. In the inset, we show the mean vertical orientation. It shows a trend of increasing vertical alignment with decreasing α. This means that the hydrodynamic interaction with the wall, combined with the external torque, are able to overcome the stronger stokeslet interactions. As a result, clusters compactify for smaller α, similar to an increased gravitational torque.

The system with $N = 110$ squirmers shows a similar trend, except that the mean cluster size appears to increase for the lowest value $\alpha = 0.3$. We can not be completely sure of this, due to a large statistical error. However, we can rationalize an increase of the cluster size at strong gravity for larger squirmer numbers, since squirmers come into close contact with each other more easily under strong confinement to the bottom wall. This increases the size of the clusters found with our classification method.

7.4 Conclusions

We have demonstrated how gyrotaxis can lead to cluster formation of a bottom-heavy squirmer suspension under strong gravity: Stokeslet vorticities result in horizontal squirmer orientations and an effective attraction between squirmers, which is then stabilized by the external torque. Measuring density distributions and radial distribution functions, we investigated the structural properties of the clustering state. For neutral squirmers, gyrotactic clusters only appear at finite torques, are initially volatile, and then stabilize with increasing torque. This happens due to a reduction of the horizontal motion of squirmers. We observe a compactification of clusters at high torques. Thus the cluster size, as well as the cluster extension, have a maximum. This maximum happens at an external torque which agrees well with the value that balances the vorticity reorientation of two squirmers at close distance.

Furthermore, the distance between clusters also decreases with increasing torque. In fact, it is a characteristic length that reliably emerges from simulations at a specific torque and does not depend on initial conditions. The clustering phenomenology is mainly a result of varying the external torque, whereas the areal density has little qualitative effect.

Introducing pusher, puller and rotlet-dipole squirmers changes the clustering dynamics significantly, due to additional flow fields and vorticities. Pullers preferentially point inwards towards the cluster center, which increases the horizontal motion and thus requires larger torques for cluster formation. We do not observe pusher clusters in our simulations. Indeed, previous studies indicate that cluster formation is difficult for pushers [41, 289]. Rotlet dipole squirmers form clusters, as long as the chirality parameter $\chi < 3$. The rotlet dipole interaction with the bottom wall induces swirling motion in the clusters.

We investigated how increasing the gravitational force impacts gyrotactic cluster formation for neutral squirmers. We find that the dominating effect is the upright directional alignment induced by the hydrodynamic wall interaction for neutral squirmers. This decreases the cluster size at lower α.

Many microswimmers are bottom-heavy or experience a shape-induced gravitational torque, including Janus colloids, Volvox algae, or phytoplankton [59, 61, 71, 91]. Both effects could be used to create gyrotactic clusters, since the source of the torque is not important for the validity of our results. This even includes other forms of directional alignment, such as phototaxis [204, 304] or aerotaxis [200]. However, as previously stated, the generic hydrodynamic effects we found cannot be applied directly to these systems: for example, the phototactic torque of a Janus particle is orientation-dependent [212], and molecular diffusion is relevant for the alignment towards an oxygen source [200].

8. Conclusions and Outlook

Swimming under gravity is an intriguing aspect of the non-equilibrium motion of squirmer microswimmers. This is demonstrated by the variety of dynamical states and collective patterns displayed by squirmers under gravity, which we found in our studies. In particular, we have shown the importance of hydrodynamic interactions with surfaces and between squirmers, highlighting the role of their vorticity fields.

We have used the mesoscale simulation technique of multi-particle collision dynamics for computing the hydrodynamic flow fields and the motion of squirmers in a Newtonian fluid. A parallelized code enabled us to consider large systems and high squirmer numbers. We presented the physical properties of the simulated fluid, and calculated the effective friction experienced by a colloidal particle under gravity. Afterwards, we used this method to simulate both single squirmer systems and collective dynamics.

While for a passive particle gravity results in confinement, single squirmers perform cruising motion, stable and recurrent floating or wall sliding in our simulations, backed up by theory. We find that floating behaviour results from a height-dependent friction coefficient and a vertical orientation of the squirmer. Furthermore, puller and pusher squirmers can be pinned to the bottom-wall, and their orientation vectors are pointing vertically up for pullers and down for pushers. The occurring states depend on the ratio between self-propulsion velocity and sedimentation velocity, as well as on the squirmer parameter β, which controls the flow fields. In particular, the squirmer orientations are determined by the hydrodynamic interactions with the bottom wall, which also influence the squirmer velocities. We demonstrate the importance and subtleties of both near field and far field hydrodynamic effects.

Introducing bottom-heaviness to the single squirmer leads to *gravitaxis*, as the orientation vector develops a strong vertical bias. Consequently, neutral squirmers and pushers continuously float above the wall. Pullers keep their wall-pinned state, and the hydrodynamic wall attraction gets even stronger with strongly vertical alignment.

We demonstrate how the addition of a second squirmer with bottom-heaviness leads to coupled oscillations, reminiscent of dancing Volvox algae. If the viscous reorientation velocity due to the squirmer flow fields is similar to the bottom-heavy angular velocity, both terms balance and stable pairs can develop. This is an example of *gyrotaxis*, where, in our case, the source of the viscous reorientation is the gravitational stokeslet vorticity.

Our study of the emergent dynamics in systems with over 900 bottom-heavy squirmers reveals both sedimentation and inverted sedimentation states, known from active Brownian particles, as well as convective patterns. Plumes of neutral squirmers form

at the top wall due to gyrotaxis and sink down, despite a strong upright bias in the orientations of the individual squirmers. We find the reason for this is a reduction in friction, resulting in collective sinking. If the gravitational torque dominates the stokeslet vorticities, plumes initially emerge but then evaporate. If both gravitational and hydrodynamic angular velocities are more balanced, plumes appear continuously and convective rolls with a macroscopic circulation pattern form at the bottom of the system. The individual meandering trajectories of squirmers in the roll are also a result of gyrotaxis. Spawning clusters appear at strong torques and α slightly above one. They float above the bottom wall and have a porous structure, where single squirmers are ejected from their gap regions. For pushers and pullers, collective sinking can also occur, and we observe plumes. However, they are more fragile, due to additional hydrodynamic squirmer-squirmer interactions. In particular, force dipole vorticities constantly disturb the squirmer orientations. For the same reason, the onset of inverted sedimentation requires larger torques in these systems.

Finally, we studied the emerging clusters of bottom-heavy squirmers more quantitatively. We demonstrate that neutral squirmer clusters start forming at finite external torques, and stabilize and later compactify with growing torques, leading to more and smaller clusters. The cluster distances are a characteristic property of the system, determined by the chosen parameters α and $r_0/(R\alpha)$. Increasing the gravity also leads to stronger interactions with the bottom wall and smaller clusters. Puller clusters have a pyramidal structure where the upper layers point inwards towards the cluster center, due to hydrodynamic squirmer-wall and squirmer-squirmer interactions. Rotlet dipole squirmers form swirling clusters, as long as the rotlet dipole parameter χ is not too large. The swirling direction is consistent with the hydrodynamic wall interaction of a single squirmer.

Our studies can stimulate further research, since our setting can easily be adapted to several interesting extensions. One idea is to change the interaction of the squirmer with the interface. For example, there is recent interest in slip walls [137]. It is known that the sense of circulation of E. coli bacteria reverses compared to no-slip walls [305], which could be used to manipulate trajectories via surface patterns [306]. Microswimmers at a soft penetrable interface have also been studied recently [307].

A further idea is to change the nature of the fluid. Non-Newtonian fluids are a better approximation to many biological fluids, which strongly implicates the dynamics of microswimmers. Viscoelastic fluids allow for the breaking of the no-scallop theorem and have been found to enhance the swimming speeds of active agents [73, 76, 99]. On the other hand, swimmers in liquid crystals experience additional rotational interactions with the nematic director, which differs between pushers and pullers and can be used for guiding swimmers [308, 309]. Extensions of the MPCD algorithm for viscoelastic or liquid crystalline fluids have already been suggested or implemented [65, 310].

The nature of the swimmer can be changed, as well. This can either occur by adapting the geometry to the non-spherical cases [71, 195, 311], as demonstrated by studies of elongated squirmers [162, 167]. We expect that their collective dynamics are strongly influenced by steric interactions, which would affect the formation of plumes and clusters. On the other hand, using other swimmer types than squirmers can be an option, for example, in order to model and simulate phoretic interactions or chemotaxis

explicitly [92, 312] or in order to study specific biological organisms [76, 161, 313, 314].

Finally, we mention the exciting possibility to use machine learning for active matter research [315]. It has been mainly applied to navigation problems [316], such as steering active particles through a potential landscape [317], or navigating swimmers through flow [318, 319]. It has been suggested that phytoplankton can adapt their body shape to surrounding flows in the ocean, and thus influence its migration via gravitaxis [71]. This suggests that learning an optimal steering strategy can also apply to motion under gravity.

In summary, our studies show that the motion under gravity, exemplified by the numerical simulation of squirmers, is an intriguing aspect of microswimmer dynamics influenced by an external field. The omnipresence of gravity gives further relevance to the phenomenology we have discovered and described. Including both single-swimmer and collective dynamics, the various future avenues of research we mentioned can further deepen our understanding and, thus, may also open the door to technological applications.

A. Lamb's solution

Lamb's solution to the Stokes equations draws on the solution of the simpler Laplace equation

$$\nabla^2 f = 0 \tag{A.1}$$

in spherical coordinates. The solution can be expressed in spherical harmonics [84]:

$$f(r, \vartheta, \varphi) = \sum_{n=-\infty}^{\infty} f_n \tag{A.2}$$

with

$$f_n = r^n \sum_{m=0}^{n} n P_n^m(\cos\vartheta)(a_{mn}\cos(m\varphi) + b_{mn}\sin(m\varphi)). \tag{A.3}$$

Here, P_n^m are the associated Legendre polynomials of degree n and order m. They are defined via the ordinary Legendre polynomials P_n

$$P_n^m(x) = (-1)^m (1-x^2)^{m/2} \frac{d^m}{dx^m} P_n(x) \tag{A.4}$$

The first three ordinary Legendre polynomials are: $P_0 = 1$, $P_1 = x$, and $P_2 = \frac{1}{2}(3x^2 - 1)$.

The usefulness of the series solution to the Stokes equation is given since taking the divergence of the Stokes equations while exploiting incompressibility leads to the Laplace equation for the pressure field

$$\nabla^2 p = 0. \tag{A.5}$$

Hence we can write the pressure as a series

$$p = \sum_{n=-\infty}^{\infty} p_n, \tag{A.6}$$

where the p_n take the form of eq. (A.3). Lamb's solution then constructs homogeneous and particular solutions to the Stokes equation [81, 82, 84], that we present in the following. For the homogeneous solution we have to solve for $\nabla^2 \mathbf{u} = 0$, therefore we can write $\mathbf{u}$ again as an expansion in spherical harmonics $\mathbf{u}_n$ which all satisfy both the Laplace equation and the relation $\nabla \cdot \mathbf{u}_n = 0$ individually [84]. Using $\nabla^2 \mathbf{u}_n =$

$\nabla(\nabla \cdot \mathbf{u}_n) - \nabla \times (\nabla \times \mathbf{u}_n)$, we immediately see that we can write

$$\nabla \times \mathbf{u}_n = \nabla \chi_n \tag{A.7}$$

with χ_n that are also harmonic. Furthermore the term $\mathbf{r} \cdot \mathbf{u}_n =: \phi_n$ is also harmonic, which can easily be verified. But then consider

$$\nabla \times (\mathbf{r}\chi_n) = \nabla \chi_n \times \mathbf{r} = (\mathbf{r} \cdot \nabla)\mathbf{u}_n - \nabla(\mathbf{u}_n \cdot r) + \mathbf{u}_n. \tag{A.8}$$

It follows with $(\mathbf{r} \cdot \nabla)\mathbf{u}_n = n\mathbf{u}_n$ (from eq. (A.3)) that

$$(n+1)\mathbf{u}_n = \nabla \phi_n + \nabla \times (\mathbf{r}\chi_n). \tag{A.9}$$

The factor $(n+1)$ is unimportant for the definition and is therefore dropped in the following. A particular solution in spherical coordinates, using the spherical harmonics of the pressure p_n, is given by [81, 82]

$$\mathbf{u} = \sum_{\substack{n=-\infty \\ n \neq 1}}^{\infty} \left[\frac{(n+3)r^2 \nabla p_n - 2n\mathbf{r}p_n}{2\eta(n+1)(2n+3)} \right]. \tag{A.10}$$

Combining the particular and the homogenous solution yields the formula for Lamb's solution in spherical coordinates, shown in Section 2.1.3.

B. Image singularities at a no-slip wall

In the following, we present the image systems of Stokes flow singularities at a no-slip wall. They can be found in Ref. [87]. The complete singularities, as with the Blake tensor, consist of the image system and the original singularity, and are zero at $z = 0$.

The image system for the stokeslet was presented in Section 2.3:

$$\begin{aligned}\mathbf{G}^*_S(\mathbf{r}-\mathbf{r}_0,\mathbf{e}) = &-\mathbf{G}_S(\mathbf{r}-\mathbf{r}^*_0,\mathbf{e})+\\ &\sin\vartheta\left[2\Delta z\mathbf{G}_D(\mathbf{r}-\mathbf{r}^*_0,\mathbf{e}_\rho,\mathbf{e}_z)-2\Delta z^2\mathbf{G}_{SD}(\mathbf{r}-\mathbf{r}^*_0,\mathbf{e}_\rho)\right]+\\ &\cos\vartheta\left[-2\Delta z\mathbf{G}_D(\mathbf{r}-\mathbf{r}^*_0,\mathbf{e}_z,\mathbf{e}_z)+2\Delta z^2\mathbf{G}_{SD}(\mathbf{r}-\mathbf{r}^*_0,\mathbf{e}_z)\right].\end{aligned} \tag{B.1}$$

The image system of the force dipole is

$$\begin{aligned}\mathbf{G}^*_D(\mathbf{r}-\mathbf{r}_0,\mathbf{e},\mathbf{e}) = &\sin^2\vartheta\left[-\mathbf{G}_D(\mathbf{r}-\mathbf{r}^*_0,\mathbf{e}_\rho,\mathbf{e}_\rho)+\right.\\ &\left.2\Delta z\mathbf{G}_Q(\mathbf{r}-\mathbf{r}^*_0,\mathbf{e}_\rho,\mathbf{e}_\rho,\mathbf{e}_z)-2\Delta z^2\mathbf{G}_{SQ}(\mathbf{r}-\mathbf{r}^*_0,\mathbf{e}_\rho,\mathbf{e}_\rho)\right]+\\ &\cos^2\vartheta\left[-\mathbf{G}_D(\mathbf{r}-\mathbf{r}^*_0,\mathbf{e}_z,\mathbf{e}_z)\right.\\ &+4\Delta z\mathbf{G}_{SD}((\mathbf{r}-\mathbf{r}^*_0,\mathbf{e}_z)+2\Delta z\mathbf{G}_Q(\mathbf{r}-\mathbf{r}^*_0,\mathbf{e}_z,\mathbf{e}_z,\mathbf{e}_z)-\\ &\left.2\Delta z^2\mathbf{G}_{SQ}(\mathbf{r}-\mathbf{r}^*_0,\mathbf{e}_z,\mathbf{e}_z)\right].\end{aligned} \tag{B.2}$$

The image system of the source dipole is

$$\begin{aligned}\mathbf{G}^*_{SD}(\mathbf{r}-\mathbf{r}_0,\mathbf{e}) = &\sin\vartheta\left[-\mathbf{G}_{SD}(\mathbf{r}-\mathbf{r}^*_0,\mathbf{e}_\rho)+\right.\\ &\left.2\mathbf{G}_Q(\mathbf{r}-\mathbf{r}^*_0,\mathbf{e}_\rho,\mathbf{e}_z,\mathbf{e}_z)-2\Delta z\mathbf{G}_{SQ}(\mathbf{r}-\mathbf{r}^*_0,\mathbf{e}_\rho,\mathbf{e}_z)\right]+\\ &\cos\vartheta\left[-3\mathbf{G}_{SD}(\mathbf{r}-\mathbf{r}^*_0,\mathbf{e}_z)\right.\\ &\left.-2\mathbf{G}_Q(\mathbf{r}-\mathbf{r}^*_0,\mathbf{e}_z,\mathbf{e}_z,\mathbf{e}_z)+2\Delta z\mathbf{G}_{SQ}(\mathbf{r}-\mathbf{r}^*_0,\mathbf{e}_z,\mathbf{e}_z)\right].\end{aligned} \tag{B.3}$$

The image system of the rotlet is

$$\begin{aligned}\mathbf{R}^*(\mathbf{r}-\mathbf{r}_0,\mathbf{e},\mathbf{e}) = &\sin\vartheta\left[-\mathbf{R}(\mathbf{r}-\mathbf{r}^*_0,\mathbf{e}_\rho)+2\Delta z\mathbf{G}_{SD}(\mathbf{r}-\mathbf{r}^*_0,\mathbf{e}_\varphi)-\right.\\ &\left.\mathbf{G}_D(\mathbf{r}-\mathbf{r}^*_0,\mathbf{e}_\varphi,\mathbf{e}_z)-\mathbf{G}_D(\mathbf{r}-\mathbf{r}^*_0,\mathbf{e}_z,\mathbf{e}_\varphi)\right]+\\ &\cos\vartheta\mathbf{R}(\mathbf{r}-\mathbf{r}^*_0,\mathbf{e}_z).\end{aligned} \tag{B.4}$$

Finally, the image system of the rotlet dipole is

$$\begin{aligned}\mathbf{R}_D^*(\mathbf{r}-\mathbf{r}_0,\mathbf{e},\mathbf{e}) = &\sin^2\vartheta\,[-\mathbf{R}_D(\mathbf{r}-\mathbf{r}_0^*,\mathbf{e}_\rho,\mathbf{e}_\rho)- \\ &\mathbf{G}_Q(\mathbf{r}-\mathbf{r}_0^*,\mathbf{e}_\rho,\mathbf{e}_\varphi,\mathbf{e}_z)-\mathbf{G}_Q(\mathbf{r}-\mathbf{r}_0^*,\mathbf{e}_\rho,\mathbf{e}_z,\mathbf{e}_\varphi)+ \\ &2\Delta z\mathbf{G}_{SQ}(\mathbf{r}-\mathbf{r}_0^*,\mathbf{e}_\rho,\mathbf{e}_\varphi)]+ \\ &\cos^2\vartheta\mathbf{R}_D(\mathbf{r}-\mathbf{r}_0^*,\mathbf{e}_z,\mathbf{e}_z)+ \\ &\sin\vartheta\cos\vartheta\,[\mathbf{R}_D(\mathbf{r}-\mathbf{r}_0^*,\mathbf{e}_z,\mathbf{e}_\rho)-\mathbf{R}_D(\mathbf{r}-\mathbf{r}_0^*,\mathbf{e}_\rho,\mathbf{e}_z)+ \\ &2\mathbf{G}_{SD}(\mathbf{r}-\mathbf{r}_0^*,\mathbf{e}_\varphi)+ \\ &\mathbf{G}_Q(\mathbf{r}-\mathbf{r}_0^*,\mathbf{e}_\varphi,\mathbf{e}_z,\mathbf{e}_z)+\mathbf{G}_Q(\mathbf{r}-\mathbf{r}_0^*,\mathbf{e}_\varphi,\mathbf{e}_\varphi,\mathbf{e}_z)- \\ &2\Delta z\mathbf{G}_{SQ}(\mathbf{r}-\mathbf{r}_0^*,\mathbf{e}_\varphi,\mathbf{e}_z)]\,.\end{aligned} \tag{B.5}$$

C. List of symbols

Table C.1: Overview of physical parameters

Parameter	R	v_0	v_{sed}	α
meaning	squirmer radius	active velocity	sedimentation velocity	velocity ratio
Parameter	β	χ	r_0	$r_0/(R\alpha)$
meaning	force dipole parameter	rotlet dipole parameter	center of mass shift	rescaled bottom-heavy torque
Parameter	γ, $\mathbf{\Gamma}$	μ, $\mathbf{M}$	Re	Pe
meaning	translational friction	translational mobility	Reynolds number	active Péclet number
Parameter	Ω	$\mathbf{u}$	$\boldsymbol{\omega}$	Δ
meaning	angular velocity	flow field	flow vorticity	typical cluster distance

Table C.2: Overview of simulation parameters

Parameter	a_0	m_0	T_0	Δt
meaning	edge length of collision cell	mass of fluid particle	temperature of fluid	duration of streaming step
Parameter	n_{fl}	η	ν	$\mathbf{d}_{\text{shift}}$
meaning	fluid particle number density	dynamic fluid viscosity	kinematic fluid viscosity	grid shift vector

List of publications

Main publications

[A] Felix Rühle, Johannes Blaschke, Jan-Timm Kuhr, and Holger Stark, *Gravity-induced dynamics of a squirmer microswimmer in wall proximity*, New J. Phys. **20**, 025003 (2018).

[B] Felix Rühle, and Holger Stark, *Emergent collective dynamics of bottom-heavy squirmers under gravity*, Eur. Phys. J. E **43**, 26 (2020).

[C] Felix Rühle, Arne W. Zantop, and Holger Stark, *Gyrotactic cluster formation of bottom-heavy squirmers*, Eur. Phys. J. E **45**, 26 (2022).

Publications connected to this work

[D] Jan-Timm Kuhr, Johannes Blaschke, Felix Rühle, and Holger Stark, *Collective Sedimentation of Squirmers under Gravity*, Soft Matter **13**, 7548 (2017).

[E] Jan-Timm Kuhr, Felix Rühle, and Holger Stark, *Collective Dynamics in a Monolayer of Squirmers Confined to a Boundary by Gravity*, Soft Matter **15**, 5685 (2019).

Other publications

(a) Felix Rühle, Matthias Sandbrink, Holger Stark, and Michael Schmiedeberg, *Effective substrate potentials with quasicrystalline symmetry depend on the size of the absorbed particles*, Eur. Phys. J. E **38**, 54 (2015).

(b) Felix Rühle, *Vielteilchendynamik in der inertialen Mikrofluidik: Eine Simulationsstudie unter Verwendung der Lattice-Boltzmann-Methode.* BestMasters book series, Springer-Verlag, 2017.

(c) Christian Schaaf, Felix Rühle, and Holger Stark, *A flowing pair of particles in inertial microfluidics*, Soft Matter **15**, 1988 (2019).

(d) Felix Rühle, Christian Schaaf, and Holger Stark, *Optimal control of colloidal trajectories in inertial microfluidics using the Saffman effect*, Micromachines **11**, 592 (2020).

(e) Akash Choudhary, Subhechchha Paul, Felix Rühle, and Holger Stark, *How inertial lift affects the dynamics of a microswimmer in Poiseuille flow*, Commun. Phys. **5**, 14 (2022)

Bibliography

[1] G. Gompper et al. The 2020 motile active matter roadmap. *J. Phys.: Condens. Mat.* **32**, 193001, 2020.

[2] S. Ramaswamy. The mechanics and statistics of active matter. *Annu. Rev. Condens. Matter Phys.* **1**, 323–345, 2010.

[3] M. Marchetti et al. Hydrodynamics of soft active matter. *Rev. Mod. Phys.* **85**, 1143, 2013.

[4] T. Vicsek and A. Zafeiris. Collective motion. *Phys. Rep.* **517**, 71–140, 2012.

[5] A. Zöttl and H. Stark. Emergent behavior in active colloids. *J. Phys.: Condens. Mat.* **28**, 253001, 2016.

[6] I. Buttinoni et al. Dynamical clustering and phase separation in suspensions of self-propelled colloidal particles. *Phys. Rev. Lett.* **110**, 238301, 2013.

[7] M. E. Cates and J. Tailleur. Motility-induced phase separation. *Annu. Rev. Condens. Matter Phys.* **6**, 219–244, 2015.

[8] I. Theurkauff, C. Cottin-Bizonne, J. Palacci, C. Ybert, and L. Bocquet. Dynamic clustering in active colloidal suspensions with chemical signaling. *Phys. Rev. Lett.* **108**, 268303, 2012.

[9] O. Pohl and H. Stark. Dynamic clustering and chemotactic collapse of self-phoretic active particles. *Phys. Rev. Lett.* **112**, 238303, 2014.

[10] M. F. Copeland and D. B. Weibel. Bacterial swarming: a model system for studying dynamic self-assembly. *Soft Matter* **5**, 1174–1187, 2009.

[11] H. Jeckel et al. Learning the space-time phase diagram of bacterial swarm expansion. *Proc. Natl. Acad. Sci. U.S.A.* **116**, 1489–1494, 2019.

[12] A. Cavagna et al. Scale-free correlations in starling flocks. *Proc. Natl. Acad. Sci. U.S.A.* **107**, 11865–11870, 2010.

[13] D. Weihs. Hydromechanics of fish schooling. *Nature* **241**, 290–291, 1973.

[14] I. Zuriguel et al. Effect of obstacle position in the flow of sheep through a narrow door. *Phys. Rev. E* **94**, 032302, 2016.

[15] J. O. Kessler. Hydrodynamic focusing of motile algal cells. *Nature* **313**, 218, 1985.

[16] J. Dunkel et al. Fluid dynamics of bacterial turbulence. *Phys. Rev. Lett.* **110**, 228102, 2013.

[17] J. Elgeti, R. G. Winkler, and G. Gompper. Physics of microswimmers-single particle motion and collective behavior: a review. *Rep. Prog. Phys.* **78**, 056601, 2015.

[18] D. Alizadehrad, T. Krüger, M. Engstler, and H. Stark. Simulating the complex cell design of Trypanosoma brucei and its motility. *PLoS Comput. Biol.* **11**, e1003967, 2015.

[19] T. Krüger, S. Schuster, and M. Engstler. Beyond blood: African trypanosomes on the move. *Trends Parasitol.* **34**, 1056–1067, 2018.

[20] G. Vizsnyiczai et al. Light controlled 3D micromotors powered by bacteria. *Nat. Commun.* **8**, 1–7, 2017.

[21] H. Xu et al. Sperm-hybrid micromotor for targeted drug delivery. *ACS nano* **12**, 327–337, 2018.

[22] M. M. Stanton et al. Magnetotactic bacteria powered biohybrids target E. coli biofilms. *ACS nano* **11**, 9968–9978, 2017.

[23] W. M. Durham et al. Turbulence drives microscale patches of motile phytoplankton. *Nat. Commun.* **4**, 1–7, 2013.

[24] J. Wang. *Nanomachines: fundamentals and applications*. John Wiley & Sons, 2013.

[25] R. Golestanian, T. B. Liverpool, and A. Ajdari. Propulsion of a molecular machine by asymmetric distribution of reaction products. *Phys. Rev. Lett.* **94**, 220801, 2005.

[26] J. R. Howse et al. Self-Motile Colloidal Particles: From Directed Propulsion to Random Walk. *Phys. Rev. Lett.* **99**, 048102, 2007.

[27] M. Schmitt and H. Stark. Swimming active droplet: A theoretical analysis. *Europhys. Lett.* **101**, 44008, 2013.

[28] S. Herminghaus et al. Interfacial mechanisms in active emulsions. *Soft Matter* **10**, 7008–7022, 2014.

[29] W. Wang, W. Duan, S. Ahmed, T. E. Mallouk, and A. Sen. Small power: Autonomous nano-and micromotors propelled by self-generated gradients. *Nano Today* **8**, 531–554, 2013.

[30] S. Sánchez, L. Soler, and J. Katuri. Chemically powered micro-and nanomotors. *Ang. Chem. Int. Edit.* **54**, 1414–1444, 2015.

[31] L. Wang, A. Kaeppler, D. Fischer, and J. Simmchen. Photocatalytic TiO2 micromotors for removal of microplastics and suspended matter. *ACS Appl. Mater. Inter.* **11**, 32937–32944, 2019.

[32] T. Vicsek, A. Czirók, E. Ben-Jacob, I. Cohen, and O. Shochet. Novel type of phase transition in a system of self-driven particles. *Phys. Rev. Lett.* **75**, 1226, 1995.

[33] P. Romanczuk, M. Bär, W. Ebeling, B. Lindner, and L. Schimansky-Geier. Active brownian particles. *Eur. Phys. J. Spec. Top.* **202**, 1–162, 2012.

[34] D. Saintillan and M. J. Shelley. Orientational order and instabilities in suspensions of self-locomoting rods. *Phys. Rev. Lett.* **99**, 058102, 2007.

[35] M. Lighthill. On the squirming motion of nearly spherical deformable bodies through liquids at very small Reynolds numbers. *Commun. Pur. Appl. Math.* **5**, 109–118, 1952.

[36] J. Blake. A spherical envelope approach to ciliary propulsion. *J. Fluid Mech.* **46**, 199–208, 1971.

[37] E. Lauga and T. R. Powers. The hydrodynamics of swimming microorganisms. *Rep. Prog. Phys.* **72**, 096601, 2009.

[38] K. Schaar, A. Zöttl, and H. Stark. Detention times of microswimmers close to surfaces: Influence of hydrodynamic interactions and noise. *Phys. Rev. Lett.* **115**, 038101, 2015.

[39] R. Aditi Simha and S. Ramaswamy. Hydrodynamic Fluctuations and Instabilities in Ordered Suspensions of Self-Propelled Particles. *Phys. Rev. Lett.* **89**, 058101, 2002.

[40] D. Saintillan and M. J. Shelley. Emergence of coherent structures and large-scale flows in motile suspensions. *J. R. Soc. Interface* **9**, 571–585, 2011.

[41] F. Alarcón and I. Pagonabarraga. Spontaneous aggregation and global polar ordering in squirmer suspensions. *J. Mol. Liq.* **185**, 56–61, 2013.

[42] A. Zöttl and H. Stark. Hydrodynamics determines collective motion and phase behavior of active colloids in quasi-two-dimensional confinement. *Phys. Rev. Lett.* **112**, 118101, 2014.

[43] J. Blaschke, M. Maurer, K. Menon, A. Zöttl, and H. Stark. Phase separation and coexistence of hydrodynamically interacting microswimmers. *Soft Matter* **12**, 9821–9831, 2016.

[44] J. Stenhammar, C. Nardini, R. W. Nash, D. Marenduzzo, and A. Morozov. Role of Correlations in the Collective Behavior of Microswimmer Suspensions. *Phys. Rev. Lett.* **119**, 028005, 2017.

[45] W. Ludwig. Zur Theorie der Flimmerbewegung (Dynamik, Nutzeffekt, Energiebilanz). *Z. vergl. Physiol.* **13**, 397–504, 1930.

[46] E. M. Purcell. Life at low Reynolds number. *Am. J. Phys.* **45**, 3–11, 1977.

[47] H. C. Berg and R. A. Anderson. Bacteria swim by rotating their flagellar filaments. *Nature* **245**, 380–382, 1973.

[48] D. R. Brumley, M. Polin, T. J. Pedley, and R. E. Goldstein. Hydrodynamic synchronization and metachronal waves on the surface of the colonial alga Volvox carteri. *Phys. Rev. Lett.* **109**, 268102, 2012.

[49] G. E. Hutchinson. The paradox of the plankton. *Am. Nat.* **95**, 137–145, 1961.

[50] F. d'Ovidio, S. De Monte, S. Alvain, Y. Dandonneau, and M. Lévy. Fluid dynamical niches of phytoplankton types. *Proc. Natl. Acad. Sci. U.S.A.* **107**, 18366–18370, 2010.

[51] H. Stark. Swimming in external fields. *Eur. Phys. J. Spec. Top.* **225**, 2369–2387, 2016.

[52] J. Tailleur and M. Cates. Sedimentation, trapping, and rectification of dilute bacteria. *Europhys. Lett.* **86**, 60002, 2009.

[53] J. Palacci, C. Cottin-Bizonne, C. Ybert, and L. Bocquet. Sedimentation and Effective Temperature of Active Colloidal Suspensions. *Phys. Rev. Lett.* **105**, 088304, 2010.

[54] M. Enculescu and H. Stark. Active colloidal suspensions exhibit polar order under gravity. *Phys. Rev. Lett.* **107**, 058301, 2011.

[55] F. Ginot et al. Nonequilibrium equation of state in suspensions of active colloids. *Phys. Rev. X* **5**, 011004, 2015.

[56] T. Pedley and J. Kessler. Hydrodynamic phenomena in suspensions of swimming microorganisms. *Annu. Rev. Fluid Mech.* **24**, 313–358, 1992.

[57] J. O. Kessler. Co-operative and concentrative phenomena of swimming microorganisms. *Contemp. Phys.* **26**, 147–166, 1985.

[58] W. M. Durham, E. Climent, and R. Stocker. Gyrotaxis in a steady vortical flow. *Phys. Rev. Lett.* **106**, 238102, 2011.

[59] B. Ten Hagen et al. Gravitaxis of asymmetric self-propelled colloidal particles. *Nat. Commun.* **5**, 4829, 2014.

[60] T. Pedley. Gyrotaxis in uniform vorticity. *J. Fluid Mech.* **762**, 2015.

[61] K. Drescher et al. Dancing volvox: hydrodynamic bound states of swimming algae. *Phys. Rev. Lett.* **102**, 168101, 2009.

[62] U. Timm and A. Okubo. Gyrotaxis: A plume model for self-focusing microorganisms. *B. Math. Biol.* **56**, 187–206, 1994.

[63] I. Llopis and I. Pagonabarraga. Dynamic regimes of hydrodynamically coupled self-propelling particles. *Europhys. Lett.* **75**, 999, 2006.

[64] A. Malevanets and R. Kapral. Mesoscopic model for solvent dynamics. *J. Chem. Phys.* **110**, 8605–8613, 1999.

[65] G. Gompper, T. Ihle, D. Kroll, and R. Winkler. "Multi-particle collision dynamics: a particle-based mesoscale simulation approach to the hydrodynamics of complex fluids". *Advanced computer simulation approaches for soft matter sciences III*. Springer, 2009, pp. 1–87.

[66] S. Uppaluri et al. Flow loading induces oscillatory trajectories in a bloodstream parasite. *Biophys. J.* **103**, 1162–1169, 2012.

[67] H. C. Berg. *E. coli in Motion*. Springer, 2004.

[68] S. Suarez and A. Pacey. Sperm transport in the female reproductive tract. *Hum. Reprod. Update* **12**, 23–37, 2006.

[69] K. Miki and D. E. Clapham. Rheotaxis guides mammalian sperm. *Curr. Biol.* **23**, 443–452, 2013.

[70] W. M. Durham, J. O. Kessler, and R. Stocker. Disruption of vertical motility by shear triggers formation of thin phytoplankton layers. *Science* **323**, 1067–1070, 2009.

[71] A. Sengupta, F. Carrara, and R. Stocker. Phytoplankton can actively diversify their migration strategy in response to turbulent cues. *Nature* **543**, 555, 2017.

[72] L. Zhu, E. Lauga, and L. Brandt. Self-propulsion in viscoelastic fluids: Pushers vs. pullers. *Phys. Fluids* **24**, 051902, 2012.

[73] E. E. Riley and E. Lauga. Enhanced active swimming in viscoelastic fluids. *Europhys. Lett.* **108**, 34003, 2014.

[74] J. R. Gomez-Solano, A. Blokhuis, and C. Bechinger. Dynamics of self-propelled Janus particles in viscoelastic fluids. *Phys. Rev. Lett.* **116**, 138301, 2016.

[75] S. Gómez, F. A. Godínez, E. Lauga, and R. Zenit. Helical propulsion in shear-thinning fluids. *J. Fluid Mech.* **812**, 2017.

[76] A. Zöttl and J. M. Yeomans. Enhanced bacterial swimming speeds in macromolecular polymer solutions. *Nat. Phys.* **15**, 554–558, 2019.

[77] L. D. Landau and E. M. Lifshitz. *Fluid Mechanics: Course of Theoretical Physics, Volume 6*. Elsevier, 2013.

[78] F. Irgens. *Continuum mechanics*. Springer Science & Business Media, 2008.

[79] R. Aris. *Vectors, tensors and the basic equations of fluid mechanics*. Courier Corporation, 2012.

[80] G. Batchelor. *An introduction to fluid dynamics*. Cambridge University Press, 1967.

[81] J. Happel and H. Brenner. *Low Reynolds Number Hydrodynamics with Special Application to Particulate Media*. Prentice-Hall, 1965.

[82] S. Kim and S. J. Karrila. *Microhydrodynamics: principles and selected applications*. Courier Corporation, 2013.

[83] C. W. Oseen. Über die Stokes' sche Formel und über eine verwandte Aufgabe in der Hydrodynamik. *Ark. Mat. Astronom. Fys.* **6**, 1, 1910.

[84] H. Lamb. *Hydrodynamics*. Cambridge University Press, 1932.

[85] C. Pozrikidis. *Boundary integral and singularity methods for linearized viscous flow*. Cambridge University Press, 1992.

[86] A. T. Chwang and T. Y.-T. Wu. Hydromechanics of low-Reynolds-number flow. Part 2. Singularity method for Stokes flows. *J. Fluid Mech.* **67**, 787–815, 1975.

[87] S. E. Spagnolie and E. Lauga. Hydrodynamics of self-propulsion near a boundary: predictions and accuracy of far-field approximations. *J. Fluid Mech.* **700**, 105–147, 2012.

[88] H. Brenner. The Stokes resistance of an arbitrary particle. *Chem. Eng. Sci.* **18**, 1–25, 1963.

[89] E. Lushi, V. Kantsler, and R. E. Goldstein. Scattering of biflagellate microswimmers from surfaces. *Phys. Rev. E* **96**, 023102, 2017.

[90] A. K. Balin, A. Zöttl, J. M. Yeomans, and T. N. Shendruk. Biopolymer dynamics driven by helical flagella. *Phys. Rev. Fluids* **2**, 113102, 2017.

[91] J. Simmchen et al. Topographical pathways guide chemical microswimmers. *Nat. Commun.* **7**, 2016.

[92] M.-J. Huang, J. Schofield, and R. Kapral. Chemotactic and hydrodynamic effects on collective dynamics of self-diffusiophoretic Janus motors. *New J. Phys.* **19**, 125003, 2017.

[93] M. Seyrich, A. Palugniok, and H. Stark. Traveling concentration pulses of bacteria in a generalized Keller–Segel model. *New J. Phys.* **21**, 103001, 2019.

[94] H. H. Wensink et al. Meso-scale turbulence in living fluids. *Proc. Natl. Acad. Sci. U.S.A.* **109**, 14308–14313, 2012.

[95] A. P. Solon, J. Stenhammar, M. E. Cates, Y. Kafri, and J. Tailleur. Generalized thermodynamics of motility-induced phase separation: phase equilibria, Laplace pressure, and change of ensembles. *New J. Phys.* **20**, 075001, 2018.

[96] H. Reinken et al. Organizing bacterial vortex lattices by periodic obstacle arrays. *Commun. Phys.* **3**, 1–9, 2020.

[97] E. Lauga. Life around the scallop theorem. *Soft Matter* **7**, 3060–3065, 2011.

[98] T. Qiu et al. Swimming by reciprocal motion at low Reynolds number. *Nat. Commun.* **5**, 1–8, 2014.

[99] K. Han, C. W. Shields IV, B. Bharti, P. E. Arratia, and O. D. Velev. Active reversible swimming of magnetically assembled "microscallops" in non-Newtonian fluids. *Langmuir* **36**, 7148–7154, 2020.

[100] O. S. Pak and E. Lauga. Generalized squirming motion of a sphere. *J. Eng. Math.* **88**, 1–28, 2014.

[101] W. Yan and J. F. Brady. The force on a boundary in active matter. *J. Fluid Mech.* **785**, 2015.

[102] B. J. Nelson, I. K. Kaliakatsos, and J. J. Abbott. Microrobots for minimally invasive medicine. *Annu. Rev. Biomed. Eng.* **12**, 55–85, 2010.

[103] H.-W. Huang et al. Adaptive locomotion of artificial microswimmers. *Sci. Adv.* **5**, eaau1532, 2019.

[104] R. F. Ismagilov, A. Schwartz, N. Bowden, and G. M. Whitesides. Autonomous movement and self-assembly. *Ang. Chem. Int. Edit.* **41**, 652–654, 2002.

[105] A. Bricard, J.-B. Caussin, N. Desreumaux, O. Dauchot, and D. Bartolo. Emergence of macroscopic directed motion in populations of motile colloids. *Nature* **503**, 95–98, 2013.

[106] J. Palacci, S. Sacanna, A. P. Steinberg, D. J. Pine, and P. M. Chaikin. Living crystals of light-activated colloidal surfers. *Science* **339**, 936–940, 2013.

[107] S. Saha, R. Golestanian, and S. Ramaswamy. Clusters, asters, and collective oscillations in chemotactic colloids. *Phys. Rev. E* **89**, 062316, 2014.

[108] J. Adler. Chemotaxis in Bacteria: Motile Escherichia coli migrate in bands that are influenced by oxygen and organic nutrients. *Science* **153**, 708–716, 1966.

[109] A. Czirok, I. M. Jánosi, and J. O. Kessler. Bioconvective dynamics: dependence on organism behaviour. *J. Exp. Biol.* **203**, 3345–3354, 2000.

[110] F. P. Bretherton and Lord Rothschild. Rheotaxis of spermatozoa. *Proc. R. Soc. Lond. B Biol. Sci.* **153**, 490–502, 1961.

[111] H.-R. Jiang, N. Yoshinaga, and M. Sano. Active Motion of a Janus Particle by Self-Thermophoresis in a Defocused Laser Beam. *Phys. Rev. Lett.* **105**, 268302, 2010.

[112] C. Lozano, B. Ten Hagen, H. Löwen, and C. Bechinger. Phototaxis of synthetic microswimmers in optical landscapes. *Nat. Commun.* **7**, 1–10, 2016.

[113] J. Burelbach and H. Stark. Determining phoretic mobilities with Onsager's reciprocal relations: Electro- and thermophoresis revisited. *Eur. Phys. J. E* **42**, 1–9, 2019.

[114] S. Auschra, A. Bregulla, K. Kroy, and F. Cichos. Thermotaxis of Janus particles. *Eur. Phys. J. E* **44**, 1–15, 2021.

[115] N. Waisbord, C. T. Lefèvre, L. Bocquet, C. Ybert, and C. Cottin-Bizonne. Destabilization of a flow focused suspension of magnetotactic bacteria. *Phys. Rev. Fluids* **1**, 053203, 2016.

[116] K. Taneda. Geotactic behavior in Paramecium caudatum. 1: Geotaxis assay of individual specimen. *Zoological science* **4**, 781–788, 1987.

[117] S. M. Block, J. E. Segall, and H. C. Berg. Impulse responses in bacterial chemotaxis. *Cell* **31**, 215–226, 1982.

[118] H. Machemer, S. Machemer-Röhnisch, R. Bräucker, and K. Takahashi. Gravikinesis in Paramecium: theory and isolation of a physiological response to the natural gravity vector. *J. Comp. Physiol. A* **168**, 1–12, 1991.

[119] M. Ooya, Y. Mogami, A. Izumikurotani, and S. A. Baba. Gravity-induced changes in propulsion of Paramecium caudatum: a possible role of gravireception in protozoan behaviour. *J. Exp. Biol.* **163**, 153–167, 1992.

[120] Y. Mogami, J. Ishii, and S. A. Baba. Theoretical and experimental dissection of gravity-dependent mechanical orientation in gravitactic microorganisms. *Biol. Bull.* **201**, 26–33, 2001.

[121] A. Roberts and F. Deacon. Gravitaxis in motile micro-organisms: the role of fore–aft body asymmetry. *J. Fluid Mech.* **452**, 405–423, 2002.

[122] S. Thutupalli, R. Seemann, and S. Herminghaus. Swarming behavior of simple model squirmers. *New J. Phys.* **13**, 073021, 2011.

[123] H. C. Berg. The rotary motor of bacterial flagella. *Annu. Rev. Biochem.* **72**, 19–54, 2003.

[124] S. H. Larsen, R. W. Reader, E. N. Kort, W.-W. Tso, and J. Adler. Change in direction of flagellar rotation is the basis of the chemotactic response in Escherichia coli. *Nature* **249**, 74–77, 1974.

[125] V. Sourjik. Receptor clustering and signal processing in E. coli chemotaxis. *Trends Microbiol.* **12**, 569–576, 2004.

[126] G. Lowe, M. Meister, and H. C. Berg. Rapid rotation of flagellar bundles in swimming bacteria. *Nature* **325**, 637–640, 1987.

[127] K. Y. Wan and G. Jékely. Origins of eukaryotic excitability. *Philos. T. R. Soc. B* **376**, 20190758, 2021.

[128] R. Jeanneret, M. Contino, and M. Polin. A brief introduction to the model microswimmer Chlamydomonas reinhardtii. *Eur. Phys. J. Spec.Top.* **225**, 2141–2156, 2016.

[129] D. Cortese and K. Y. Wan. Control of helical navigation by three-dimensional flagellar beating. *Phys. Rev. Lett.* **126**, 088003, 2021.

[130] K. Josef, J. Saranak, and K. W. Foster. Ciliary behavior of a negatively phototactic Chlamydomonas reinhardtii. *Cell Motil. Cytokel.* **61**, 97–111, 2005.

[131] S. Michelin and E. Lauga. Efficiency optimization and symmetry-breaking in a model of ciliary locomotion. *Phys. Fluids* **22**, 111901, 2010.

[132] T. J. Pedley, D. R. Brumley, and R. E. Goldstein. Squirmers with swirl: a model for Volvox swimming. *J. Fluid Mech.* **798**, 165–186, 2016.

[133] R. Dreyfus et al. Microscopic artificial swimmers. *Nature* **437**, 862–865, 2005.

[134] T. Mirkovic, N. S. Zacharia, G. D. Scholes, and G. A. Ozin. Nanolocomotion—catalytic nanomotors and nanorotors. *small* **6**, 159–167, 2010.

[135] I. Buttinoni, G. Volpe, F. Kümmel, G. Volpe, and C. Bechinger. Active Brownian motion tunable by light. *J. Phys.: Condens. Mat.* **24**, 284129, 2012.

[136] A. Walther and A. H. Müller. Janus particles: synthesis, self-assembly, physical properties, and applications. *Chem. Rev.* **113**, 5194–5261, 2013.

[137] K. Dietrich et al. Two-dimensional nature of the active Brownian motion of catalytic microswimmers at solid and liquid interfaces. *New J. Phys.* **19**, 2017.

[138] E. Yariv. "Force-free" electrophoresis? *Phys. Fluids* **18**, 031702, 2006.

[139] A. Choudhary, T. Renganathan, and S. Pushpavanam. Inertial migration of an electrophoretic rigid sphere in a two-dimensional Poiseuille flow. *J. Fluid Mech.* **874**, 856–890, 2019.

[140] A. Boymelgreen, J. Schiffbauer, B. Khusid, and G. Yossifon. Synthetic electrically driven colloids: a platform for understanding collective behavior in soft matter. *Curr. Opin. Colloid Interface Sci.* 101603, 2022.

[141] I. Buttinoni et al. Dynamical clustering and phase separation in suspensions of self-propelled colloidal particles. *Phys. Rev. Lett.* **110**, 238301, 2013.

[142] T. Toyota et al. Listeria-like motion of oil droplets. *Chem. Lett.* **35**, 708–709, 2006.

[143] C. Krüger. "Liquid crystal microswimmers - from single entities to collective dynamics". PhD thesis. Georg-August-Universität Göttingen, 2016.

[144] C. Krüger, C. Bahr, S. Herminghaus, and C. C. Maass. Dimensionality matters in the collective behaviour of active emulsions. *Eur. Phys. J. E.* **39**, 1–9, 2016.

[145] T. Toyota, N. Maru, M. M. Hanczyc, T. Ikegami, and T. Sugawara. Self-propelled oil droplets consuming "fuel" surfactant. *J. Am. Chem. Soc.* **131**, 5012–5013, 2009.

[146] E. Guyon, J.-P. Hulin, L. Petit, and C. D. Mitescu. *Physical hydrodynamics*. Oxford University Press, 2015.

[147] M. Schmitt and H. Stark. Marangoni flow at droplet interfaces: Three-dimensional solution and applications. *Phys. Fluids* **28**, 2016.

[148] C. Jin, C. Krüger, and C. C. Maass. Chemotaxis and autochemotaxis of self-propelling droplet swimmers. *Proc. Natl. Acad. Sci. U.S.A.* **114**, 5089–5094, 2017.

[149] K. Y. Wan and R. E. Goldstein. Rhythmicity, recurrence, and recovery of flagellar beating. *Phys. Rev. Lett.* **113**, 238103, 2014.

[150] P. Langevin. Sur la théorie du mouvement brownien. *Compt. Rendus* **146**, 530–533, 1908.

[151] R. Kubo. Statistical-Mechanical Theory of Irreversible Processes. I. General Theory and Simple Applications to Magnetic and Conduction Problems. *J. Phys. Soc. Jpn.* **12**, 570–586, 1957.

[152] R. Kubo. The fluctuation-dissipation theorem. *Rep. Prog. Phys.* **29**, 255, 1966.

[153] A. Imperio, J. T. Padding, and W. Briels. Force calculation on walls and embedded particles in multiparticle-collision-dynamics simulations. *Phys. Rev. E* **83**, 046704, 2011.

[154] E. Lauga. *The Fluid Dynamics of Cell Motility*. Cambridge University Press, 2020.

[155] J. K. Dhont. *An introduction to dynamics of colloids*. Elsevier, 1996.

[156] S. Chattopadhyay, R. Moldovan, C. Yeung, and X. Wu. Swimming efficiency of bacterium Escherichia coli. *Proc. Natl. Acad. Sci. U.S.A.* **103**, 13712–13717, 2006.

[157] I. M. Jánosi, J. O. Kessler, and V. K. Horváth. Onset of bioconvection in suspensions of Bacillus subtilis. *Phys. Rev. E* **58**, 4793, 1998.

[158] K. Wolff, A. M. Hahn, and H. Stark. Sedimentation and polar order of active bottom-heavy particles. *Eur. Phys. J. E.* **36**, 1–6, 2013.

[159] Y. Fily and M. C. Marchetti. Athermal phase separation of self-propelled particles with no alignment. *Phys. Rev. Lett.* **108**, 235702, 2012.

[160] J. Bialké, H. Löwen, and T. Speck. Microscopic theory for the phase separation of self-propelled repulsive disks. *Europhys. Lett.* **103**, 30008, 2013.

[161] M. Knežević and H. Stark. Collective motion of active particles exhibiting non-reciprocal orientational interactions. *arXiv preprint arXiv:2204.06089* 2022.

[162] M. Theers, E. Westphal, K. Qi, R. G. Winkler, and G. Gompper. Clustering of microswimmers: interplay of shape and hydrodynamics. *Soft Matter* **14**, 8590–8603, 2018.

[163] T. Bäuerle, R. C. Löffler, and C. Bechinger. Formation of stable and responsive collective states in suspensions of active colloids. *Nat. Commun.* **11**, 1–9, 2020.

[164] J. Tailleur and M. Cates. Statistical mechanics of interacting run-and-tumble bacteria. *Phys. Rev. Lett.* **100**, 218103, 2008.

[165] M. E. Cates and J. Tailleur. When are active Brownian particles and run-and-tumble particles equivalent? Consequences for motility-induced phase separation. *Europhys. Lett.* **101**, 20010, 2013.

[166] M. Theers, E. Westphal, G. Gompper, and R. G. Winkler. Modeling a spheroidal microswimmer and cooperative swimming in a narrow slit. *Soft Matter* **12**, 7372–7385, 2016.

[167] A. W. Zantop and H. Stark. Squirmer rods as elongated microswimmers: flow fields and confinement. *Soft Matter* **16**, 6400–6412, 2020.

[168] A. Zöttl. "Hydrodynamics of microswimmers in confinement and in Poiseuille flow". PhD thesis. Technische Universität Berlin, 2014.

[169] E. Lauga, W. R. DiLuzio, G. M. Whitesides, and H. A. Stone. Swimming in circles: motion of bacteria near solid boundaries. *Biophys. J.* **90**, 400–412, 2006.

[170] W. R. DiLuzio et al. Escherichia coli swim on the right-hand side. *Nature* **435**, 1271–1274, 2005.

[171] P. Mueller and J.-L. Thiffeault. Fluid transport and mixing by an unsteady microswimmer. *Phys. Rev. Fluids* **2**, 013103, 2017.

[172] A. J. Mathijssen, R. Jeanneret, and M. Polin. Universal entrainment mechanism controls contact times with motile cells. *Phys. Rev. Fluids* **3**, 033103, 2018.

[173] B. V. Hokmabad et al. Emergence of bimodal motility in active droplets. *Phys. Rev. X* **11**, 011043, 2021.

[174] R. Rusconi and R. Stocker. Microbes in flow. *Curr. Opin. Microbiol.* **25**, 1–8, 2015.

[175] W. Uspal, M. N. Popescu, S. Dietrich, and M. Tasinkevych. Self-propulsion of a catalytically active particle near a planar wall: from reflection to sliding and hovering. *Soft Matter* **11**, 434–438, 2015.

[176] B. Liebchen, D. Marenduzzo, and M. E. Cates. Phoretic interactions generically induce dynamic clusters and wave patterns in active colloids. *Phys. Rev. Lett.* **118**, 268001, 2017.

[177] H. Faxén. Der Widerstand gegen die Bewegung einer starren Kugel in einer zähen Flüssigkeit, die zwischen zwei parallelen ebenen Wänden eingeschlossen ist. *Ann. Phys.* **373**, 89–119, 1922.

[178] J. Blake. "A note on the image system for a Stokeslet in a no-slip boundary". *Mathematical Proceedings of the Cambridge Philosophical Society*. Vol. 70. Cambridge Univ Press. 1971, pp. 303–310.

[179] J. Blake and A. Chwang. Fundamental singularities of viscous flow. *J. Eng. Math.* **8**, 23–29, 1974.

[180] G. Perkins and R. Jones. Hydrodynamic interaction of a spherical particle with a planar boundary: II. Hard wall. *Physica A* **189**, 447–477, 1992.

[181] H. Brenner. The slow motion of a sphere through a viscous fluid towards a plane surface. *Chem. Eng. Sci.* **16**, 242–251, 1961.

[182] N. Liron and S. Mochon. Stokes flow for a stokeslet between two parallel flat plates. *J. Eng. Mech.* **10**, 287–303, 1976.

[183] S. Bhattacharya and J. Bławzdziewicz. Image system for Stokes-flow singularity between two parallel planar walls. *J. Math. Phys.* **43**, 5720–5731, 2002.

[184] R. Jones. Spherical particle in Poiseuille flow between planar walls. *J. Chem. Phys.* **121**, 483–500, 2004.

[185] S. Bhattacharya, J. Bławzdziewicz, and E. Wajnryb. Many-particle hydrodynamic interactions in parallel-wall geometry: Cartesian-representation method. *Physica A* **356**, 294–340, 2005.

[186] M. D. A. Cooley and M. E. O'Neill. On the slow motion generated in a viscous fluid by the approach of a sphere to a plane wall or stationary sphere. *Mathematika* **16**, 37–49, 1969.

[187] T. Ishikawa, M. Simmonds, and T. Pedley. Hydrodynamic interaction of two swimming model micro-organisms. *J. Fluid Mech.* **568**, 119–160, 2006.

[188] R. G. Cox and H. Brenner. The slow motion of a sphere through a viscous fluid towards a plane surface—II Small gap widths, including inertial effects. *Chem. Eng. Sci.* **22**, 1753–1777, 1967.

[189] D. Jeffrey and Y. Onishi. Calculation of the resistance and mobility functions for two unequal rigid spheres in low-Reynolds-number flow. *J. Fluid Mech.* **139**, 261–290, 1984.

[190] A. Roberts. Mechanisms of gravitaxis in Chlamydomonas. *Biol. Bull.* **210**, 78–80, 2006.

[191] A. I. Campbell and S. J. Ebbens. Gravitaxis in spherical Janus swimming devices. *Langmuir* **29**, 14066–14073, 2013.

[192] R. Nash, R. Adhikari, J. Tailleur, and M. Cates. Run-and-tumble particles with hydrodynamics: sedimentation, trapping, and upstream swimming. *Phys. Rev. Lett.* **104**, 258101, 2010.

[193] I. Jung, K. Guevorkian, and J. M. Valles. Trapping of Swimming Microorganisms at Lower Surfaces by Increasing Buoyancy. *Phys. Rev. Lett.* **113**, 218101, 2014.

[194] M. Verworn. *Psycho-physiologische Protisten-Studien: Experimentelle Untersuchungen.* G. Fischer, 1889.

[195] A. Roberts. The mechanics of gravitaxis in Paramecium. *J. Exp. Biol.* **213**, 4158–4162, 2010.

[196] I. M. Jánosi, A. Czirók, D. Silhavy, and A. Holczinger. Is bioconvection enhancing bacterial growth in quiescent environments? *Environ. Microbiol.* **4**, 525–531, 2002.

[197] N. Sato, K. Sato, and M. Toyoshima. Analysis and modeling of the inverted bioconvection in Chlamydomonas reinhardtii: emergence of plumes from the layer of accumulated cells. *Heliyon* **4**, e00586, 2018.

[198] B. Cichocki and K. Hinsen. Stokes drag on conglomerates of spheres. *Phys. Fluids* **7**, 285–291, 1995.

[199] M. Hennes, K. Wolff, and H. Stark. Self-induced polar order of active Brownian particles in a harmonic trap. *Phys. Rev. Lett.* **112**, 238104, 2014.

[200] A. Sokolov, R. E. Goldstein, F. I. Feldchtein, and I. S. Aranson. Enhanced mixing and spatial instability in concentrated bacterial suspensions. *Phys. Rev. E* **80**, 031903, 2009.

[201] S. Kitsunezaki, R. Komori, and T. Harumoto. Bioconvection and front formation of Paramecium tetraurelia. *Phys. Rev. E* **76**, 046301, 2007.

[202] Y. Mogami, A. Yamane, A. Gino, and S. A. Baba. Bioconvective pattern formation of Tetrahymena under altered gravity. *J. Exp. Biol.* **207**, 3349–3359, 2004.

[203] M. Bees and N. Hill. Wavelengths of bioconvection patterns. *J. Exp. Biol.* **200**, 1515–1526, 1997.

[204] C. Williams and M. Bees. Photo-gyrotactic bioconvection. *J. Fluid Mech.* **678**, 41–86, 2011.

[205] N. Hill and T. Pedley. Bioconvection. *Fluid Dyn. Res.* **37**, 1, 2005.

[206] M. S. Plesset and H. Winet. Bioconvection patterns in swimming microorganism cultures as an example of Rayleigh-Taylor instability. *Nature* **248**, 441, 1974.

[207] S. Childress, M. Levandowsky, and E. Spiegel. Pattern formation in a suspension of swimming microorganisms: equations and stability theory. *J. Fluid Mech.* **69**, 591–613, 1975.

[208] A. C. Newell and J. A. Whitehead. Finite bandwidth, finite amplitude convection. *J. Fluid Mech.* **38**, 279–303, 1969.

[209] N. Hill, T. Pedley, and J. O. Kessler. Growth of bioconvection patterns in a suspension of gyrotactic micro-organisms in a layer of finite depth. *J. Fluid Mech.* **208**, 509–543, 1989.

[210] S. Ghorai and N. Hill. Development and stability of gyrotactic plumes in bioconvection. *J. Fluid Mech.* **400**, 1–31, 1999.

[211] N. Desai and A. M. Ardekani. Modeling of active swimmer suspensions and their interactions with the environment. *Soft Matter* 6033–6050, 2017.

[212] D. P. Singh, W. E. Uspal, M. N. Popescu, L. G. Wilson, and P. Fischer. Photogravitactic microswimmers. *Adv. Funct. Mat.* **28**, 1706660, 2018.

[213] V. Girault and P.-A. Raviart. *Finite element approximation of the Navier-Stokes equations*. Springer Berlin, 1979.

[214] I. Demirdžić, Ž. Lilek, and M. Perić. A collocated finite volume method for predicting flows at all speeds. *Int. J. Numer. Meth. Fl.* **16**, 1029–1050, 1993.

[215] Y. Nakayama and R. Yamamoto. Simulation method to resolve hydrodynamic interactions in colloidal dispersions. *Phys. Rev. E* **71**, 036707, 2005.

[216] H. Shum, E. Gaffney, and D. Smith. Modelling bacterial behaviour close to a no-slip plane boundary: the influence of bacterial geometry. *Proc. R. Soc. A* **466**, 1725–1748, 2010.

[217] P. Hoogerbrugge and J. Koelman. Simulating microscopic hydrodynamic phenomena with dissipative particle dynamics. *Europhys. Lett.* **19**, 155, 1992.

[218] B. Dünweg and A. J. Ladd. "Lattice Boltzmann simulations of soft matter systems". *Advanced computer simulation approaches for soft matter sciences III*. Springer, 2009, pp. 89–166.

[219] U. Frisch, B. Hasslacher, and Y. Pomeau. Lattice-gas automata for the Navier-Stokes equation. *Phys. Rev. Lett.* **56**, 1505, 1986.

[220] B. Hasslacher et al. Lattice gas hydrodynamics in two and three dimensions. *Complex Syst.* **1**, 649–708, 1987.

[221] H. Noguchi, N. Kikuchi, and G. Gompper. Particle-based mesoscale hydrodynamic techniques. *Europhys. Lett.* **78**, 10005, 2007.

[222] R. Kapral. Multiparticle collision dynamics: Simulation of complex systems on mesoscales. *Adv. Chem. Phys.* **140**, 89, 2008.

[223] M. Ripoll, R. Winkler, and G. Gompper. Star polymers in shear flow. *Phys. Rev. Lett.* **96**, 188302, 2006.

[224] D. A. Reid, H. Hildenbrandt, J. Padding, and C. Hemelrijk. Flow around fishlike shapes studied using multiparticle collision dynamics. *Phys. Rev. E* **79**, 046313, 2009.

[225] C. Prohm, M. Gierlak, and H. Stark. Inertial microfluidics with multi-particle collision dynamics. *Eur. Phys. J. E* **35**, 1–10, 2012.

[226] Y.-G. Tao and R. Kapral. Swimming upstream: self-propelled nanodimer motors in a flow. *Soft Matter* **6**, 756–761, 2010.

[227] H. Noguchi and G. Gompper. Dynamics of vesicle self-assembly and dissolution. *J. Chem. Phys.* **125**, 164908, 2006.

[228] M. T. Downton and H. Stark. Simulation of a model microswimmer. *J. Phys.: Condens. Mat.* **21**, 204101, 2009.

[229] I. O. Götze and G. Gompper. Mesoscale simulations of hydrodynamic squirmer interactions. *Phys. Rev. E* **82**, 041921, 2010.

[230] S. Mandal and M. G. Mazza. Multiparticle collision dynamics simulations of a squirmer in a nematic fluid. *Eur. Phys. J. E.* **44**, 1–10, 2021.

[231] A. Zöttl and H. Stark. Simulating squirmers with multiparticle collision dynamics. *Eur. Phys. J. E.* **41**, 61, 2018.

[232] T. Ihle and D. M. Kroll. Stochastic rotation dynamics. I. Formalism, Galilean invariance, and Green-Kubo relations. *Phys. Rev. E* **67**, 066705, 2003.

[233] H. Noguchi and G. Gompper. Transport coefficients of off-lattice mesoscale-hydrodynamics simulation techniques. *Phys. Rev. E* **78**, 016706, 2008.

[234] H. C. Andersen. Molecular dynamics simulations at constant pressure and/or temperature. *J. Chem. Phys.* **72**, 2384–2393, 1980.

[235] I. O. Götze, H. Noguchi, and G. Gompper. Relevance of angular momentum conservation in mesoscale hydrodynamics simulations. *Phys. Rev. E* **76**, 046705, 2007.

[236] J. F. Ryder. "Mesoscopic simulations of complex fluids". PhD thesis. University of Oxford, 2005.

[237] A. Malevanets and R. Kapral. Solute molecular dynamics in a mesoscale solvent. *J. Chem. Phys.* **112**, 7260–7269, 2000.

[238] C. Pooley and J. Yeomans. Kinetic theory derivation of the transport coefficients of stochastic rotation dynamics. *J. Phys. Chem. B* **109**, 6505–6513, 2005.

[239] H. B. Callen. *Thermodynamics and an Introduction to Thermostatistics*. 1998.

[240] A. W. Zantop and H. Stark. Multi-particle collision dynamics with a non-ideal equation of state. I. *J. Chem. Phys.* **154**, 024105, 2021.

[241] A. W. Zantop and H. Stark. Multi-particle collision dynamics with a non-ideal equation of state. II. Collective dynamics of elongated squirmer rods. *J. Chem. Phys.* **155**, 134904, 2021.

[242] T. Ihle, E. Tüzel, and D. M. Kroll. Equilibrium calculation of transport coefficients for a fluid-particle model. *Phys. Rev. E* **72**, 046707, 2005.

[243] N. Kikuchi, C. Pooley, J. Ryder, and J. Yeomans. Transport coefficients of a mesoscopic fluid dynamics model. *J. Chem. Phys.* **119**, 6388–6395, 2003.

[244] J. D. Weeks, D. Chandler, and H. C. Andersen. Role of repulsive forces in determining the equilibrium structure of simple liquids. *J. Chem. Phys.* **54**, 5237–5247, 1971.

[245] L. Verlet. Computer "experiments" on classical fluids. I. Thermodynamical properties of Lennard-Jones molecules. *Phys. Rev.* **159**, 98, 1967.

[246] J. T. Padding, A. Wysocki, H. Löwen, and A. A. Louis. Stick boundary conditions and rotational velocity auto-correlation functions for colloidal particles in a coarse-grained representation of the solvent. *J. Phys.: Condens. Mat.* **17**, S3393, 2005.

[247] J. Padding and A. Louis. Hydrodynamic interactions and Brownian forces in colloidal suspensions: Coarse-graining over time and length scales. *Phys. Rev. E* **74**, 031402, 2006.

[248] A. Lamura, G. Gompper, T. Ihle, and D. Kroll. Multi-particle collision dynamics: Flow around a circular and a square cylinder. *Europhys. Lett.* **56**, 319, 2001.

[249] J. T. Hynes. Statistical mechanics of molecular motion in dense fluids. *Annu. Rev. Phys. Chem.* **28**, 301–321, 1977.

[250] S. H. Lee and R. Kapral. Friction and diffusion of a Brownian particle in a mesoscopic solvent. *J. Chem. Phys.* **121**, 11163–11169, 2004.

[251] B. Dünweg and K. Kremer. Molecular dynamics simulation of a polymer chain in solution. *J. Chem. Phys.* **99**, 6983–6997, 1993.

[252] M. Wagner and M. Ripoll. Solvent-induced depletion interactions in multiparticle collision dynamic simulations. *Int. J. Mod. Phys. C* **30**, 1941008, 2019.

[253] S. Ramaswamy, R. Aditi Simha, and J. Toner. Active nematics on a substrate: Giant number fluctuations and long-time tails. *Europhys. Lett.* **62**, 196, 2003.

[254] L. Giomi and M. C. Marchetti. Polar patterns in active fluids. *Soft Matter* **8**, 129–139, 2012.

[255] G. O'Toole, H. B. Kaplan, and R. Kolter. Biofilm formation as microbial development. *Annu. Rev. Microbiol.* **54**, 49–79, 2000.

[256] S. Babel, H. Löwen, and A. M. Menzel. Dynamics of a linear magnetic "microswimmer molecule". *Europhys. Lett.* **113**, 58003, 2016.

[257] W.-T. L. Fan, O. S. Pak, and M. Sandoval. Ellipsoidal Brownian self-driven particles in a magnetic field. *Phys. Rev. E* **95**, 032605, 2017.

[258] S. Klumpp, C. T. Lefèvre, M. Bennet, and D. Faivre. Swimming with magnets: from biological organisms to synthetic devices. *Phys. Rep.* **789**, 1–54, 2019.

[259] A. Cēbers and M. Ozols. Dynamics of an active magnetic particle in a rotating magnetic field. *Phys. Rev. E* **73**, 021505, 2006.

[260] A. Ghosh and P. Fischer. Controlled propulsion of artificial magnetic nanostructured propellers. *Nano Lett.* **9**, 2243–2245, 2009.

[261] D. A. Bazylinski et al. Magnetococcus marinus gen. nov., sp. nov., a marine, magnetotactic bacterium that represents a novel lineage (Magnetococcaceae fam. nov., Magnetococcales ord. nov.) at the base of the Alphaproteobacteria. *Int. J. Syst. Evol. Microbiol.* **63**, 801–808, 2013.

[262] A. Zöttl and H. Stark. Nonlinear dynamics of a microswimmer in Poiseuille flow. *Phys. Rev. Lett.* **108**, 218104, 2012.

[263] A. Zöttl and H. Stark. Periodic and quasiperiodic motion of an elongated microswimmer in Poiseuille flow. *Eur. Phys. J. E.* **36**, 4, 2013.

[264] J. F. Jikeli et al. Sperm navigation along helical paths in 3D chemoattractant landscapes. *Nat. Commun.* **6**, 2015.

[265] G.-J. Li and A. M. Ardekani. Hydrodynamic interaction of microswimmers near a wall. *Phys. Rev. E* **90**, 013010, 2014.

[266] J. S. Lintuvuori, A. T. Brown, K. Stratford, and D. Marenduzzo. Hydrodynamic oscillations and variable swimming speed in squirmers close to repulsive walls. *Soft Matter* **12**, 7959–7968, 2016.

[267] Q. Brosseau et al. Metallic microswimmers driven up the wall by gravity. *Soft Matter* **17**, 6597–6602, 2021.

[268] S. Wakiya. Research report 9. *Faculty of Engineering, Niigata University, Japan* 1960.

[269] A. P. Berke, L. Turner, H. C. Berg, and E. Lauga. Hydrodynamic attraction of swimming microorganisms by surfaces. *Phys. Rev. Lett.* **101**, 038102, 2008.

[270] J. L. Moran and J. D. Posner. Phoretic self-propulsion. *Annu. Rev. Fluid Mech.* **49**, 511–540, 2017.

[271] M. Cencini, G. Boffetta, M. Borgnino, and F. De Lillo. Gyrotactic phytoplankton in laminar and turbulent flows: a dynamical systems approach. *Eur. Phys. J. E* **42**, 1–15, 2019.

[272] T. Ishikawa, T. Pedley, K. Drescher, and R. E. Goldstein. Stability of dancing Volvox. *J. Fluid Mech.* **903**, 2020.

[273] D. Saintillan and M. J. Shelley. Instabilities and pattern formation in active particle suspensions: kinetic theory and continuum simulations. *Phys. Rev. Lett.* **100**, 178103, 2008.

[274] G. Kokot and A. Snezhko. Manipulation of emergent vortices in swarms of magnetic rollers. *Nat. Commun.* **9**, 1–7, 2018.

[275] P. Watnick and R. Kolter. Biofilm, city of microbes. *J. Bacteriol.* **182**, 2675–2679, 2000.

[276] A. Genin, J. S. Jaffe, R. Reef, C. Richter, and P. J. Franks. Swimming against the flow: a mechanism of zooplankton aggregation. *Science* **308**, 860–862, 2005.

[277] A. Théry et al. Self-organisation and convection of confined magnetotactic bacteria. *Sci. Rep.* **10**, 1–9, 2020.

[278] H.-P. Zhang, A. Be'er, E.-L. Florin, and H. L. Swinney. Collective motion and density fluctuations in bacterial colonies. *Proc. Natl. Acad. Sci. U.S.A.* **107**, 13626–13630, 2010.

[279] F. R. Koessel and S. Jabbari-Farouji. Controlling stability and transport of magnetic microswimmers by an external field. *Europhys. Lett.* **125**, 28001, 2019.

[280] N. Uchida and R. Golestanian. Synchronization and collective dynamics in a carpet of microfluidic rotors. *Phys. Rev. Lett.* **104**, 178103, 2010.

[281] E. Lushi, H. Wioland, and R. E. Goldstein. Fluid flows created by swimming bacteria drive self-organization in confined suspensions. *Proc. Natl. Acad. Sci. U.S.A.* **111**, 9733–9738, 2014.

[282] J.-T. Kuhr, J. Blaschke, F. Rühle, and H. Stark. Collective sedimentation of squirmers under gravity. *Soft Matter* **13**, 7548–7555, 2017.

[283] J.-T. Kuhr, F. Rühle, and H. Stark. Collective dynamics in a monolayer of squirmers confined to a boundary by gravity. *Soft Matter* **15**, 5685–5694, 2019.

[284] Z. Shen and J. S. Lintuvuori. Gravity induced formation of spinners and polar order of spherical microswimmers on a surface. *Phys. Rev. Fluids* **4**, 123101, 2019.

[285] C. Hosoya, A. Akiyama, A. Kage, S. A. Baba, and Y. Mogami. Reverse bioconvection of Chlamydomonas in the hyper-density medium. *Biol. Sci. Space* **24**, 145–152, 2010.

[286] I. A. Lasso and P. Weidman. Stokes drag on hollow cylinders and conglomerates. *Phys. Fluids* **29**, 3921–3934, 1986.

[287] M. Reichert and H. Stark. Hydrodynamic coupling of two rotating spheres trapped in harmonic potentials. *Phys. Rev. E* **69**, 031407, 2004.

[288] M. Reichert and H. Stark. Circling particles and drafting in optical vortices. *J. Phys.: Condens. Mat.* **16**, S4085, 2004.

[289] A. A. Evans, T. Ishikawa, T. Yamaguchi, and E. Lauga. Orientational order in concentrated suspensions of spherical microswimmers. *Phys. Fluids* **23**, 111702, 2011.

[290] G. Pessot, H. Löwen, and A. M. Menzel. Binary pusher–puller mixtures of active microswimmers and their collective behaviour. *Mol. Phys.* **116**, 3401–3408, 2018.

[291] A. Harashima, M. Watanabe, and I. Fujishiro. Evolution of bioconvection patterns in a culture of motile flagellates. *Phys. Fluids* **31**, 764–775, 1988.

[292] S. Bianchi, F. Saglimbeni, and R. Di Leonardo. Holographic imaging reveals the mechanism of wall entrapment in swimming bacteria. *Phys. Rev. X* **7**, 011010, 2017.

[293] A. J. Mathijssen et al. Oscillatory surface rheotaxis of swimming E. coli bacteria. *Nat. Commun.* **10**, 1–12, 2019.

[294] K. Drescher, R. E. Goldstein, N. Michel, M. Polin, and I. Tuval. Direct measurement of the flow field around swimming microorganisms. *Phys. Rev. Lett.* **105**, 168101, 2010.

[295] K. Drescher, J. Dunkel, L. H. Cisneros, S. Ganguly, and R. E. Goldstein. Fluid dynamics and noise in bacterial cell–cell and cell–surface scattering. *Proc. Natl. Acad. Sci. U.S.A.* **108**, 10940–10945, 2011.

[296] F. Peruani et al. Collective motion and nonequilibrium cluster formation in colonies of gliding bacteria. *Phys. Rev. Lett.* **108**, 098102, 2012.

[297] B. V. Hokmabad. "Active Emulsions. Physicochemical Hydrodynamics and Collective Behavior". PhD thesis. Georg-August-Universität Göttingen, 2020.

[298] K. E. Peyer, L. Zhang, and B. J. Nelson. Bio-inspired magnetic swimming microrobots for biomedical applications. *Nanoscale* **5**, 1259–1272, 2013.

[299] P. J. Vach, D. Walker, P. Fischer, P. Fratzl, and D. Faivre. Pattern formation and collective effects in populations of magnetic microswimmers. *J. Phys. D Appl. Phys.* **50**, 11LT03, 2017.

[300] R. Benzi et al. Population dynamics in compressible flows. *Eur. Phys. J. Spec. Top.* **204**, 57–73, 2012.

[301] K. Ishimoto and E. A. Gaffney. Squirmer dynamics near a boundary. *Phys. Rev. E* **88**, 062702, 2013.

[302] F. Fadda, J. J. Molina, and R. Yamamoto. Dynamics of a chiral swimmer sedimenting on a flat plate. *Phys. Rev. E* **101**, 052608, 2020.

[303] P. M. Chaikin, T. C. Lubensky, and T. A. Witten. *Principles of condensed matter physics*. Cambridge University Press, 1995.

[304] A. A. Fragkopoulos et al. Self-generated oxygen gradients control collective aggregation of photosynthetic microbes. *J. R. Soc. Interface* **18**, 20210553, 2021.

[305] R. Di Leonardo, D. Dell'Arciprete, L. Angelani, and V. Iebba. Swimming with an image. *Phys. Rev. Lett.* **106**, 038101, 2011.

[306] J. Hu, A. Wysocki, R. G. Winkler, and G. Gompper. Physical sensing of surface properties by microswimmers–directing bacterial motion via wall slip. *Sci. Rep.* **5**, 1–7, 2015.

[307] C. Feng, J. J. Molina, M. S. Turner, and R. Yamamoto. Dynamics of microswimmers near a soft penetrable interface. *arXiv preprint arXiv:2205.10919* 2022.

[308] J. S. Lintuvuori, A. Würger, and K. Stratford. Hydrodynamics defines the stable swimming direction of spherical squirmers in a nematic liquid crystal. *Phys. Rev. Lett.* **119**, 068001, 2017.

[309] S. Zhou et al. Dynamic states of swimming bacteria in a nematic liquid crystal cell with homeotropic alignment. *New J. Phys.* **19**, 055006, 2017.

[310] T. N. Shendruk and J. M. Yeomans. Multi-particle collision dynamics algorithm for nematic fluids. *Soft Matter* **11**, 5101–5110, 2015.

[311] S. Heckel et al. Beyond Janus geometry: Characterization of flow fields around nonspherical photocatalytic microswimmers. *Adv. Sci.* **9**, 2105009, 2022.

[312] P. Bayati, M. N. Popescu, W. E. Uspal, S. Dietrich, and A. Najafi. Dynamics near planar walls for various model self-phoretic particles. *Soft Matter* **15**, 5644–5672, 2019.

[313] S. B. Babu and H. Stark. Modeling the locomotion of the African trypanosome using multi-particle collision dynamics. *New J. Phys.* **14**, 085012, 2012.

[314] J. Hu, M. Yang, G. Gompper, and R. G. Winkler. Modelling the mechanics and hydrodynamics of swimming E. coli. *Soft Matter* **11**, 7867–7876, 2015.

[315] S. Muiños-Landin, K. Ghazi-Zahedi, and F. Cichos. Reinforcement learning of artificial microswimmers. *arXiv preprint arXiv:1803.06425* 2018.

[316] B. Liebchen and H. Löwen. Optimal navigation strategies for active particles. *Europhys. Lett.* **127**, 34003, 2019.

[317] E. Schneider and H. Stark. Optimal steering of a smart active particle. *Europhys. Lett.* **127**, 64003, 2019.

[318] S. Colabrese, K. Gustavsson, A. Celani, and L. Biferale. Flow navigation by smart microswimmers via reinforcement learning. *Phys. Rev. Lett.* **118**, 158004, 2017.

[319] A. Daddi-Moussa-Ider, H. Löwen, and B. Liebchen. Hydrodynamics can determine the optimal route for microswimmer navigation. *Commun. Phys.* **4**, 1–11, 2021.

Acknowledgment

At this point, I would like to express my gratitude to all who supported me during the last years and without whom none of this work would have been possible.

First and foremost, Prof. Dr. Holger Stark has been supporting me for many years of my academic life and has introduced me to a wide range of interesting subjects and projects within the realms of soft matter physics, active systems and hydrodynamics. He has guided me through this doctoral project and I am grateful for his supervision. In particular, he has always recognized and respected any particular circumstances of my life and created good conditions for me to work under these circumstances. For this I am very thankful.

Furthermore, I thank Prof. Dr. Andreas Menzel for kindly examining this work.

It has been my privilege to collaborate with my distinguished colleagues Dr. Jan-Timm Kuhr, Dr. Johannes Blaschke, and Arne W. Zantop on MPCD simulations of squirmers. They have always supported my work, provided time for discussions and always had an open ear for questions. The same applies to Dr. Christian Schaaf on anything involving IT or inertial microfluidics.

Special thanks go to the collaborators and supervisors of previous projects, who played a big role in getting me acquainted with research and kept me connected with a rich variety of subjects. I want to specifically mention Dr. Philipp Kählitz, Prof. Dr. Michael Schmiedeberg, Dr. Christopher Prohm, Prof. Dr. Fredi Tröltzsch, Dr. Akash Choudhary, and Subhechchha Paul.

I thank the German Research Foundation (DFG) for funding under the priority program SPP 1724, and the program's chairman Prof. Dr. Gerhard Gompper. Furthermore, many numerical simulations would not have been possible without the resources provided by the HLRN.

The help and support of my colleagues over the years has been invaluable. Furthermore, numerous friends and relatives have supported me, counseled me or kept me company during those years. An extra thanks goes to my parents who have been incredibly generous with every and any imaginable resource. In summary, I want to express my gratitude, to all of the following: Reinier van Buel, Ryan Daniel, Julia Eckert, Josua Grawitter, Eva and Frank Huhn, Therese and Paul Huhn, Dr. Philipp Kanehl, Heike Klemz, Dr. Miloš Knežević, Agnes Künzel, Dr. Rico Raber, Boitumelo and Eberhard Rühle, Brigitte and Siegfried Rühle, Lilly Rühle, Mónica Sánchez Vargas, Andrea Schulze, Dr. Maximilian Seyrich, Shahajhan Sorathiya, Aylin Yüksel, and Maria Zeitz.